RIVISTA DEL NUOVO CIMENTO Vol. 34, N. 5 2011
DOI 10.1393/ncr/i2011-10065-4

Transport properties of supercooled confined water

F. Mallamace([1])([2])([3])(*), P. Baglioni([4]), C. Corsaro([1]), J. Spooren([1]), H. E. Stanley([3]) and S.-H. Chen([2])

([1]) *Dipartimento di Fisica and CNISM, Università di Messina - I-98166, Messina, Italy*
([2]) *Department of Nuclear Science and Engineering, Massachusetts Institute of Technology Cambridge, MA 02139, USA*
([3]) *Department of Physics, Center for Polymer Studies, Boston University Boston, MA 02215, USA*
([4]) *Dipartimento di Chimica, Università di Firenze and CSGI Via Lastruccia 3, 50019 Firenze, Italy*

(ricevuto l'11 Gennaio 2011)

Summary. — We present an overview of recent experiments performed on water in the deeply supercooled region, a temperature region of fundamental importance in the science of water. We examine data generated by nuclear magnetic resonance, quasi-elastic neutron scattering, Fourier-transform infrared spectroscopy, and Raman spectroscopy, and study water confined in nanometer-scale environments. When contained within small pores, water does not crystallize and can be supercooled well below its homogeneous nucleation temperature T_H. On this basis, it is possible to carry out a careful analysis of the well-known thermodynamic anomalies of water. Studying the temperature and pressure dependencies of water dynamics, we show that the liquid-liquid phase transition (LLPT) hypothesis represents a reliable model for describing liquid water. In this model, liquid water is a mixture of two different local structures: a low density liquid (LDL) and a high-density liquid (HDL). The LLPT line terminates at a low-T liquid-liquid critical point. We discuss the following experimental findings: i) the crossover from non-Arrhenius behavior at high T to Arrhenius behavior at low T in transport parameters; ii) the breakdown of the Stokes-Einstein relation; iii) the existence of a Widom line, which is the locus of points corresponding to a maximum correlation length in the P-T phase diagram and which ends in the liquid-liquid critical point; iv) the direct observation of the LDL phase; and v) the minimum in the density at approximately 70 K below the temperature of the density maximum. In our opinion these results strongly support the LLPT hypothesis. *All of the basic science and technology community should be impressed by the fact that, although the few ideas (apparently elementary) developed concerning water approximately 27 centuries ago have changed very little up to now, because of the current expansion in our knowledge in this area, they can begin to change in the near future.*

PACS 65.20.-w – Thermal properties of liquids.
PACS 05.60.-k – Transport processes.
PACS 87.15.-v – Biomolecules: structure and physical properties.
PACS 83.85.Hf – X-ray and neutron scattering.

(*) Corresponding author: francesco.mallamace@unime.it

© Società Italiana di Fisica

254 1. Introduction
260 2. Current hypotheses
263 2˙1. Selected experimental results
263 2˙2. Selected results from simulations
264 3. Understanding "static heterogeneities"
265 3˙1. Potentials with two characteristic length scales: physical arguments
267 3˙2. Potentials with two characteristic length scales: tractable models
269 4. Understanding "dynamic heterogeneities"
271 5. Possible significance of the Widom line
272 6. Methods employed to study dynamic crossover in confined water
273 7. Hamiltonian model of water
275 8. Recent experiments on confined water
277 8˙1. The sample
278 8˙2. Nuclear Magnetic Resonance
280 8˙3. The neutron scattering
289 8˙4. Fourier transform infrared spectroscopy
291 9. The fragile-to-strong crossover (dynamical crossover) and the breakdown of the Stokes-Einstein relation
295 10. The low-density-liquid phase and the water density minimum
299 11. The specific heat and the glass transition
302 11˙1. The non-ergodicity and measurement methods of the specific heat in glass forming systems
309 11˙2. Other calorimetric methods and the water heat capacity
322 12. The NMR technique as a method to measure the configurational heat capacity
327 13. Water confined in biomolecules
330 14. The NMR and FTIR results on the two dynamical crossovers of biological macromolecules
338 15. The low-temperature (protein glass transition) dynamical crossover
338 15˙1. Neutron results
346 16. The violation of the Stokes-Einstein relation
346 17. The simulation results
358 18. The high-temperature (protein denaturation) dynamical crossover
368 19. Concluding remarks

1. – Introduction

Water in its various forms is the substance most essential to life on earth. From ancient times, understanding the role of water in its many aspects has been a perennial quest in both philosophy and science. Four millennia ago, Homer in the Iliad (Iliad XIV vv 201 and 244) described water as an "ocean," a big river that circumscribes and encircles the "fecund earth," and "[that] from which all the gods proceed." In his First Book on Metaphysics (Metaph. A 3, 983 b 6), Aristotle initiated Western philosophy's search for the "principle element" of all things, an element out of which all other things would be generated and into which they would be resolved at their end. Though it all the element itself would be unchanged. Thales of Miletus (VI century BC), "the father of geometry," often considered the first philosopher of Western history, also sought this principle element and came to the conclusion that it was indeed water. Both Aristotle and Theophrastus in response to the Thales speculation and based on their own empirical observations concurred that water was the "principle" of biology and thus of all living

things. Sometime later (V century BC), water came to be considered one of the four root elements —earth, air, fire, and water— constituting all cosmological material existence.

On earth, water is ubiquitous —oceans, seas, lakes, rivers, polar ice caps, glaciers, clouds— and every aspect of human life is controlled or influenced by water. Biological processes cannot take place without it. It exists in approximately 13 different crystalline forms, some of which are stable in certain temperature-pressure ranges, while others remain metastable. Although the stable form of water at sufficiently low temperatures is crystalline, inside the stable crystalline temperature range, water can also exist in liquid form. When this occurs, water is said to be supercooled. The supercooled state is metastable (its equilibrium is precarious), and a simple perturbation such as a tiny particle of dissolved impurity or a gentle mechanical shake can trigger its collapse into the stable crystalline phase. Supercooled water occurs naturally in the form of small droplets in clouds. If liquid water is cooled quickly enough, the crystalline phase can be bypassed and a non-crystalline (amorphous) solid, *i.e.*, a glass, is the result. This amorphous glass phase of water is polymorphic, that is, it can exist in two different forms. It is ironic that forming glassy water in a laboratory requires an elaborate procedure because glassy water is undoubtably the most common form of water in the universe. It constitutes the bulk of matter in comets, is thought to play a role in planetary activity, and has been observed as a frost in stellar dust. Scientists puzzle over the anomalous properties of glassy water: when it is cooled it becomes more compressible, when compressed it is less viscous and, when cooled sufficiently, it expands.

Despite the many centuries of research on water and water-based systems, its complex and unusual properties, anomalous when compared to "normal" liquids, are far from being understood. Water research constitutes a borderline scientific area that has intrigued physicists, chemists, and biologists working in many subfields. When physicists study the properties of water, they use sophisticated experimental methods and highly developed tools of statistical physics. These include the theories and methods developed to study critical and phase separation phenomena, aggregation kinetics, clustering processes, constrained dynamics, polymers, colloids, amphiphiles, liquid crystals, molecular motors, turbulence, systems with hierarchical structures of dynamics, and complex systems in general [1]. The same approaches are used in the study of such biological systems as proteins, enzymes, DNA, cells, and systems of modern advanced molecular biology [1]. In essense, these studies agree with the Greek philosophers in that water is essential to life, and that water and biological processes can, in principle, be placed within a unified conceptual framework that is able to explain life phenomena and living systems.

In current research, and from the point of view of condensed matter physics in particular, there are several active problems of fundamental interest concerning the relevant chemistry and physics of water. Among these are the anomalies exhibited by water in its thermodynamical response functions, the localization (or the existence) of its glass transition, the way in which it forms a glass and, when in a pure substance, the existence of a second critical point. All of these problems have biological relevance and, if carefully defined, can point the way to a deeper comprehension of the many biological processes in which water plays an essential role. Our study of the anomalies of water below its melting temperature focuses on its metastable states, *i.e.*, its supercooled regime and its two glassy states.

Although water is generally associated with bulk water —*e.g.*, oceans, lakes, rivers, reservoirs, or aqueducts— our focus is on biological water, *i.e.*, water located in such living systems as muscles, trees, plants, cells, membranes, and proteins. In biological phenomena, water may be located on surfaces, in little cavities or bilayers, inside macro-

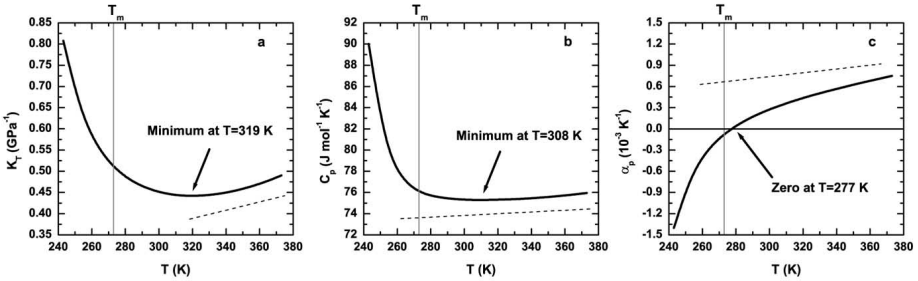

Fig. 1. – Examples of water's thermodynamic anomalies. Dependence on temperature of (a) the isothermal compressibility K_T, (b) the isobaric specific heat C_P and (c) the coefficient of thermal expansion α_P. The behavior of water is indicated by the solid line; that of a typical liquid by the dashed line. The anomalous thermodynamics and fluctuations of liquid water are apparent above the melting temperature T_m and they become more striking as one supercools below T_m. Data from [7, 8].

molecules, vesicles, or emulsions, or near specific chemical groups (*e.g.*, hydration water). It tends to be distributed on surfaces or confined in microscopic or mesoscopic structures. One example of the complexity of water in biology is that of water-amphiphile systems. As is well known, amphiphilic molecules are nearly linear molecules characterized by a hydrophilic head and hydrophobic terminal groups that can organize into biological membranes. When water is mixed with these systems, the competition between hydrophilicity and hydrophobicity causes an entropy decrease that gives rise to the build-up of micellar structures that, depending on variables such as temperature and concentration, can assume different geometric forms (spheres, ellipsoids, cylinders, layers and bilayers). In addition, hydrophobicity and hydrophilicity have different effects on the local structure of water; hydrophilicity enhances this local structure but hydrophobicity weakens it. It thus seems clear that the complexity of physico-chemical phenomena is due to water when it hydrates a biological structure, *e.g.*, in proteins there are many hydrophilic and hydrophobic groups distributed with some specific order inside the macromolecule. This suggests at least two questions: i) If biological water is a form of confined water, does the physics of biological water differ from that of bulk water? ii) Does water drive the properties of a biological system or do those properties function independently of water? We will attempt to answer both questions.

The first anomalous property of liquid water was observed 300 years ago [2]. Although most liquids contract as temperature decreases, liquid bulk water begins to expand when its temperature drops below 277 K. Indeed, a simple kitchen experiment demonstrates that the bottom layer of a glass of unstirred iced water remains at 277 K while colder layers of 273 K water float on top (see fig. 1 of ref. [3]). The anomalous properties of liquid bulk water become more pronounced in the supercooled region below 273 K (the melting temperature, T_m) [4-6].

A salient characteristic of liquid water at ambient pressure is that its thermodynamic response functions (response of density ρ or of the entropy S to changes in temperature T or pressure P) sharply increase in magnitude upon cooling. As shown in fig. 1, the increase begins at 319 K for the isothermal compressibility (fig. 1(a)) $K_T = (\partial \ln \rho / \partial \ln P)_T$, at 308 K for the isobaric specific heat (fig. 1(b)) $C_P = T(\partial S/\partial T)_P$, and at 277 K for the magnitude of the thermal expansion coefficient (fig. 1(c)) $\alpha_P = -(\partial \ln \rho / \partial T)_P$. In partic-

ular, while the anomalies displayed by liquid water are apparent above T_m, they become more striking as one supercools below T_m. In fact, extrapolated from their values at moderately supercooled states, below the lowest temperatures measurable, all these functions appear to diverge at a singular temperature around $T_S = 228\,\mathrm{K}$ [4, 9].

Each thermodynamic response function is associated with microscopic fluctuations. For example, the isothermal compressibility is proportional to volume fluctuations (δV): $K_T = \langle(\delta V)^2\rangle/k_B TV$, where V is the mean value of the fluctuating volume for a fixed number of molecules, k_B is Boltzmann's constant; at the same time C_P is proportional to the entropy fluctuations at fixed pressure: $C_P = \langle(\delta S)^2\rangle/k_B$ and $\alpha_P = \langle\delta S\delta V\rangle/k_B TV$ reflects the entropy and volume cross-correlations. In typical liquids, density and entropy fluctuations become smaller as the temperature decreases. In water the fluctuations of these quantities become more pronounced as the temperature decreases. Volume and entropy fluctuations in most liquids are positively correlated: an increase in volume results in a corresponding increase in entropy. In water for $T < 277\,\mathrm{K}$, δS and δV are anti-correlated, thus an increase in volume brings about a decrease in entropy.

The microscopic origin of these anti-correlations, which become increasingly pronounced in the supercooled state, lies in the tetrahedral symmetry of the local order around each water molecule. Each water has two positively charged lobes containing the protons and two lone pairs of electrons. Because of this structure, as water is cooled, the nearest-neighbor molecules begin to order themselves, via a hydrogen bonding (HB) interaction, and gradually take on the four-coordinated geometry characteristic of the local structure of water. HB is the non-covalent interaction between an electro-positive hydrogen atom on one molecule and an electronegative oxygen atom on another molecule. In water, HB favors local tetrahedral symmetry. Hence, in ordinary ice, each water molecule has four nearest neighbors and acts as a hydrogen donor to two of them and as a hydrogen acceptor from the other two. These nearest neighbors are located near the vertices of a regular tetrahedron surrounding the central oxygen atom. The H-O-H bond angle of an isolated water molecule, 104.5°, is in fact very close to the tetrahedral angle 109.5°. Whereas solid crystalline water (ice) is a permanent tetrahedral network held together by hydrogen bonds, liquid water's tetrahedrality is local and transient. Regions of local tetrahedral order possess a larger specific volume than the average-unlike region of, say, local close-packed order. The entropy, on the other hand, always decreases upon cooling, because the specific heat is, of necessity, positive. As T decreases, the local specific volume increases due to the progressive increase in tetrahedral order. Thus the entropy and volume can become anti-correlated, and α_p can become negative. Other liquids with local tetrahedral symmetry, such as silica, display the same property.

When water is sufficiently cold, its diffusivity increases and its viscosity decreases upon compression. Pressure disrupts the tetrahedral HB network, and the molecular mobility consequently increases. In contrast, compression of most other liquids leads to a progressive loss of fluidity as molecules are squeezed closer together. The anomalous pressure dependence of water's transport coefficients [4-6] occurs below about 306 K for the viscosity and below about 283 K for the diffusivity, and persists up to pressures of around 2 kbar. One qualitative physical explanation of this anomalous pressure dependence is Le Chatelier's principle: *when a thermodynamic system is at equilibrium and external conditions are altered, the equilibrium will adjust so as to oppose the imposed change.* In water the significant large-volume clustering in the supercooling region under pressure will be strongly altered: clusters will be reduced in size and number, so water will become more like a normal liquid. Recent studies on diffusion show that, as the temperature approaches the supercooled region, motion becomes increasingly complex. Simulations in

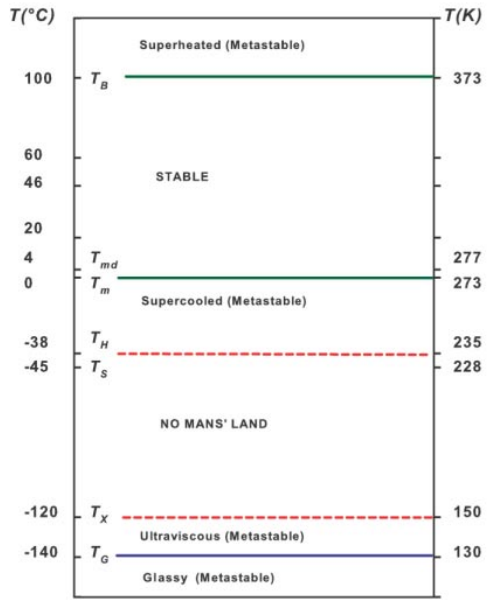

Fig. 2. – Schematic illustration of different temperature domains, at atmospheric pressure, of H_2O. T_m is the melting temperature line, T_H represents the homogeneous nucleation temperature line, whereas T_{md} corresponds to the temperature line of maximum density for bulk water. Only one domain is stable, the others are metastable. All the indicated values are experimentally observed, except the value denoted T_S obtained by fitting, with a power law, data of a measured thermodynamic response (the isothermal compressibility K_T [4, 9]) function. The region between the homogeneous nucleation curve $T_H(P)$ and the crystallization curve $T_X(P)$ is a kind of "No Man's Land," as experiments on the liquid phase cannot be performed. The temperatures denoted 60 °C, 46 °C, 20 °C, and 4 °C indicate the onset of anomalies in the sound velocity, isothermal compressibility, shear viscosity, and density, respectively. T_B is the boiling temperature and T_g the glass transition temperature.

particular show that during a randomly selected picosecond time interval most of water molecules are confined or "caged" by the HB network. Only a small fraction of the caged molecules is able to break out of their cages. Rather than being isolated, these newly freed molecules appear to form clusters not altogether unlike the dynamic heterogeneities that are believed to be distinguishing features of supercooled liquids in general [5]. Thus in the supercooled state water is both spatially and dynamically heterogeneous.

Figure 2 gives a schematic illustration of different temperature domains, at atmospheric pressure, of H_2O. In fig. 2, T_m is the melting temperature line, and T_H represents the homogeneous nucleation temperature line, whereas T_{md} corresponds to the temperature line of maximum density for bulk water. One domain is stable; the others are metastable. All the indicated values are experimentally observed, except the number denoted T_S which is a fitting parameter that emerges from assuming the existence of a power law singularity in the measured thermodynamic response (the isothermal compressibility K_T [4, 9]) functions. The region between the homogeneous nucleation curve

$T_H(P)$ and the crystallization curve $T_X(P)$ is a kind of "No Man's Land," as experiments on the liquid phase cannot be performed. The temperatures denoted 60 °C, 46 °C, 20 °C, and 4 °C indicate the onset of anomalies in the sound velocity, isothermal compressibility, shear viscosity, and density, respectively. T_B is the boiling temperature and T_g the glass transition temperature. Water can also exist in a glassy form at the lowest temperatures.

Depending on T and P, water has two amorphous (glassy) phases with different structures: a low (LDA) and a high (HDA) density amorphous ice; thus it shows a polyamorphism. LDA can be formed from HDA and vice versa; LDA if heated, undergoes a glass-to-liquid transition transforming into a highly viscous fluid, then crystallizes into cubic ice at $T_X = 150\,\mathrm{K}$ [10-12].

Water, like any liquid, can be heated above its boiling point without undergoing a phase transition. The attainable temperature of such superheating is controlled by the rate of nucleation, and is about 553 K at atmospheric pressure, 180 K above the boiling point. Kinetics also controls the attainable extent of supercooling. At atmospheric pressure, it is possible to supercool water to its homogeneous nucleation temperature $T_H \approx 231\,\mathrm{K}$, at which the nucleation rate suddenly becomes very large. Thus the temperature range over which water can exist as a liquid (231–553 K) is more than three times larger than the normal stability range (273–373 K). Limits of supercooling or superheating, being kinetic in nature, are not absolute. They can be bypassed provided that the observation time is shorter than the nucleation time.

Thus an experimentally inaccessible T region exists in bulk water between T_H and T_X. This interval between the glassy and liquid phase of water is a frontier domain whose experimental exploration is a key to a full understanding of metastable water. The observation of liquid bulk water in this experimental range is challenging regardless of whether one attempts to enter the No Man's Land by cooling liquid water or by heating glassy water [6]. Supercooling is challenging because the nucleation time becomes extremely short below T_H. In the 140–150 K range, water's extremely large viscosity causes the nucleation rate to slow down, allowing in principle much longer observation times; however, if one heats glassy water, it crystallizes at about 150 K (T_X). Figure 3 illustrates the amorphization process that reveals the transition from the HDA to the LDA phase, and finally from LDA to cubic ice Ic [12].

Glasses are non-equilibrium materials, so their physical properties depend on the process used to make them and, in principle, different glassy forms can be obtained by following different preparation protocols. It is thus not surprising that water can have different glassy phases. However, water is unusual in that the transformation between different forms can be sharp and reversible and is accompanied by large changes in fundamental physical properties such as the density, a behavior suggestive of a thermodynamic phase transition. Two forms of glassy water, which correspond to two different local tetrahedral arrangements, have been extensively studied: *low-density* and *high-density* amorphous ice (LDA and HDA, respectively). The first form was discovered 60 years ago [13], while the second in 1984 [10,11,14]. HDA has a structure similar to that of high-pressure liquid water, suggesting that HDA may be a glassy form of high-pressure water [15,16], just as LDA may be a glassy form of low-pressure water. Recently, very-high-density amorphous ice (VHDA) has been proposed as a new, distinct form of glassy water [17,18]. Water has thus at least two different amorphous solid forms, a phenomenon called *polyamorphism* [8,12,19-23], and recently additional forms of glassy water have been the focus of active experimental and computational investigations [17,18,24-30]. The glassy states differ in structure as revealed by neutron scattering, X-ray diffraction and Raman spectroscopy, and in thermodynamical properties such as density. Different routes to the

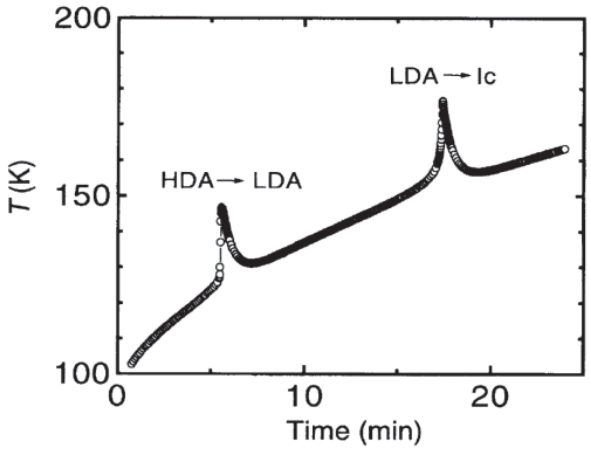

Fig. 3. – The water amorphization process that reveals the transition from the HDA to the LDA phase, and from the LDA to cubic ice Ic [12].

formation of glassy water are possible. HDA is formed by pressure-induced amorphization of ordinary ice (ice Ih), compression of LDA, rapid cooling of emulsified liquid water at high pressure, or constant-volume (isochoric) heating of VHDA. LDA is formed by rapid cooling of water vapor or liquid water after annealing. It is also formed by heating decompressed HDA or VHDA. VHDA is formed by annealing HDA at high pressure. All of these processes are irreversible, whereas a reversible route is the transformation between LDA and HDA by pressure cycling at about 135 K and 2 kbar.

The commonly accepted value for water's glass transition temperature at ambient pressure is $T_g = 136$ K (assigned to the LDA glass transition). Increasing the temperature leads to the formation of very viscous liquid water and crystallization to cubic ice at 150 K. An alternative suggestion is that T_g is located at a different temperature value [31, 32]; however this reassignment has been controversial. Due to the importance of this subject, we will discuss the glass transition temperature location and its interpretation in a next section.

2. – Current hypotheses

Many classic "explanations" for the mysterious behavior of liquid bulk water have been developed [33-38], including a simple two-state model dating back to Röntgen [39] and a clathrate model dating back to Pauling [40]. However a truly coherent picture of the thermodynamics of metastable water should clarify:

a) the anomalous behavior in the thermodynamical parameters in the supercooled region, *i.e.*, the sharp increase in isothermal compressibility, the isobaric specific heat, and the magnitude of the thermal expansion coefficient;

b) properties and nature of the transition between the two glassy phases LDA and HDA; and

c) the relationship between supercooled and glassy water.

Three hypotheses attempting rationalize these experimental observations are under current discussion:

i) The *stability limit conjecture* [41], which assumes that the spinodal temperature line $T_{sp}(P)$ between two liquids with different densities in the pressure-temperature (P-T) phase diagram connects at negative P to the locus of the liquid-to-gas spinodal for superheated bulk water. Liquid water cannot exist when cooled or stretched beyond the line $T_{sp}(P)$.

ii) The *singularity-free scenario* [42], which considers the possibility that the observed polyamorphic changes in water resemble a genuine transition, but are not. For example, if water is a locally structured transient gel comprised of molecules held together by hydrogen bonds whose number increases as temperature decreases [43-45], then the local "patches" or bonded sub-domains [46, 47] lead to enhanced fluctuations of specific volume and entropy and negative cross-correlations of volume and entropy whose anomalies closely match those observed experimentally. In this scenario the amorphous states are the corresponding vitreous forms of the *low-density liquid* (LDL) and *high-density liquid* (HDL). Upon supercooling, the response functions increase sharply but remain finite displaying pronounced maxima with respect to temperature. The transition between LDA and HDA is continuous. Because sharp maxima in the response functions imply large changes in entropy and volume, the transition between LDA and HDA is predicted to occur in a narrow interval of temperature and pressure that is difficult to distinguish experimentally from a true line when glassy phases are involved. In this viewpoint the increase in response functions upon supercooling is not a reflection of an underlying singularity but the inevitable consequence of the existence of a line along which water's thermal expansion coefficient vanishes. In this singularity-free scenario, the fluctuations between LDL and HDL remain finite, and the predicted density and enthalpy changes, along any thermodynamic path, remain continuous. Diffraction measurements during the LDA-HDA transition have been interpreted as consistent with the possibility of a continuous transition [25].

iii) The *liquid-liquid phase transition (LLPT) hypothesis* [48] arose from MD studies on the structure and equation of state of supercooled bulk water. According to this model, the transition between LDA and HDA is a low-temperature manifestation of a first-order transition between two phases of liquid water: low-density liquid (LDL) and high-density liquid (HDL); LDA and HDA are, also in this hypothesis, simply their corresponding vitreous forms. The transition terminates at a liquid-liquid (LL) critical point. Below this hypothesized *second* critical point (C') the liquid phase separates thus into two distinct liquid phases: a low-density liquid (LDL) phase at low pressures and a high-density liquid (HDL) at high pressure (fig. 4). Bulk water near the known critical point at 647 K is a fluctuating mixture of molecules whose local structures resemble the liquid and gas phases. Similarly, bulk water near the hypothesized LL critical point is a fluctuating mixture of molecules whose local structures resemble the two phases, LDL and HDL. The "critical fluctuations" that are enhanced well above the critical temperature influence the properties of liquid bulk water, thereby leading to the observed anomalous behavior (dramatic increase) in quantities such as the isothermal compressibility, isobaric specific heat, and thermal expansion coefficient. This second low-T liquid-liquid critical point, C', is predicted by the theory to be located at $T_{C'} \approx 200\,\mathrm{K}$, $P_{C'} \approx 1\,\mathrm{kbar}$ [49].

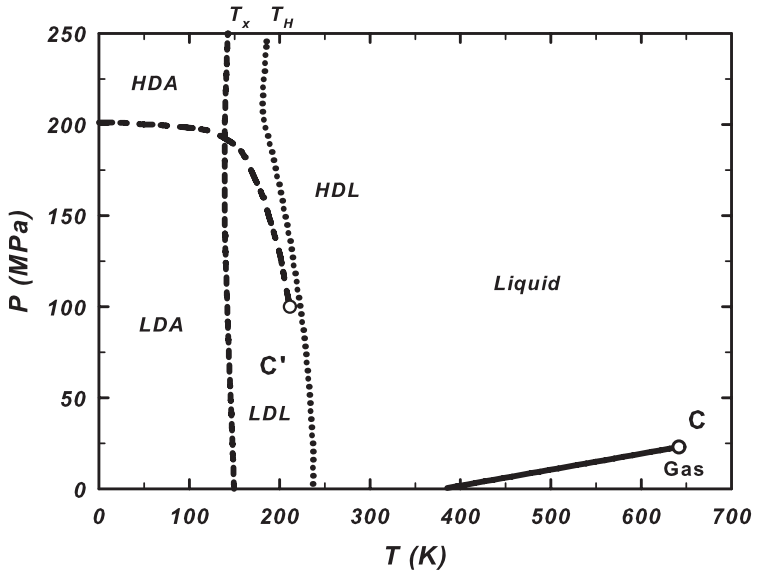

Fig. 4. – Detailed version of the projection onto the P-T plane of the equilibrium $V = V(P,T)$ surface. The phase relations between liquid water, LDL, HDL, LDA and HDA: C and C' denote the known critical point and the hypothesized second critical point, respectively. The line of first-order phase transition that emanates from C' and separates the high-density and low-density phases that occur for temperatures below $T_{C'}$ is also reported.

The third approach has received support from various theoretical studies. The exothermic nature of the changes involved in going from HDA to LDA implies that HDA has a greater entropy. According to the Clausius-Clapeyron relation, which connects the slope of the coexistence curve to the entropy and volume changes of the phase transition, for a transition in which a denser phase is more disordered, the coexistence line has a negative slope in the P-T plane. The second LL critical point thus would occur at the low-pressure, high-temperature end of the LDA-HDA equilibrium locus (fig. 4) [50-58].

In both the last two scenarios (singularity-free and LLPT), the amorphous states are smoothly connected to the liquid states. In the LLPT picture, LDL is smoothly connected to LDA, HDL to HDA, and, at sufficiently low temperatures and high pressures, discontinuous LDA-HDA transition occurs. In the singularity-free picture, the LDL-LDA and HDL-HDA connections are also smooth, but no discontinuity exists between LDA and HDA. The continuity of states between supercooled and glassy water has been verified by calorimetry, neutron diffraction and computer simulation.

However, in all the proposed scenarios from a structural point of view, the key role is played by the local HB interaction pattern having a tetrahedral geometry. In the liquid state this HB network governs the overall structure and dynamics of water.

Further, the LLPT approach suggests to focus careful interest on the so called Widom line, *i.e.*, the locus of the maximum correlation length [59-61]. The existence of a critical point induces large fluctuations in a region that extends to temperatures and pressures far away in the phase diagram. For example, experiments show that the effect of the

gas-liquid critical point C on the thermodynamic response functions is evident even at a temperature twice as high than the critical one. A similar behavior is expected also for the hypothesized critical point C'. Above $T_{C'}$ the thermodynamic response functions have an extreme (minimum or maximum) at the Widom line. On decreasing T, the Widom line converges to the critical point, where the correlation length diverges together with the response functions. Therefore, along the Widom line, the response functions show extremes and finally diverge at the critical point. Since far above a critical point the maxima of correlation length and the extremes of response functions become smooth and flat, the Widom line is broadened in a region whose size increases at higher T. As a consequence, different response functions show extremes along different lines, all around the Widom line and all converging at the critical point.

Up to few years ago, the phase diagram reported in fig. 4, together with the fashioning physical scenario proposed by the LLPT hypothesis (and in particular the Widom line), especially for the experimental difficulties to explore the No Man's Land, remained only hypothesized, but not completely proved. The power law approach, considered for many years to explain water singularities, corresponds to the extension of a first-order transition line beyond the critical point. Thus, the thermodynamic response functions, when experimentally approaching the Widom line, should behave as though they are going to diverge with critical exponents, but do not. However, computer simulations, using tried and tested models for liquid water, confirm the broad features of this proposed phase diagram [62].

2˙1. *Selected experimental results.* – Many precise experiments have been performed to test the various hypotheses discussed in the previous section, but there is as yet no widespread agreement on which physical picture, if any, is correct. The connection between liquid water and the two amorphous ices predicted by the LLPT hypothesis is difficult to prove experimentally because supercooled water freezes spontaneously below the homogeneous nucleation temperature T_H, and amorphous ice crystallizes above the crystallization temperature T_X [63-65]. Crystallization makes experimentation on the supercooled liquid state between T_H and T_X almost impossible. However, comparing experimental data on amorphous ice at low temperatures with that of liquid water at higher temperatures allows an indirect discussion of the relationship between the liquid and amorphous states. It is found from neutron diffraction studies [16] and simulations that the structure of liquid water changes toward the LDA structure when the liquid is cooled at low pressures and changes toward the HDA structure when cooled at high pressures, which is consistent with the LLPT hypothesis [16]. The amorphous states (LDA and HDA) are presently considered to be smoothly connected thermodynamically to the liquid state if the entropies of the amorphous states are small [66, 67], and experimental results suggest that their entropies are indeed small [68].

In principle, it is possible to investigate experimentally the liquid state in the region between T_H and T_X during the extremely short time interval before the liquid freezes to crystalline ice [12, 65, 69]. Because high-temperature liquid bulk water becomes LDA without crystallization when it is cooled rapidly at one bar [22, 70], LDA appears directly related to liquid water. A possible connection between liquid bulk water at high pressure and HDA can be seen when ice crystals are melted using pressure [12]. Other experimental results [65] on the high-pressure ices [38, 71] that might demonstrate a LL first-order transition in the region between T_H and T_X have been obtained.

2˙2. *Selected results from simulations.* – Water is challenging to simulate because it is a molecular liquid and there is presently no precise yet tractable intermolecular

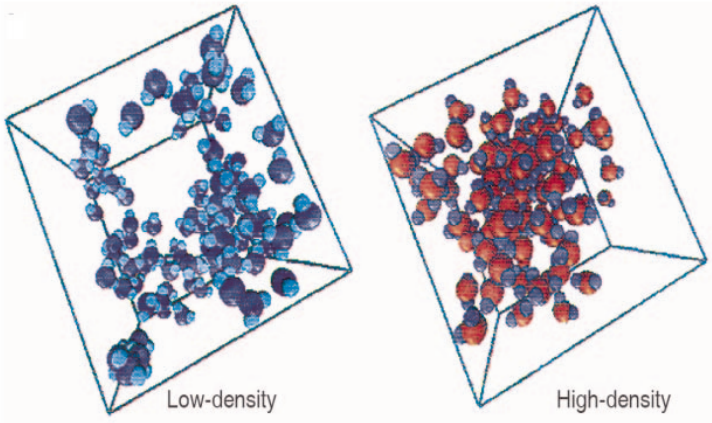

Fig. 5. – Molecular dynamics snapshots of LDL and HDL, coexisting and separating in liquid water. The subset of water molecules identified in the left panel have a smaller local density than the average, while those shown in the right panel have a larger local density [6].

potential that is universally agreed on. Nevertheless there are some distinct advantages of simulations over experiments. Experiments cannot probe the "No Man's Land" that arises in bulk water from homogeneous nucleation phenomena, but simulations have the advantage that they can probe the structure and dynamics well below T_H since nucleation does not occur on the time scale of computer simulations. Of the three hypotheses above, the LLPT hypothesis is best supported by simulations, some using the ST2 potential which exaggerates the real properties of bulk water, and others using the SPC/E and TIP4P potentials which underestimate them [48,72-76]. Recently, simulations have begun to appear using the more reliable TIP5P potential [62, 77, 78]. The precise location of the LL critical point is difficult to obtain since the continuation of the first-order line is a locus of maximum compressibility [72, 73, 75].

Further, computer simulations may be used to probe the local structure of water. At low temperatures, many water molecules appear to possess one of two principal local structures, one resembling LDA and the other HDA [48,72,74,79]. Experimental data can also be interpreted in terms of two distinct local structures [80-82]. Figure 5 represents a MD snapshot of LDL and HDL phases coexisting and separating in liquid water. The subset of water molecules in the left panel have a smaller local density than the average, whereas the ones reported in the right panel have a larger local density [6].

3. – Understanding "static heterogeneities"

The systems in which water can be confined are diverse, including the rapidly developing field of artificial "nanofluidic" systems (man-made devices in the order of nanometer or less that convey fluids). Among the special reasons for our interest in confined water is that phenomena occurring at a given set of conditions in bulk water, occur under perturbed conditions for confined water [83-96]. For example, the coordinates of the hy-

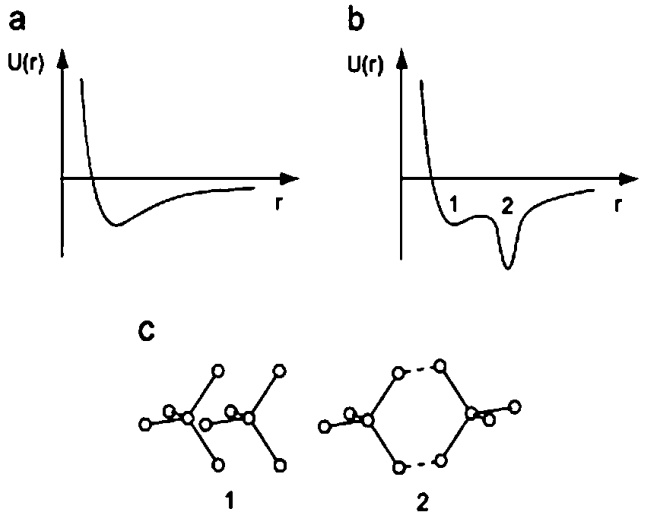

Fig. 6. – (a) Idealized system characterized by a pair interaction potential with a single attractive well. At low enough T ($T < T_C$) and high enough P ($P > P_C$), the system condenses into the "liquid" well shown. (b) Idealized system characterized by a pair interaction potential whose attractive well has two sub-wells, the outer of which is deeper and narrower. For low enough T ($T < T_{C'}$) and low enough P ($P < P_{C'}$), the one-phase liquid can "condense" into the narrow outer "LDL" sub-well, thereby giving rise to a LDL phase, and leaving behind the high-density liquid phase occupying predominantly the inner subwell. (c) Two idealized interaction clusters of water molecules in configurations that may correspond to the two sub-wells of (b). Figure adapted from [6].

pothesized LL critical point lie in the experimentally inaccessible No Man's Land of the bulk water phase diagram, but appear to lie in an accessible region of the phase diagrams of both two-dimensionally and one-dimensionally confined water [97, 98]. Many studies have been carried out to understand the effect of purely geometrical confinement [99-105] and of the interaction with hydrophilic [106-110] or hydrophobic [111-114] surfaces. It is interesting also to study the effects that confinement may have on the phase transition properties of supercooled water [104], in order to clarify the possible presence of a LLPT in water. A recent work on the phase behavior of confined water suggests a sensitive dependence on the interaction with the surfaces [113], as a LLPT appears to be consistent with simulations of water confined between two parallel flat hydrophobic walls [102]. Progress is made to extend this work to hydrophilic pores, such as those in Vycor glasses or biological situations, and to hydrophobic hydrogels, systems of current experimental interest [101, 102, 115-129].

3˙1. *Potentials with two characteristic length scales: physical arguments.* – A critical point appears if the pair potential between two particles of the system exhibits a minimum, and fig. 6(a) sketches the potential of such an idealized system. At high temperature, the system's kinetic energy is so large that the potential well does not have an effect, and the system is in a single "fluid" (or gas) phase. At low enough temperature ($T < T_C$) and large enough pressure ($P > P_C$), the fluid is sufficiently influenced by the

minimum in the pair potential that it can condense into the low specific volume liquid phase. At lower pressure ($P < P_C$), the system explores the full range of distances, the large specific volume gas phase.

If the potential well has the form shown in fig. 6(b), the attractive potential well of fig. 6(a) is now bifurcated into a deeper outer sub-well and a more shallow inner sub-well. Such a two-minimum ("two length scale") potential can give rise to the occurrence at low temperatures of a LL critical point at $(T_{C'}, P_{C'})$ [130]. At high temperature, the system's kinetic energy is so large that the two sub-wells have no appreciable effect on the thermodynamics and the liquid phase can sample both sub-wells. However, at low enough temperature ($T < T_{C'}$) and not too high pressure ($P < P_{C'}$), the system must respect the depth of the outer sub-well so the liquid phase "condenses" into the outer sub-well (the LDL phase). At higher pressure it is forced into the shallower inner sub-well (the HDL phase).

The above arguments concern the average or "thermodynamic" properties, but they may also be useful in anticipating the local properties in the neighborhood of individual molecules [131]. Consider, again, an idealized fluid with a potential of the form of fig. 6(a) and suppose that T is, say, $1.2T_C$ so that the macroscopic liquid phase has not yet condensed out. Although the system is not entirely in the liquid state, small clusters of molecules begin to coalesce into the potential well, thereby changing their characteristic interparticle spacing (and hence their local specific volume) and their local entropy, so the fluid system will experience spatial fluctuations characteristic of the liquid phase even though this phase has not yet condensed out of the fluid at $T = 1.2T_C$. Specific volume fluctuations are measured by the isothermal compressibility and entropy fluctuations by the constant-pressure specific heat, so these two functions should start to increase from the values they would have if there were no potential well at all. As T decreases toward T_C, the magnitude of the fluctuations (and hence of the compressibility and the specific heat) increases monotonically and in fact diverges to infinity as $T \to T_C$. The cross-fluctuations of specific volume and entropy are proportional to the coefficient of thermal expansion, and this (positive) function should increase without limit as $T \to T_C$.

Consider an idealized fluid with a potential of the form of fig. 6(b), and suppose that T is now *below* T_C but is 20 percent *above* $T_{C'}$, so that the LDL phase has not yet condensed out. The liquid can nonetheless begin to sample the two sub-wells and clusters of molecules will begin to coalesce in each well, with the result that the liquid will experience spatial fluctuations characteristic of the LDL and HDL phase even though the liquid has not yet phase separated. The specific volume fluctuations and entropy fluctuations will increase, and so the isothermal compressibility K_T and constant-pressure specific heat C_p begin to diverge. Moreover, if the outer well is narrow, then when a cluster of neighboring particles samples the outer well it has a larger specific volume and a smaller entropy, so the anti-correlated cross-fluctuations of specific volume (the isothermal expansion coefficient α_p) are now *negative*, and approaching $-\infty$ as T decreases toward $T_{C'}$.

Now, if by chance the value of $T_{C'}$ is lower than the value of T_H, then the phase separation discussed above would occur only at temperatures so low that the liquid would have frozen! In this case, the "hint" of the LL critical point C' is the presence of these local fluctuations whose magnitude would grow as T decreases, but which would never actually diverge if the point C' is never actually reached. Thermodynamic functions would be observed experimentally to increase as if they would diverge to ∞ or $-\infty$ but at a temperature below the range of experimental accessibility.

However, also considering a complex (and unknown) nonlinear potential between water molecules, the tetrahedrality of water dictates that the outermost well corresponds to the ordered configuration with lower entropy. Thus, although we do not know the actual form of the intermolecular potential in bulk water, it is not implausible that the same considerations apply as those discussed for the simplified potential of fig. 6(b). Indeed, extensive studies of such pair potentials have been carried out recently and the existence of the LL critical point has been demonstrated in such models [52, 53, 55-58, 132-139].

More concrete and plausible conclusions are obtained with a bifurcated potential well of the form of fig. 6(b), considering that one can crudely approximate water as a collection of 5-molecule groups called Walrafen pentamers (fig. 6(c)) [81]. The interaction strength of two adjacent Walrafen pentamers depends on their relative orientations. The first and the second energy minima of fig. 6(b) correspond to the two configurations of adjacent Walrafen pentamers with different mutual orientations (fig. 6(c)).

The two local configurations (1 and 2) in fig. 6(c) are i) a high-energy, low-specific-volume, high-entropy, non-bonded state 1), or ii) a low-energy, high specific volume, low-entropy, bonded state 2). The difference in their local structure resembles the difference in the local structure between a high-pressure crystalline ice (such as ice VI or ice VII) and a low-pressure crystalline ice (such as ice Ih) [38] (fig. 6(c)).

The region of the P-T plane along the line continuing from the LDL-HDL coexistence line extrapolated to higher temperatures above the second critical point is the locus of points where the LDL, on the low-pressure side, and the HDL, on the high-pressure side, are continuously transforming. This is called the Widom line and is defined to be the locus of points where the correlation length is maximum. Near this line, two different kinds of local structures, having either LDL or HDL properties, "coexist" [79, 140, 141]. The entropy fluctuations are largest near the Widom line, so here C_P shows a maximum, displaying a λ-like appearance [142]. The increase in C_P [67] resembles the signature of a glass transition as suggested by mode-coupling theory [143-145]. Careful measurements and simulations of static and dynamic correlation functions [140, 146-149] may be useful in determining the exact nature of the apparent singular behavior near 220 K.

3˙2. *Potentials with two characteristic length scales: tractable models.* – The above discussion is consistent with the possible existence of two well-defined classes of liquids: simple and water-like. The former interacts via spherically symmetric non-softened potentials and do not exhibit thermodynamic or dynamic anomalies. One can calculate translational and orientational order parameters (t and q), and project equilibrium state points onto the (t, q)-plane thereby generating what is termed the Errington-Debenedetti (ED) order map [47, 150]. In water-like liquids, interactions are orientation-dependent; these liquids exhibit dynamic and thermodynamic anomalies, and their ED "order map" is in general two-dimensional but becomes linear (or quasi-linear) when the liquid exhibits structural, dynamic or thermodynamic anomalies.

Hemmer and Stell [151] showed that in fluids interacting via pairwise-additive, spherically symmetric potentials consisting of a hard core plus an attractive tail, softening of the repulsive core can produce additional phase transitions. This pioneering study elicited a considerable body of work on so-called core-softened potentials which can generate water-like density and diffusion anomalies [134-139, 151-161]. This important finding implies that strong orientational interactions, such as those that exist in water and silica, are not a necessary condition for a liquid to have thermodynamic and dynamic anomalies.

A softened-core potential has been used [130] to explain the iso-structural solid-solid critical point present in materials such as Cs and Ce, for which the shape of the effective pair potential obtained from scattering experiments is "core-softened" [5, 130, 154, 162-164]. Analytical work in 1D suggested a LLPT, and the existence at $T = 0$ of low- and high-density phases. Recent work using large-scale MD simulations reported anomalous behavior in 2D as well [154, 156]. Furthermore, in 3D a squared potential with a repulsive shoulder and an attractive well displays a phase diagram with a LL critical point and no density anomaly [134-137, 165-167]. The continuous version of the same shouldered attractive potential showed not only the LL critical point, but also the density anomaly [138, 139]. The soft-core potential was used to investigate the relationship between configurational entropy $S_{\rm conf}$ and diffusion coefficient D. Recent work using the SPC/E potential [167] suggested that the temperature-density dependence of $S_{\rm conf}$ may correlate with D, and that the maximum of $S_{\rm conf}$ tracks the density maxima line.

Two questions arise naturally from this emerging taxonomy of liquid behavior. First, is structural order in core-softened fluids hard-sphere or water-like? Second, is it possible to seamlessly connect the range of liquid behavior from hard spheres to water-like by a simple and common potential, simply by changing a physical parameter?

In recent works, Yan *et al.* [168-170] used a simple spherically symmetric "hard-core plus ramp" potential to address the first question. They found that this core-softened potential, with two characteristic length scales, not only gives rise to water-like diffusive and density anomalies, but also to an ED water-like order map, implying that orientational interactions are not necessary in order for a liquid to have structural anomalies. They investigated the evolution of dynamic, thermodynamic and structural anomalies, using the ratio λ of hard-core and soft-core length scales as a control parameter. They intended to show that the family of tunable spherically symmetric potentials so generated evolves continuously between hard-sphere- and water-like behavior; the aim was to demonstrate that essential aspects of the wide range of liquid behavior encompassed by hard spheres and tetrahedrally coordinated network-formers can be systematically traversed by varying a single control parameter. They studied the equation of state, diffusion coefficient, and structural order parameters t and q. The calculations seem to reveal a negative thermal expansion coefficient (static anomaly) and an increase of the diffusion coefficient upon isothermal compression (dynamic anomaly) for $0 \leq \lambda < 6/7$. As in bulk water, the regions where these anomalies occur are nested domes in the (T, ρ)- or (T, P)-planes, with the "thermodynamic anomaly dome" contained within the "dynamic anomaly dome." The ED order map evolves from water-like to hard-sphere-like upon varying between 4/7 and 6/7. Thus, the range of liquid behavior encompassed by hard spheres ($\lambda = 1$) and water-like ($\lambda \sim 4/7$) was traversed by simply varying the ratio of hard to soft-core diameters.

To establish whether a ratio of competing length scales close to 0.6 is generally associated with water-like anomalies in other core-softened potentials new measurements are needed, *e.g.*, achieving two characteristic length scales by using a linear combination of Gaussian [171] potentials of different widths.

Motivated by the need to better understand the phenomenon of liquid polyamorphism [173-175], a systematic study was carried out on the effects of λ and the ratio of characteristic energies on the existence of a LL transition, the positive or negative slope of the line of first-order LL transition in the (P, T)-plane, and the relationship, if any [134, 135], between the LL transition and density anomalies. Calculations were performed in parallel for both confined and bulk water. In that case a spherically symmetric

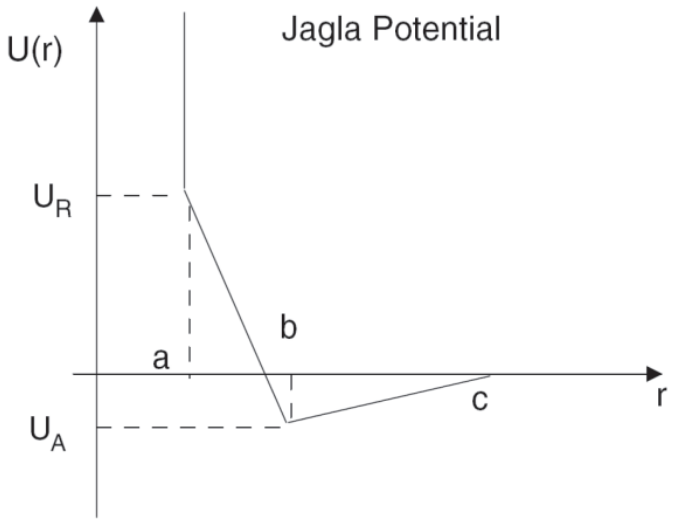

Fig. 7. – The "two-scale" Jagla ramp potential with attractive and repulsive ramps [172].

potential with two different length scales called the Jagla potential with both attractive and repulsive parts was used [134-138, 152-157, 162]. The potential is defined as

$$U(r) = \begin{cases} \infty, & \text{for } r < a, \\ U_A + (U_A - U_R)(r-b)/(b-a), & \text{for } a < r < b, \\ U_A(c-r)/(c-b), & \text{for } b < r < c, \\ 0, & \text{for } r > c, \end{cases}$$

where $U_R = 3.5U_0$ is the repulsive energy, $U_A = -U_0$ is the attractive part, a is the hard-core diameter, $b = 1.72a$ is the well minimum, and $c = 3a$ is the cutoff at large distance (see fig. 7).

By properly using this "two scale" potential in molecular dynamics simulations [134-138, 154-157], a liquid-liquid phase transition has been observed with a positively sloped coexistence line ending at a critical point well above the equilibrium melting line, allowing the study of the dynamic behavior in the vicinity of this liquid-liquid critical point. Below the critical point, the dynamics in the more ordered high density liquid (HDL) are much slower than the dynamics in the less ordered low density liquid (LDL), identifying thus a dynamical crossover and a Widom line (*i.e.*, the extension of the coexistence line into the one-phase region). In addition, the model has suggested a possible general relation between a liquid-liquid phase transition and the change in dynamics (see figs. 8(c) and (d)).

4. – Understanding "dynamic heterogeneities"

Both simulations and experiments are consistent with the possibility that the LL critical point, if it exists at all, lies in the experimentally inaccessible No Man's Land. If

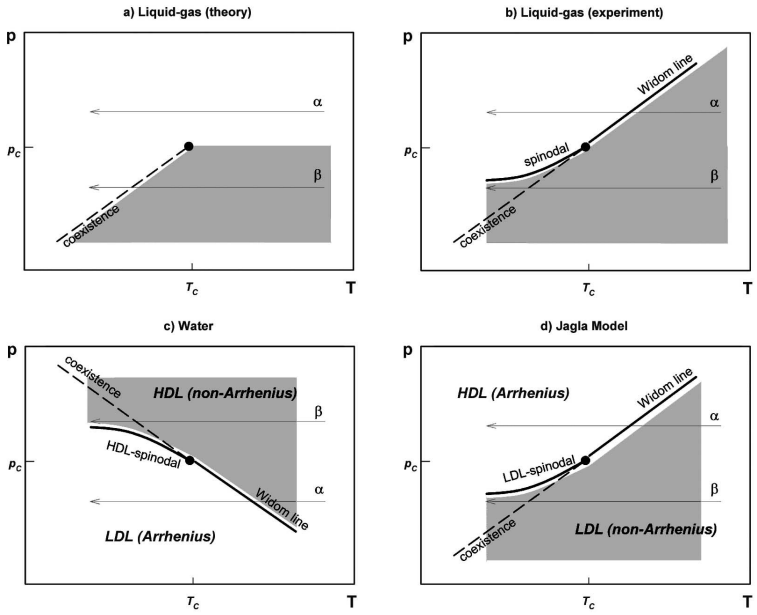

Fig. 8. – (a) Schematic phase diagram for the critical region associated with a liquid-gas critical point. Two features display singularities: the critical point and the liquid-gas coexistence. (b) Same, with the addition of the gas-liquid spinodal and the Widom line. Along the Widom line, thermodynamic response functions have extrema in their T dependence. (c) A hypothetical phase diagram for water of possible relevance to recent confined water scattering experiments [98, 176-178]. (d) A sketch of the P-T phase diagram for the two-scale Jagla model. Figure adapted from [172].

this statement is valid, then at least two reactions are possible:

i) if something is not experimentally accessible, then it does not deserve discussion; and

ii) if something is not experimentally accessible, but its influence *is* experimentally accessible, then discussion is warranted.

Option ii) has guided most research thus far, since the manifestations of a critical point extend far away from the actual coordinates of that point. Indeed, accepting option i) means there is nothing more to discuss. However if we confine water, the homogeneous nucleation temperature decreases allowing to enter the No Man's Land and hence to look for the LL critical point. In fact, recent experiments at MIT and Messina by the Chen and Mallamace groups, demonstrate that for nanopores of typically 1.5 nm diameter, the No Man's Land actually ceases to exist; one can supercool the liquid state all the way down to the glass temperature. Hence studying confined water offers the opportunity of directly testing, for the first time, the LLPT hypothesis.

Using two independent techniques, neutron scattering and nuclear magnetic resonance (NMR), the MIT and Messina groups found a sharp kink in the dynamic properties

(a "dynamic crossover") at the same temperature $T_L \approx 225\,\mathrm{K}$ [98, 176-178]. The calculations on *bulk* models [172] are not inconsistent with one tentative interpretation of this dynamic crossover as resulting from the system passing from the high-temperature high-pressure "HDL" side of the Widom line (where the liquid might display fragile behavior) to the low-temperature low-pressure "LDL" side of the Widom line (where the liquid might display strong behavior). By definition, the Widom line, defined to be the line in the pressure-temperature plane where the correlation length has its maximum, arises only if there is a critical point. Hence interpreting the MIT-Messina experiments in terms of a Widom line is of potential relevance to testing experimentally, for *confined* water, the liquid-liquid critical point hypothesis.

The interpretation of the dynamic crossover could have implications for nanofluidics and perhaps even for natural confined water systems, *e.g.*, some proteins appear to undergo a change in their flexibility at approximately the same temperature T_L that the MIT-Messina experiments identify for the dynamic crossover in pure confined water.

5. – Possible significance of the Widom line

The conjectured interpretation of the MIT-Messina experiments relies on the concept of the Widom line, a concept not widely appreciated even though it has been known by experimentalists dating back to the 1958 Ph.D. thesis of J. M. H. Levelt (now Levelt-Sengers) [60]. Since a Widom line arises only from a critical point, if the MIT-Messina experiments can be rationalized by the existence of a Widom line, then they are consistent with the existence of a LL critical point in confined water.

By definition, in a first-order phase transition, thermodynamic functions discontinuously change as one cools the system along a path crossing the equilibrium coexistence line (fig. 8(a), path β). However in a *real* experiment, this discontinuous change may not occur at the coexistence line since a substance can remain in a supercooled metastable phase until a limit of stability (a spinodal) is reached [5] (fig. 8(b), path β).

If the system is cooled isobarically along a path above the critical pressure P_C (fig. 8(b), path α), the state functions continuously change from the values characteristic of a high-temperature phase (gas) to those characteristic of a low-temperature phase (liquid). The thermodynamic response functions which are the derivatives of the state functions with respect to temperature (*e.g.*, C_P) have maxima at temperatures denoted $T_{\max}(P)$. Remarkably these maxima are still prominent far above the critical pressure [60, 61], and the values of the response functions at $T_{\max}(P)$ (*e.g.*, $C_P^{\max}$) diverge as the critical point is approached. The lines of the maxima for different response functions asymptotically approach one another as the critical point is approached, since all response functions become expressible in terms of the correlation length. This asymptotic line is sometimes called the Widom line, and is often regarded as an extension of the coexistence line into the "one-phase regime".

Suppose now that the system is cooled at constant pressure P_0. i) If $P_0 > P_C$ ("path α"), experimentally measured quantities will change dramatically but continuously in the vicinity of the Widom line (with huge fluctuations as measured by, *e.g.*, C_p). ii) If $P_0 < P_C$ ("path β"), experimentally measured quantities will change discontinuously if the coexistence line is actually seen. However the coexistence line can be difficult to detect in a pure system due to metastability, and changes will occur only when the spinodal is approached where the gas phase is no longer stable.

In the case of water, the most important solvent for biological functions [179, 180], a significant change in dynamical properties has been suggested to take place in deeply

supercooled states [49, 181-183]. Unlike other network forming materials [184], water behaves as a fragile liquid in the experimentally accessible window [49, 185, 186]. Based on analogies with other network forming liquids and with the thermodynamic properties of the amorphous forms of water, it has been suggested that, at ambient pressure, liquid water should show a crossover between fragile behavior at high-T to strong behavior at low-T [152, 153, 182, 187, 188] in the deep supercooled region of the phase diagram below the homogeneous nucleation line. This region may contain the hypothesized LL critical point [48], the terminal point of a line of first order LLPT. Recently, dynamic crossovers in confined water were studied experimentally [98, 104, 177, 189] since nucleation can be avoided in confined geometries. Also, a dynamic crossover has been associated with the LLPT in both silicon and silica [190, 191]. In the following, a tentative interpretation of the observed fragility transition in water is presented as arising from crossing the Widom line emanating from the hypothesized LL critical point [191] (figs. 8(c) and (d), path α).

6. – Methods employed to study dynamic crossover in confined water

Using MD simulations [192], three models, each of which has a LL critical point were studied. Two of the models (the TIP5P [77] and the ST2 [193]) treat water as a multiple-site rigid body, interacting via electrostatic site-site interactions complemented by a Lennard-Jones potential. The third model is the spherically symmetric "two-scale" Jagla potential with attractive and repulsive ramps which has been recently studied in the context of LLPT and liquid anomalies [157, 162]. For all three models, the loci of maxima of the relevant response functions, K_T and C_p, which coincide close to the critical point and give rise to the Widom line, were evaluated. The hypothesis that, for all three potentials, a dynamic crossover occurs when the Widom line is crossed, was carefully explored.

For TIP5P a LL critical point [62,78], from which the Widom line develops, was found. The coexistence curve is negatively sloped, so the Clapeyron equation implies that the high-temperature phase is a high-density liquid (HDL) and the low-temperature phase is a low-density liquid (LDL). The diffusion coefficient D was evaluated from the long time limit of the mean squared displacement along isobars. It was found that isobars crossing the Widom line (path α) show a clear crossover i) from a *non-Arrhenius behavior at high* T (which can be well fitted by a power law function $D \sim (T - T_{\mathrm{MCT}})^{\gamma}$, consistent with the mode coupling theory predictions [194]), ii) to an *Arrhenius behavior at low* T (which can be described by $D \sim \exp(-E_a/T)$). The crossover between these two functional forms takes place when crossing the Widom line.

For paths β, crystallization occurs in TIP5P [62], so the hypothesis that there is no fragility transition cannot be checked at low temperature. Hence a related potential, ST2, was considered for which crystallization is absent within the time scale of the simulation whose details are described in ref. [195]. This potential also displays a LL critical point [48, 195]. Along paths α a fragility transition may take place, while along paths β the T dependence of D does not show any sign of crossover to Arrhenius behavior and the fragile behavior is retained down to the lowest studied temperature. Thus, for paths β, the entire T dependence can be fit by a power law $(T - T_{\mathrm{MCT}})^{\gamma}$.

If indeed TIP5P and ST2 water models support the connection between the Widom line and the dynamic fragility transition, it is natural to ask which features of the water molecular potential are responsible for the properties of water, especially because water's unusual properties are shared by several other liquids whose inter-molecular potential has two energy (length) scales such as silicon and silica [190, 191, 196]. Hence the two-scale

spherically symmetric Jagla potential [152, 153, 162] was also investigated, displaying, without the need to supercool, a LL coexistence line which, unlike water, has a positive slope, implying that the Widom line is now crossed along α paths with $P > P_C$. A crossover in the behavior of $D(T)$ occurs when the Widom line ($C_p^{\max}$ line) is crossed, such that at high temperature, D exhibits an Arrhenius behavior, while at low temperature it follows a non-Arrhenius behavior, consistent with a power law. Along a β path ($P < P_C$), $D(T)$ appears to follow the Arrhenius behavior over the entire studied temperature range. Thus the dynamic crossover coincides with the location of the $C_p^{\max}$ line, extending the conclusion of the TIP5P and ST2 potentials to a general two-scale spherically symmetric potential.

7. – Hamiltonian model of water

In ref. [197], the generality of the dynamic crossover in a Hamiltonian model of water which displays a LLPT at low temperatures is investigated. A cell model that reproduces the fluid phase diagram of water and other tetrahedral network forming liquids was considered [55-58]. The model is based on the experimental observations that on decreasing P at constant T, or on decreasing T at constant P, i) water displays an increasing local tetrahedrality [165], ii) the volume per molecule increases at sufficiently low P or T, and iii) the O-O-O angular correlation increases [82], consistent with simulations [166].

The system is divided into cells $i \in [1, \dots, N]$ on a regular square lattice, each containing a molecule with volume $v \equiv V/N$, where $V \geq N v_0$ is the total volume of the system, and v_0 is the hard-core volume of one molecule. The cell volume v is a continuous variable that gives the mean distance $r \equiv v^{1/d}$ between molecules in d dimensions. The van der Waals attraction between the molecules is represented by a truncated Lennard-Jones potential with characteristic energy $\epsilon > 0$

$$U(r) \equiv \begin{cases} \infty, & \text{for } r \leq R_0, \\ \epsilon \left[\left(\frac{R_0}{r}\right)^{12} - \left(\frac{R_0}{r}\right)^{6} \right], & \text{for } r > R_0, \end{cases} \tag{1}$$

where $R_0 \equiv v_0^{1/d}$ is the hard-core distance [197].

Each molecule i has four bond indexes $\sigma_{ij} \in [1, \dots, q]$, corresponding to the nearest-neighbor cells j. When two nearest-neighbor molecules have the facing σ_{ij} and σ_{ji} in the same relative orientation, they decrease the energy by a constant J, with $0 < J < \epsilon$, and form a bond, *e.g.*, a (non-bifurcated) hydrogen bond for water, or an ionic bond for SiO_2. The choice $J < \epsilon$ guarantees that bonds are formed only in the liquid phase. Bonding (B) and intramolecular (IM) interactions are accounted for by the two Hamiltonian terms

$$\mathcal{H}_{\mathrm{B}} \equiv -J \sum_{\langle i,j \rangle} \delta_{\sigma_{ij}\sigma_{ji}}, \tag{2}$$

where the sum is over nearest-neighbor cells, $0 < J < \epsilon$ is the bond energy, $\delta_{a,b} = 1$ if $a = b$ and $\delta_{a,b} = 0$ otherwise, and

$$\mathcal{H}_{\mathrm{IM}} \equiv -J_\sigma \sum_i \sum_{(k,\ell)_i} \delta_{\sigma_{ik}\sigma_{i\ell}}, \tag{3}$$

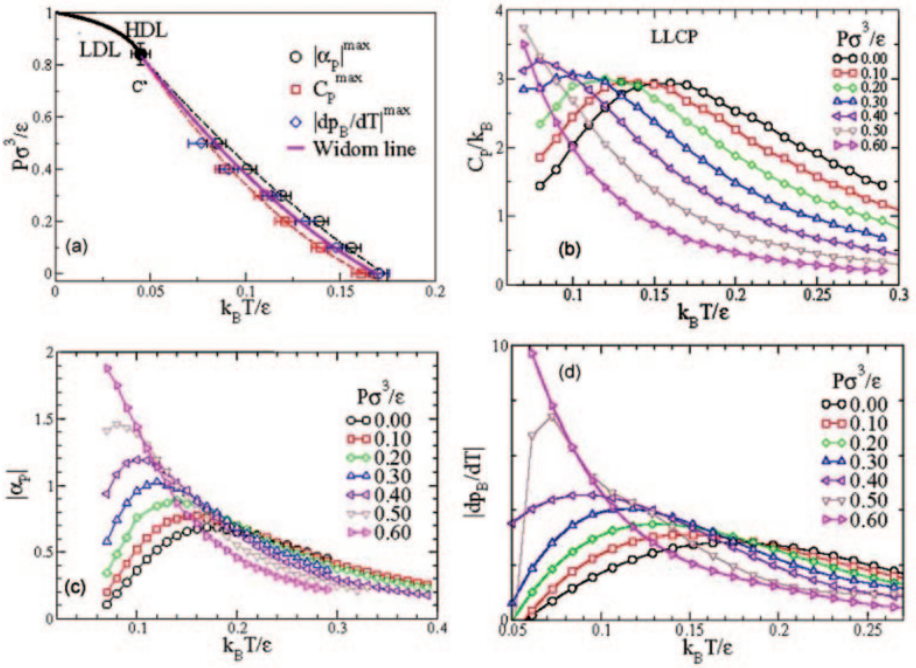

Fig. 9. – (a) Phase diagram below $T_{\rm MD}$ line shows that $|{\rm d}p_{\rm B}/{\rm d}T|^{\rm max}$ ($\diamond$) coincides with the Widom line $T_{\rm W}(P)$ (solid line) within error bars: C' is the HDL-LDL critical point, end of first-order phase transition line (thick line) [164]; symbols are maxima for $N = 3600$ of $|\alpha_p|^{\rm max}$ ($\circ$), $C_p^{\rm max}$ ($\square$), and $|{\rm d}p_{\rm B}/{\rm d}T|^{\rm max}$ ($\diamond$); upper and lower dashed line are quadratic fits of $|\alpha_p|^{\rm max}$ and $C_p^{\rm max}$, respectively, consistent with C'; $|\alpha_p|^{\rm max}$ and $C_p^{\rm max}$ are consistent within error bars. Maxima are estimated from panels (b), (c) and (d), where each quantity is shown as functions of T for different $P < P_{C'}$. In (d) $|{\rm d}p_{\rm B}/{\rm d}T|^{\rm max}$ is the derivative of $p_{\rm B}$ from simulations in ref. [164].

where $\sum_{(k,\ell)_i}$ denotes the sum over the IM bond indexes (k, l) of the molecule i and $J_\sigma > 0$ is the IM interaction energy with $J_\sigma < J$, which models the angular correlation between the bonds on the same molecule. The total energy of the system is the sum of the van der Waals interaction of eqs. (2) and (3).

Different response functions such as C_p and α_p (see fig. 9) show maxima, and these maxima increase and seem to diverge as the critical pressure is approached, consistent with the picture of Widom line discussed for other water models in the sections above.

Moreover the temperature derivative of the number of hydrogen bonds ${\rm d}N_{\rm HB}/{\rm d}T$ displays a maximum in the same region where the other thermodynamic response functions have maxima suggesting that the fluctuation in the number of hydrogen bonds is maximum at the Widom line temperature $T_{\rm W}$. To further test if this model system also displays a dynamic crossover as found in the other models of water, the total spin relaxation time of the system as a function of T for different pressures was studied. For $J_\sigma/\epsilon = 0.05$ (*liquid-liquid phase transition hypothesis*) the crossover occurs at $T_{\rm W}(P)$ for $P < P_{C'}$ (fig. 10(a)). For completeness, the system was also studied in the case of a *singularity-free scenario*, corresponding to $J_\sigma = 0$. For $J_\sigma = 0$ the crossover is at $T(C_p^{\rm max})$, the temperature of $C_p^{\rm max}$ (fig. 10(b)).

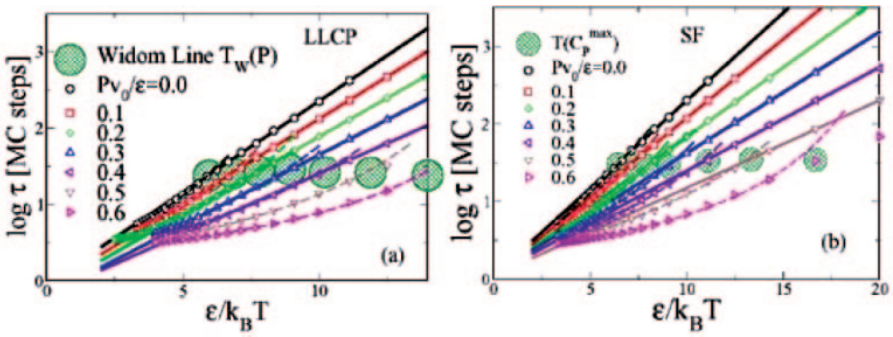

Fig. 10. – Dynamic crossover (large hatched circles of a radius approximately equal to the error bar) in the orientational relaxation time τ for a range of different pressures. (a) The liquid-liquid phase transition (LLPT) hypothesis, with crossover temperature at $T_{\rm W}(P)$. (b) The singularity-free (SF) scenario, with crossover temperature at $T(C_p^{\max})$. Solid and dashed lines represent Arrhenius and non-Arrhenius fits, respectively. Notice that the dynamic crossover occurs at approximately the same value of τ for all seven values of pressure studied. Figure adapted from [164].

Then the Arrhenius activation energy $E_{\rm A}(P)$ from the low-T slope of $\log\tau$ *vs.* $1/T$ (fig. 11(a)) was calculated and the temperature $T_{\rm A}(P)$ at which τ reaches a fixed macroscopic time $\tau_{\rm A} \geq \tau_{\rm C}$, with $T_{\rm A}(P)$ smaller than the crossover temperature, was extrapolated. For $\tau_{\rm A} = 10^{14}$ Monte Carlo (MC) steps $> 100\,$s [145] (fig. 11(b)) $E_{\rm A}(P)$ and $T_{\rm A}(P)$ decrease upon increasing P in both scenarios, providing no distinction between the two interpretations. Instead, there is a dramatic difference in the P dependence of the quantity $E_{\rm A}/(k_B T_{\rm A})$ in the two scenarios, increasing for the LL critical point and approximately constant for the singularity free (fig. 11(c)).

8. – Recent experiments on confined water

As previously said, a possibility to enter into the inaccessible temperature range of water, is shown by confining water in nanosize pores [103-105]. When contained within these pores, water does not crystallize, and can be supercooled well below $T_H = 231\,$K. Porous hydrophilic silica glass [105], micellar systems or layered vermiculite clay [104] are examples of confining nanostructures. Using this trick, the Messina and MIT experimentalists were able to study, by means of different experimental techniques like Neutron scattering, Nuclear Magnetic Resonance (NMR) and Raman and/or Fourier Transform Infrared (FTIR) spectroscopy, the structural and dynamical properties of water in the temperature range $170\,{\rm K} < T < 290\,{\rm K}$. In recent experiments [98,176] on confined water as a function of temperature and pressure, it has been shown that the theoretical LLPT approach is able to describe coherently some of the strange properties of water. By using the neutron scattering technique, an evidence of the LL critical point, C', located at $T_{C'} = 200\,{\rm K}$ and $P_{C'} = 1.6\,{\rm kbar}$ was obtained.

As shown in the previous section, this result has been also qualitatively confirmed by an extensive MD simulation analysis [172]. In particular, in this MD study by using three different models (namely: TIP5P, ST2 and the Jagla potential) the loci of maxima of the relevant water response functions (isothermal compressibility and isobaric specific

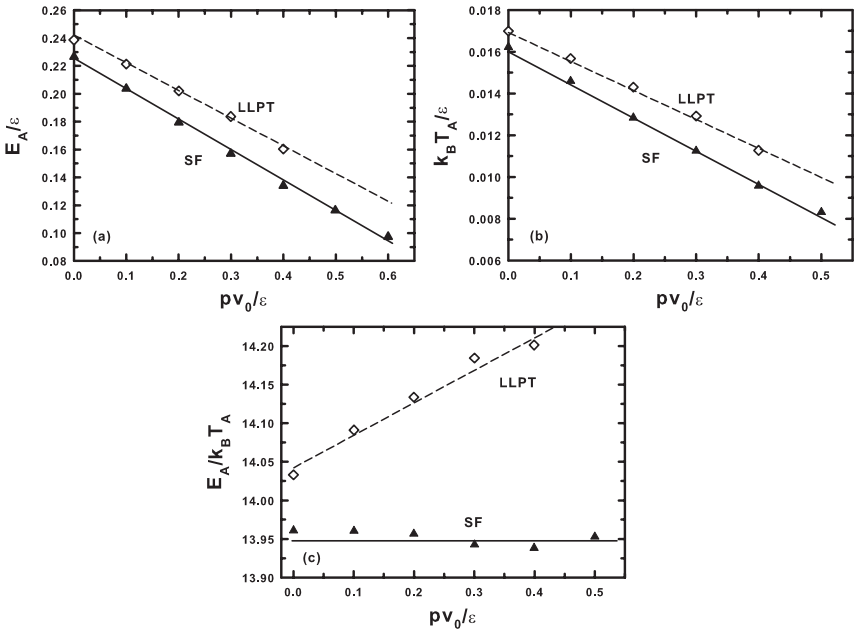

Fig. 11. – Effect of pressure on the activation energy E_A. (a) Demonstration that E_A decreases linearly for increasing P for both the LLPT and the singularity-free scenarios. The lines are linear fits to the simulation results (symbols). (b) T_A, defined such that $\tau(T_A) = 10^{14}$ MC steps > 100 s [145], decreases linearly with P for both scenarios. (c) P dependence of the quantity $E_A/(k_B T_A)$ is different in the two scenarios. In the LLPT scenario, $E_A/(k_B T_A)$ increases with increasing P, and it is approximately constant in the singularity-free (SF) scenario. Figure adapted from [164].

heat), which coincide close to the critical point and give rise to the Widom line, have been evaluated. These experiments [98,172,176] are of primary interest because their findings have stimulated much of the recent work on water. It has been suggested that a significant change in water dynamics takes place in the deeply supercooled state [49,173,198]. It has been proposed that, at ambient pressure, liquid water should show a dynamical crossover from non-Arrhenius at high T to Arrhenius (strong glass former) behavior at low T [187]. The study of refs. [98,172,176], focused on this fragile-to-strong dynamic crossover (FSC), points out in a general way the connections among the Widom line and the FSC, and associates the crossing of the Widom line with the changes in the HB structure of liquid water. It has been evidenced that upon crossing the Widom line on decreasing T, a breakdown of the Stokes-Einstein relation (BSE) is observed at $T < T_W(P)$ [199]. Both the phenomena, FSC and BSE, take place at T_W and are related with the changes in water structural and dynamical properties from those of HDL to those of LDL. The LDL phase has been observed for the first time in a recent FTIR experiment [200]. It is thus possible that other new phenomena can occur in water on crossing this line, all of them being related to the changes in the local water structure that take place when the system changes from the "HDL-like" side to the "LDL-like" side. Examples

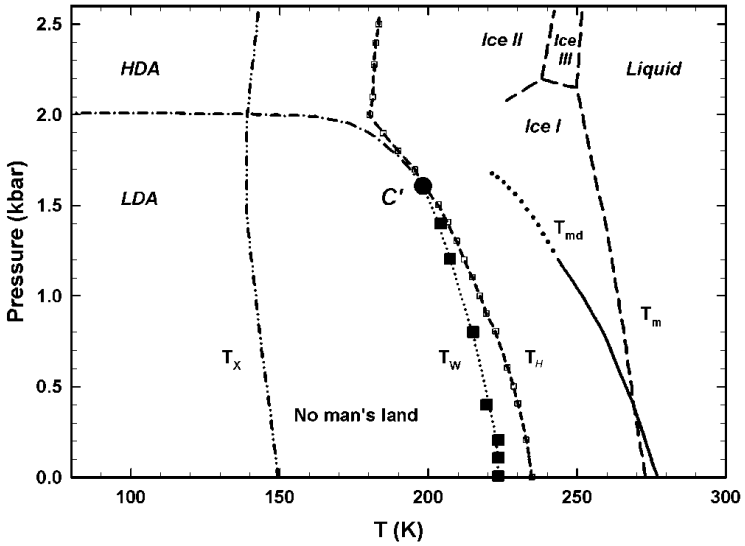

Fig. 12. – The phase diagram of water in the P-T plane (refs. [5,6]). T_H denotes the homogeneous nucleation temperature line, T_X the crystallization line of amorphous water, T_m the melting temperature line and T_{md} the maximum density line. $T_{\rm W}$ indicates the Widom line traced by means of neutron scattering experiments (squares) [98]. Figure adapted from [206].

are: i) systematic changes in the static structure factor $S(q)$, and the corresponding pair correlation function $g(r)$, revealing that, according to the FTIR results [200], for $T < T_{\rm W}$, the system structure resembles more that of LDL than that of HDL, ii) the appearance, for $T < T_{\rm W}$, of a shoulder (Boson peak) in the dynamic structure factor $S(q, \omega)$ at a frequency $\omega \approx 60\,{\rm cm}^{-1}$ [201, 202], iii) a rapid increase in hydrogen bonding degree for $T < T_{\rm W}$ [58, 203], iv) a minimum in the density at low temperature [78, 204], and v) a scaled equation of state near the critical point C' [205]. In the following a review will be given of the FSC, the BSE, the observation, by means of local vibrational modes of the $S(q, \omega)$, of the LDL phase and the observation, by means of scattering methods, of a water density minimum in the very supercooled region at about 200 K. These results are entirely connected to the changes of the water local structure when the system evolves from the HDL to the LDL phase.

The intriguing properties of water are well represented in its pressure-temperature (P-T) phase diagram (fig. 12), characterized by specific regions of existence of the liquid, solid and amorphous phases.

8˙1. *The sample.* – To confine water, a micelle template mesoporous silica matrix MCM-41-S (having 1D cylindrical tubes arranged in a hexagonal structure), synthesized using the methods of zeolite seeds [98] has been used. Similar to synthesizing MCM-48-S [207], to make mesoporous materials together with short chain surfactant (C_{12}TMAB), small quaternary ammonium ions, TEAOH, to separately develop a zeolitic nanocluster as the silica precursors, are employed. In this way, MCM-41-S (S denotes seed) with smaller pore sizes and stronger silica walls than traditional ways was obtained

(MCM-41) [208, 209]. Initially, sodium aluminate, sodium hydroxide, and tetraethylammonium hydroxide (20 wt% aqueous solution) were mixed in a vessel. Then the fumed silica was added into the above mixture and the whole system was stirred for 4 hours. The solution was transferred to autoclaves and heated at 373 K for 18 hours, yielding zeolite precursors. A mixture of C_{12}TMAB or C_{10}TMAB and deionized water was added into the zeolite precursors. The resulting mixture was transferred to autoclaves, and again heated at 393–423 K in an oven. After 18–48 hours of crystallization, the solid product was filtered, washed with water, and dried at 333 K in air for 2 hours. Calcination of the sample was carried out at 853 K for 6 hours in air to remove the templates. (The molar ratio of reactants is $NaAlO_2$: SiO_2 : NaOH : TEAOH : C_{12}TMAB : H_2O = 1 : 37–60 : 1.5–9 : 11–22 : 18.3 : 3000–3500.) The synthesized materials were characterized using X-Ray powder Diffraction (XRD) nitrogen absorption-desorption, and Differential scanning Calorimetry (DSC), figs. 1 and 2 of ref. [210], respectively. From XRD patterns it is shown that all MCM-41-S samples exhibit high hydrothermal stability. From DSC, in the case of sample having pore sizes of 18 Å, any abrupt melting transition near 273 K is not observed, indicating that there is no water residing outside the channel. With the same technique the melting/freezing behavior of water in the full hydrated MCM samples was checked. According to the Gibbs-Thomson equation, a general behavior is observed for which the liquid state of water persists to very low temperatures for little pore sizes. However, depending on the pore size, a gradual change of enthalpy from 173 K to 223 K seems to be observed. This could be due to some second-order transition or glass transition. However this type of MCM sample, in comparison with other nanotubes of the same family, has the advantage that the silanol groups are nearly completely removed. Thus the effect of the chemical species on the water at the tube surface are minimized.

The investigated samples have hydration levels of $h \simeq 0.5$ (0.5 grams H_2O per gram of MCM). As shown by X-ray diffraction (XRD) [211], differential scanning calorimetry (DSC) [212, 213] and NMR [214, 215] experiments, this water confining system can be regarded as one of the most suitable adsorbent models currently available. The geometrical constraints and the chemistry of the guest material surface may significantly affect the structure and dynamics of confined water displaying a marked hysteresis in a cooling/warming cycle. Examples are pore channel intersections (with networking effects), pore polydispersity, charges and chemical impurities. In the studied MCM-41-S nanotube samples, as shown by X-ray [211], and DSC experiments [212], the hysteresis is absent or negligible. DSC shows that repeated freezing and melting cycles (FMC) do not cause any significant change in the position and shape of DSC peaks for a given sample; the melting temperature was reproducible even after several months. Thus, water, in repeated FMC, does not affect the pore walls of these silica samples. In addition, the XRD data through the diffracted wave vector, Q_0, of the first sharp water diffraction peak, give the following results: water in MCM-41-S with a pore diameter $\phi = 42$ Å has a sudden freezing at $T \approx 232$ K, whereas for $\phi = 24$ Å, it remains in a liquid state down to ~ 160 K. Moreover, in the MCM-41-S samples water freezes with a Q_0 value that is nearly the same as that of the LDA phase ($Q_0^{\text{ice-c}} = 1.71\,\text{Å}^{-1}$) [97], in contrast to the stable ice-h, usually obtained by freezing bulk water ($Q_0^{\text{ice-h}} = 1.6\,\text{Å}^{-1}$) [4]. In both the samples no Bragg peak, characteristic of crystallization, is observed.

8˙2. *Nuclear Magnetic Resonance.* – Dynamical properties of water confined in fully hydrated MCM-41-S samples with $\phi = 24$, 18, and 14 Å, were studied at ambient pressure and different temperatures by using a Bruker AVANCE NMR spectrometer, operating at

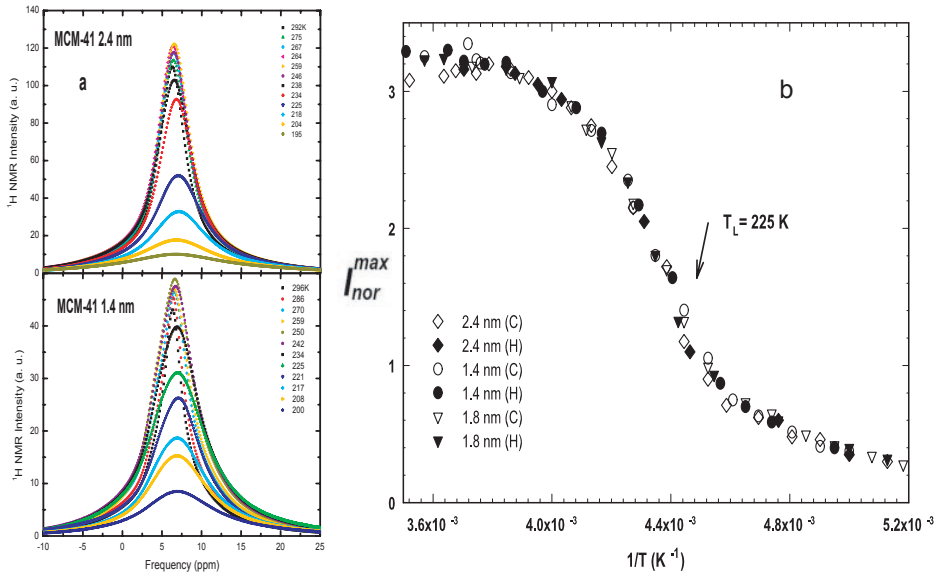

Fig. 13. – (a) The ^{1}H NMR spectra of water in MCM samples with $\phi = 24$ and 14 Å, upon cooling. (b) the normalized NMR intensities, $I^{\max}_{\mathrm{Nor}}$ *vs.* $1/T$, for $\phi = 14$, 18, and 24 Å samples, upon both cooling and heating, corrected for the Curie effect (ref. [176]).

700 MHz ^{1}H resonance frequency. In these NMR experiments, the self-diffusion coefficient of water D, and the maximum intensity $I^{\max}$ of the ^{1}H-NMR spectra (obtained by the free-induction decay (FID)) were measured. The explored temperature range was 190–298 K with an accuracy of ±0.2 K. D was measured with the pulsed gradient spin-echo technique (^{1}H-PGSE) and its thermal behavior will be shown in a next section.

The ^{1}H NMR spectra of water in MCM samples with $\phi = 24$ and 14 Å, upon cooling are shown in fig. 13(a). Before discussing the overall results of these spectra, it must be stressed that all the reported spectra are characterized by only one resonance peak centered at about 7 ppm. Such a result is completely different from the one obtained from a MCM sample with silanol groups on the internal surface; in that case the spectra are characterized by two resonance peaks like the case of sample prepared just to improve surface effects on the contained water [215]. The full width at half-height of these spectra, $\Delta\nu_{1/2} \sim 1/T_2^*$, is the rate of the so-called *apparent* spin-spin relaxation time T_2^*. As can be observed, the maximum intensity of the spectra ($I^{\max}$) decreases and the corresponding linewidth increases upon decreasing T; the crystalline ice phase (characterized by a very large linewidth) is not observed. The NMR signal intensity is directly related with the system equilibrium magnetization, M_0 (or the susceptivity χ_0) which depends linearly on the total number of mobile spins per unit volume, the mean square value of nuclear magnetic moment and on $1/T$ (Curie law). Figure 13(b) shows $I^{\max}$, for $\phi = 14$, 18, and 24 Å samples, upon both cooling and heating, corrected for the Curie effect and normalized to the pore volume, as $I^{\max}_{\mathrm{Nor}}$ *vs.* $1/T$. As can be noticed, the T behavior of confined water is independent of the pore size. Figure 13(b) clearly shows that there is a steep decrease of $I^{\max}_{\mathrm{Nor}}$ on decreasing T, at around 225 K (T_L). This

behavior indicates that $T \sim 225\,\mathrm{K}$ is a crossover temperature for the dynamical behavior of water. In general, relaxations measured in an NMR experiment are caused by random fluctuations of the magnetic field at the position of a resonating spin originating by the thermal motion of neighboring spins. In our case the fluctuating magnetic dipole-dipole interactions between ^{1}H spins are due to the tumbling of molecules under the local caging structure. Hence, the observed behavior of $I_{\mathrm{Nor}}^{\mathrm{max}}$ can be related, according to the LLPT hypothesis, to the water structure and in particular to its packing density. The probability of tumbling of a water molecule is higher in the HDL phase, compared to that in the LDL phase; the temperature behavior of $I_{\mathrm{Nor}}^{\mathrm{max}}$ shown in fig. 13(b) reflects just such a situation, indicating $T \sim 225\,\mathrm{K}$ as the possible crossover temperature between the HDL and the LDL phase.

8˙3. *The neutron scattering.* – The neutron scattering methods have been largely used in the past to explore water in both structural and dynamical properties. An example of these works is represented by the study made by A. K. Soper and M. A. Ricci in which, by means of neutron diffraction, the two phases of the water polymorphism were detailed, *i.e.*, the LDL and the HDL [82]. These experiments are made on compressed water, in a temperature regime where the anomalous properties of water are most visible, namely close to the ice I/ice III triple point ($T = 251\,\mathrm{K}$, $P = 209\,\mathrm{MPa}$). From the diffraction data they extracted the OO, OH, and HH partial structure factors and the site-site radial distribution function between distinct atoms. They also did a computer simulation of the liquid at the density and temperature of the system under question, using SPC/E (extended simple point charge) model [216] as the starting interatomic potential energy function, including an empirical potential structure refinement (EPSR) [217]. By introducing perturbations to this potential derived from the difference between measured and simulated structure factors, the simulated distributions were constrained to reproduce the measured structure factors as closely as possible. Once this has been achieved, the simulation was used to accumulate ensemble averaged values for the site-site distributions and other structural quantities. By assuming that the structure of water can be represented as a linear combination of the structures of the end points, namely the structures of HDL and LDL, they obtained two different value for the densities: $\rho_{\mathrm{HDL}} = 1.20\,\mathrm{g/cm^3}$ (0.0402 molecules/Å^3) and $\rho_{\mathrm{LDL}} = 0.88\,\mathrm{g/cm^3}$ (0.0295 molecules/Å^3). These values are quite close to the reported densities of high-density and low-density amorphous ice [64]. To identify the structural differences between the two phases, the simulated molecular distributions were used to estimate the spatial density functions [218] of water in each phase (fig. 14).

As is shown in fig. 14, the first coordination shell is tetrahedral in shape for both high and low-density forms of water. The second shell retains its overall orientational symmetry between the two forms, but for LDL it sits at approximately the tetrahedral distance, while for HDL it has substantially collapsed, to a point where it is almost coincident with the first shell. This work of Soper and Ricci constitutes an important step in the water physics because it no only verifies the structure of both HDL and LDL, but gives the densities of these two phases. In addition, such a work well represents the correct approach necessary for scattering experiment. In fact the obtained findings come out only because the structure factors, OO, OH and HH, were determined separately for cold water as a function of pressure. Indeed, all three structure factors are needed to construct unambiguously the distribution of molecular centers, the spatial dependence of this distribution, and the relative orientations of neighboring molecules. The behavior of the water structure as a function of density that emerges from this analysis indicates that the main

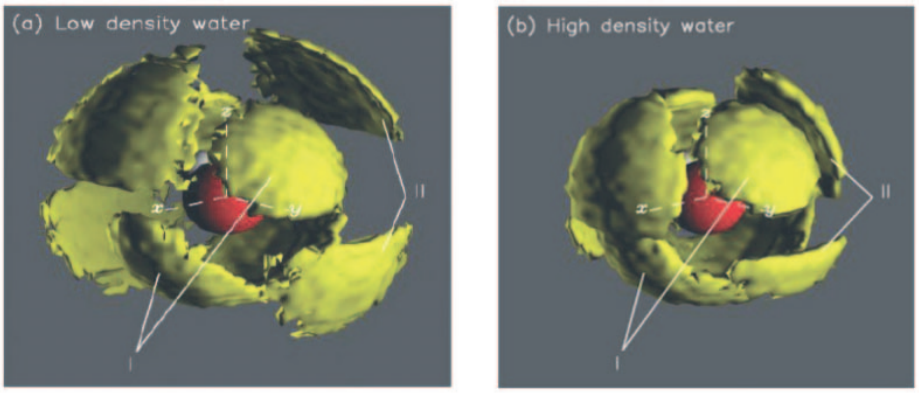

Fig. 14. – Spatial density function for water as determined from the EPSR simulation of (a) low- and (b) high-density water. A central water molecule lies in the (z, y)-plane of the coordinate system. Pronounced lobes (I) are observed opposite each OH vector on the central molecule and in a broad band of density at right angles to these underneath the central molecule, corresponding to the first shell of (approximately) tetrahedrally bonded water molecules. A second shell is seen (labelled II) which is in antiphase with the first shell. Note how this shell collapses in going from LDL to HDL, and in the (x, z)-plane merges with the first shell near the x-axis. This collapse is the primary signature of the structural transformation that occurs as water density is increased. Figure adapted from [82].

structural changes occur in the second shell: the primary effect of the increased pressure is to break the hydrogen bonds between the first and second neighbor water shells.

The properties of confined water have been investigated in the P-T phase diagram with different neutron scattering methods: elastic neutron scattering (ENS), quasi-elastic neutron scattering (QENS) and inelastic neutron scattering (INS). These methods offer many advantages for the study of hydrogen atom dynamics in confined water especially in a protein (and in its hydration water) [219]. Because of the exponential slowing down of water dynamics upon supercooling, the combined application of a time-of-flight (TOF) and a backscattering spectrometer has been necessary to study water from $T = 235\,\mathrm{K}$ down to $T = 200\,\mathrm{K}$. It can be shown generally that the double differential scattering cross-section is proportional to the self-dynamic structure factor of the scattered atoms through the following relation [220, 221]:

$$\mathrm{d}^2\sigma/\mathrm{d}\Omega\mathrm{d}\omega = N\frac{\sigma}{4\pi\hbar}\frac{k_f}{k_i}S(Q,\omega), \tag{4}$$

where $E = E_i - E_f = \hbar\omega$ is the energy transferred by a neutron to the sample in the collision process; and $\hbar\vec{Q} = \hbar\vec{k}_i - \hbar\vec{k}_f$ the momentum transferred in the scattering process, N the number of atoms in the scattering volume, and $\mathrm{d}\Omega$ the scattering solid angle. The self-dynamic structure factor $S(Q,\omega)$ embodies the elastic, quasi-elastic and inelastic scattering contributions. It can be expressed as a Fourier transform of the self-Intermediate Scattering Function (ISF) of a typical atom according to

$$S(Q,\omega) = \frac{1}{2\pi\hbar}\int_{-\infty}^{\infty}\mathrm{d}t\exp(-iEt/\hbar)F(Q,t), \tag{5}$$

$F(Q,t)$ is the atom density-density time correlation function of the tagged atom being measured by neutron scattering. In the case of water, this function relative to the hydrogen atoms, $F_H(Q,t)$, is the quantity of primary theoretical interest related to the experiment and can be calculated in a straightforward way by a molecular-dynamics simulation of a model water as well. A proper model is the relaxing cage model (RCM) [222] developed just to treat supercooled water.

The RCM is a model applied to study the single particle dynamics of water in incoherent quasi-elastic scattering, $E \approx 0$, experiments; it has been developed in past years just for the description of the translational and the rotational dynamics of water at supercooled temperatures. The model has been tested with MD simulations of SPC/E water, and has been found to be accurate. In principle, the single-particle dynamics of bulk or confined water should include both the translational and the rotational motions of a rigid water molecule, thus the ISF of the hydrogen atoms $F_H(Q,t)$, in the investigated Q-t range, is $F_H(Q,t) \approx F_T(Q,t)F_R(Q,t)$, where F_T (alternatively called F_{CM}, *i.e.*, the ISF of the hydrogen center of mass) and F_R are the translational and the rotational ISF, respectively. These contributions for the supercooled water dynamics can be separated in a short-time and in a long-time part [222]. The RCM assumes that the short-time translational dynamics of the tagged (or the trapped) water molecule can be treated approximately as the motion of the center of mass in an isotropic harmonic potential well provided by the mean field generated by its neighbors. Then the short-time part of the translational ISF in the Gaussian approximation connecting it to the velocity auto-correlation function $\langle v_{\mathrm{CM}}(\tau)v_{\mathrm{CM}}(0)\rangle$ can be written

$$F_T^s(Q,t) = \exp\left(-\frac{Q^2}{2}\left\langle r_{\mathrm{CM}}^2\right\rangle\right) = \exp\left(-Q^2\left[\int_0^t (t-\tau)\left\langle v_{\mathrm{CM}}(\tau)v_{\mathrm{CM}}(0)\right\rangle \mathrm{d}\tau\right]\right). \tag{6}$$

Since the translational density of states, $Z_T(\omega)$, is the time Fourier transform of the normalized center of mass velocity auto-correlation function, one can express the mean squared deviation, $\langle r_{\mathrm{CM}}^2(t)\rangle$,

$$\left\langle r_{\mathrm{CM}}^2(t)\right\rangle = \frac{2}{3}\left\langle v_{\mathrm{CM}}^2\right\rangle \int_{-\infty}^{\infty} \mathrm{d}\omega \frac{Z_T(\omega)}{\omega^2}(1-\cos\omega t), \tag{7}$$

where $\langle v_{\mathrm{CM}}^2\rangle = \langle v_x^2\rangle + \langle v_y^2\rangle + \langle v_z^2\rangle = 3v_0^2 = 3k_BT/M$ is the average center-of-mass square velocity, and M is the mass of a water molecule. Experiments and MD results show that the translational harmonic motion of a water molecule in the cage gives rise to two peaks in $Z_T(\omega)$ at about 10 and 30 meV, respectively [92]. Thus the Gaussian functional form used to represent approximately the translational part of the density of states is

$$Z_T(\omega) = \frac{(1-C)\omega^2}{\omega_1^2\sqrt{2\pi\omega_1^2}}\exp\left(-\frac{\omega^2}{2\omega_1^2}\right) + \frac{C\omega^2}{\omega_2^2\sqrt{2\pi\omega_2^2}}\exp\left(-\frac{\omega^2}{2\omega_2^2}\right). \tag{8}$$

Using eq. (8) the fit of MD results gives $C = 0.44$, $\omega_1 = 10.8$ THz, and $\omega_2 = 42$ THz. Finally, using eqs. (6)–(8), an explicit expression is

$$F_T^s(Q,t) = \exp\left\{-Q^2v_0^2\left[\frac{(1-C)}{\omega_1^2}\left(1-\exp\left(-\frac{\omega_1^2t^2}{2}\right)\right) + \frac{C}{\omega_2^2}\left(1-\exp\left(-\frac{\omega_2^2t^2}{2}\right)\right)\right]\right\}, \tag{9}$$

representing the short-time behavior of the translational ISF. It starts from unity at $t = 0$ and decays rapidly to a flat plateau determined by an incoherent Debye-Waller factor $A(Q)$,

$$A(Q) = \exp\left[-Q^2 v_0^2 \left(\frac{(1-C)}{\omega_1^2} + \frac{C}{\omega_2^2}\right)\right] = \exp(-Q^2 a^2/3), \tag{10}$$

where a is the root-mean-square vibrational amplitude of the water molecules in the cage in which the particle is constrained during its short-time movements. Both MD simulations and QENS gave the value of the mean-square vibrational amplitude $a \approx 0.5\,\text{Å}$ in the supercooled region (a value that is fairly temperature independent) [144, 222]. On the other hand, the cage relaxation at long-time can be described by the standard α-relaxation model, according to the Mode-Coupling Theory (MCT), with a stretched exponential having a structural relaxation time τ_T and a stretch exponent β. Therefore, the translational ISF, valid for the entire time range, can be written as a product of the short time part and a long time part,

$$F_T(Q,t) \approx F_T^s(Q,t) \exp\left[-(t/\tau_T)^\beta\right]. \tag{11}$$

The Q-t dependence of F_R then can be treated in terms of the well-known Sears exact expansion [92]. Let $\vec{b}(t)$ denotes a vector from the center of mass to the hydrogen atom. This vector will acquire a time dependence as the water molecule rotates around the center of mass

$$F_R(Q,t) = \left\langle \exp(-i\vec{Q}\vec{b}(0)) \exp(i\vec{Q}\vec{b}(t)) \right\rangle = \sum_{l=0}^{\infty} (2l+1) j_l^2(Qb) C_l(t), \tag{12}$$

where $j_l(x)$ is the l-th order spherical Bessel function, $C_l(t)$ is the l-th order rotational correlation function, and $b = 0.98\,\text{Å}$, which is approximately the length of the O-H bond in a water molecule. This expansion is very useful for a typical Q range encountered in QENS experiments, for which generally $Q < 2.5\,\text{Å}^{-1}$. In this case, the expansion needs to be carried out to at most $l = 3$ terms. The advantage of using this expansion is that the Q dependence of the rotational ISF is exactly given and one needs to make a model for a few lower-order rotational correlation functions, which are Q-independent quantities. A model for the function $C_l(t)$ is given explicitly in ref. [222] where other higher-order rotational correlation functions are approximately generated by using the maximum entropy method.

The l-th order rotational correlation function is defined as $C_l(t) = \langle P_l(\mu(t)) \rangle$, where $\theta(t)$ is the angle between the vector $\vec{b}(0)$ and $\vec{b}(t)$ and $\mu(t) = \cos\theta(t)$. The statistical average, denoted by the pointed brackets, can be calculated in terms of a probability distribution function $P(\mu, t)$. The short-time dynamical approximation of the rotation of the vector $\vec{b}(t)$ around the center of mass must be well described by a harmonic motion of the angle $\theta(t)$, *i.e.*, $\ddot{\theta}(t) + \omega\theta(t) = 0$ and in terms of the well known Bloch theorem $\langle e^{\alpha\theta} \rangle = \exp[\langle(\alpha\theta)^2\rangle/2]$; one can obtain

$$C_1^S(t) = \langle \cos\theta(t) \rangle = \left\langle \frac{e^{i\theta} + e^{-i\theta}}{2} \right\rangle = \exp\left[-\left\langle \theta^2(t) \right\rangle/2\right]. \tag{13}$$

Furthermore, it is possible to consider the angular velocity of the hydrogen atom around the center of mass as $\vec{\omega}(t) = (1/b)(\mathrm{d}\vec{b}/\mathrm{d}t) = \mathrm{d}\vec{\theta}/\mathrm{d}t$ and also as

$$\left\langle \left[\int_0^t \mathrm{d}t' \omega_x(t') \right]^2 \right\rangle = \left\langle \int_0^t \mathrm{d}t' \int_0^t \mathrm{d}t'' \omega_x(t') \omega_x(t'') \right\rangle = 2 \int_0^t \mathrm{d}\tau (t - \tau) \left\langle \omega_x(0) \omega_x(\tau) \right\rangle . \tag{14}$$

Finally we derive

$$C_1^S(t) = \exp \left[- \int_0^t \mathrm{d}\tau (t - \tau) \left\langle \omega_x(0) \omega_x(\tau) + \omega_y(0) \omega_y(\tau) \right\rangle \right] = \exp \left[- \frac{2}{3} \int_0^t \mathrm{d}\tau (t - \tau) \left\langle \vec{\omega}(0) \vec{\omega}(\tau) \right\rangle \right] . \tag{15}$$

If we define the normalized angular velocity autocorrelation function $\psi_R(t) = \langle \vec{\omega}(0) \vec{\omega}(t) \rangle / \langle \omega^2 \rangle$, and its spectral density function (normalized to 1 for ω from 0 to ∞)

$$Z_R(\omega) = \frac{1}{\pi} \int_{-\infty}^{\infty} e^{i\omega t} \psi_R(t) \mathrm{d}t, \tag{16}$$

then the short-time approximation of the first-order rotational correlation function can be written

$$C_1^S(t) = \exp \left[- \frac{4}{3} \left\langle \omega^2 \right\rangle \int_0^{\infty} \mathrm{d}\omega Z_R(\omega) \frac{1 - \cos \theta(t)}{\omega^2} \right] . \tag{17}$$

Thus, from inspecting the MD-generated $Z_R(\omega)$ (see fig. 15), the spectral density function can be modeled by a Gaussian-like function

$$Z_R(\omega) = \frac{2\omega^6}{15\omega_3^6 \sqrt{2\pi\omega_3^2}} \exp \left[- \frac{\omega^2}{2\omega_3^2} \right] , \tag{18}$$

where the peak position is located at $\sqrt{6}\omega_3$. The MD data show that this so-called hindered rotation peak is located approximately at 70 meV, fairly independent of temperature. In this model the short-time part of the first-order rotational correlation function can be written as

$$C_1^S(t) = \exp \left[- \frac{2}{3} \left\langle \omega^2 \right\rangle \int_0^{\infty} \mathrm{d}\omega Z_R(\omega) \frac{1 - \cos \theta(t)}{\omega^2} \right] = \exp \left[- \frac{4 \left\langle \omega^2 \right\rangle}{45\omega_3^2} \left[3(1 - e^{-\omega_3^2 t^2/2} + 6\omega_3^2 t^2 e^{-\omega_3^2 t^2/2} - \omega_3^4 t^4 e^{-\omega_3^2 t^2/2}) \right] \right] . \tag{19}$$

It starts from unity at $t = 0$, exhibits an oscillation at time 0.05 ps and then decays to a flat plateau determined by $\exp(-4\langle\omega^2\rangle/15\omega_3^2)$ for times longer than 0.1 ps. The relaxation at longer times can be described by a relaxation model, which describes the

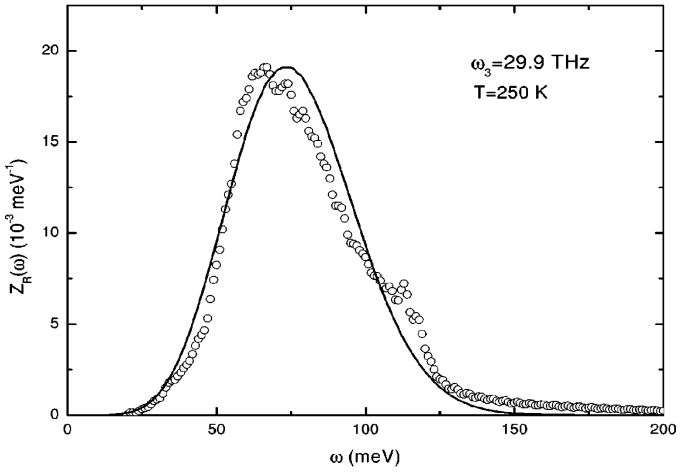

Fig. 15. – The spectral density function $Z_R(\omega)$ of the normalized angular velocity autocorrelation function at $T = 250\,\mathrm{K}$. The open circles represent the results of the simulation and the solid line the resulting fit in terms of the proposed model (eq. (18)). Figure adapted from [222].

relaxation of the cage surrounding the central water molecule. Thus the expression for $C_1(t)$ in the entire time range is given as

$$C_1(t) = C_1^S(t) \exp\left[-(\tau/\tau_R)^{\beta_R}\right]. \tag{20}$$

Thus the whole picture resembles the relaxing cage model of the translational dynamics. At short times, the orientation of the central water molecule is fixed by the H bonds with its neighbors. It performs nearly harmonic oscillations around the hydrogen-bond direction. This dynamics is described by $C_1^S(t)$. At longer times, the bonds break and the cage begins to relax. So the particle can reorient itself, losing memory of its initial orientation. Thus the first-order rotational correlation function eventually decays to zero by a stretched exponential relaxation. To calculate $C_2(t)$ and $C_3(t)$ from $C_1(t)$, one needs to know the functional form of the distribution function $P(\mu, t)$. According to the scheme, the distribution function based on maximization of the informational entropy subjected to a condition that $C_1(t)$ is known, is $P(\mu, t) = e^{\alpha+\beta\mu}$. Being $\int \mathrm{d}\Omega P(\mu, t) = 1$, then $e^{\alpha} = (1/2\pi)(\beta/(e^{\beta} - e^{-\beta}))$, so

$$C_1(t) = \int \mathrm{d}\Omega e^{\alpha+\beta\mu}\mu = -\left[1/\beta(t)\right] + \coth\beta(t). \tag{21}$$

The higher-order correlation functions are thus determined from $C_1(t)$ and the connection of $C_1(t)$ to the higher-order rotational correlation functions is given in terms of $\beta(t)$; the corresponding results are $C_2(t) = 1 - [3/\beta(t)]\ C_1(t)$ and $C_3(t) = (-5/\beta(t)) + (1 + 15/\beta^2(t))C_1(t)$.

For a proper data analysis it is important to consider the validity of the decoupling approximation $F_H(Q, t) = F_T(Q, t)F_R(Q, t)$. When dealing with a correlation function that is a product of four terms, each one with a (Q, t) dependence, it is always possible

to rewrite it as the sum of all the possible binary factorizations of its terms plus another irreducible term called the connected intermediate scattering function $F_{\rm con}(Q,t)$. $F_{\rm con}(Q,t)$ contains the contribution coming from the four factors coupled together in the correlation function and generally speaking it is different from zero. This procedure is applicable also to the correlation function $F_H(Q,t)$ which is just the product of four factors $F_H(Q,t) = \langle e^{-i\vec{Q}\vec{R}(0)} e^{-i\vec{Q}\vec{b}(0)} e^{i\vec{Q}\vec{R}(t)} e^{i\vec{Q}\vec{b}(t)} \rangle$ that can be written

$$F_H(Q,t) - F_{\rm con}(Q,t) = \left\langle e^{-i\vec{Q}\vec{R}(0)} e^{i\vec{Q}\vec{R}(t)} \right\rangle \left\langle e^{-i\vec{Q}\vec{b}(0)} e^{i\vec{Q}\vec{b}(t)} \right\rangle + \left\langle e^{-i\vec{Q}\vec{R}(0)} e^{i\vec{Q}\vec{b}(t)} \right\rangle \left\langle e^{i\vec{Q}\vec{R}(t)} e^{-i\vec{Q}\vec{b}(0)} \right\rangle . \tag{22}$$

The contributions arising from all the terms composed of products of $\vec{R}$ and $\vec{b}$ variables at arbitrary times, are zero on average, due to the statistical independence between the two, confirming the relation

$$F_H(Q,t) = F_T(Q,t) F_R(Q,t) + F_{\rm con}(Q,t), \tag{23}$$

where $F_{\rm con}(Q,t)$ describes the strength of the coupling between translational and rotational motions as a function of Q and t, as observed by QENS.

In the graphs in fig. 16 the following five quantities are shown in a semilogarithmic scale: $F_{\rm CM}(Q,t)$ (also denoted as $F_T(Q,t)$), $F_H(Q,t)$, $F_{\rm CM}(Q,t)F_R(Q,t)$, $F_{\rm con}(Q,t)$ and $F_{\rm CM}(Q,t) - F_H(Q,t)$. These functions are shown for a temperature 225 K at three Q values. These Q values are also quite close to the maximum and the minimum Q value that can be probed by a typical QENS experiment. $F_H(Q,t)$ has the same short-time features as $F_{\rm CM}(Q,t)F_R(Q,t)$ but the same long-time feature as $F_{\rm CM}(Q,t)$. So that $F_{\rm con}(Q,t)$ is very small at times smaller than 1 ps but becomes non-negligible for long times. On the contrary $F_{\rm CM}(Q,t) - F_H(Q,t)$ is negligible at times longer than 1 ps but large at short times. Both $F_{\rm con}(Q,t)$ and $F_{\rm CM}(Q,t) - F_H(Q,t)$ increase substantially with the increasing of Q value, but never reach 0.09 in magnitude.

This analysis shows that the decoupling approximation for the ISF $F_H(Q,t)$ is an acceptable tool for analyses of QENS data from water in bulk or in a confined geometry. More precisely, the decoupling approximation is excellent up to $t = 0.5$ ps and progressively becomes poorer for times longer than 1 ps. However, the maximum deviation does not exceed 0.09 even for large Q. Within this approximation, one only needs to compute $F_{\rm CM}(Q,t)$ and $F_R(Q,t)$ separately. Thus also for $F_R(Q,t)$ the RCM model represents a good analytical model, a model in which an essential input quantity to the theory is the translational density of states of the hydrogen atom.

In QENS experiments on water confined in a different material, one has to take into account only the signal coming from the hydrogen atoms of confined water. Denoting the elastic contribution arising from the material in which water is confined by p, one can analyze the experimental normalized data,

$$S(Q,\omega) = pR(Q_0,\omega) + (1-p)\text{F.T.}\{F_H(Q,t)R(Q_0,t)\}, \tag{24}$$

where $F_H(Q,t) \sim F_T(Q,t)$, $R(Q_0,\omega)$ is the experimental resolution function, and the F.T. denotes the Fourier transform from time t to frequency ω. $F_H(Q,t)$ calculated according to the equations of RCM. Both F_T^s and C_1^S were calculated using the parameters obtained from MD simulations, which are in agreement with experimental results [92].

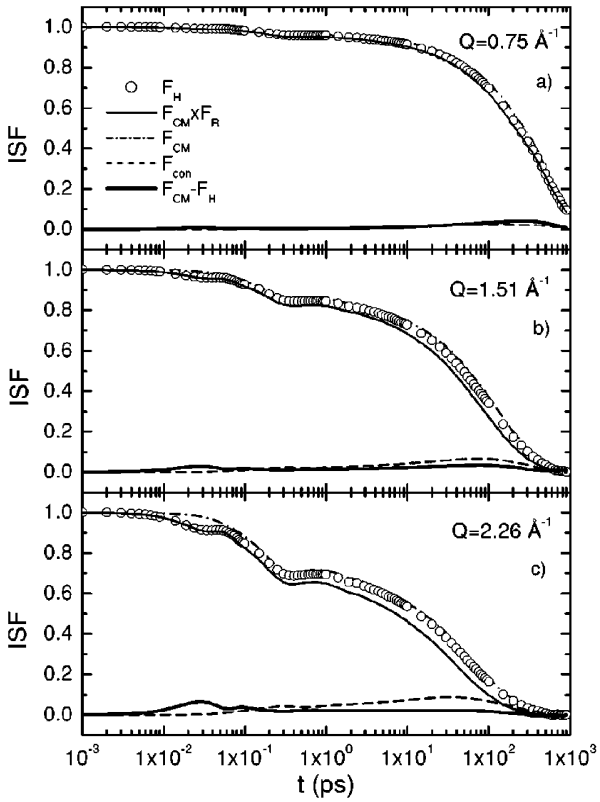

Fig. 16. – The neutron intermediate scattering function (ISF) at three Q values as a function of the time, t, in a semi-logarithmic scale. Figure adapted from [222].

Because [222] τ_T obeys to the power law $\tau_T = \tau_0(aQ)^{-\gamma}$, the measured spectra, recorded at any T, have been fitted using four parameters τ_0, τ_R, γ, and β, with satisfactory results. Figure 17 reports the QENS spectra at four temperatures, just above and below the FSC transition for water confined in MCM-41 nanotubes with a diameter $d = 18$ Å. The continuous line represents the result of the fit; the dashed line is the elastic component; the dotted, dash-dot, and dash-dot-dot lines represent contributions to the scattering from the first three terms of the Sears expansion, respectively. These spectra regard QENS measurements that were performed at NIST Center for Neutron Research using the disk chopper (DCS) and the backscattering (HFBS) spectrometers. For DCS the incident neutron wavelength was 6.0 Å and the Gaussian energy resolution ~ 30 meV. For HFBS, the resolution was ~ 1.0 meV and the dynamic range was ± 36 meV. The investigated range of elastic wave vector transfer, $Q_0 = 4\pi/\lambda \sin(\theta/2)$, was from 0.27 to 1.93 Å^{-1} and from 0.25 to 1.68 Å^{-1}, in the case of DCS and HFBS, respectively. The spectra were corrected for scattering from the sample holder, standardized using vanadium run and converted to the differential scattering cross-section using NIST standard routines.

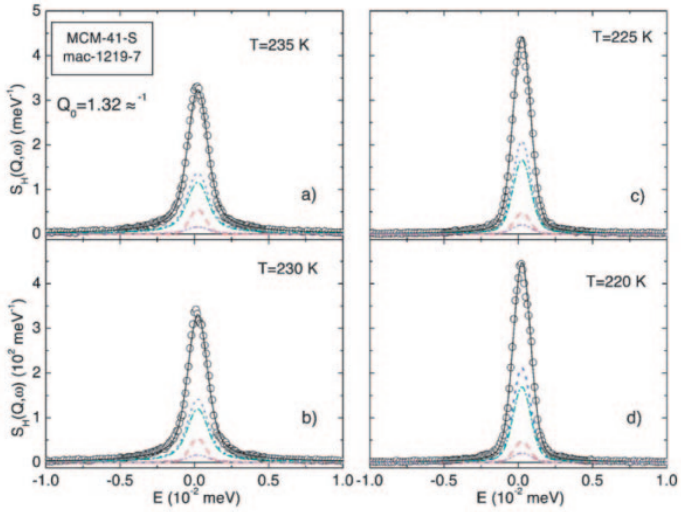

Fig. 17. – The QENS spectra of hydrated MCM samples ($\phi = 18$ Å) and their analysis in terms of the RCM model (ref. [98]). The continuous line represents the result of the fit; the dashed line is the elastic component; the dotted, dash-dot, and dash-dot-dot lines represent contributions to the scattering from the first three terms of the Sears expansion, respectively. Figure adapted from [177].

Figure 18 reports the temperature dependence of the product $\beta\gamma$, as obtained from the previous fits. The inset shows the behavior of β. In the measured temperature range, both DCS and HFBS spectra give $\beta \approx 0.5$, roughly constant in T. The product $\beta\gamma$ is

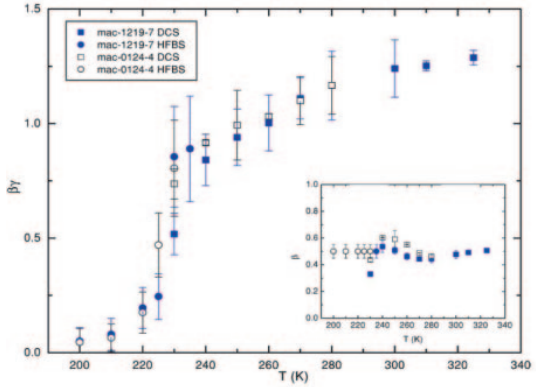

Fig. 18. – Temperature dependence of $\beta\gamma$, which is the exponent expressing the Q-dependence of the translational ISF, for the same sample as fig. 17. Note that the figure shows a sharp break at $\approx$ 225 K. The inset reports the T-dependence of the stretch exponent β. Figure adapted from [177].

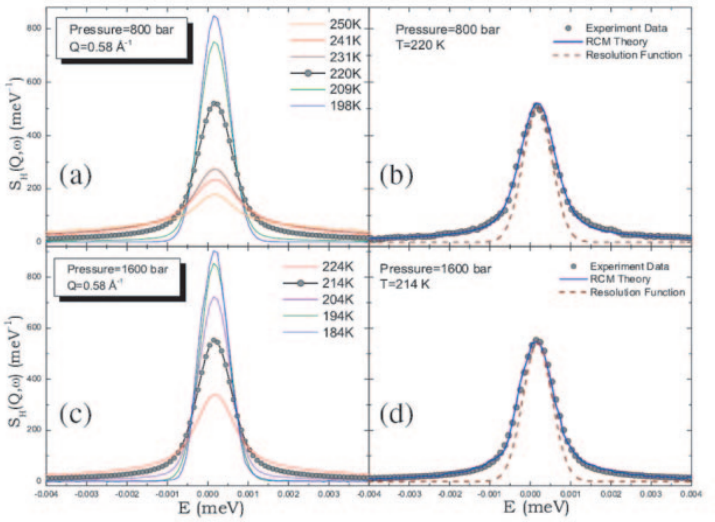

Fig. 19. – The analysis of QENS spectra of hydrated MCM samples ($\phi = 14\,\text{Å}$) in terms of the RCM model (ref. [98]).

the actual exponent of the Q-dependence of the ISF. One knows that $\beta\gamma = 2$ for a free diffusion case. The value of $\beta\gamma$ in fig. 18 starts from 1.3 at 325 K then decreases gradually until just before $T \approx 225\,\text{K}$. It drops from 0.80 to 0.25 just at this temperature, and further to nearly zero at 200 K. This precipitous drop of $\beta\gamma$ signals a drastic change of the dynamical behavior of water at 225 K. $\beta \approx 0.5$ clearly indicates that the long-time dynamics of water is non-exponential. Non-exponential behavior is common in supercooled liquids close to the kinetic glass transition. The decreasing value of γ with temperature has already been reported for supercooled confined water in vycor glass [92]. The vanishing value of $\beta\gamma$ indicates the Q-independence of the ISF. It seems that at 200K water is structurally arrested. It should be noted that the non-exponential and subdiffusive behavior is retained also at room temperature, whereas in MCM with larger pores ($> 20\,\text{Å}$) a diffusive dynamics is recovered in the limit of high temperature.

Figure 19 reports typical QENS spectra. Figures 19(a) and (c) (left panels) show the spectra measured at $Q = 0.58\,\text{Å}^{-1}$, at two pressures, 800 bar and 1600 bar, and at a series of temperatures. Figures 19(b) and (d) (right panels) show the RCM analysis of one of the spectra from each pressure. The resolution function in each case is shown by a dashed line. From τ_0 and β the average relaxation time $\langle\tau_T\rangle = (\tau_0/\beta)\Gamma(1/\beta)$, has been obtained (see fig. 20).

8˙4. *Fourier transform infrared spectroscopy.* – FTIR absorption measurements were performed at ambient pressure in the HOH bending and O-H stretching (OHS) vibrational spectral regions, by using a Bomem DA8 Fourier transform spectrometer. The investigated samples were the same as those of QENS and NMR experiments. The obtained spectra, are reported in figs. 21(a) and (b). It must be noticed that the HOH bending spectra have a Gaussian-like form quite different from the nearly flatten form typical of polycrystalline ice, revealing that confined water remains in its liquid state in

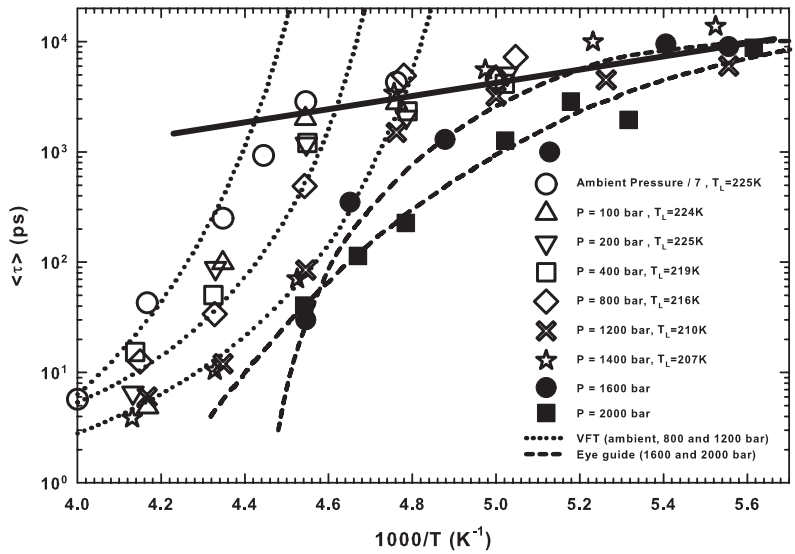

Fig. 20. – QENS results of hydrated MCM samples ($\phi = 14\,\text{Å}$) fitted in terms of the RCM analysis (ref. [98]). The temperature dependence of $\langle \tau_T \rangle$, at different pressures, are plotted in a log-lin scale *vs.* $1/T$. As can be seen, a well-defined FSC is observed only for $P < 1600\,\text{bar}$. Data from [98, 223].

all the studied T-range (fig. 21(a)). Scattering methods have been largely used to study structural and dynamical properties of water and constitute the most used experimental approach to understand its properties. Indeed, neutron [82, 98], X-ray [224], Raman and IR [225-228] scattering, have given evidence that water is characterized by the presence of two coexisting main HB structural phases, involving hydrogen bonded (HB) and non-hydrogen-bonded (NHB) molecules. Thus, it became customary to analyze OHS spectra by considering two general classes of O-H oscillators. These classes encompass broad Gaussian components, each referring to structures that involve a range of bond angles and distances distributed around the component peak position [227]. The spectral deconvolution was made by using a best fit procedure. In the fitting process all the spectral parameters were left to be free. One can notice that the corresponding Full Widths at Half Maximum (FWHM) and intensities (integrated areas) show changes whereas the wave-numbers fluctuate within the experimental error ($\pm 20\,\text{cm}^{-1}$). Figure 21(c) also reports the fitting results.

OHS spectra of water, as measured by Raman scattering and Infrared absorption in the range $30 < T < 647\,\text{K}$ (*i.e.*, from the LDA phase to nearly the first critical point of water) have been described by the following Gaussian component peak positions (wave numbers) [227]: (I) $3120\,\text{cm}^{-1}$, (II) $3220\,\text{cm}^{-1}$, (III) $3400\,\text{cm}^{-1}$, (IV) $3540\,\text{cm}^{-1}$ and (V) $3620\,\text{cm}^{-1}$. All of them have been unambiguously classified as HB, NHB, or OHS oscillators. The situation may be summarized as follows (see, *e.g.*, fig. 21(c)):

i) Component I dominates the intensity of the LDA phase (Raman [229]) so that it represents the OHS contribution of water molecules forming the "random tetrahedral network" (RTN);

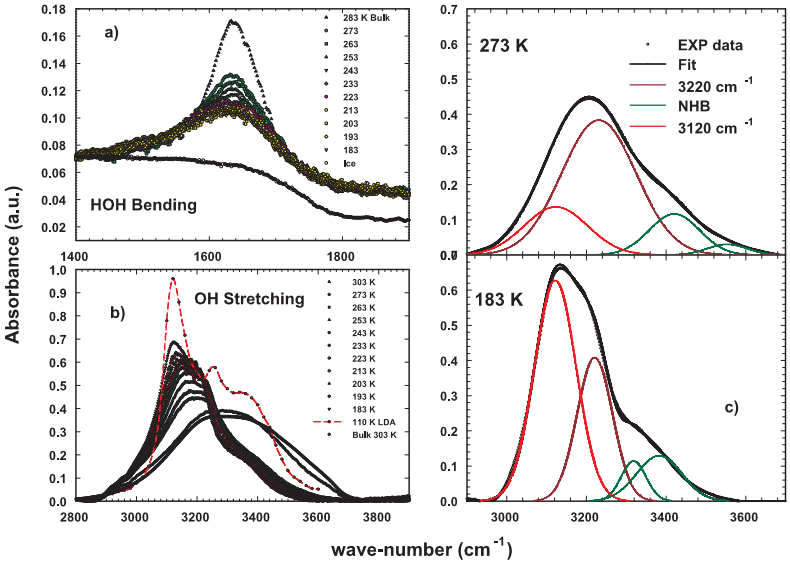

Fig. 21. – (a) The HOH bending and (b) the O-H stretching (OHS) vibrational spectra of MCM confined water at the different investigated temperatures (ref. [200]). (c) Examples of the spectral fitting results.

ii) components II and III have been associated with water molecules having an average degree of connectivity larger than that of monomers, but lower than that involved in the HB networks. Thus they can be identified as partial HB (PHB) molecules [225, 227, 228]; and

iii) because components IV and V are the only ones present in the Raman and IR spectra of bulk water in the T region near the first critical point ($630 < T < 647\,\mathrm{K}$), they arise from NHB monomeric water (or to molecules poorly connected to their environment) [225, 227].

The integrated intensities of PHB and NHB water show an opposite temperature behavior for $T > 300\,\mathrm{K}$. While the intensities of NHB increase with increasing T, those of PHB decrease. The classification of these contributions reflects that used in the percolation hypothesis for water (f_i species of water, with i indicating the number of bonds) [45]. Thus, the HB component I is f_4, the NHB components IV and V are f_0, and finally PHB components II and III are f_1, f_2 and f_3. We have to stress that according to the LLPT hypothesis, the HDL phase is represented by both the NHB and PHB.

9. – The fragile-to-strong crossover (dynamical crossover) and the breakdown of the Stokes-Einstein relation

Figure 20 is a log-linear plot that shows the temperature variation of the average translational relaxation time $\langle \tau_T \rangle$ for water molecules, obtained by the QENS spectra using the relaxing cage model (RCM), at different pressures. Figure 20 deals with the

thermal behavior of $\langle\tau_T\rangle$ for pressures in the range $1 < P < 2000$ bar. A transition from a Vogel-Fulcher-Tammann (VFT or "Super Arrhenius") law, $\langle\tau_T\rangle = \tau_0 \exp[BT_0/(T-T_0)]$, where B is a constant providing the measure of fragility and T_0 the ideal glass transition temperature, to an Arrhenius law, $\langle\tau_T\rangle = \tau_0 \exp(E_A/k_BT)$, where E_A is the activation energy for the relaxation process, can be observed. This transition from a VFT to an Arrhenius behavior is the signature of the FSC dynamic transition. The crossover temperature T_L is calculated by $1/T_L = 1/T_0 - Bk_B/E_A$. Summarizing all the results, in fig. 12 the observed pressure dependence of T_L (squares) and its estimated continuation, denoted by a dashed line, are reported. One should note that the T_L line has a negative slope, parallel to the T_{md} line, indicating a lower density liquid on the lower T side. This T_L line also approximately tracks the T_H line, and terminates in the upper end intersecting the T_H line at 1660 bar and 200 K, at which point the character of dynamical transition changes. According to the previous results, confined water remains in the disordered liquid state both above and below the FSC. Furthermore, by considering that the obtained activation energy barrier for initiating the local structure relaxation is $E_A = 5.4$ kcal/mol for the low-T strong liquid, it is reasonable to conclude that the high-T liquid corresponds to the HDL, while the low-T liquid to LDL. Thus, according to the MD simulation study [172], the FSC transition observed at T_L is caused by the crossing of the Widom line and that $T_L \equiv T_{\mathrm{W}}$. The $\langle\tau_T\rangle$ behavior for $P > 1600$ bar is well different (fig. 20). At these high pressures the cusp-like behavior characterizing the FSC is not observed. In terms of the LLPT, and of its critical point C' above the critical temperature $T_{C'}$ and below the critical pressure $P_{C'}$, we are in the one-phase region, whereas for $P > P_{C'}$ there is the two-phase region. Thus, an experiment made in this "mixed state" on crossing the LL coexistence line, is not characterized by the large fluctuations observed in the one phase region. In this latter case the thermal behavior of $\langle\tau_T\rangle$ does not show a clear-cut FSC. Such a picture explains the dynamical behavior reported in fig. 20, in which a clear FSC is observed up to 1400 bar and beyond 1600 bar the crossover is rounded off. These results indicate that the liquid-liquid critical point, C', can be located at $T_{C'} = 200 \pm 10$ K and $P_{C'} = 1600 \pm 300$ bar (fig. 12).

Figure 22 shows the $\langle\tau_T\rangle$ (QENS data) as a function of $1/T$ (fig. 22(a)) and the inverse of the self-diffusion coefficient of water $1/D$ measured at ambient pressure by NMR (fig. 22(b)) for the fully hydrated MCM-41-S samples with pore diameters of 14 Å and 18 Å.

As can be observed, the measured values of D and $\langle\tau_T\rangle$ are independent of the pore size of the samples. This indicates that NMR field-gradient measurements, having a length scale larger than the sizes of the pores, are insensitive to the system geometry. In both the figures, the solid line denotes the data fit to the VFT law $[1/D = 1/D_0 \exp(BT_0/(T-T_0))]$ whereas the dashed line denotes the fit to the Arrhenius law. From the NMR data it has been obtained: $1/D_0 = 2.4 \cdot 10^7$ (s/m^2), $B = 1.775$, and $T_0 = 187$ K, $E_A = 3.98$ kcal/mol and $T_L = 224.5$ K; whereas from the $\langle\tau_T\rangle$ data at the ambient pressure the corresponding measured values are: $T_0 = 200$ K, $E_A = 5.4$ kcal/mol, and $T_L = 225.8$ K. The agreement between NMR and QENS results is thus satisfactory, especially regarding the two relevant quantities E_A and T_L. The interpretation of the FSC transition as a variant of the structural arrest transition (as predicted by the ideal mode coupling theory) was the essence of the QENS study of the structural relaxation time and of the MD study of the self-diffusion coefficient [98, 172]. The NMR results presented above thus constitute, by means of a direct measurement of the self-diffusion coefficient of supercooled water, an independent confirmation of the existence of FSC in water.

Let us now focus on the Stokes-Einstein relation (SE) that relates the self-diffusion

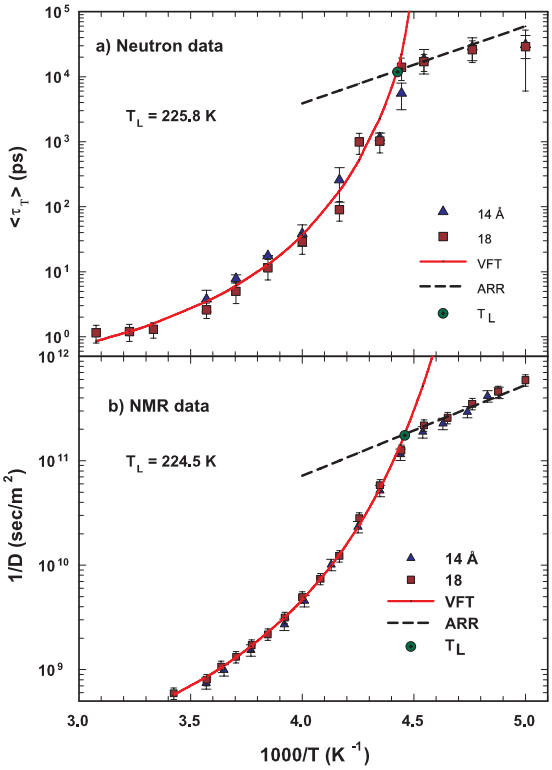

Fig. 22. – The $\langle \tau_T \rangle$ (QENS data) as a function of $1/T$ (a) and the inverse of the self-diffusion coefficient of water $1/D$ measured at ambient pressure by NMR (b) for the fully hydrated MCM-41-S samples with pore diameters of 14 Å and 18 Å. Solid lines are the VFT law fit of the experimental data and the dashed lines are the Arrhenius law fit (ref. [199]).

coefficient D, viscosity η, and temperature T as $D \propto T/\eta$, which, as it is well known, is usually accurate for normal and high temperature liquids. Since $\langle \tau_T \rangle$ is proportional to the viscosity, the relationship between D and $\langle \tau_T \rangle$ is examined in the inset of fig. 23, where the quantity $D\langle \tau_T \rangle/T$ is reported as a function of T. Triangles and squares represent its values coming from the experimental data of samples with $\phi = 14$ and $\phi = 18$ Å, respectively, whereas the dashed line represents the same quantity obtained using the corresponding fitting values reported in figs. 22(a) and (b). The temperature dependence of $D\langle \tau_T \rangle/T$ shows that this quantity is constant at higher T, but increases steeply as T goes below the FSC temperature. Therefore, in the supercooled region the temperature behavior of D and $\langle \tau_T \rangle$ is inconsistent with the SE law, signaling a marked decoupling between these two transport parameters on decreasing T. In recent studies on some supercooled liquids, it has been reported that the SE law breaks down as the glass transition is approached. The water self-diffusion coefficient shows an enhancement of orders of magnitude from that expected from SE [230-234].

These decouplings of the transport coefficients, observed as a SE violation, have

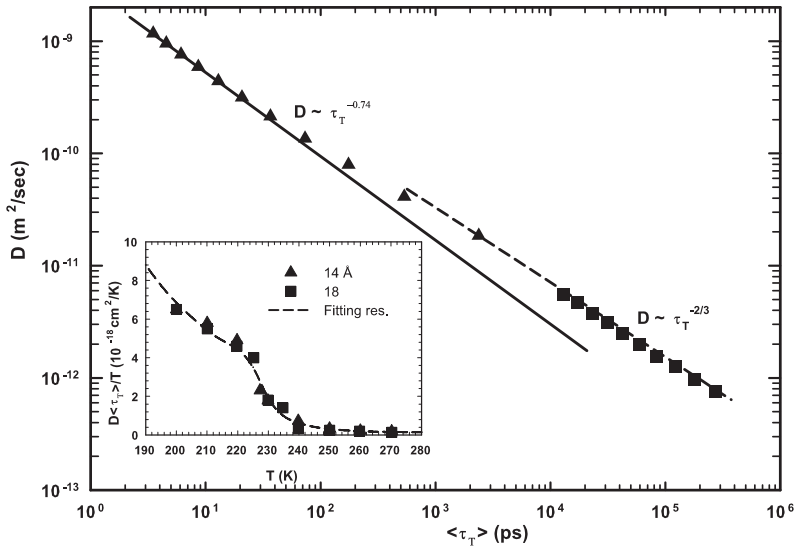

Fig. 23. – The breakdown of the Stokes-Einstein relation, $D\langle\tau_T\rangle/T$ *vs.* T (inset). Scaling representation of the BSE in a log-log scale of D *vs.* $\langle\tau_T\rangle$ (ref. [199]).

been attributed to the occurrence of dynamical heterogeneities in structural glass formers [230,232,235,236]. Thus, in supercooled liquids there exist regions of varying dynamics, *i.e.*, fluctuations that dominate their transport properties near the glass transition. Furthermore, the non-monotonic variation of $D\langle\tau_T\rangle/T$ around the crossover region agrees with the theoretical findings reported by a recent study of the FSC using a kinetic lattice gas model [237].

The observed breakdown of the Stokes-Einstein relation (BSE) can be described using scaling concepts, in particular, the law $D \sim \tau^{-\xi}$, where $\xi = \alpha(T)/\beta(T)$ with α and β being temperature-dependent scaling exponents of D and τ, respectively [238]. Recently, it has been shown that for tris-naphthylbenzene (a fragile glass former) $\xi = 0.77$ [232], whereas a MD simulation of Lennard-Jones binary mixture has given $\xi = 0.75$ [239]. Figure 23 shows the D *vs.* $\langle\tau_T\rangle$ plot in a log-log scale; triangles represent data corresponding to temperatures above T_L, where water behaves as a fragile glass former, and squares pertain to the strong Arrhenius region. As can be observed, the data clearly show two different scaling behaviors above and below the FSC temperature; in particular $\xi \simeq 0.74$ on the fragile side (solid line) and $\sim 2/3$ on the strong side (dashed line). These results agree with those of a recent theoretical study in which the decoupling of transport coefficients in supercooled liquids was investigated by using two classes of models, one describing diffusion in a strong glass former, and the other in a fragile one [238]. The main result of this study is that, while in the fragile case the SE violation is weakly dependent on the dimensionality d, with $\xi = 0.73$, in the strong case the violation is sensitive to d, going as $D \sim \tau^{-2/3}$ for $d = 1$, and as $D \sim \tau^{-0.95}$ for $d = 3$. On considering the geometry of the used confining system (1d cylindrical tubes, with a length of some μm and pore diameters of $\phi = 14\,\text{Å}$ and $18\,\text{Å}$), the scalings showed in fig. 23 compare

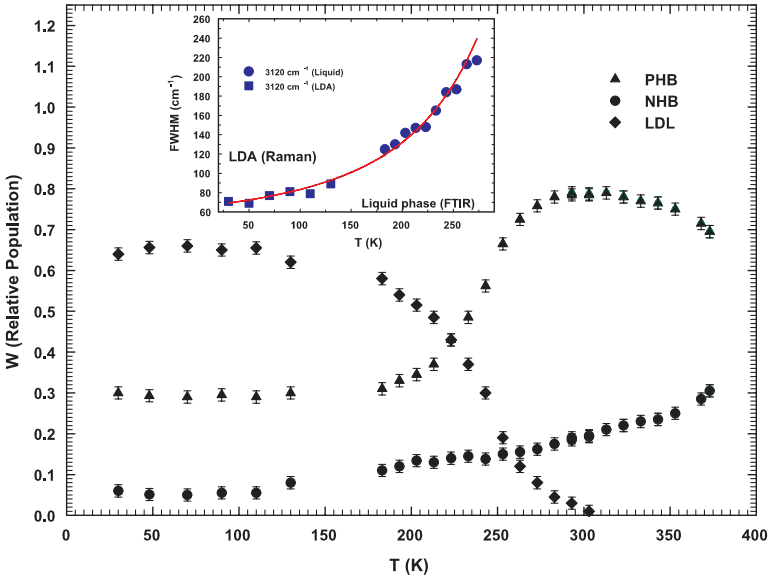

Fig. 24. – The FWHM values of the OH stretching spectral component I ($3120\,\mathrm{cm}^{-1}$) *vs.* T, measured in confined water and in the LDA phase [200, 229] (inset). Temperature dependence of the fractioned relative populations of the LDL, W_{LDL}, (diamonds) and of the HDL, W_{HDL}, (triangles and circles) water phases. For the HDL phase, NHB (circles) and PHB (triangles) contributions are reported separately (ref. [240]).

remarkably well with the findings of theoretical investigation [238], on both the fragile and strong sides.

10. – The low-density-liquid phase and the water density minimum

Coming back to the FTIR measurements on confined water, the proof that the OHS spectral component (I) $3120\,\mathrm{cm}^{-1}$ represents the LDL liquid phase is given on considering the temperature behavior of its full width at half maximum (FWHM) measured in the LDA phase [229] and the one measured in MCM confined water [200].

The inset of fig. 24 reports such a quantity *vs.* T in the interval $30 < T < 290\,\mathrm{K}$. As it can be observed, the reported data can be certainly connected with continuity, from the liquid to the LDA region, by means of a unique analytical curve. The behavior shown indicates a direct link between the contribution (I) of the OHS spectrum and the LDL water phase, demonstrating the idea proposed by the LLPT hypothesis of a striking correspondence between LDA and LDL. Next considerations are based on the fundamental law of the scattering theory for which the integrated intensity of the measured spectra $I(Q,\omega)$ is directly proportional to the number of the different species of scatterers. Namely, $I(Q,\omega) = (N/V)P(Q)S(Q,\omega)$, where $P(Q)$ is the scatterer form factor, while N denotes the number of scatterers in the scattering volume V. In fig. 24 the fractional relative populations of the LDL, W_{LDL}, (diamonds) and of the HDL, W_{HDL}, (triangles and circles) water phases, calculated as the ratio of the component integrated area to the

total OHS area, are reported in the interval $30 < T < 373\,\mathrm{K}$. For the latter phase, NHB (circles) and PHB (triangles) contributions are reported separately. According to the scattering theory, the relative populations are defined as $W_i = N_i/N$, where N_i and N are the number of the particles of the phase i and the total number of scattering particles, respectively. Data are collected from different experiments: for the temperature region 30–130 K the data come out from the analysis of OHS Raman of LDA spectra [229], for $183 < T < 303\,\mathrm{K}$ the data are those obtained on supercooled confined water [200], whereas for $253 < T < 373\,\mathrm{K}$ Raman data of bulk water [225, 227, 228] were analyzed. It is apparent that the thermal behavior of all three species is continuous across the different temperature ranges, although coming from different data sets. This is of relevant interest, especially for the component (I), because it confirms the observation, in terms of the corresponding FWHM, that it is the LDL liquid phase. As it can be observed, the NHB and PHB contributions are present at all temperatures, whereas the LDL phase exists only in the range 30–303 K. The LDA phase is dominated by the LDL species, whereas in the stable liquid phase for $T > 303\,\mathrm{K}$ only the HDL is present. The PHB population has a maximum at about 303 K, decreases on decreasing T in the entire supercooled region, crosses LDL at about 225 K, and finally becomes stable ($W \sim 0.29$) in the LDA phase.

From these results, it is evident that the HB random tetrahedral network is formed essentially inside the metastable supercooled regime. It is also important to note that NHB and PHB are also present in the LDA phase, indicating that the dynamics of LDA is not completely frozen even at $T = 30\,\mathrm{K}$, in agreement with experimental observations [241].

The results reported in fig. 24 have been used to obtain the H_2O density and to explore, by using optical methods, the possibility of a minimum in this thermodynamical variable. Very recently, the existence of a density minimum in the supercooled phase has been observed in confined D_2O, by using neutron scattering, at the temperature $T_{\min} = 210 \pm 5\,\mathrm{K}$ [204]. The idea of a minimum, located approximately 70 K below the temperature of the density maximum T_{md}, has been also suggested by MD simulation studies [78], in which both the TIP5P-E and the ST2 potential models for water have been used [78, 195]. Such a possibility may also be inferred from simple arguments on considering the density data of supercooled bulk water, ice Ih and LDA water [181]. After the maximum, the density of bulk water decreases rapidly with decreasing T before T_H, whereas the ice Ih has a smaller density than that of the liquid and, contrary to supercooled bulk water, has a normal positive expansivity, *i.e.*, density increases as T decreases. The same behavior is observed for LDA at its highest temperatures. From the structural point of view, ice Ih represents the limiting case of a perfectly ordered tetrahedral network of HB, whereas LDA, that forms from deeply supercooled water, has a structure that very closely approaches that of a "random tetrahedral network" (RTN). Thus, ice Ih sets a lower bound for the density that supercooled water could in principle attain. From these arguments, if the structure of deeply supercooled water approaches that of a RTN, and if nucleation can be avoided, it is then possible that a density minimum could occur in the deeply supercooled liquid.

Since only water contributes to the reported OHS spectra, its total density can be obtained only from the respective densities of its phases: the LDL and HDL. MD simulations [5], and proper neutron scattering data give estimated values of the corresponding densities [82]: $\rho_{\mathrm{HDL}} \approx 1.2\,\mathrm{g/cm^3}$ and $\rho_{\mathrm{LDL}} \approx 0.88\,\mathrm{g/cm^3}$. The density of LDA was experimentally measured as [242]: $\rho_{\mathrm{LDA}} \approx 0.94\,\mathrm{g/cm^3}$. Since the LDL phase exists only for $T < 303\,\mathrm{K}$, the HDL water is only given for $T > 303\,\mathrm{K}$ by the remaining spectral contributions classified as NHB and PHB.

Water density was calculated from the fractionated populations W_{LDL} and W_{HDL} and

their individual local densities ρ_{LDL} and ρ_{HDL}. The W quantities are T-dependent in all the studied liquid regime and also the individual densities may in principle change with temperature. This may be verified on considering for instance the region $T > 303\,\mathrm{K}$, where only the PHB and NHB species contribute to the OHS spectra [225, 228]. Thus, in the interval $303 < T < 373\,\mathrm{K}$, the densities ρ_{PHB} and ρ_{PNB} can be obtained from the bulk water density as: $\rho_{\mathrm{H_2O}} = \rho_{\mathrm{PHB}} W_{\mathrm{PHB}} + \rho_{\mathrm{NHB}} W_{\mathrm{NHB}}$, being the $\rho_{\mathrm{H_2O}}(T)$ values well known in the range $239 < T < 423\,\mathrm{K}$ [7, 243, 244]. By considering all the W_{PHB} and W_{NHB} data points measured in that T interval, the result is: $\rho_{\mathrm{PHB}} \simeq 1.10 \pm 0.02\,\mathrm{g/cm^3}$ and $\rho_{\mathrm{NHB}} \simeq 0.59 \pm 0.02\,\mathrm{g/cm^3}$. Indeed, these values are temperature independent within the reported experimental error. This finding is not surprising, considering the literature data on proton magnetic resonance chemical shift of liquid water in a temperature range 273–363 K. This quantity, that as well known, reflects entirely the system local structure, does not exhibit any singularity or discontinuity in the above temperature range [245]. From this analysis it emerges that: (a) in the considered T range, ρ depends on T only through W; (b) $\rho_{\mathrm{NHB}} \simeq 0.59 \pm 0.02\,\mathrm{g/cm^3}$, according to Kell's representation [7] of bulk water density as a function of T, corresponds to the density value of H_2O at $T \sim 625\,\mathrm{K}$. Such a value is smaller than that used ($0.66\,\mathrm{g/cm^3}$ for $T = 673\,\mathrm{K}$, at a pressure of 800 bar) in a neutron scattering experiment in the supercritical region, where no distinct HB peaks are observable in the O-H radial distribution function g_{OH} [246]. Thus, the value of ρ_{NHB} reasonably represents that of NHB water, which dominates vibrational spectra in the region above the critical temperature (C). In addition, $\rho_{\mathrm{PHB}} \simeq 1.10 \pm 0.02\,\mathrm{g/cm^3}$ is comparable with the value proposed for the HDL water [82]. Therefore, the contribution of HDL to the total H_2O density, Δ_{HDL}, can be obtained in all the explored T range ($30 < T < 373\,\mathrm{K}$), by extending the calculation made for ρ_{NHB} and ρ_{PHB} to the lowest temperatures. By using similar arguments the density value of the ρ_{LDL} contribution of that phase, Δ_{LDL}, to the total $\rho_{\mathrm{H_2O}}$ has been calculated. In that case, the H_2O density values at temperatures around T_{md} [7] have been considered, obtaining $\rho_{\mathrm{LDL}} = 0.87 \pm 0.02\,\mathrm{g/cm^3}$ [240], a value that closely matches that proposed by neutron diffraction data analysis for LDL water [82]. Thus $\rho_{\mathrm{H_2O}}$ has been calculated as $\rho_{\mathrm{H_2O}} = \Delta_{\mathrm{HDL}} + \Delta_{\mathrm{LDL}}$ for the temperature interval $30 < T < 370\,\mathrm{K}$. Figure 25 reports the plot of the obtained water density *vs.* T. For comparison, the values measured in bulk water in the range $239 < T < 423\,\mathrm{K}$ are also reported [7, 243].

As it can be observed, there is a good agreement between these "optically measured" density data and the literature ones for $\rho_{\mathrm{H_2O}}$ in the supercooled regime (where, contrary to the range 273–373 K, data were not used to extract the values of ρ_{NHB}, ρ_{PHB}, and ρ_{LDL}). Two findings are remarkable: the minimum at about $203 \pm 5\,\mathrm{K}$ and the value of $\rho = 0.940 \pm 0.003\,\mathrm{g/cm^3}$ in the LDA phase, nearly the same as that measured in the LDA ice at $T = 120\,\mathrm{K}$ [242]. This result, together with those obtained for $T > 303\,\mathrm{K}$, confirms that the LDL and HDL local structures are essentially temperature independent so that the thermal evolution of water density comes only from that of W_{LDL} and W_{HDL}. Looking carefully at the data in the region of deep supercooling (around 250 K), it is possible to observe that the data, evaluated for confined water, are slightly lower than those measured in bulk; this may be due to the confinement effect of water inside the nanotubes. However, the difference is not relevant enough to affect the overall result. In fig. 25 the $\rho_{\mathrm{D_2O}}(T)$ data obtained by neutron measurements [98] and the results of the quoted MD simulation of H_2O with the TIP5P-E potential are also reported. The $\rho_{\mathrm{D_2O}}$ data have been properly scaled over the $\rho_{\mathrm{H_2O}}$ taking into account the temperature shift of the corresponding [78] maxima (about 7 K) and the absolute value of the $\rho_{\mathrm{D_2O}}^{\mathrm{max}}$. As can be observed there is a good agreement in the overall thermal behavior between the $\rho_{\mathrm{D_2O}}(T)$

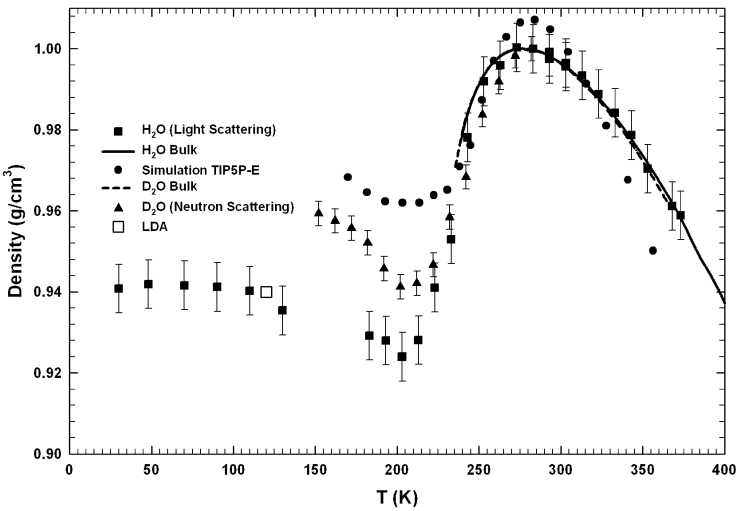

Fig. 25. – The measured $\rho_{H_2O}(T)$ *vs.* T (squares, ref. [240]); the solid and dashed lines refer to bulk densities of H_2O and D_2O, respectively [7, 243, 244]. Triangles represent the $\rho_{D_2O}(T)$ measured by means of neutron scattering [98]. Dots are the bulk density values calculated by the MD simulation [78]. The open square represents the density of the LDA water at $T = 120\,\mathrm{K}$ [242]. Heavy water densities are properly scaled over the ρ_{H_2O} ones.

and $\rho_{H_2O}(T)$ data, with the only difference that $\rho_{H_2O}(T)$ includes the densities within the LDA phase. There is a marked difference between the experimental densities and the MD simulation ones [78]. It is reasonably possible that, with the use of another water potential, MD simulation might give more reliable results compared to the experimental ones.

Besides the density minimum, an important result emerges from these experiments by estimating the derivative of the density with respect to temperature $(\partial\rho/\partial T)_P$, shown in fig. 26. As can be observed, such a quantity (proportional to the thermal expansion coefficient) has a maximum just at the inflection point between the maximum and the minimum in $\rho_{H_2O}(T)$ where the temperature T_L corresponding to crossing of the Widom line at ambient pressure is located. Different phenomena have been correlated with the existence of the Widom line, like for example the SEV, the sharp change in the temperature derivative of the mean squared displacement and the maximum in the temperature derivative of the number of hydrogen bonds per molecule. As above mentioned, the SEV is due to the onset of dynamical heterogeneities whose typical length scale is a few water molecules size. The maximum in $(\partial\rho/\partial T)_P$, is thus not influenced by possible confinement effects. A proof of this argument is represented by the same quantity obtained from the density data of pure supercooled bulk water [7] reported in the same figure as a continuous line. Here, the temperature behavior of water density, in the supercooled regime, has been described as mainly driven by the LDL phase. Thus, $(\partial\rho/\partial T)_P$ reflects the change of the local tetrahedral order with respect to temperature. In addition, it is of relevant interest, from a thermodynamic point of view, that the maximum in $(\partial\rho/\partial T)_P$ occurs at the same temperature as the Widom line: the temperature T_L is the locus

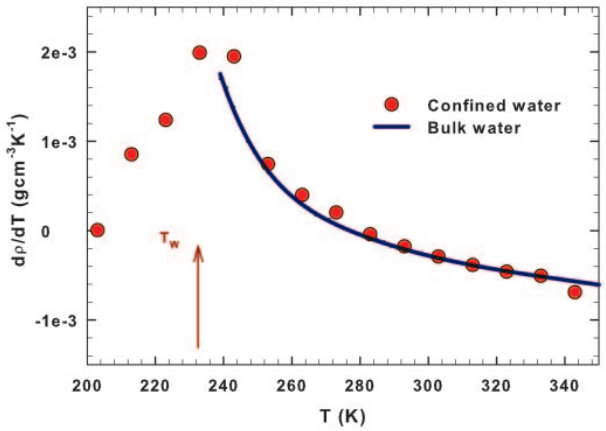

Fig. 26. – The derivative of the density with respect to temperature $(\partial\rho/\partial T)_P$. As can be observed such a quantity is characterized by a maximum just at the Widom temperature $T_{\rm W}$, indicated by the arrow. $(\partial\rho/\partial T)_P$, related with the cross-correlation between the entropy and volume fluctuations, is proportional to the thermal expansion coefficient. Figure adapted from [240].

of the correlation length maximum, whereas the density derivative is related with the cross-correlation between the entropy and volume fluctuations.

11. – The specific heat and the glass transition

The glass transition is one of the most studied condensed matter properties and represents today a challenging research argument. Understanding glass formation is not straightforward, because the existence of a true glass state, distinct from liquid and solid, remains elusive. A common interpretation of glasses is that they are liquids that have become too viscous to flow: why does the viscosity of glass-forming liquids increase so dramatically when approaching the glass transition? Such a phenomenon otherwise described as "molecular jamming" or dynamical arrest is accompanied by the freezing in the system of molecular degrees of freedom. Despite decades of research, a clear explanation of this phenomenon, common to materials as diverse as molecular glasses, polymers, granular matter, and colloids, is still lacking [247-249]. The puzzle of the glass transition process is that the static structure factor of a glass is indistinguishable from that of the corresponding liquid, with no sign of increasing correlation length scales accompanying the transition. Numerical studies and theoretical approaches reveal instead the existence of collective phenomena with a growing dynamic length scale [250-252] associated with dynamical heterogeneities [230, 232, 235, 236]. To give an idea, it seems that, as the glass transition is approached, the system dynamics becomes sluggish, because of increasingly larger regions in the material that have to move simultaneously to flow. Such a description also clarifies the most important glass transition thermodynamical property like the glass transition temperature T_g. This "critical temperature" represents the point of separation of two completely different statistical regions; in the first one, above T_g, the system is a true ergodic liquid whereas in the region below such a temperature becomes

non-ergodic. In this latter condition the system needs extremely long times, much longer than the experimental ones, to explore the phase space. Thus, in the liquid side, and also in its metastable supercooled region, the system is in thermal equilibrium, whereas the glassy phase is out of equilibrium. This situation has considerable effects on the system dynamics. The very slow evolution of the glass to the equilibrium is a widely studied and interesting phenomenon named physical aging [253]. From the scientific point of view it is very interesting to consider what happens in the system, not only when it approaches T_g, but also well inside the glass phase (*i.e.*, for temperatures T_1 less than T_g).

In real experiments, at the glass transition, the underlying thermodynamics is masked by kinetic effects, so that static equilibrium measurements cannot be obtained as a result of diverging relaxation times. The specific heat, C_p, is of particular importance since it is the basis of the well known Kauzmann paradox, one clear indication that some sort of transition must occur between the liquid and the glass. The specific heat of the supercooled liquid is greater than that of the crystal. If this situation were to continue to a low enough temperature the entropy of the supercooled liquid would become less than that of the crystal. In all known cases the glass transition intervenes and C_p drops at a slightly higher temperature than where this catastrophe would occur.

In the glassy state, molecular motions occur about an equilibrium position at the potential energy minimum and the probability of the molecules to jump to a new equilibrium position at some distance is vanishingly small. As the temperature of the glass is increased, this probability increases; thus, by increasing the temperature of the system (*i.e.*, approaching the glass-softening T range), when this becomes high enough so that Brownian diffusion becomes observable on a laboratory time scale, the glass is said to become a liquid.

In the liquid state, molecules also oscillate around a mechanical equilibrium configuration, as in a crystalline solid, and hence a liquid in which Brownian diffusion occurs has also a solid like rigidity, which is numerically defined by its high-frequency (terahertz) shear modulus. Thus, the molecular dynamics during softening of a glass on heating, and in the vitrification range of a liquid on cooling, are currently of much interest. In particular, the relations of the dynamics with the thermal energy and the entropy changes, proposing the specific heat $C_p(T)$ and its changes as the "observable" quantity, are of primary significance in the study of the vitrification processes and of the different phenomena accompanying it. This dynamics has been discussed by means of different approaches [254-257], including fluctuation of a liquid's thermodynamic state point in a potential energy landscape [248, 258-260], the last being a description of how the energy of a system changes with the geometry of molecular arrangement, particularly with reference to structural relaxation and viscosity.

It is commonly accepted that to the specific heat C_p and entropy of glass contribute mostly the vibrational motions, whereas in the liquid phase they have two components: i) a vibrational component arising from change in the force constants and frequency as different energy levels are occupied with changing T, and ii) a configurational component arising from change in the number of arrangements with changing T that the structure of liquid explores [261]. Both contributions change on cooling until the supercooled liquid vitrifies. Thus, C_p of the glass has mostly a vibrational contribution $C_{p,\mathrm{vib}}$. On heating through its softening temperature T_g, this C_p begins to gain the configurational contribution in a time- and temperature-dependent manner, reaching the full value in the ultraviscous state. Both the vibrational and configurational parts of an equilibrium ultraviscous state's C_p and entropy vary with T. In fig. 27 the specific heat of glycerol measured at constant pressure C_p in a freezing-heating cycle by using a specially designed

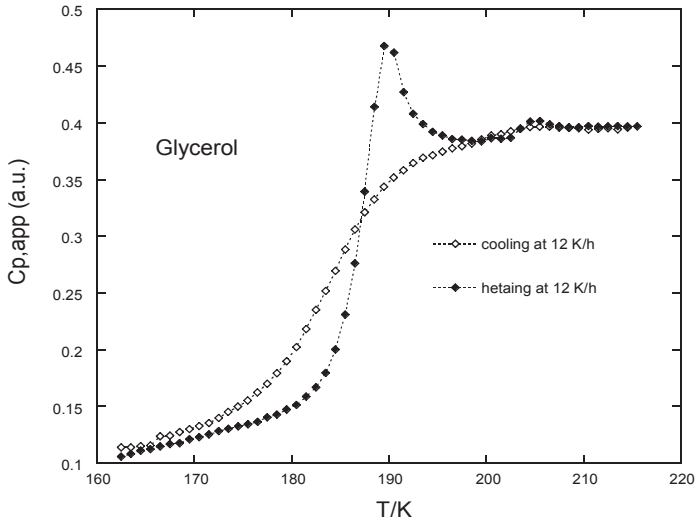

Fig. 27. – The specific heat measured in glycerol. The maximum gives a clear indication of the onset of the glass transition.

calorimeter is reported [261]. It can be used for measurements in both the adiabatic mode and temperature scanning mode, but for the reported data, it was used only with temperature modulation in the scanning mode. Thus, C_p was measured at different temperatures during both the cooling of the sample and heating. The instrument was calibrated by using dodecane as a standard and absolute C_p values were determined. Measurements made with different samples showed a reproducibility of better than 0.5% for C_p and 100 W for $\mathrm{d}H/\mathrm{d}t$. The glycerol glass transition temperature is $T_g \approx 190\,\mathrm{K}$ (the temperature of the C_p maximum just before the jump from the liquid value to that on the arrested glass phase) and the configurational contribution is roughly represented by the difference between the C_p values above and below the jump.

The vibrational part in the specific heat is determined by the shape of the potential function, curvature of its minima, and anharmonic forces of the explored configurational energy minima. The configurational part is determined by the number of molecular arrangements or the configurational energy minima that a liquid of a fixed energy and volume can explore. Thermodynamic properties of a glass should be derivable from the vibrational partition function, and that of a liquid by configurational and vibrational partition functions. These concepts are at the basis of the potential energy landscape description of liquids and disordered solids.

The way a glassy system goes toward equilibrium is then not only an interesting problem by itself but it is also of great relevance in view of a deeper understanding of the nature and the underlying physics of the glass phase. Also in this respect, many efforts have been devoted for understanding the role played by the potential energy landscape in the equilibrium dynamics of supercooled liquids. The trajectory of the representative point in the $3N$ configuration space can be mapped into a sequence of locally stable points (the so-called inherent structures, IS [262, 263]) that are the local

minima of the total potential energy V: to each instantaneous configuration during the dynamical evolution of the system one can associate an IS by a steepest-descent path in the V surface. The properties of the IS have been found to be very useful to clarify many features in the dynamics and the thermodynamics of supercooled liquids [257, 264-266] in and off equilibrium [267, 268]. Thus a detailed topological analysis of the potential energy landscape, including all stationary points of V (*e.g.*, minima and saddles) can give the better representation of the system during the equilibrium dynamics.

11˙1. *The non-ergodicity and measurement methods of the specific heat in glass forming systems.* – As previously stated, glasses, due to the loss of ergodicity, are thermodynamical systems not in thermal equilibrium.

The approaching of the glass transition has a strong dynamical signature, as is seen in the thermodynamical response functions *e.g.* the measurements of transport parameters like viscosity, self-diffusion constant, ultrasonics, relaxation times (coming especially from dielectric relaxation). These measurements show that the response functions relaxation times of the liquid increase rapidly as the glass transition is approached from above. Such a situation regards, in general, the dynamical arrest and characterizes many different systems, not only molecular liquids but also the so called "complex liquids" disordered magnets, dipolar glasses, polymers, colloid glasses and granular materials [269-272]. In addition, the thermodynamic and dynamic signatures are strongly related: as the relaxation times of the liquid increase, one must wait an ever longer time for any thermodynamic quantity to attain its equilibrium value. Thus at the T_g and below the time that the system need to equilibrate itself becomes infinity and consequently relaxation times diverge and the system physics is dominated by the non-linearity.

The problem, in these conditions, with studying static thermodynamical quantities such as C_p, is that their significance changes in a temperature interval near T_g, where the system falls out of the equilibrium. In addition there is also the following problem: how does one interpret a quantity, such as C_p in a non-equilibrium state? This is the typical situation in which the dynamics of how a measurement is performed affect the measured values. Thus, if one wants to study well-defined equilibrium quantities in the liquid state, and still learn something about the glass transition, then he must look explicitly at their dynamic behaviors. It must be also noticed that in this situation these measurements were not in the linear-response regime, so that non-equilibrium and non-linear behavior could get intervened.

A way to obtain more information, than conventional experiments on C_p, is the use of a technique that, working in a complex situation like that, enables the measurement of the linear response of the sample to a small perturbation from equilibrium. Technically the traditional measurements of the specific heat C_p involve cooling or heating the sample at a constant rate. But the temperature at which the specific heat changes abruptly, signaling the equilibrium–to–non-equilibrium (and viceversa) crossover (T_g), is strongly dependent by the heating/cooling rate of the experiment [51]. In fact, when the system is cooled slower, T_g is lower because the system has more time to equilibrate at each temperature.

A technique just developed to approach these problems is the so-called "specific-heat spectroscopy" [273]. The technique, invented to measure the frequency (ω) dependence of C_p also allows the measure of the enthalpy (h) derivative $\partial h/\partial T$, and the real and imaginary part of the specific heat, C_p' and C_p'', respectively. It must be emphasized that the technique was arranged to study the dynamics of the liquid, not that of the glass. The main aim, of the use of such a calorimeter was to show that the thermodynamic, as

well as the relaxational properties of the glass transition, are apparent in the equilibrium state and also to test whether the relaxation times probed by specific-heat spectroscopy are the same of those probed by other techniques such as dielectric spectroscopy. Only by working in a large frequency range (five decades) it is possible to probe the linear response of supercooled liquids to small perturbation from the equilibrium and to obtain, by means of calorimetry, thermodynamic information on the zero frequency (by the extrapolation of the obtained data).

The frequency-dependent $C_p(\omega)$ is defined (like the dielectric constant or the compressibility) as a dynamic susceptibility. The well-known relation for which the heat that the system can adsorb from its surroundings for a ΔT change (q) is equal to the change in enthalpy h per volume, $q = h = C_p \Delta T$, is an equilibrium expression. In general, however, h is a function of the time, t, after a T change. Such a situation is evident by considering that the system contains some degrees of freedom that relax slowly to equilibrium. For a T step at $t = 0$,

$$q(t) \equiv \begin{cases} 0, & \text{for } t < 0, \\ \{C_{p\infty} + (C_{p0} - C_{p\infty})[1 - \Phi(t)]\}\, \Delta T, & \text{for } t > 0, \end{cases} \tag{25}$$

where $\Phi(t)$ is a relaxing function describing the slow time-dependent degrees of freedom (with $\Phi(0) = 1$ and $\Phi(\infty) = 0$) whereas $C_{p\infty}$ includes the faster ones and C_{p0} is the equilibrium specific heat. In the case that $T(t)$ stays close a certain value, C_{p0} and $C_{p\infty}$ will be constant,

$$q(t) = \int_{-\infty}^{t} \mathrm{d}t' \left\{C_{p\infty} + (C_{p0} - C_{p\infty}) \left[1 - \Phi(t - t')\right]\right\} \partial T(t')/\partial t'. \tag{26}$$

Obviously, as the linear susceptibility, C_p can be measured in the t as well as in the ω domains; the integration and the Fourier transform of eq. (26) will give

$$q(t) = C_p(\omega) T(\omega), \quad \text{with} \quad C_p(\omega) = C_{p\infty} + (C_{p0} - C_{p\infty}) \int_0^{\infty} -\partial\Phi(t)/\partial t e^{i\omega t} \mathrm{d}t. \tag{27}$$

The static specific heat is then $C_p(\omega = 0) = C_{p0}$. If the system has some slowly relaxing degrees of freedom ($C_{p0} - C_{p\infty} > 0$), then $C_p(\omega)$ must be a complex susceptibility. The heat oscillations lag in phase behind the T oscillations whenever the inverse of the measurement frequency is comparable to the characteristic relaxation time of slow modes. The real and imaginary parts of $C_p(\omega)$, obey the Kramers-Kronig relation and can be related to an equilibrium t-dependent correlation function. The static specific heat is related with the entropy fluctuations, whereas at constant P these are proportional to the fluctuations of enthalpy, hence $C_p = V/k_B T^2 \langle [h(t) - \overline{h}]^2 \rangle$; being in the liquid ergodic phase the angular brackets can be thought of either as an ensemble average or as a time average, and $\overline{h}$ is the average of the $h(t)$. In terms of the fluctuation-dissipation theorem such a result can be generalized giving a dynamical susceptibility. The dynamics which governs how a system responds to an external perturbation are the same as those which govern how spontaneous fluctuations decay. If the slow and fast modes are explicitly included in the relaxing function the complete form is: $\Phi(t) = \langle [h(t) - \overline{h}][h(0) - \overline{h}] \rangle / \langle [h(t) - \overline{h}]^2 \rangle$. The ω-dependent specific heat will

then be

$$C_p(\omega) = (V/k_B T^2) \int_0^\infty -\frac{\mathrm{d}}{\mathrm{d}t} \left\langle \left[h(t) - \overline{h}\right] \left[h(0) - \overline{h}\right] \right\rangle e^{i\omega t} \mathrm{d}t. \tag{28}$$

At temperatures below the T_g, where due to tunneling effects the specific heat has a ω-dependence, also supercooled liquids have such a property. In that case $C_p(\omega)$ has mainly two contributions: one which equilibrates quickly, and another which equilibrates more and more slowly as the dynamical arrest is approached.

The traditional adiabatic method of measuring C_p consists of applying a short heat pulse to a well-isolated sample and then measuring the temperature increase after the heat has diffused in the sample. Alternatively, adiabatic measurements in the frequency domain are possible by applying a sinusoidal current at a frequency ω and measuring the consequent T oscillations at that frequency. In either case the measurement time must be long if compared with the sample thermal-diffusion time τ_D. For a distance d that heat must traverse is $\tau_D = C_p d^2/\kappa$ (with κ the thermal diffusivity). One has also to consider that the measurement time must be short compared with the time τ_{ext} it takes the sample temperature to decay back to the temperature of the surrounding heat bath. Then $\tau_D \ll 1/\omega \ll \tau_{\mathrm{ext}}$. This is a constraint for a correct measurement of C_p. However, on approaching the arrest, relaxation time diverges so that the interest is to cover as wide a ω-range as possible. The C_p spectroscopy is essentially based on heat diffusion from a heater which is producing a heat flux sinusoidal in time, and which is immersed in a bath of the liquid to be studied. With a proper geometry the temperature oscillations at the heater will be simply related to the thermal properties of the surrounding liquids. The apparatus is made as follows: a current of frequency $(\omega/2)$ passes through the heater $I(t) = I_0 \cos(\omega t/2)$. The power dissipated in the heater has two components, a DC component (producing a constant temperature gradient in the cell) and a second one oscillating at frequency ω (that originates a diffusive thermal wave),

$$P(t) = (I_0^2 R/2)[1 + \cos(\omega t)], \tag{29}$$

where the temperature of the heater oscillates at the frequency ω of the heat oscillations $T = T_{\mathrm{DC}} + T_\omega \cos(\omega t - \varphi)$, T_{DC} is the heater average temperature and T_ω is the oscillations amplitude. The phase lag φ depends both on the geometry and on the thermal properties of the medium. Being the resistance of the heater (a metal) dependent on T, it has a small component that oscillates at the same frequency of the T oscillations,

$$R = R_{\mathrm{DC}} + R_\omega \cos(\omega t - \varphi), \tag{30}$$

and

$$R_\omega = \alpha R_{\mathrm{DC}} T_\omega, \tag{31}$$

where α is the temperature coefficient of resistance of the heater. The resulting voltage across the heater is the product of the current traversing it (at a frequency $\omega/2$) and its resistance (which has a small ω component). The mixing of these two frequencies gives

$$V(t) = I(t)R(t) = V_{\omega/2} \cos(\omega t/2 - \varphi') + V_{3\omega/2} \cos(3\omega/2 - \varphi), \tag{32}$$

where $V_{\omega/2} = I_0 R_{\rm DC}$ plus a small contribution coming from mixing I_0 and R_ω; moreover $V_{3\omega/2} = I_0 R_\omega/2$ and proportional to T_ω. A special experimental care to measure the small voltage $V_{3\omega/2}$ in the presence of the much larger $V_{\omega/2}$ is necessary; a typical frequency interval available with such a technique is $0.01 < f < 6\,\text{kHz}$, ($\omega = 2\pi f$) [274].

To complete the description of such an apparatus, we consider the heat-diffusion process. The heat density q (or entropy density times T) is related with the heat current j_q by means of the expressions $\dot{q} + \boldsymbol{\nabla} \cdot \mathbf{j}_q = 0$ and of $\mathbf{j}_q = -\kappa \nabla T$ (κ is the thermal conductivity) that combined give

$$\dot{q} = \kappa \nabla^2 T. \tag{33}$$

By considering that $\dot{q} = -i\omega q(\omega) = -i\omega C_p(\omega) T(\omega)$ it follows that

$$-i\omega C_p(\omega) T(\omega) = \kappa \nabla^2 T, \tag{34}$$

representing a differential equation simple to solve by considering in a proper way the appropriate experimental geometry; the simplest are that of a plane [273] or cylindrical [274] heater. In the first case it can be assumed that the heater (having infinite area and zero thickness) lies in the $x = 0$ plane; a window glass substrate over which is placed the heater fills the region $x < 0$ and the liquid surroundings the heater fills all the space for $x > 0$. The heat flux from the heater (equal to the power dissipated for unit area of the heater) is $j_q(t) = Re(j_0 e^{-i\omega t})$. With the boundary conditions $T \to T_{\rm DC}$ as $x \to \pm\infty$ the steady-state solution of eq. (34) is

$$T(x,t) \equiv T_{\rm DC} + \begin{cases} Re\left\{T(x=0,\omega) e^{-kx} e^{-i\omega t}\right\}, & \text{for } x > 0, \\ Re\left\{T(x=0,\omega) e^{k_{\rm sub} x} e^{-i\omega t}\right\}, & \text{for } x < 0, \end{cases} \tag{35}$$

where $T(x=0,\omega) = T_\omega e^{i\varphi}$ is the complex amplitude of the temperature oscillations on the heater. Here k is the thermal wave vector describing the diffusive waves

$$k = \left(\frac{\omega C_p}{\kappa}\right)^{1/2} e^{-i\pi/4} = \left(\frac{\omega C_p}{2\kappa}\right)^{1/2} (1-i). \tag{36}$$

The substrate wave vector $k_{\rm sub}$ has the same form of k except that it contains the same thermal parameters of the substrate $C_{\rm sub}$ and $\kappa_{\rm sub}$ which are real and frequency independent on the contrary of C_p and κ (the liquid parameter) that are in principle complex and frequency dependent. $T(x=0,\omega)$ can be obtained from the boundary condition relating j_q with ∇T at $x = 0$. On considering the experimental geometry and the two heater sides we write

$$j_q(t) = \kappa_{\rm sub} \left.\frac{\partial T}{\partial x}\right|_{x \to 0^-} - \kappa \left.\frac{\partial T}{\partial x}\right|_{x \to 0^+}. \tag{37}$$

By considering on eq. (37) the results on $T(x,t)$, eq. (35), we obtain

$$T(x=0,\omega) = \frac{j_0}{(\kappa k + \kappa_{\rm sub} k_{\rm sub})} = \frac{j_0 e^{i\pi/4}}{\left[(\omega C_p \kappa)^{1/2} + (\omega C_{\rm sub} \kappa_{\rm sub})^{1/2}\right]}. \tag{38}$$

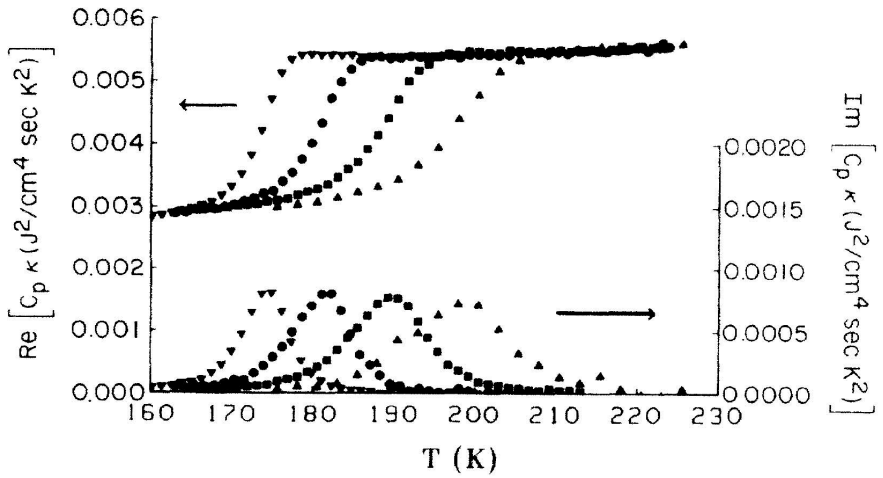

Fig. 28. – The real and imaginary part of the specific heat, $C_p\kappa$, measured in propylene glycol as a function of the temperature. The measurement frequencies are (triangles down) $f = 0.11$ Hz, (circles) $f = 4$ Hz, (squares) $f = 110$ Hz and (triangles up) $f = 1900$ Hz. Figure from [273].

To have $C_p\kappa$ it is necessary to measure the substrate contribution $C_{\rm sub}\kappa_{\rm sub}$ (making a measurement with the cell empty) over the whole T range of the experiment. The subtraction of this contribution from the data obtained with the full sample cell gives $C_p\kappa$ of the sample. In some cases, like the calorimeter in the cylindrical geometry, to subtract the substrate contribution two identical cells working in parallel are used, one with the sample and the second one empty; in such a case the subtraction is made in real time.

From eq. (38), in the case of C_p and κ real and ω-independent, as they are in a normal liquid far from the arrest, it follows that the amplitude of the T oscillations will be $\sim \omega^{-1/2}$, and their phase lag will be $\varphi = \pi/4$ with respect to the heat oscillations. There are two criteria to determine the performance of the plane heater. As the sample approaches the glass transition region, $C_p\kappa$ becomes complex and ω-dependent and, due to the complex specific heat, the phase lag deviates from $\pi/4$; also the amplitude of the thermal oscillation no longer varies as $\omega^{-1/2}$. It must be stressed that with such a geometry (plane heater) the product $C_p\kappa$ rather than just C_p is measured, as do the conventional adiabatic measurements. Figure 28 illustrates such a situation, in the supercooled propylene glycol for some different frequency values [273].

Instead in the case of a specific-heat spectroscopy, in which it is used a cylindrical geometry working with a differential cell configuration (like a differential scanning calorimeter DSC), the complex $C_p(\omega)$ is measured. This type of calorimeter named temperature modulated scanning calorimetry (TMSC) is a heat-modulated variant of the DSC. In fact it consists (like the DSC) of two identical measuring cells one containing the liquid sample and the second, acting as a reference, is kept empty. The difference with the DSC is in the operation way working the TMSC in modulation of temperature. The cells are in fact heated by a sinusoidal power signal, $P(t)$ of known amplitude and frequency, superimposed on a constant value $P_0 = I_0^2 R/2$, such that $P(t) = (I_0^2 R/2)[1 + \cos(\omega t)]$.

Thus in the TMSC the rate of that part of the heat stored or released which reverses with reversal of the temperature is measured. The components of the complex heat capacity oscillating in-phase, C_p', and out-of-phase, C_p'', with the temperature during the modulation cycle are calculated. The two components are related to the modulation amplitude, and the modulation period, $1/f$.

This type of instrument within the framework of linear response, can be described as an electrical circuit with distributed loss and storage components. The complex temperature T_x of the cell sensor is related to the complex equivalent electrical admittance $Y = i\omega C_p$ by $T_x - T_0 = AY/(1 + BY)$ where T_0 is the complex temperature of the cell without the sample and A and B are the instrument's constants which are ω- and T-dependent.

In DSC heat capacity $C_{p,\mathrm{DSC}}$ is measured from the rate of heat flow and calculated as

$$C_{p,\mathrm{DSC}} = \beta^{-1} \frac{\mathrm{d}h(T,t,x_i)}{\mathrm{d}t}\,, \tag{39}$$

where $(\mathrm{d}h(T,t,x_i)/\mathrm{d}t)$ is the measured rate of enthalpy change and β is the temperature scanning (heating or cooling) rate. This form can be generalized by taking into account other time-dependent quantities, for example: i) the temperature T and ii) the mole fraction of the material x_i undergoing some physical change. Therefore

$$C_{p,\mathrm{DSC}} = \left[\frac{\partial h}{\partial T} + \left(\frac{\partial h}{\partial x_i(T)}\right)\left(\frac{\mathrm{d}x_i}{\mathrm{d}T}\right)\right] + (\beta^{-1})\left[\frac{\partial h}{\partial t} + \left(\frac{\partial h}{\partial x_i(t)}\right)\left(\frac{\mathrm{d}x_i}{\mathrm{d}t}\right)\right], \tag{40}$$

where $\partial h/\partial T$ is the true thermodynamic heat capacity at the equilibrium ($\partial h/\partial T = C_p$). Thus $C_{p,\mathrm{DSC}}$ measures together the true C_p and all the other possible contributions coming out, for example, from the fact the system is out of the equilibrium or changes its physical properties. This explains the reason for which $C_{p,\mathrm{DSC}}$ is also reported as the apparent specific heat *i.e.* $C_{p,\mathrm{DSC}} = C_{p,\mathrm{app}}$. In fig. 29 typical results of the measured $C_{p,\mathrm{app}}$ are reported.

However, the comparison of the data obtained from the DSC and TMSC techniques is simpler when $C_p'' = 0$, as for liquids far from the arrest; in that case, the magnitude of C_p' is given by the first term in the square brackets on the right-hand side of eq. (40). Hence,

$$C_{p,\mathrm{app}} = C_p' + (\beta^{-1})\left[\frac{\partial h}{\partial t} + \left(\frac{\partial h}{\partial x_i(t)}\right)\left(\frac{\mathrm{d}x_i}{\mathrm{d}t}\right)\right]. \tag{41}$$

According to the generalized form of $C_{p,\mathrm{app}}$ three conditions for the occurrence of a chemical and/or physical process in terms of the enthalpy change can be identified:

a) When $(\partial h/\partial x_i) = 0$, or when $(\mathrm{d}x_i/\mathrm{d}T) = 0$, and the quantities $(\mathrm{d}x_i/\mathrm{d}t) = 0$ and $(\partial h/\partial t) = 0$, *i.e.*, there is neither a chemical nor a physical process for producing a temperature and time-dependent change in the enthalpy. In this case, the measured value of C_p from a DSC experiment is given by $C_{p,\mathrm{app}} = C_p' = \partial h/\partial T$.

b) When $(\partial h/\partial x_i) \neq 0$, or when $(\mathrm{d}x_i/\mathrm{d}T) \neq 0$, but $(\mathrm{d}x_i/\mathrm{d}t) = 0$ and $(\partial h/\partial t) = 0$, *i.e.*, there is a fast reversible (chemical or physical) process that restores the original state of the sample at any time within the time period of the temperature modulation cycle, and there is no irreversible (physical or chemical) process. Therefore, the last term

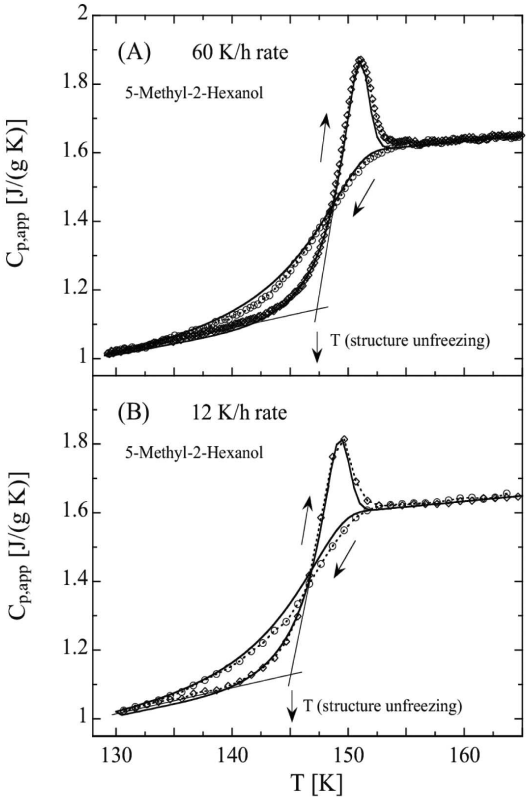

Fig. 29. – The specific heat measured in 5-Methyl-2-Hexanol in two different thermal rates (60 K/h and 12 K/h). The thermal cycle procedure used is represented in the figure by the arrows: the sample has first been cooled and afterwards heated [275].

in the square brackets in eq. (40) is zero. In this case, the measured value is given by $C_{p,\mathrm{app}} = \partial h/\partial T + (\partial h/\partial x_i(T))(\partial x_i/\partial T) = C'_p$.

c) When $(\partial h/\partial x_i) \neq 0$, or when $(\mathrm{d}x_i/\mathrm{d}T) \neq 0$, but $(\mathrm{d}x_i/\mathrm{d}t) \neq 0$ and $(\partial h/\partial t) \neq 0$, *i.e.*, there are slow and irreversible (chemical or physical) processes that occur at that T, *i.e.*, the rate of these processes is slow such that the original state is not restored during the modulation cycle, and there is also a time-dependent enthalpy arising from an irreversible (chemical or physical) process. In this case, $C_{p,\mathrm{app}} \neq C'_p$. This situation is illustrated in fig. 30 for 5-Methyl-2-Hexanol in the glass transition region, in the same figure the measured C''_p is reported.

These data of C'_p and C''_p are obtained from the temperature modulated calorimetry where the real (in-phase component) C'_p and the imaginary (out-of-phase) component C''_p of the complex heat capacity were calculated from the equation, $C_p = C'_p - iC''_p$. In the case of a water solution of a protein (lysozyme, a small globular protein of 129 amino acid residues,) there is the condition $C''_p = 0$ being, in fact, very far from a condition of dynamical arrest. However, as it will be discussed in the next calorimetric data it

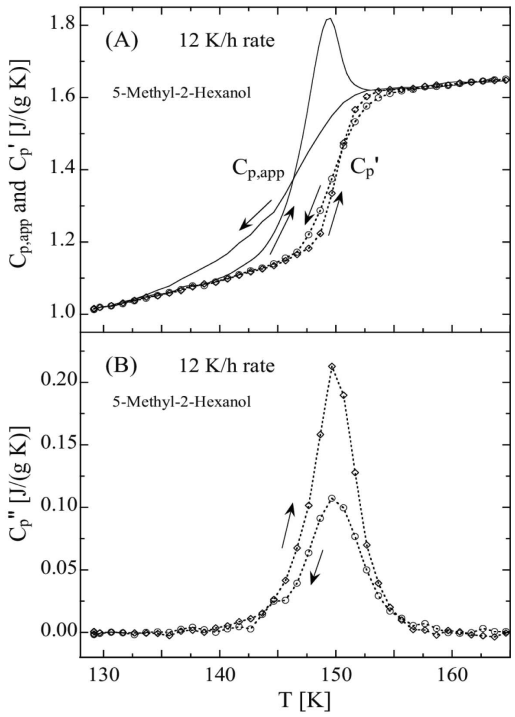

Fig. 30. – The real and imaginary parts of the specific heat measured in 5-Methyl-2-Hexanol during the cooling and heating at a rate of 12 K/h [275].

reveals in a very deeper way the important phenomenon of the protein folding/unfolding process, determinant in biology. Figure 31 illustrates such a situation [276].

11˙2. *Other calorimetric methods and the water heat capacity.* – As previously said, one of the unusual behaviors of water regards just the way in which it forms a glass. According to the previous discussion the way in which the system adsorbs (or releases) the thermal energy (heat capacity and enthalpy behaviors), as a function of the thermodynamical variables, may be considered a signature of the glass transition phenomenon. In fact at the vitrification the liquid translational and rotational degrees of freedom, by which the system absorbs energy and flows, are arrested and thus its specific heat suddenly drops. The heat capacity changes thus at the glass transition temperature, T_g, from a high value, characteristic of a liquid, to a value characterizing a solid (with only vibrational degrees of freedom) and there is usually a big difference, making it detectable. We must notice that a definitive proof that these specific heat jumps (and maxima) are due to the glass transition can only be given if the physical effects (like aging) due to the transition in non-ergodic states are also observed. However, if compared with other molecular liquids, water is also strange on this regard; in fact, the glass transition signature in the measured specific heat is so weak that the assignment of its T_g is controversial [5, 277]. In particular it is possible that: $130 < T_g < 160$ K [31, 32]. The glass

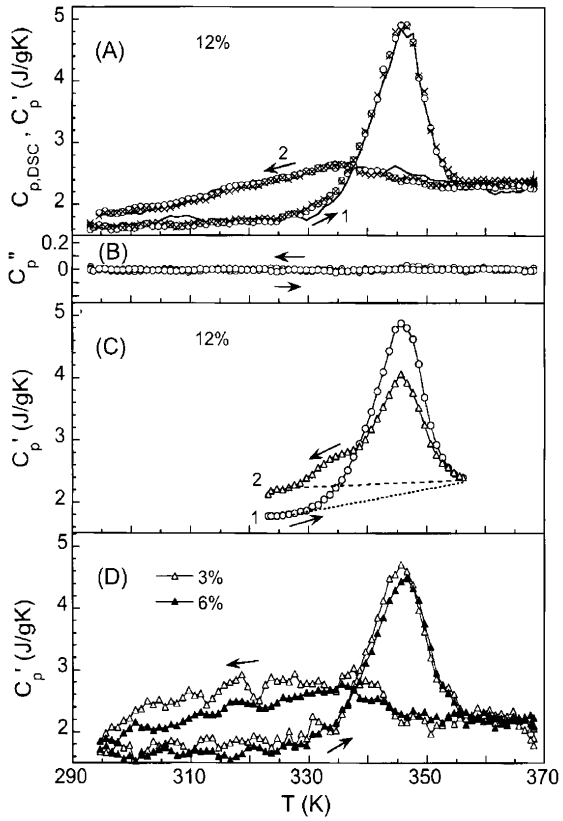

Fig. 31. – The measured C_p' and C_p'' of lysozyme solutions as a function of the temperature. Arrows indicate the temperature scanning direction (1-heating scan or 2-cooling scan) of measurements. (A) Data for C_p' of lysozyme obtained from two different 12% solutions, one is shown by crosses and another by circles. Data for $C_{p,\mathrm{DSC}}$ are shown by continuous line. (B) Data for C_p'' from the 12% solution. (C). Data for C_p' from 12% solution heated only to 356 K (circles) and then immediately cooled (triangles). (D) Data for C_p' of lysozyme from 3% and 6% solutions as denoted. The temperature of the peak and the area under it is not affected by the concentration of lysozyme solution. Figure adapted from [276].

transition has also flow consequences: below T_g in the supercooled metastable regime, the substance, when stressed, flows like a liquid (but it flows very slowly), whereas in the glass phase it bends elastically like a solid. As it is well known, glass forming liquids can be divided in two main classes: *fragile* and *strong* [278]. In a fragile glass the change in heat capacity at T_g happens very sharply and is completed in just a few degrees. In fact, the relaxation time (τ) of a fragile liquid changes very rapidly with temperature, in VFT fashion; instead in strong materials (with high T_g values) it takes hundreds of degrees to complete the transition. Some authors consider water, near its T_g, to be a strong glass forming liquid [182, 183], whereas for others it is a very fragile system [279], depending on the temperature and the cooling rate. Still others think it is both [187]. In any case,

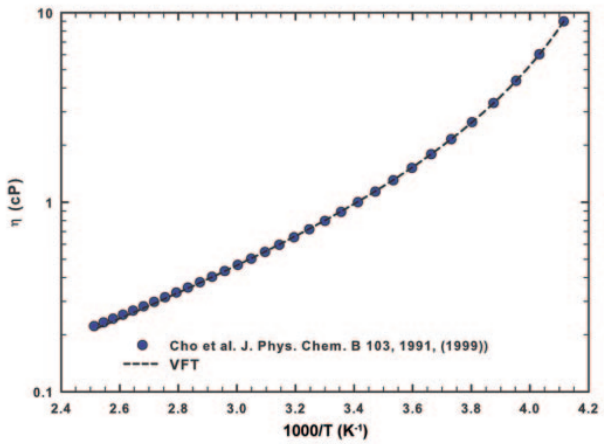

Fig. 32. – The water viscosity plotted in a log-linear scale *vs.* $1000/T$.

the temperature behavior of the water viscosity in the supercooled regime [280], as it can be observed from fig. 32, can be represented by means of a VFT equation with the indication, at least in this regime, that water is a fragile glass former.

However, it is very important to focus the attention on both the regions of the water phase diagram in which the specific heat C_p of liquid water has been measured. Figure 33 reports the temperature behavior of C_p measured in bulk water (down to 244.5 K), where the obtained data are fitted according to the scaling law: $C_p = A[(T - T_c)/T_c]^{-x} + B$ (with $A = 0.44$, $B = 74.3$, $T_c = 222\,\mathrm{K}$ and $x = 2.5$ [281]).

Specific heat data are available in all the temperature range except the No Man's Land. In particular, data are available in the supercooled region ($T > 236\,\mathrm{K}$, limit of supercooling), in the region of H_2O vapor deposit (with $T_g \sim 136\,\mathrm{K}$) and in that of the hyper-quenched (LDA) glassy water (estimated $T_g \sim 165\,\mathrm{K}$), *i.e.*, for $30 < T < 150\,\mathrm{K}$. In this second case the estimated T_g value is given by the following considerations: studying the thermal behavior of hyperquenched LDA when heated toward its T_g, it has been noticed that the release of heat (enthalpy relaxation) does not occur until the sample is very close to its glass transition temperature [31, 32]. Such a behavior is contrary to what is observed in many other glass-forming liquids, in which thermal relaxation begins at lower values of T/T_g. Normal behavior is restored only if to water's T_g is reassigned a value of 165 K [31, 32]. This reassignment is controversial because spontaneous crystallization to cubic ice (Ic) at around 150 K precludes direct observation of this higher T_g. It is of interest that in this low-temperature region the T_g values of some molecular and ionic water solutions are also found (fig. 1 of [32] gives a nice reproduction of such a situation). A comparison is possible between the calorimetric data measured in these solutions and the ones measured in pure laboratory water. Thus, if the change in the heat capacity (ΔC_p) at the T_g of these molecular and ionic water solutions (see, *e.g.*, fig. 1 of [32]) are compared with that measured in pure laboratory water at $T_g = 136\,\mathrm{K}$ [282, 283], it emerges that the pure water ΔC_p is only 2% of that of its solutions [284]. The solution of hydrazine N_2H_4 has a maximum at $T_g \sim 140\,\mathrm{K}$ with $C_p \sim 75\,\mathrm{J\,mol^{-1}\,K^{-1}}$, a value that is higher than that of the LDA water [32] but

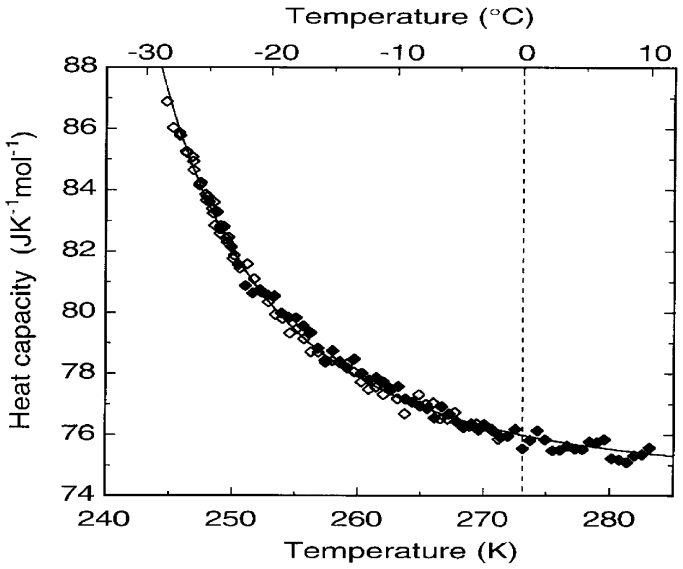

Fig. 33. – Heat capacity of bulk water measured as a function of temperature. Different symbols deal with the two studied samples; the full line is the curve fitting the experimental points [281].

lower if compared with the one measured in water in the region immediately below its freezing point. These latter water data, obtained in an emulsion [4, 284, 285] of about $1\,\mu$M, have been criticized as artificial [286]; lately it has been established as correct by bulk water (large samples of extreme purity) studied up to a temperature of 243 K [281]. Calorimetric data of water confined in emulsion and data of pure bulk water are, within the experimental error, about the same and are characterized by a diverging-like behavior; in particular they have been fitted by means of a proper scaling law [281]. In the emulsified water at the lowest studied temperature ($T = 236\,\mathrm{K}$) $C_p \sim 103\,\mathrm{J\,mol^{-1}\,K^{-1}}$ was measured, a value higher than the maximum of the water-hydrazine solution. Such a result gives an idea of the challenging research results that can be found in the No Man's Land gap if calorimetric studies, for the case in which water does form the HB network but does not crystallize, are possible. The question is fascinating because we can look for behaviors along a continuous path in $C_p(T)$ between the large and diverging value of the supercooled liquid phase, and the tiny value at 130–150 K.

The problem of how water should behave if crystallization did not occur inside the No Man's Land gap have now a direct route: *i.e.*, by studying its properties in nanoscopic confinements. There is a large literature for calorimetric experiments in confined water in the very supercooled regime [212, 213, 287-291]. Many of these have been devoted to study water at different hydration values, more precisely the behavior of water near the pore surface. Only recently the heat capacity of nanoscopically confined water was reported by using the adiabatic method [292, 293]. Such a technique is especially sensitive for a situation like that of water in which the specific heat jump (connected with the glass transition) is small or occurs in a wide temperature range. The method is based on the

specific properties of a glass accompanying the aging phenomenon. In these experiments different confining materials like silica gels CARiACT Q-50, Q-10, Q-6, and Q-3 [292] and MCM-41 [293] nanotubes of different pore sizes have been used with the aim to separate the properties of the "surface" water from those of "internal" water. In order to consider such a situation, these samples are different from the ones used in previous experiments; in fact on the contrary of MCM-41-S nanotubes, the actual confining materials used in these calorimetric experiments are characterized by the presence of silanol groups.

The first adiabatic calorimetric study was carried out for water (H_2O and D_2O) confined within the voids of silica-gel materials CARiACT Q-50, Q-10, Q-6, and Q-3, having the following average pore diameters $\phi = 52$, 12, 6, and 1.1 nm, respectively [292]. The data analysis is performed according to the idea of a separation between the pore wall water (interfacial) and the one located at the center of the pores. The obtained results have been summarized originally in such a way. Most of the water was found to crystallize within the pores above about 2 nm in diameter, but for pores less than about 1.6 nm in diameter it remains in the liquid state down to 80 K. In particular Oguni and coworkers found that: internal pores water aggregates undergo a glass transition at 160 and 165 K for ordinary and heavy water, respectively, and the interfacial water on the pore wall which exhibits a glass transition over the range 115–139 K, is composed roughly of one layer. It is suggested that the glass transition of bulk supercooled water takes place potentially at 160 K or above due to the development of an energetically more stable HB network of water molecules at low temperatures.

The presence of a calorimetric glass transition may be ordinarily identified through finding a heat-capacity jump in the DSC. However, like in water, it is rather difficult to identify it when the heat-capacity jump is small or occurs in a wide temperature range. It is however interesting to consider, after the frequency-dependent calorimeters [273, 294], also adiabatic calorimeters [295], instruments that operate by means of the direct observation of the enthalpy relaxations by means of different thermal rates.

However, before giving details on such a technique, it is important to spend some words on the fact that such a method is based on analogous physical effects accompanying the aging phenomenon, and is thus valid to give additional information on T_g. Ordinarily, measurements are carried out by heating (or cooling) the sample in the intermittent way under adiabatic conditions [295]. The sample temperature is followed to determine the initial temperature T_i, increased at a certain rate R (*e.g.*, 0.1 K/min) with the supply of electrical power P, and then followed again to determine the final one, T_f. In these conditions the heat capacity is evaluated as $C_p = P/(T_f - T_i)$. When the sample absorbs (or releases) heat, to reach the equilibrium state, a spontaneous temperature drift $\mathrm{d}T/\mathrm{d}t$ is observed. The enthalpy relaxation rate is then evaluated by an equation $(-\mathrm{d}H/\mathrm{d}t) = C_p(\mathrm{d}T/\mathrm{d}t)$. Figure 34 illustrates how the H relaxation is observed in the T_g region (especially below it).

In the glass transition region the equilibrium configurational enthalpy decreases with decreasing the temperature; at the same time, by decreasing T the molecular configurational relaxation time τ increases. At the glass transition, relaxations proceed from non-equilibrium to equilibrium states. Due to the system's non-ergodicity, the non-equilibrium states at a certain constant temperature and the corresponding rate of enthalpy relaxations, are strongly dependent on the sample thermal history, such as the rate of pre-cooling. Figure 34 illustrates this. When the liquid vitrifies through rapid cooling, τ deviates from the equilibrium dependence at relatively high temperature, and H becomes much higher than for the equilibrium situation (fig. 34(a)). From this rapid

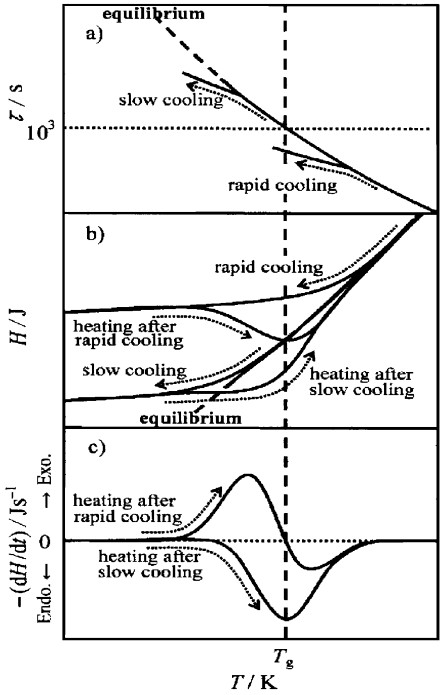

Fig. 34. – Relationship between a) the relaxation time τ, b) the enthalpy H, and c) the spontaneous enthalpy-relaxation rate $-\mathrm{d}H/\mathrm{d}t$ as a function of T, observed in the dynamical arrest region with a single characteristic time for the molecular rearrangement. T_g was determined empirically as the point at which the rapidly cooled sample showed a change (against temperature) in $\mathrm{d}H/\mathrm{d}t$ from positive to negative and the slowly cooled sample showed a minimum $\mathrm{d}H/\mathrm{d}t$ value [296].

cooling (or quenching) the configurational structure is frozen to the one corresponding to a high temperature and the associated enthalpy, will result rather higher than for the equilibrium situation (fig. 34(b)).

Vice versa when the temperature of the glass is increased, τ becomes short and gradually approaches an observable timescale (*e.g.*, $10^2 < \tau < 10^6$ s). The T increase corresponds to the situation when H starts to relax and decreases toward its equilibrium value (fig. 34(b)) and an exothermic enthalpy-relaxation effect is observed. $-\mathrm{d}H/\mathrm{d}t$ increases with an increase in temperature due to the shortening of τ (fig. 34(c)). A further T increase results in the H crossing the equilibrium line at around T_g and taking on smaller values than at equilibrium. Therefore, $-\mathrm{d}H/\mathrm{d}t$ exhibited a positive peak, became zero at the crossing of H with the equilibrium line, and then took on negative values (fig. 34(c)). As the temperature was increased further, τ became shorter and shorter and the liquid exhibited no relaxation phenomenon in the experimental timescale, consequently $\mathrm{d}H/\mathrm{d}t$ returned to zero, while the glass reached its equilibrium state.

If the liquid were vitrified through a very slow cooling, τ and H deviated from their respective equilibrium lines at relatively lower T's with H considerably lower if compared with the previous situation of fast cooling.

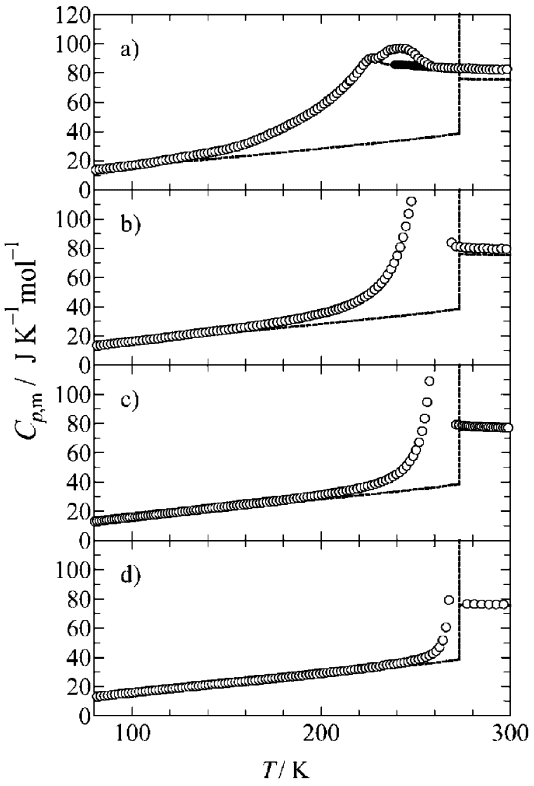

Fig. 35. – Heat capacities of mixtures of water and ice confined in silica gel of (a) 1.1 nm, (b) 6 nm, (c) 12 nm, and (d) 52 nm average pore diameter [293]. Lines represent the literature results of bulk water and ice [297], and filled circles (a) represent the data obtained for the sample cooled to 235 K and measured in the heating direction.

Also in that case, upon heating the liquid, an endothermic enthalpy relaxation appeared after H crossed the equilibrium line and took on lower values than at equilibrium; $-\mathrm{d}H/\mathrm{d}t$ exhibited a negative peak. As τ became shorter with increasing T, H, which had deviated below the equilibrium line, gradually returned to it at essentially the same temperature as in the case for the rapidly cooled liquid. A kind of hysteresis loop is obtained in the relaxation rates depending on the pre-cooling rates. This is just the calorimetric characteristic of a glass transition and has the same physical origin of the phenomena observed in the aging processes. These observations of a set of exothermic and endothermic $-\mathrm{d}H/\mathrm{d}t$ values for the rapidly and slowly cooled samples, respectively, indicate the presence of a glass transition [298, 299]. The T_g value is empirically determined as the temperature at which the rapidly cooled sample showed a change (against temperature) in $-\mathrm{d}H/\mathrm{d}t$ from heat evolution to heat absorption effects, and the slowly cooled sample showed a maximum in the heat-absorption effect [296,299]. In particular, in the case of vitrified ice well defined maxima are observed

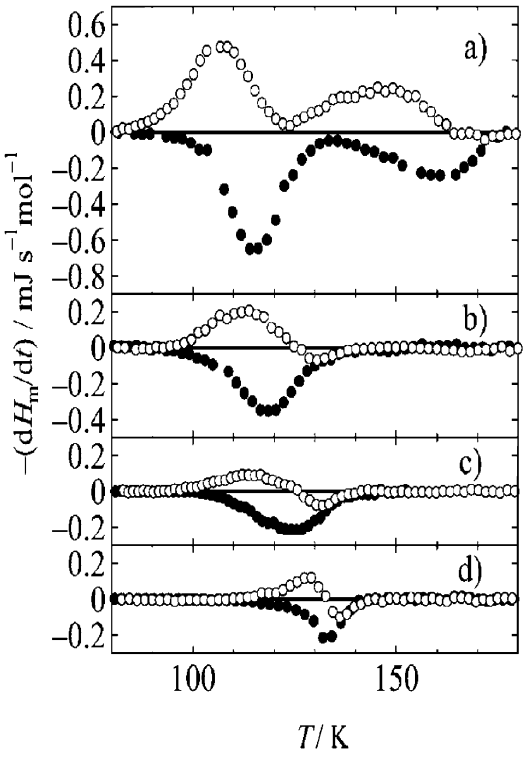

Fig. 36. – T dependence of the rates of spontaneous heat release and absorption, observed in the heat-capacity measurements in water confined in pores of silica gels (data from ref. [293]). Average pore diameter: (a) 1.1 nm, (b) 6 nm, (c) 12 nm, and (d) 52 nm. Open circles: sample cooled rapidly at around 5 K min^{-1} before the measurements, dots sample cooled slowly at 10 mK min^{-1}. The observed behavior in the heat evolution for the rapidly and slowly cooled samples are characteristic of a glass transition.

in the C_p/T at different temperature (around 110 K) depending on the temperature samples treatments.

By using such a technique in water confined in silica-gel materials (CARiACT Q-50, Q-10, Q-6, and Q-3) [292] and MCM-41 [300], the T dependence of the heat capacity (C_p), fig. 35, and the enthalpy relaxation rates $-\mathrm{d}H/\mathrm{d}t$ or the rate of spontaneous heat release or absorption are thus separately measured, fig. 36. In any case it is just this latter quantity, measured in the thermometry periods of heat capacity measurements upon intermittent heating, that gives the correct indication of the water glass transition temperature. In these experiments the enthalpy relaxation $-\mathrm{d}H/\mathrm{d}t$ was evaluated as $-\mathrm{d}H/\mathrm{d}t = C_p(\mathrm{d}T/\mathrm{d}t)/n_\mathrm{W}$ in which C_p is the measured heat capacity and n_W is the amount of water within the pores. In both the cases of H_2O and D_2O when the sample was cooled rapidly in this temperature range before measurement, heat release (positive $-\mathrm{d}H/\mathrm{d}t$) and then heat absorption (negative $\mathrm{d}H/\mathrm{d}t$) effects were observed in the

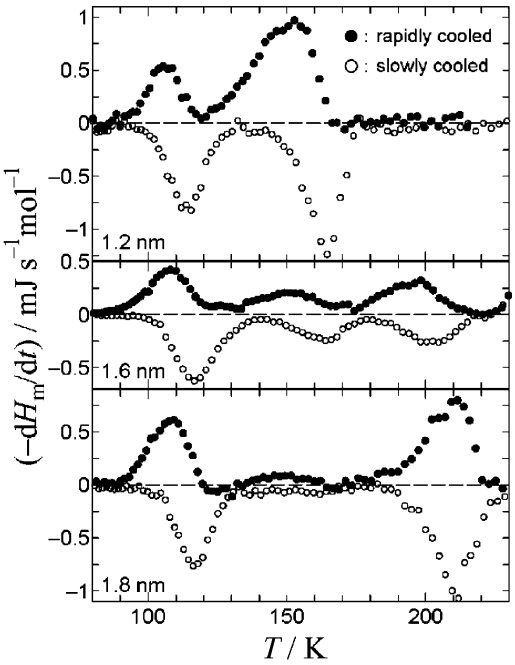

Fig. 37. – Spontaneous enthalpy release and absorption rates of the water confined within nanopores of silica MCM-41 with the following pore diameter: 1.2 nm (diamonds), 1.6 nm (circles), and 1.8 nm (squares) [300].

measurements. When the sample was cooled slowly, on the other hand, only the heat-absorption effect was observed. This dependence reflects the enthalpy relaxation of the water due to its structural change and is characteristic of a glass transition as described above. The T_g values, at which τ becomes 1 ks, were estimated to be 119 K, 124 K, and 132 K for the $\phi = 6$, 12, and 52 nm pores, respectively, according to the empirical relation stated above. In the case of the 1.1 nm pores, two sets of heat release and absorption effects were found in the ranges 90–130 K and 130–170 K, indicating the presence of two glass transitions. The T_g values were estimated in the same way to be about 115 K and 160 K. The rate of spontaneous heat release or absorption observed for confined heavy water are quite similar to that for ordinary water.

It must be stressed that a very large dominant peak is observable in C_p. Calorimetry was performed in the heating direction with repetition of energy supply and thermometry periods under adiabatic conditions. Most of the water crystallized as ice on cooling before measurement in the cases of the pores with 6 nm, 12 nm, and 52 nm average diameters. In the 1.1 nm pores, as there was a certain pore size distribution present, only a small part of the water crystallized; the majority remained in the liquid state down to 80 K. This large dominant C_p peak is observable in the heat capacities experimentally derived from the mixture of ordinary water and ice confined within $\phi = 1.1, 6, 12$, and 52 nm pores, and is found to be dependent on the pore size in the temperature region 260–270 K. It

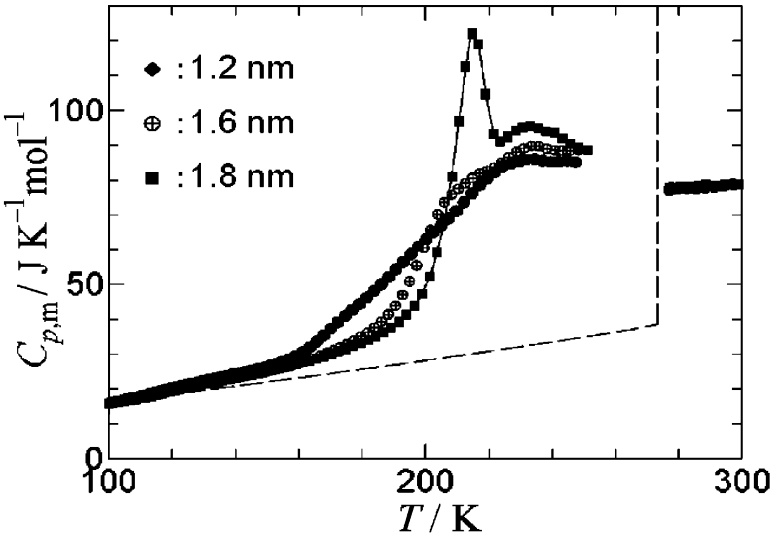

Fig. 38. – The molar heat capacity $C_{p,m}$ measured in water-confined in silica nanotubes (MCM-41 samples with a pore diameter of 1.2 nm, 1.6 nm, and 1.8 nm). The results are compared with specific heat data of ice (dashed line) and bulk water (symbols at $T \geq 270$ K) [300].

was considered to be mainly due to fusion of ice [212,301,302]. In the $\phi = 1.1$ nm pores, a small hump at 227 K and a peak at around 240 K were found. Given that the data around 227 K are smoothly connected with those of the sample that was cooled only to 235 K and expected to remain entirely in the liquid state, the hump at 227 K may reflect the order/disorder process of water molecules in the liquid state [4], and the peak at around 240 K is attributed to fusion of ice [212,301,302]. In that work the heat capacities derived from a mixture of heavy water and ice confined within $\phi = 1.1$, 6, 12, and 52 nm pores, are also reported. The corresponding behavior resembles that of ordinary water, except that the temperatures of fusion are a little higher than those of H_2O in the respective pores. The situation in MCM sample with $\phi = 1.2$, 1.6, and 1.8, pore size for $-\mathrm{d}H/\mathrm{d}t$ and C_p is reported in figs. 37 and 38 [300].

Figure 38 shows the results of molar heat capacities C_p of the water confined within the MCM-41 nanotubes of 1.2, 1.6, and 1.8 nm in diameter. Whereas the crystallization is observed, as shown from the enthalpy of fusion, for water within the 1.8 nm, in the cases of 1.2 and 1.6 nm pores water remains liquids up to about 160 K. According to the previous analysis for water confined in silica gels, glass transitions are observed at about 115, 165 K and only in the case of water confined in 1.6 nm pores at about 205 K. Figure 39 represents another result obtained in water confined in silica gel voids of $\phi = 1.1$ nm (CARiACT Q-3); in particular, data of the emulsified water are also reported [4].

Very recently [32] Austen Angell gave an interesting analysis of these calorimetric data of nanoconfined water. He stated that the form of the excess $C_p(T)$ reported in these latter experiments is completely different from that of common glass formers, but resembles that of the classical order-disorder transition. In particular, the case of H_2O confined in the $\phi = 1.1$ nm pore size system and the total C_p component of the

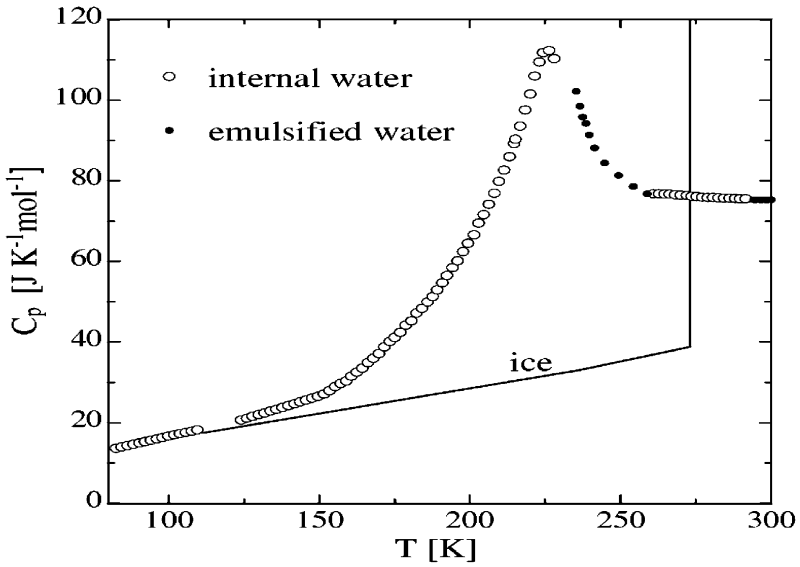

Fig. 39. – Heat capacity of internal, emulsified water and ice [32, 300].

water internal to the nanopore (and its peak at about 225 K) is considered. Angell's observations are the following:

i) the measured heat capacity is remarkably similar to that given by a thermodynamic analysis (*i.e.*, the molar excess heat capacity of supercooled water deduced by assuming phase continuity of supercooled water and vitreous ice and requiring adherence of water's properties to the first and second laws of thermodynamics through the No Man's Land [183]);

ii) a reversible behavior and thus the indication that the peak appearance is a liquid-state phenomenon, not a glass transition; and

iii) the form of the excess C_p of water reported in the 1.1 nm pores is completely different from that of common glass formers but resembles that of the classical order-disorder transition seen in superlattice alloys and rotator phases.

Angell's analysis comes out from the comparison of the pure water vitrification with that of molecular solutions rich of water and by considering, for the explanation of the low-temperature water behavior, a directly compatibility among the thermal behavior of water and that of the rotator phase of the fullerene C_{60}, which is dielectrically active in its crystalline state. In fact, in fullerene, studied by using different techniques [303-305], the total heat capacity exhibits a sharp peak at 250 K (the rotator phase) and a heat capacity anomaly (a tiny step) at about 90 K. The first one (250 K peak) has been identified as a λ transition, and the tiny step at 90 K is identified as the ergodicity-restoring glass transition. Thus, according to such an interpretation, it is an order-disorder transition that drives the thermal behavior of nanoconfined water, *i.e.*, a class of transition seen in molecular and ionic crystalline materials. Thus, whereas the true glass transition

occurs at a very low temperatures $T_g \sim 160\,\mathrm{K}$ the reversible sharp peak ($\approx 225\,\mathrm{K}$) is due to the order-disorder transition. Although in the case of the $\phi = 1.1\,\mathrm{nm}$ pores, two sets of heat release and absorption effects ($-\mathrm{d}H/\mathrm{d}t$) were found, indicating the possible presence of two glass transitions, with the corresponding T_g values estimated to be 115 and 160 K. However, for samples with $\phi > 1.1\,\mathrm{nm}$ essentially all the water crystallizes in the range that goes from 240 K to T_m and the crystallization temperature increases on increasing ϕ. In the Angell explanation it is the specific potential energy landscape that determines the thermodynamical properties of the system. In particular, from such an explanation, water-like fullerene is characterized by a distinctive "folding funnel" energy landscape that originates the extreme weakness of the glass transition as well as the consequent confusion that has characterized water scientific history; it also explains the very small excess entropy at the glass transition temperature. Angell also discussed the relation of confined-water behavior to that of bulk and in this frame the "fragile-to-strong" transition for supercooled water is interpreted by adding a "critical point-free" scenario to the two competing scenarios for understanding supercooled bulk water.

It must be outlined that there is not much distinction between the order-disorder transition (critical point-free) scenario and the second-critical-point scenario, which associates all water anomalies with the existence of a second critical point.

The question that must be addressed to understand water complexity may be the following: is the second critical point to be regarded as the source of the anomalies of water, or is the cooperation of the configurational excitations to be seen as the primary phenomenon to be interpreted, one that may, at some parameter or some thermodynamic field choice, produce a critical point? The cooperation of the configurational excitation is implied by the form of the heat capacity extracted by confined water. In particular that of water confined in silica-gel materials (CARiACT [292]) of $\phi = 1.1\,\mathrm{nm}$. This one is a sample in which water remains in the liquid state also at very low T and shows a C_p peak at around 227 K (see, *e.g.*, fig. 39).

The hump at 227 K can give justification of the order/disorder process of water molecules in the liquid state [4]. In addition, it seems that in such a silica-gel sample the enthalpy relaxation $-\mathrm{d}H/\mathrm{d}t$ does not give a water glass transition at this temperature, and the 227 K peak can be attributed to an order/disorder process; in that sample the T_g is located at lower temperatures.

This scenario on the basis of recent calorimetric results made by the same team (Oguni *et al.* [292]) for water confined in MCM-41 samples of different ϕ have been reconsidered. In this very recent study, adiabatic calorimetry was carried out for water confined within pores of silica MCM-41 with diameters of $\phi = 12, 16$ and 18 Å (figs. 37 and 38). According to the idea of a separation between the pore wall water and the one located at the center of the pores, the obtained results can be summarized in such a way:

i) glass transitions seems to be founded at $T_g = 115$ and 165 K in the 12 Å case, 117, 165, and 205 K in the 16 Å, and 118 and 210 K in the 18 Å;

ii) the transition at $T_g = 115$–118 K has been interpreted as caused by the freezing of the rearrangement of the water molecules located on the pore wall and interacting with silanol groups;

iii) and those at $T_g = 165$ and 205–210 K of the water located in the center of the pores.

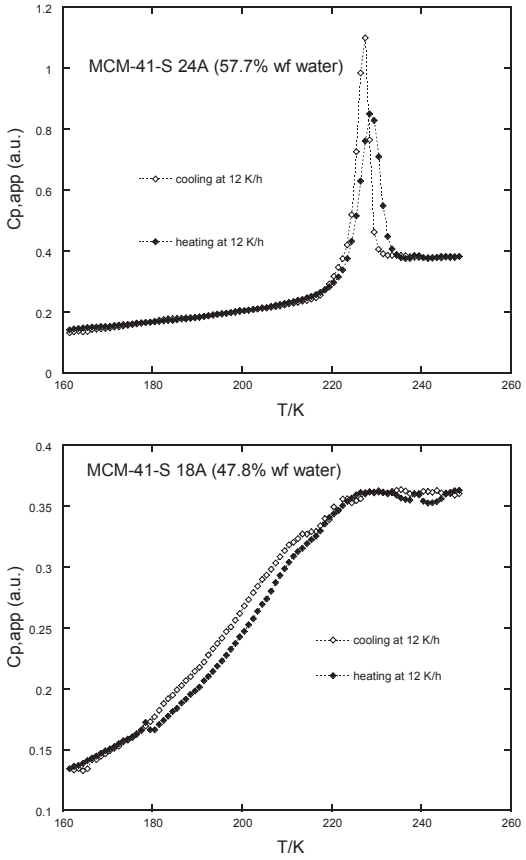

Fig. 40. – The specific heat $C_{p,\mathrm{app}}$ in water confined in MCM-41-S sample with a diameter of 2.4 nm (upper figure) and 1.8 nm (lower figure) measured by using a modulated calorimeter. In both the experiments the heating and cooling rate is of 12 K/h.

The authors of such experiments point out that T_g increased discretely with increasing the pore diameter from 115 to 165 to 210 K, indicating that T_g and therefore the activation energy for the water structural rearrangement are strongly connected with the development of the HB network and furthermore with the number of bonds formed by each water molecule. On the basis of all these facts they strongly suggested that bulk water undergoes the glass transition at $T_g = 210$ K rather than at 136 and 165 K debated hitherto and showed the change from fragile to strong behaviors in the relaxation times with cooling down to 210 K.

Figure 40 reports the just mentioned result of a very recent experiment in water confined in MCM-41-S samples with $\phi = 24$ and 18 nm, obtained by using modulated calorimetry. As can be observed a large similarity between these data and the ones obtained by means of the adiabatic calorimetry is evident (fig. 38); however, the interpretation is completely different.

By considering the results obtained for the water transport coefficients, represented by the NMR and neutron data, and the evidence from these of the dynamical crossover from the fragile-to-strong glass former (fig. 22) and the violation of the Stokes- Einstein relation (fig. 23) there are enough arguments to assume that these maxima in C_p at about 225 K are related with the crossover phenomenon rather than with a glass transition process.

In addition, taking into account the results of the FTIR experiments (see, *e.g.*, fig. 24) we consider that these maxima are probably due to the water polymorphism, more precisely to the change in the relative population of the high- and low-density liquid water phases that takes place just at the crossover temperature $T_L \simeq 225\,\mathrm{K}$. A confirmation of such an approach has been obtained, as shown in the next section, by considering the configurational contribution to the specific heat.

12. – The NMR technique as a method to measure the configurational heat capacity

Now we report results of a study in which it is demonstrated that the NMR chemical shift can be used to measure the configurational specific heat of a material. In particular, it will be shown that such an experimental approach can give detailed information on water inside the very supercooled regime. Specifically these studies regard confined water in nanotubes and in macromolecules of biological interest [306].

Scattering experiments (using neutrons and X-rays) have given precise values of the Pair Correlation Function (PCF), providing important benchmarks for testing models of water structure. The PCF represents only an isotropically averaged measure of the structure. Thus, in many cases, PCFs may not faithfully reproduce the subtle hydrogen bond geometry responsible for water's thermal anomalies. By measuring the NMR proton chemical shift δ, it is possible to provide additional information on the local hydrogen bond geometry and, in particular, the average number of the possible configurations ($\langle N_{\mathrm{HB}} \rangle$) of the local molecular hydrogen bonding geometry. If a water molecule in a dilute gas is taken to be an isolated-state reference, the chemical shift δ accounts for the change of the value of the magnetic shielding with respect to that of such a reference. Hence the chemical shift is related to the "non-dilute" or "virial" interaction of a water molecule with its surroundings, providing a picture of the intermolecular geometry [307-312]. Originally, it has been proposed, especially in the high-temperature regime, that δ represents the number of hydrogen bonds (HB), N_{HB}, with which a water molecule is involved at a certain temperature [313-315]. Nowadays, it is accepted that, especially after a lot of theoretical and experimental studies, the proton chemical shift of water is a function not only of the number of HB but also of the intermolecular distances and angles, *i.e.*, $\langle N_{\mathrm{HB}} \rangle$ [309]. Thus a careful study of δ *vs.* T gives details of the thermal evolution of the water configurations especially in the supercooled regime where there is the onset of complex clustering phenomena (percolation like [45]) just driven by the HB interaction [10, 11, 13, 41, 82]. Here an approach is proposed for which the T derivative of the chemical shift can give an estimate of the configurational specific heat and measure the water proton chemical shift as a function of temperature by studying confined water in two different systems recently used to measure water thermodynamical parameters under very supercooling conditions: i) a micelle-templated mesoporous silica matrix, comprised of quasi-1D cylindrical tubes (MCM-41-S) [98, 162, 172, 176, 199, 200] and ii) the hydration water in the protein lysozyme in the temperature range $180\,\mathrm{K} < T < 360\,\mathrm{K}$, a system also object of detailed studies by using both theoretical and experimental approaches [201, 202, 276, 316-318].

The NMR chemical shift δ is an assumed linear response of the electronic structure of a system under investigation to an external magnetic field B_0, as $B(j) = (1 - \delta_j)B_0$, where j is an index identifying the chemical environment [319,320]. It is measured in an NMR experiment by the free induction decay, FID. In the early days, NMR technique was only used to accurately measure the nuclear magnetic moment. After the discovery of the chemical-shift effect the technique was utilized by the chemical physics community. In fact the FID contains information about the set of all nuclear species in the studied sample whose resonance frequencies lie within the harmonic content of the NMR radio frequency (RF) pulse. Thus NMR, by means of the chemical shift δ, is selective of the nucleus chosen to be studied and is highly sensitive to its local environment. The FID is indeed specifically related to the magnetic shielding tensor $\boldsymbol{\sigma}$, which in turn relates to the local field experienced by the magnetic moment of the observed nucleus. The magnetic shielding tensor $\boldsymbol{\sigma}$, strongly dependent on the local electronic environment, is a useful probe of the local geometry and, in particular, for the hydrogen bond structure for water and aqueous systems and solutions [321]. Of interest are the isotropic part, $\sigma_{\rm iso} \equiv \mathrm{Tr}(\boldsymbol{\sigma}/3)$, and the shielding anisotropy $\Delta\sigma \equiv \sigma_{33} - (\sigma_{11} + \sigma_{22})/2$, where σ_{11}, σ_{22}, and σ_{33} are the three principal components of $\boldsymbol{\sigma}$. $\sigma_{\rm iso}$ is experimentally obtained via the measured proton chemical shift relative to a reference state through the relation [322]

$$\delta = \sigma_{\rm iso}^{\rm ref} - \sigma_{\rm iso} + \left(A - \frac{1}{3}\right)(\chi^{\rm ref} - \chi). \tag{42}$$

Here χ is the magnetic susceptibility, and the factor A depends on the sample shape and orientation: $A = 1/3$ for a spherical sample. Since the magnetic field exerted on a proton is $B_0[1 + (4\pi/3)\chi(T)]$, the resonance frequency is $\omega(T) = \gamma H_0[1 - \sigma(T) + (4\pi/3)\chi(T)]$, where γ is the proton gyromagnetic ratio. Thus the deviation of $\sigma(T)$ from a reference value gives $\delta(T)$. Since the magnetic susceptibility per water molecule, χ_0, can be assumed to be T- and P-independent, $\chi(T)$ is simply given by $\chi_0\rho(T)$, where $\rho(T)$ is the density at a temperature T. In the liquid and gas phases, $\omega(T)$ and $\rho(T)$ can be obtained directly from the experiment. Considering that water molecules in the gas phase at 473 K are isolated, one can set $\delta_g(473K) = 0$, where g indicates the gas. Thus $\delta(T) = (\omega(T) - \omega_g)/\omega_g - (4\pi/3)\chi_0(\rho(T) - \rho_g)$ and can be determined from $\omega(T)$ and $\rho(T)$. Hence, an isolated water molecule in a dilute gas can be taken to be the reference for δ, so that δ represents the effect of the interaction of water with the surroundings providing, in particular, a rigorous picture of the intermolecular geometry [307]. In liquid water, the shielding tensor is isotropically averaged by fast molecular tumbling, so the NMR frequency provides information only on $\sigma_{\rm iso}$. In addition, the $\Delta\sigma$ contribution escapes detection because ^{1}H relaxation is heavily dominated by the strong magnetic dipole field from nearby protons [323]. However, δ is directly related to the average number of local configurations in which a water molecule is involved [307-310]. The water proton chemical shift has been studied in the same confined geometry used in the previous experiments and the confining substrate is a micelle-templated mesoporous silica matrix MCM-41-S [200]. In this case two different samples having tube diameters of $d = 2.4$ nm and 1.4 nm were studied. Both have hydration levels of $h \simeq 0.5$ gram H_2O per gram of MCM-41-S. In this case static NMR experiments at ambient pressure P in the temperature interval $195\,\mathrm{K} < T < 293\,\mathrm{K}$ using a Bruker AVANCE NMR spectrometer operating at 700 MHz proton resonance frequency were performed. At $h \simeq 0.5$ both the samples are fully hydrated and the measured $\delta(T)$ are, within the experimental uncertainty of ± 0.05 ppm, pore size independent. The second studied system consists

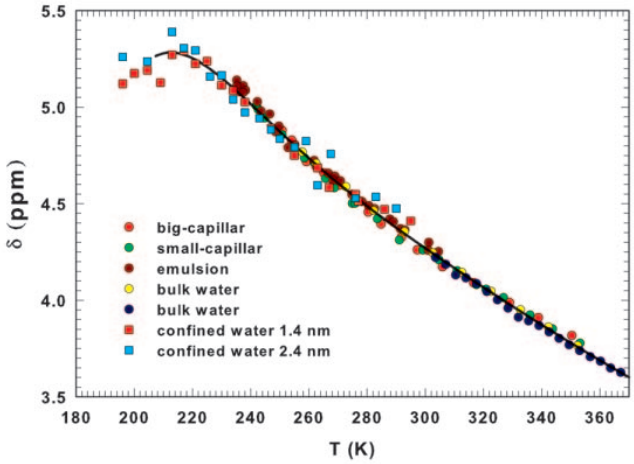

Fig. 41. – The proton chemical shift of water, δ, as a function of temperature. Literature data are plotted as circles and the present data are plotted as squares. The line is a guide for the eye. Figure adapted from [306].

of the first-shell hydration water of lysozyme. In that case hen egg white lysozyme obtained from Fluka (L7651 three times crystallized, dialyzed and lyophilized) was used without further purification. Samples were dried, hydrated isopiestically and controlled by means of a precise procedure [202]. The hydration levels of the protein-water samples was $h = 0.3$.

Figure 41 shows our $\delta(T)$ data in MCM samples, after correcting for the magnetic susceptibility $\chi(T) = \chi_0\rho(T)$. Figure 41 also shows, from the work of Hindman [314], all the experimentally available $\delta(T)$ data in the temperature range of stable bulk liquid water, as well as the δ values from $T = 350\,\mathrm{K}$ down to $235\,\mathrm{K}$, of three different samples: large (80–120 μm) and small (10–20 μm) capillaries, and water confined in an emulsion [324]. Although for the δ data of refs. [314, 324] the reference material was CH_4, all measured values, after the proper correction, nicely fall onto a single master curve, whereby the reference system is a water molecule in a diluted gas in supercritical conditions [307]. Figure 41 reports such a situation in the range $180\,\mathrm{K} < T < 370\,\mathrm{K}$ and shows agreement between our data and the previous $\delta(T)$ measurements. One can see that the behavior of these literature data (circles) is characterized by a continuous increase on decreasing T that becomes more pronounced in the lower temperature region. At lower T the situation changes: on decreasing T there is a round-off in $\delta(T)$ with a possible maximum at about $215\,\mathrm{K}$. Because different experiments quote (with respect to the isolated water molecule) $\delta = 7.4\,\mathrm{ppm}$ for a single crystal of hexagonal ice I_h [325], the data show that $\delta(T)$ does not evolve in a simple monotonic way from the liquid to the ice phase. The continuous increase in the proton chemical shift with T decreasing down to the supercooled regime has been originally interpreted in terms of a cooperative increase in HB formation rate. Thus there is a continuous development of a considerable degree of short-range order or "clustering." In addition, since the T region below $225\,\mathrm{K}$ is dominated by the LDL local structure [200], this confirms the idea that this liquid water phase has a local geometry different from the high-density-liquid (HDL) local structure prevalent in the stable liquid regime.

The recently measured relative population of the two main local structures, LDL-like and HDL-like [200, 240], in the region $30\,\mathrm{K} < T < 373\,\mathrm{K}$ (fig. 24), provides a qualitative explanation for the observed $\delta(T)$. From a structural point of view, the temperature range can be divided into three intervals:

– $\mathcal{R}_{\mathrm{HDL}}$ ($T > 250\,\mathrm{K}$) dominated by molecules with local HDL geometry,

– $\mathcal{R}_{\mathrm{LDL}}$ ($T \lesssim 220\,\mathrm{K}$) dominated by local LDL geometry, and an intermediate region in which the population of these local geometries are comparable, and

– $\mathcal{R}_{\mathrm{int}}$ ($220\,\mathrm{K} \lesssim T < 250\,\mathrm{K}$).

Visual inspection of $\delta(T)$ shows three different behaviors, as temperature decreases, in the three different regions: i) a continuous increase in $\mathcal{R}_{\mathrm{HDL}}$, ii) an inflection point at around 250 K with a sudden change in the derivative in the $\mathcal{R}_{\mathrm{int}}$ interval and finally iii) a flattening at about 220 K followed by a slow decrease in the $\mathcal{R}_{\mathrm{LDL}}$ region. These results support a picture in which the main role is played by the LDL and HDL local geometric structure, characterized by different local electronic distributions, thus by different local environments of the hydrogen atom. A proper analysis of their fractional weights allows to calculate the absolute value of water density $\rho(T)$ in the range $30\,\mathrm{K} < T < 373\,\mathrm{K}$. In addition to the well-known maximum at 277 K there appears a minimum in $\rho(T)$ at $203 \pm 5\,\mathrm{K}$ [240]. Moreover, the coefficient of thermal expansion $\alpha_\rho = -(\partial\rho/\partial T)_P$, related to the cross-correlation between the entropy and volume fluctuations, shows a well-defined maximum on crossing the Widom line $T_{\mathrm{W}}(P)$. In the first interval $\mathcal{R}_{\mathrm{HDL}}$, in which the normal liquid region (273–353 K) and a region of moderate supercooling lie, $\delta(T)$ increases as T decreases. Both the normal liquid and the supercritical regions have been considered from both the theoretical and experimental points of view. This explains how the proton chemical shift reflects the properties of the local order [307, 309, 310] in regions in which there is a direct relation between $\delta(T)$ and the average number of hydrogen bonds $\langle N_{\mathrm{HB}}\rangle$, in which a water molecule is involved: $\delta(T) \propto \langle N_{\mathrm{HB}}\rangle$. On the basis of the thermal evolution of the LDL and HDL local structures (fig. 24), we consider that such a situation holds also in the other two temperature regions, $\mathcal{R}_{\mathrm{int}}$ and $\mathcal{R}_{\mathrm{LDL}}$, where there is the progressive build-up of the expanded tetrahedral HB network with decreasing temperature.

The chemical shift $\delta(T)$ is related to the number of possible configurations of the water molecules in the HB network. Considering that this number is inversely proportional to $\langle N_{\mathrm{HB}}\rangle$, according to the entropy definition one can assume $S \approx -k_B \ln\langle N_{\mathrm{HB}}\rangle$. Therefore the temperature derivative of the measured fractional chemical shift,

$$-\left(\frac{\partial \ln\delta(T)}{\partial T}\right)_P \approx -\left(\frac{\partial \ln\langle N_{\mathrm{HB}}\rangle}{\partial T}\right)_P \approx \left(\frac{\partial S}{\partial T}\right)_P, \tag{43}$$

should be proportional to the constant pressure specific heat $C_P(T)$ ($C_P = T(\partial S/\partial T)_P$), a quantity never experimentally measured in the deep supercooled regime below 250 K for liquid bulk water.

Figure 42 reports (left side) the derivative $-T\partial \ln\delta(T)/\partial T$ obtained from the $\delta(T)$ data of fig. 41 [306]. Also shown are the $C_P(T)$ values measured in bulk water in the interval $244.5\,\mathrm{K} < T < 290\,\mathrm{K}$ [281] and the same quantity obtained by means of a simulation study from the TIP5P model of water for $210\,\mathrm{K} < T < 290\,\mathrm{K}$ (right side) [326].

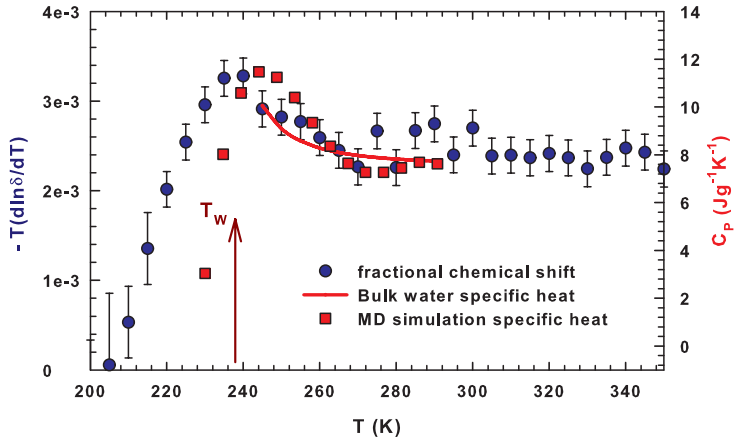

Fig. 42. – The temperature derivative of the measured fractional chemical shift $-T\partial \ln \delta(T)/\partial T$ (blue symbols, left-hand side), the specific heat at constant pressure, C_P (right-hand side), measured in bulk water in the supercooled regime (red line, ref. [281]), and C_P calculated for the TIP5P model of water (red squares, ref. [326]). The configurational heat capacity, obtained from $\delta(T)$ by means of eq. (43), is plotted on the left-hand sides. The comparison with respect to the measured C_P values is made by means of the double scale plot (on the right-hand side of these figures). The only difference is one adjustable parameter: the amplitude of the signal. Figure adapted from [306].

All these data display an analogous thermal behavior. In fact, within the error bars, there is good agreement between the C_P data. The "configurational" specific heat obtained from the measured δ and the $C_P(T)$ calculated in simulation display maxima at about the same temperature ($\simeq 235\,\mathrm{K}$) of the maximum in $(\partial\rho/\partial T)_P$ [240] upon crossing the Widom line temperature, T_W (fig. 26) [58, 199, 327]. Whereas $(\partial\rho/\partial T)_P$ is directly related to the cross-correlation between the entropy and volume fluctuations $\langle(\Delta S \Delta V)\rangle$, C_P is proportional to the square of the entropy fluctuations. It is also important to stress that very recent calorimetric data on water confined in silica gel, which cover the range $100\,\mathrm{K} < T < 300\,\mathrm{K}$, show a behavior that agrees with our results [293].

Such an approach has been also confirmed by considering the temperature evolution of the chemical shift δ of the hydration water proton for lysozyme at the hydration level $h = 0.3$, a condition in which only one monolayer of water is supposed to be on the surface of each protein. The explored temperature range was $200\,\mathrm{K} < T < 370\,\mathrm{K}$ for the following reasons: i) in such a system, water dynamics displays the fragile-to-strong crossover phenomena (FSC) observed in confined and simulated water [202,326]; in particular, the crossover temperature T_W is nearly coincident among these water-confined forms [202,326]; ii) another phenomenon governing biological properties of proteins occurs at high temperatures, just below the onset of protein denaturation. In the first case the FSC is entirely due to the complete development of the LDL water phase (*i.e.*, of the HB tetrahedral network) located just at the Widom line [202, 326]. However the corresponding results will be reported in the next chapter of this paper regarding water confined in biological systems. Finally, the agreement between δ and C_P, aside from different prefactors, supports the physical idea that both C_P and δ are measures of the temperature derivative of an entropy-like quantity. Since δ is related to *orientational*

local order, as opposed to other *translational* local order, this finding is consistent with the possibility that the contribution of the orientational disorder to entropy is dominant. This work is also consistent with molecular dynamics simulations using the TIP5P model which demonstrate that in protein hydration water and in bulk water, $|\mathrm{d}Q/\mathrm{d}T|$ has a maximum at the crossing of the Widom line $T_{\mathrm{W}}(P)$ [201].

In conclusion of this section, NMR proton chemical shift measurements may be considered a new method for estimating the configurational part of the heat capacity $C_P(T)$ that results from the hydrogen bonding of the water molecules. Because the NMR technique also gives the chemical shift of each sample nucleus with non-zero spin, such an approach may be applicable to more complex materials.

13. – Water confined in biomolecules

A research field of paramount importance is represented by water confined around biomolecules. Considering the numerous physico-chemical anomalies of water, the fundamental role they play in controlling the structure and dynamics of biopolymers is a fascinating research subject. While water has been considered as "life's solvent" (*i.e.*, a uniform background) for a long time, only recently it has became an active constituent of cell biochemistry [328]. A striking example of the importance of water in biosystems is that, without water, proteins cannot perform their function. Without water a protein cannot function but a single layer of water surrounding it (called the first hydration layer) restores the biological activity [329-331]. Hydration can be considered as a process, that of adding water incrementally to the dry protein, until a level of hydration is reached beyond which further addition of water produces no change of the essential properties of the protein and only dilutes the protein [329]. The hydration shell can be defined as the water associated with the protein at the hydration end point. This shell represents a monolayer coverage of the protein surface. Water outside the monolayer is perturbed to a significantly smaller extent, typically not detected by measurements of properties such as heat capacity, volume or heat content. Proper measurements of the reaction of lysozyme with the hexasaccharide of N-acetylglucosamine over the full hydration range have given a threshold hydration level of $h = 0.2$, [330] where h is the ratio between grams of water and grams of dry protein. In this work it is clearly showed that enzymatic activity closely parallels the development of surface motion, which is thus responsible for the functionality of the protein.

Understanding the relationship between the structure and dynamics of proteins [331] and the water associated with proteins [4-6] is thus an ongoing challenge. Therefore, many biological functions [330], such as enzyme catalysis, can only be understood with a precise knowledge of the structure and function of the first hydration layer. When a protein is in solution, there are two categories of water molecules identifiable in close proximity to the protein: i) the bound internal water, ii) surface water usually called hydration water. The bound internal water molecules, located in the internal cavities of the protein, play a structural role in the folded protein itself. At low temperatures, a protein exists in a state [32, 332] without conformational flexibility. As T increases, the atomic motional amplitude initially increases linearly, as in a harmonic solid. In hydrated proteins, at $T \sim 220\,\mathrm{K}$, the rate of amplitude suddenly increases with temperature signaling the onset of more liquid-like motion [333-335].

This *dynamical transition* of proteins (or the so called *protein glass transition*) may be triggered by the coupling of the protein with the hydration water through hydrogen bonding, since protein hydration water shows a dynamic transition at a similar temper-

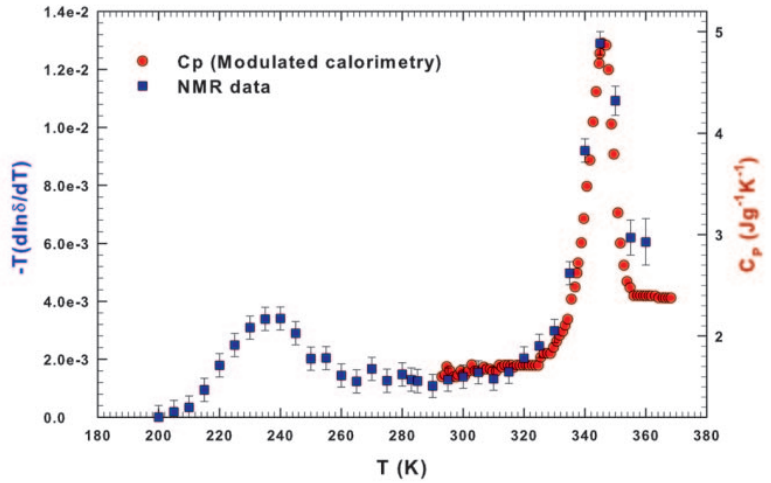

Fig. 43. – The figure, reporting data coming from the water-protein (lysozyme) system, shows a detailed comparison between the conformational heat capacity obtained from the NMR data and previous C_P data (ref. [276]). Figure adapted from [306].

ature [335]. Another phenomenon governing biological properties of proteins occurs at high temperatures, just below the onset of protein denaturation. A protein is in the native state up to a given temperature and evolves, on increasing T, into a region characterized by a reversible unfolding-folding process. This latter phenomenon depends on the chemical nature of the protein and the solvent. In the case of the water-lysozyme system such a phenomenon occurs in the temperature range 310–360 K. Above 355 K, lysozyme denatures irreversibly. For such a system, calorimetric measurements [276, 336] show a broad peak in the specific heat around that temperature. More precisely, all the observed data of such an experiment characterized by the peak in C_P at $T = 346$ K are consistent with the point of view that the first step of denaturation of a small one-domain globular protein like lysozyme is a reversible conformational (unfolding) transition, and the second step is irreversible. Hence the dramatic change in the protein structure, is driven by the HBs between the protein and its hydration water. The rate constant varies with T according to an Arrhenius law, with an activation energy typical of the strength of the hydrogen bond (HB) [276], so hydration water appears to play a determinant role also for this transition. It is just the consideration that HBs structure is strictly related to the chemical shift δ that has given the opportunity to use the NMR in order to measure water configurational specific heat. Figure 43, reporting the specific-heat results of the hydrated protein lysozyme with an hydration factor $h = 0.3$ and the $C_P(T)$ data, obtained by means of a more conventional calorimetric experiments in the same protein with $h = 8.3$ [276], well illustrates such a situation characterized by these two crossovers [306]. In particular it is shown, in a double scale plot, the configurational heat capacity, $-T(\partial \ln \delta(T)/\partial T)_P$ for lysozyme hydration water in the left-hand side and $C_P(T)$ measured in the temperature region, including the reversible unfolding-folding process, the right-hand side. One sees that $-T(\partial \ln \delta(T)/\partial T)$ displays two maxima, the first on crossing the Widom line $T_W(P)$ as proposed by experiments and simulation studies on hydrated proteins [202, 326], and

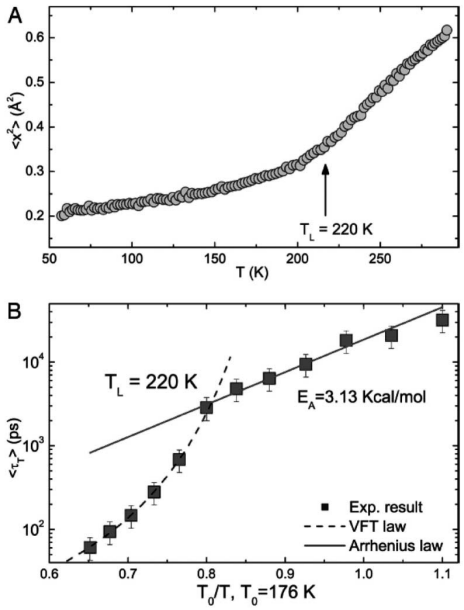

Fig. 44. – Evidence for the dynamic transition in lysozyme. (A) The temperature dependence of the mean-squared atomic displacement of the hydrogen atom at 2 ns time scale measured by an elastic scan with resolution of 0.8 eV. (B) Temperature dependence of the average translational relaxation times plotted *vs.* T_0/T, where T_0 is the ideal glass transition temperature [202].

the second at a temperature nearly coincident with the associated protein denaturation process. The first maximum, at about 240 K, *i.e.*, the same temperature of that of confined water, is a proof that both are due to the same structural change of water. In fact, at T_{W} the LDL phase dominates water properties [200, 316].

On the base of these considerations, in the following are reported the results obtained by experiments and MD simulations on the dynamics of the hydration water in biomolecules (a powder of the globular protein lysozyme, DNA and RNA). The related findings explain unambiguously the role played by water, by means of its characteristic structural (HB) and dynamical properties, on driving the biomolecules activity. Specifically, we report the results of light (FTIR, Raman) and Neutron (Elastic, Quasi-elastic, inelastic) scattering [202, 337], NMR spectroscopy [316] and calorimetry [276].

The possibility to explore in detail the properties of this "biology water" starts just from the observation that also proteins hydration water present a dynamical strong-fragile crossover (the same of that revealed in MCM-41 confined water) that comes out from neutron scattering experiments [202]. Figure 44 reports the results of such an observation by showing the water mean square displacement (MSD), $\langle x^2 \rangle$, as a function of the temperature T and the average translational relaxation time for lysozyme.

However, the interest is focused on both the two dynamical biopolymers transitions: the strong-fragile crossover at low temperatures and the folding/unfolding phenomenon at high T. The aim is to explain these phenomena on a molecular level with the idea to highlight the role of water around and inside the macromolecules.

14. – The NMR and FTIR results on the two dynamical crossovers of biological macromolecules

Subsequently to these neutron experiments, the use of the FTIR technique furnishes a detailed mapping, in the temperature range $180\,\mathrm{K} < T < 360\,\mathrm{K}$, of the three main species of water at the protein surface, namely: the LDL, the HB bonded water and the non-hydrogen-bonded molecules (NHB). These results have been obtained from the analysis of the thermal evolution of spectra of the OH-stretching vibration modes, by using the same experimental procedure used to study water in nanotubes [202, 316]. Figure 45 shows the OHS-FTIR spectra for the protein hydration water (hydration level $h = 0.3$) and reveals significant variations, on changing T, in the HB and NHB populations as the presence in the deep supercooled regime of the same spectral contribution assigned to the LDL phase (at about $3100\,\mathrm{cm}^{-1}$). Thus the corresponding spectral deconvolution of the measured OHS was done with three Gaussian components: the LDL phase, a second one that is the HB component ($3220\,\mathrm{cm}^{-1}$) and finally a third Gaussian (at the highest frequencies) related to the contribution of the NHB (or weakly HB) water molecules. In comparison with the MCM-41 case, the following correspondence exists: f_4 (LDL), $f_1 + f_2 + f_3$ (HB) and finally f_0, for the NHB component [316].

As can be observed in fig. 45, the LDL contribution plays the main role below T_L whereas at the highest T the NHB component is dominant. Such a situation is well represented in fig. 46 which reports the relative weights (integrated area) of these three OHS components, for three different measured hydration levels ($h = 0.3$, 0.37, and 0.48).

However, the remarkable result shown in fig. 46(a) is that there are two main crossovers in the population of the three species of oscillators (areas): a low-temperature transition at about T_L (the protein dynamical transition and the FSC) and a high-temperature transition at T_D (temperature of the maximum C_P, which is inside the folding-unfolding reversible region and below the temperature of irreversible denaturation). The low-temperature transition is due to the crossing between fraction of LDL phase (which increases on lowering T) and that of the HB phase, which decreases. The high-temperature transition appears on increasing T, from the crossing between the increasing population of the NHB phase with the one of the HB. Both these results demonstrate the role of water in determining the protein stability and dynamics.

More precisely, from the data reported in fig. 46(a), it is evident that the HB formation and its increasing lifetime or probability, by decreasing T, acts like a glue that stabilizes the protein in the temperature range $T_L < T < T_D$ and arrests its dynamics below T_L. In fact, the onset of a stable HB network, involving also the protein, at around T_L and below the first transition results in the loss of the protein conformational flexibility; whereas at about 346 K (above the second transition) when the large amount of hydration water molecules are unbonded, the protein unfolds. This FTIR experiments combined with NMR data (self-diffusion D and spin-lattice relaxation time T_1) give a more detailed clarification on the role of water in the two protein dynamical transitions. Figure 46(b) shows the inverse of the NMR measured self-diffusion constant D as function of $1/T$, for $h = 0.3$, compared with that of bulk water. The thermal behavior is analogous, in fact hydration and bulk water follow a Vogel-Fulcher-Tamman (VFT) law. For bulk water, the ideal glass transition temperature is $T_0 = 175\,\mathrm{K}$, whereas for the protein hydration water $T_0 = 182\,\mathrm{K}$. However, there is a factor of 10 between the $1/D$ of bulk water and that of protein hydration water.

In analogy with the FTIR data, also in the behaviour of $1/D$, two main crossovers can be observed. One crossover is at high T, where the protein changes from its native

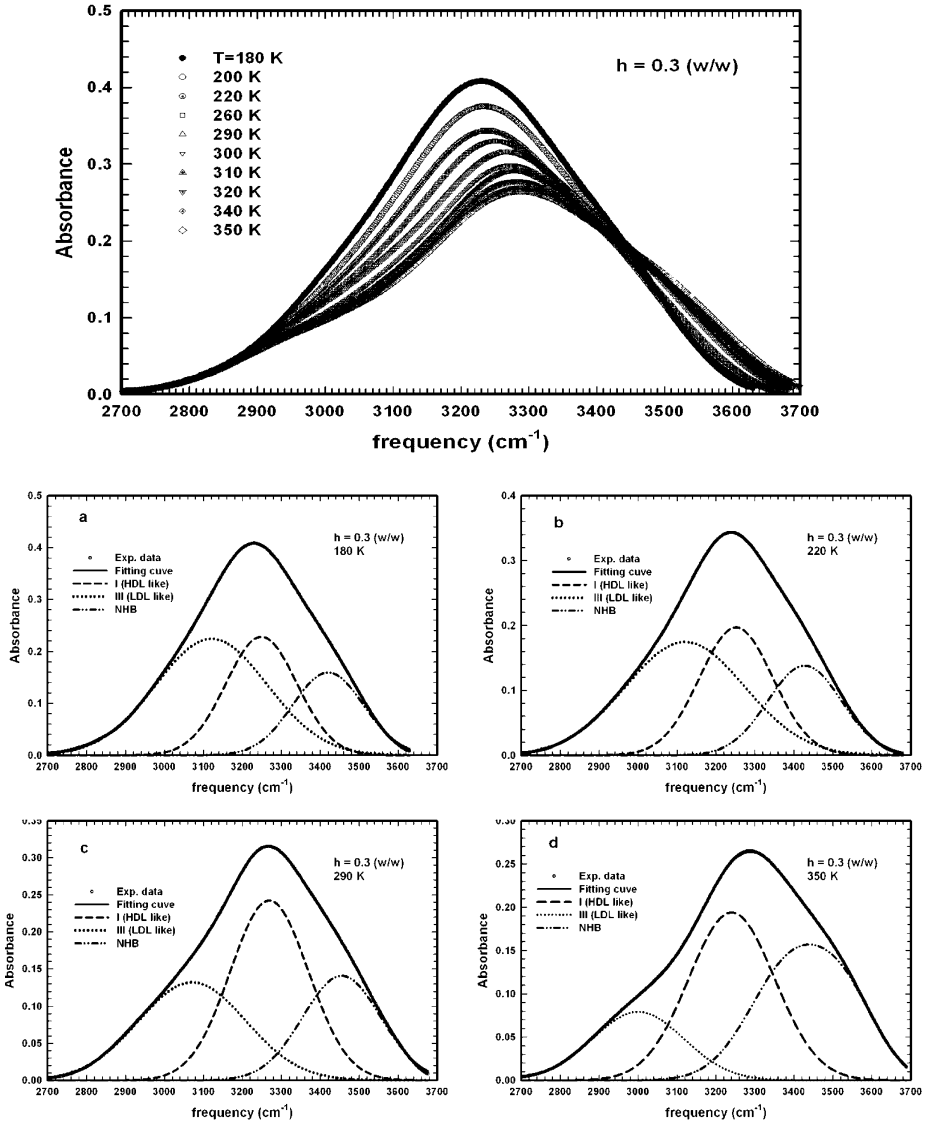

Fig. 45. – Main panel: the OH stretch (OHS) bands, in the 2700–3700 cm^{-1} range, of lysozyme hydration water at a hydration level of $h = 0.3$, measured at different temperatures. Bottom panels: the deconvolution of the OHS spectra at $T = 180$ (a), 220 (b), 290 (c), and 350 K (d). In all the figures, dots represent the experimental data, and the black continuous lines are the best fits. The dotted and dashed lines are the contributions to OHS oscillators from the low-density water (LDL) and the hydrogen-bonded molecules (HB), respectively. The dot-dashed lines indicate the spectral contributions of the non-hydrogen-bonded molecules (NHB). The dotted line refers to component III centered at 3100 cm^{-1}, and the dashed line to component I centered at 3220 cm^{-1} [316].

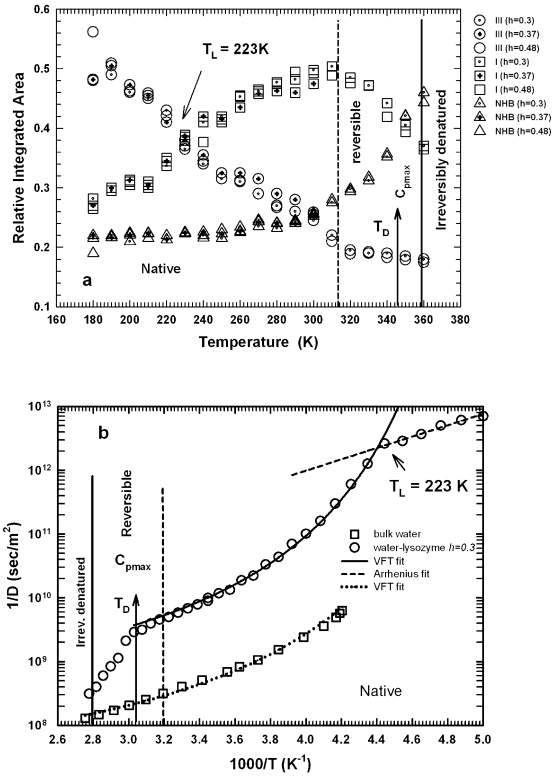

Fig. 46. – (a) The relative integrated areas of the three FTIR components at three different lysozyme hydration level $h = 0.3$, 0.37, and 0.48. Squares indicate the fractional contribution of the component HB ($3220\,\mathrm{cm}^{-1}$), circles the fractional contribution of the component LDL at $3100\,\mathrm{cm}^{-1}$, and triangles represent the non-hydrogen-bonded (NHB) water. Three different regions of lysozyme behavior: native, reversible unfolding, and irreversible denaturation are also indicated. Arrows show the temperature of maximum specific heat T_D and the FSC crossover temperature T_L. (b) The inverse of the NMR self diffusion coefficient D as a function of $1/T$ (circles). Squares represent the values measured in bulk water. In the native region, $1/D$ of both bulk water and lysozyme hydration water obey a VFT law, but the protein hydration water displays an abrupt transition to an Arrhenius law behavior at the FSC temperature $T_L \sim 223\,\mathrm{K}$. This crossover temperature agrees with earlier neutron scattering experiments on the crossover temperature at which the protein loses its function. At a higher temperature (T_D), the NMR self-diffusion data also show a second dynamical transition of the hydration water associated with the denaturation process of the protein [316].

state to its unfolded state. On increasing T, $1/D$ decreases toward the value of pure bulk water. The second crossover takes place at $T_L = 223\,\mathrm{K}$, location of the FSC, thus fully confirming the neutron scattering results on the same system [202]. The activation energy of the Arrhenius process in the strong region is $E_A = 3.48\,\mathrm{kcal/mol}$, whereas the neutron experiment gives $3.13\,\mathrm{kcal/mol}$. Thus, also these D data show unambiguously that T_L is the temperature characterizing the protein dynamical transition.

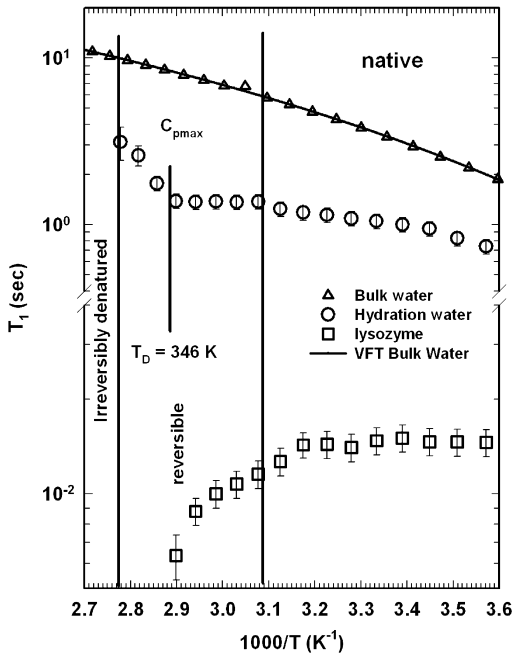

Fig. 47. – The temperature evolution of the NMR longitudinal spin-lattice relaxation time T_1 for temperatures above and below the region of protein denaturation. Triangles correspond to bulk water, circles to protein hydration water, and squares to protons in the protein. The dramatic changes in T_1 further demonstrate the role played by hydration water in the denaturation process [316].

To probe further the role of hydration water in the high-temperature crossover (characterizing the onset of reversible folding-unfolding as shown by calorimetry [276]), the NMR proton spin-lattice relaxation time constant T_1 of the lysozyme-water system with $h = 0.3$ in the temperature interval $275 < T < 355\,\mathrm{K}$ has been also measured (fig. 47). T_1 represents the longitudinal relaxation time of protons, and is connected, together with the spin-spin proton relaxation time T_2 (transverse relaxation), to the system viscosity [338].

Figure 47 also shows T_1 for pure bulk water. One can see that the hydration water spin-lattice relaxation time is characterized by two contributions, one coming from the hydration water protons and the other one from the protein protons. The first T_1 is of the order of seconds (as in bulk water), whereas the second one is of the order of 10ms. Moreover, fig. 47 shows that on increasing T, the bulk water T_1 follows the VFT law in the whole studied temperature interval. Instead, the T_1 of hydration water is characterized by two different behaviors above and below the onset of the reversible unfolding regime. In the protein native state, the T_1 of hydration water increases with T, following a behavior that is similar to that of bulk water, whereas the T_1 of the protein protons remains nearly constant. The situation changes dramatically when T approaches the region of the high-temperature protein dynamical transition: the proton spin-lattice relaxation time of the protein protons drops abruptly and disappears just at T_D. Conversely, the T_1 of hydration water remains nearly constant, and afterwards it

shows a sudden increase toward the values of bulk water, before irreversible denaturation intervenes. This behavior is analogous to that of the self-diffusion coefficient $D(T)$.

Therefore, NMR data are consistent with the possibility that the high-temperature dynamical transition of the protein might be driven by the dominance of the NHB fraction of hydration water, as supported by fig. 46(a). The protein denaturation process, accompanied by an early stage of reversibility starts just when the population of NHB molecules approaches that of the HB ones, *i.e.*, just when the probability for water molecules to form a HB is about the same of that to be non-bonded.

Now, the state of the art in both the two dynamical crossovers in macromolecules of biological interest like proteins, RNA and DNA will be illustrated; the two phenomena will be considered separately, before the crossover at the biomolecules glass transition and after the denaturation process. In both cases the related physics will be discussed by considering, mainly, the results of neutron scattering and molecular dynamic simulation. The approach to treat neutron scattering in biomolecules is essentially the same used in the case of confined water, there are only some little adjustments.

The quantity of main interest to describe the dynamical properties of both biomolecules and their hydration water is the mean squared atomic displacement $\langle X^2(T)\rangle$ (MSD) a quantity that can be obtained experimentally from the neutron scattering and also from the molecular dynamic simulation (MD). A good and fruitful practice before measuring the MSD in a neutron scattering experiment consists to execute a calculation, if possible, on the same quantity by using the MD technique. Choosing an appropriate water potential, it is in fact very useful to compare the obtained results with the ones coming out from experiments.

Previously, we have reported the application of the relaxing cage model (RCM) of the single particle dynamics of water in the study of water in bulk and confined phases. In particular we have considered water confined in the MCM 41 nanotubes. Here we show how the same technique can be used to describe the properties of both biopolymers (proteins, RNA and DNA) and their hydration water. In particular we describe by means of neutron scattering experiments the strong coupling of dynamics between a protein and its hydration water.

The key to this strong coupling is the existence of a fragile-to-strong dynamic crossover (FSC) phenomenon occurring at around $T_L = 225 \pm 5\,\mathrm{K}$ in the hydration water. On changing the temperature and the pressure toward FSC, the structure of hydration water makes a transition from predominantly the high-density form (HDL), a more fluid state, to predominantly the low-density form (LDL), a less fluid state, derived from the existence of a liquid-liquid critical point at an elevated pressure. Neutron data (together with the FTIR and NMR results) evidence that this sudden switch in the dynamical behavior of hydration water on Lysozyme, B-DNA and RNA triggers the so-called glass transition in these biopolymers. In the glassy state, the biopolymers lose their vital conformational flexibility resulting in a sharp decrease in their biological activities.

As previously reported, incoherent neutron scattering methods, elastic (ENS), QENS, and inelastic (INS) offer many advantages for the study of hydrogen atom dynamics in a protein and its hydration water: the RCM represents a fruitful example. Here the combined use of QENS, ENS ($E = 0$) and INS ($E \neq 0$) is discussed.

In the INS case, the intermediate scattering function (ISF) for a hydrogen atom harmonically bound to a molecule can be written

$$F_H(Q,t) = \langle \exp(iQX_H(0)) \exp(iQX_H(t)) \rangle \,, \tag{44}$$

where Q is the magnitude of the $\vec{Q}$ vector, pointing in the x-direction in the isotropic powder sample. Then it can be shown that in the Gaussian approximation, which is exact for the harmonically bound particle, one can write [221]

$$F_H(Q,t) = \exp\left(-Q^2\left\langle X_H^2\right\rangle\right)\exp\left(Q^2\left\langle X_H(0)X_H(t)\right\rangle\right), \tag{45}$$

where the first factor, $\exp(-Q^2\langle X_H^2\rangle)$, is called the Debye-Waller factor, which gives rise to the elastic scattering, and the second factor, which involves the displacement-displacement time correlation function, gives rise to the inelastic scattering such as phonons. In the classical regime, the last equation can further be written as

$$F_H^{\mathrm{cl}}(Q,t) = \exp\left(-\frac{1}{2}Q^2W(t)\right), \tag{46}$$

where the width function can be written as [221]

$$W(t) = 2V_0^2\int_0^\infty \mathrm{d}\omega\frac{f_H(\omega)}{\omega^2}(1-\cos(\omega t)), \tag{47}$$

$f_H(\omega)$ is the Fourier transform of the normalized velocity of the correlation function of a hydrogen atom, which is sometimes called the *spectral density function* of the hydrogen atom. Thus

$$f_H(\omega) = \frac{1}{2\pi}\int_{-\infty}^{\infty}\mathrm{d}te^{i\omega t}\frac{\left\langle V_X^H(0)V_X^H(t)\right\rangle}{\left\langle (V_X^H)^2\right\rangle}, \tag{48}$$

where $\langle (V_X^H)^2\rangle = V_0^2 = k_BT/M_H$ with M_H the hydrogen mass. In the case of elastic scattering $(t=\infty)\exp(Q^2\langle X_H(0)X_H(t)\rangle) = 1$, and $F_H(Q,t) = \exp(-Q^2\langle X_H^2\rangle)$, which is just the Debye-Waller factor; by combining this result with the ISF in the classical regime one obtains

$$\left\langle X_H^2\right\rangle = \frac{1}{2}W(\infty) = V_0^2\int_0^\infty \mathrm{d}\omega\frac{f_H(\omega)}{\omega^2}, \tag{49}$$

hence the mean square deviation (MSD) of the hydrogen atoms can be obtained from the integral of the reduced *spectral density function* of the same atom.

From the inelastic scattering intensity dominated by the incoherent scattering from hydrogen atoms, the Q-dependent vibrational Density-Of-States (Q-DOS) of hydrogen atoms can be calculated by

$$G_H(Q,E) = \frac{2M_H}{\hbar^2}\frac{E}{n(E)+1}\left\langle\frac{\exp(Q^2\langle X_H^2\rangle)}{Q^2}S_H(Q,E)\right\rangle, \tag{50}$$

in the case of protein. Whereas in the case of hydration water

$$G_{\mathrm{H_2O}}(Q,\omega) = \frac{\omega^2}{Q^2}S_{\mathrm{H_2O}}(Q,\omega). \tag{51}$$

The true hydrogen DOS, $f_H(\omega)$, is obtained in the $Q \to 0$ limit of the $G_H(Q,E)$. In the case of water, $Q \to 0$ limit means $Q < 1\,\text{Å}^{-1}$, thus

$$G_{\text{H}_2\text{O}}(Q,\omega) = \lim_{Q\to 0} G_{\text{H}_2\text{O}}(Q,\omega) = f_{\text{H}_2\text{O}}(\omega)\frac{k_B T}{M_{\text{H}_2\text{O}}}. \tag{52}$$

Neutron scattering can be also used to measure the protein softness by the analysis of the obtained MSD results. The flexibility of proteins is generally known to be essential for their enzymatic catalysis and for their other biological activities. It has been described qualitatively as a consequence of protein's conformational disorder. But the description from the concept of dynamics can be more precise —the flexibility of proteins pertains to respond to applied forces, which are known to maintain biological structure and govern atomic motions in macromolecules [339]. At room temperature a biological matter can be looked upon as being "soft." This "softness" can be estimated from the displacement X of a given atom in response to a given applied force F. Assuming the atom is bound to the protein by a spring with a spring constant K, then X is given by the ratio F/K (Hook's law). Thus for a given F/K, the smaller the spring constant K, the larger the displacement X, meaning the softer is the biological material. One way of calculating the magnitude of K in protein is to use the equi-partition theorem, which states that the average potential energy $\langle V\rangle$ of the harmonically bound atom is equal to one half $k_B T$,

$$\langle V\rangle = \frac{1}{2}K\langle X^2\rangle = \frac{1}{2}k_B T. \tag{53}$$

Therefore K is proportional to the inverse of the derivative of the MSD with respect to T, namely

$$K = k_B\left[\frac{\partial\langle X^2\rangle}{\partial T}\right]^{-1}. \tag{54}$$

Hence by plotting the MSD, measured by means of ENS as a function of the temperature, the steeper the curve, the softer is the biological material at a given temperature.

As previously stated the MSD $\langle X^2(T)\rangle$ from both the hydration water and biomolecules can be obtained from both the neutron scattering and MD techniques. Practically, different approaches are used to obtain the MSD of hydrogen atoms from scattering. One is the so called "fixed window scan" used in the study of the FSC. The experiment consists of an elastic scattering measurement with a fixed resolution window of FWHM of $\pm 0.8\,\mu$eV [340] in the temperature range from 40 K to 290 K, covering completely the supposed crossover temperature T_L. Since the system is in a stationary metastable state at temperature below and above T_L, the measurements were performed by heating and cooling respectively at a heating/cooling rate of 0.75 K/min and observe exactly the same results. $\langle X^2\rangle$ is calculated from the Debye-Waller factor, $S_H(Q,\omega=0) = \exp[-Q^2\langle X_H^2\rangle]$ by a linear fitting of the logarithm of $S_H(Q,\omega=0)$ *vs.* Q^2 plot. $S_H(Q,\omega=0)$ can be easily calculated by taking the ratio of the temperature-dependent elastic scattering intensity $I_{EL}(Q,T,\omega=0)$ and its low temperature limit, $S_H(Q,\omega=0) = I_{EL}(Q,T,\omega=0)/I_{EL}(Q,T=0,\omega=0)$. Figure 48(a) shows the elastic scattering intensity I_{EL} as a function of temperature at a specific Q value ($0.469\,\text{Å}^{-1}$). One can see from the figure a sudden decrease in the elastic scattering intensity above

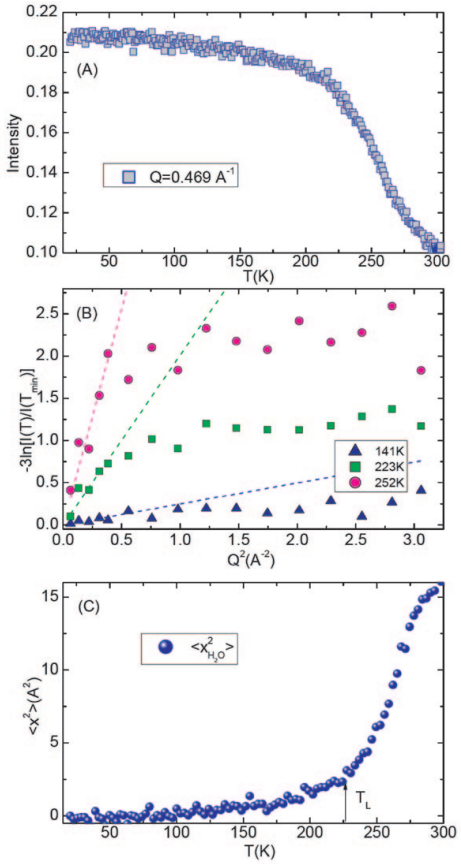

Fig. 48. – Method of data analysis to obtain $\langle X^2_{\mathrm{H_2O}}\rangle$ of RNA hydration water. Panel (A) shows the intensity of elastic scattering within the resolution window of $\pm 0.8\,\mu$eV as a function of T (the so-called elastic scan). The intensity plotted in the figure is taken from the difference between the H_2O hydrated and D_2O hydrated samples. Panel (B) shows plots of logarithm of intensity *vs.* Q^2 at three temperatures. The slope of the linear fit to the first five points (low-Q points) is used to extract the MSD from the data. Panel (C) shows the extracted MSD of the hydration water as a function of temperature.

about 220 K, which implies a sudden increase in the MSD of hydration water. Figure 48(b) shows this fitting procedure for three different temperatures (below, at and above the crossover temperature). $I_{EL}(Q,T,\omega=0)/I_{EL}(Q,T=0,\omega=0)$ is plotted as a function of Q^2. Since the exponential form of the Debye-Waller factor is a low Q approximation, and the Q^2 dependence is not linear for high Qs, only the lowest Q points have been used in the fitting to obtain the MSD. The dashed lines in fig. 48(b) show the linear fitting of the lowest five Q values and fig. 48(c) shows the temperature dependence of $\langle X^2_{\mathrm{H_20}}\rangle$ extracted from the fitting.

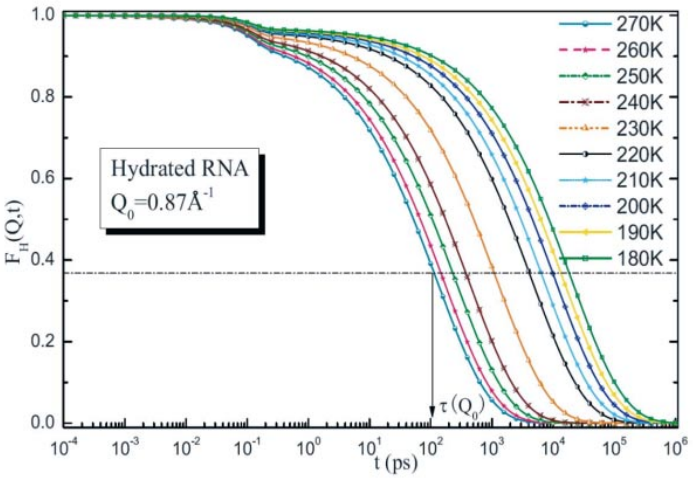

Fig. 49. – Intermediate scattering functions ISF at Q_0 of hydrogen atoms in RNA hydration water, as a function of temperature. They are extracted from the analysis of the quasi-elastic spectra by using the relaxing-cage model. It is seen that the ISF exhibits a two-step decay consisting of the beta and the alpha relaxation processes. Figure adapted from [341].

15. – The low-temperature (protein glass transition) dynamical crossover

15˙1. *Neutron results*. – First of all, the results obtained by means of the relaxing cage model in the region of the low temperature dynamical crossover in the case of the ribonucleic acid (RNA), are shown in fig. 48. From the results of RCM analysis of experimental $S_H(Q,\omega)$, one obtains, according to the previous discussion, the three parameters, τ_0, β, and γ, and is able to calculate the theoretical intermediate scattering function ISF from eq. (11), under the reported condition that τ_T obeys to the power law $\tau_T = \tau_0(aQ)^{-\gamma}$ [222]. Figure 49 reports the ISF of the hydrogen atoms in RNA hydration water for each different temperature. As can be observed they show clearly the two-step relaxation process (typical of the observation made in the density-density relaxation processes in glass transition phenomena [194]: the beta relaxation for the short-time process and the alpha relaxation for the long-time one) described by the RCM. The alpha relaxation time can be easily extracted from these ISF by taking $1/e$ points for each temperature (*e.g.*, the arrow in the figure).

The average translational relaxation time $\langle\tau_T\rangle$ can also be calculated from the fitted parameters τ_0, β, and γ. Figure 50 shows the $\log\langle\tau_T\rangle$ *vs.* $1/T$ plot. Also in that case it is possible to observe the dynamical crossover typical of confined water at $T_L = 220\,\mathrm{K}$.

At high temperatures, above 220 K, $\langle\tau_T\rangle$ obeys a Vogel-Fulcher-Tammann VFT law ($\langle\tau_T\rangle = \tau_0 \exp[DT_0/(T - T_0)]$), Below 220 K, the $\langle\tau_T\rangle$ switches over to an Arrhenius behavior. Figure 50(a) shows the FSC phenomenon of the hydration water in RNA (where the activation energy $E_A = 3.03\,\mathrm{kcal/mol}$), whereas fig. 50(b) shows the same plot for the DNA hydration water ($E_A = 3.48\,\mathrm{kcal/mol}$) [337]. It can be seen that the crossover temperature from the super-Arrhenius to Arrhenius behavior, T_L, in both RNA and DNA hydration water is, within the experimental error, approximately the same. For

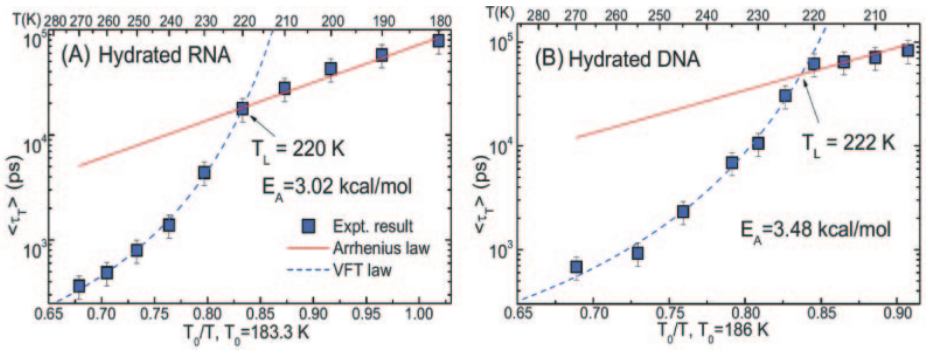

Fig. 50. – (A) The extracted average translational relaxation $\langle \tau_T \rangle$ fitting of the quasi-elastic spectra by the relaxing cage model plotted in a log scale against T_0/T. It shows clearly a well-defined cusp-like dynamic crossover behavior occurring at $T_L = 220\,\mathrm{K}$. The dashed line represents fitted curves using the VFT law, while the solid line is the fitting according to the Arrhenius law. (B) Result of a similar analysis for a hydrated DNA case for the purpose of comparison [337]. Note the crossover temperature, $T_L = 222\,\mathrm{K}$ in this case. Figure adapted from [341].

the same samples the mean square atomic displacement (MSD) $\langle X^2 \rangle$ is obtained by means of a proper experimental procedure: a series of elastic scans through the temperature range of interest (typically from 5 to 400 K) that covers completely the supposed crossover temperature T_L. Since in the supercooled regime (above and below T_L) the system is in a stationary metastable state, the measurements are made by heating and cooling, respectively, and observing exactly the same result. The corresponding MSD are thus calculated from the Debye-Waller factor, $S_H(Q, \omega = 0) = \exp(-Q^2 \langle X_H^2 \rangle)$, by linearly fitting the logarithm of $S_H(Q, \omega = 0)$ with Q^2.

Figure 51 illustrates the $\langle X^2 \rangle$ data taken from the D_2O and H_2O hydrated lysozyme samples, from which both MSDs from lysozyme $\langle X^2_{\mathrm{lysozyme}} \rangle$ and its hydration water $\langle X^2_{\mathrm{H_20}} \rangle$, can be extracted respectively. In order to show the synchronization of the temperature dependence of the two MSDs thus extracted, the $\langle X^2_{\mathrm{lysozyme}} \rangle$ is multiplied by a factor 4.2, so both curves superpose onto each other. This figure illustrates that the crossover temperatures for both protein and its hydration water defined by a sudden change of slope of MSD from a low-temperature behavior to a high-temperature behavior is coincident within the experimental errors. Note the crossover temperature of hydration water (T_L) and the protein dynamic (or glass transition) (T_C) agree with each other.

Figure 52 shows the change of softness, defined as the slope of the MSD *vs.* the temperature T, below and above the crossover temperature in both the RNA and its hydration water [341].

Figure 52(A) shows the MSD of the hydration water molecule, $\langle X^2_{\mathrm{H_20}} \rangle$, obtained in the observational time interval of about 2 ns (corresponding to the energy resolution of $0.8\,\mu$eV). Figure 52(B) shows the MSD of the hydrogen atoms of the RNA macromolecule. From these two latter figures, one can easily observe that the dynamical transition temperature of the hydration water (T_L) and the glass transition temperature of the RNA molecule (T_C) are, within the error bars of the kink positions, approximatively

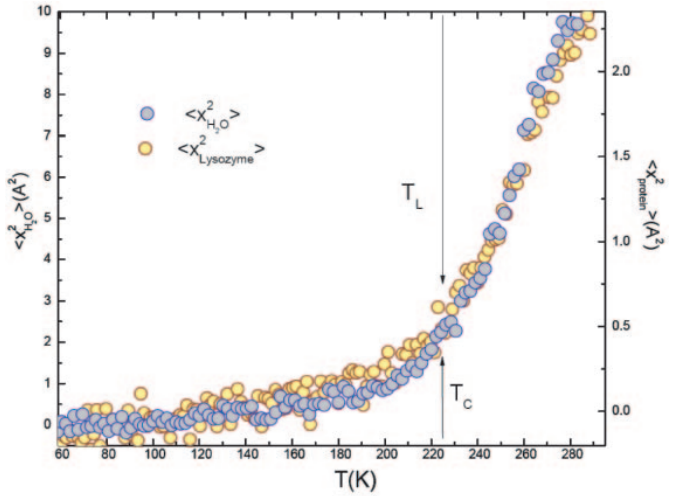

Fig. 51. – Comparison of MSDs measured for the protein and its hydration water. Note that the MSD for hydration water is plotted using the scale on the left-hand side and MSD for the protein using the scale on the right-hand side (the multiplication factor of the left and right scales is 4.2). MSD for the protein is taken from the elastic scan of D_2O hydrated sample. Note the crossover temperature of the hydration water (T_L) and the crossover temperature of the protein (T_C) agree with each other.

the same. The change of slope in MSD of RNA happens at a temperature $T_C \approx 240\,\mathrm{K}$, slightly higher than $T_L \approx 220\,\mathrm{K}$ of hydration water, suggesting that there is a sort of delay in the induced transition in RNA to a more flexible form after the sharp FSC dynamic transition in its hydration water. As previously reported at the FSC (the locus in which the Widom line is crossed) the relative proportion of the low-density water (LDL) to the high-density water is about 50 : 50; probably one may need to have a high concentration of partially bonded water (*i.e.*, more HDL water than LDL) which happens 20 K after crossing the Widom line to generate enough mobility of hydration water to restore the RNA (or protein like the case of lysozime) activity. Beside some possible controversial aspects regarding the FSC definition (see refs. [24]–[26] of ref. [341]), the data of figs. 51 and 52, regarding hydrated lysozyme and RNA, show that the dynamic crossover of the hydration water triggers the onset of the protein glass transition. From the slope of the straight lines going through the low temperature points one can estimate the softness of hydration water and RNA. It is striking to see that by crossing the crossover temperature (T_L), the softness of RNA and its hydration water increase by a factor of 15 and 20, respectively. However a comparison of fig. 50 with figs. 51 and 52 reveals that the dynamic crossover is cusp-like, in the case of average translational relaxation time $\langle \tau_T \rangle$, and thus it sharply defines T_L much more accurately than that indicated by the MSD $\langle X^2_{\mathrm{H_20}} \rangle$.

It is very interesting to consider also the protein MSD and the corresponding softness as a function of the pressure; the low-temperature behavior of proteins under pressure is a phenomenon not as extensively investigated as that at normal pressure. Such a situation is of deeper interest; as is well known, some bacteria can survive under extremely high

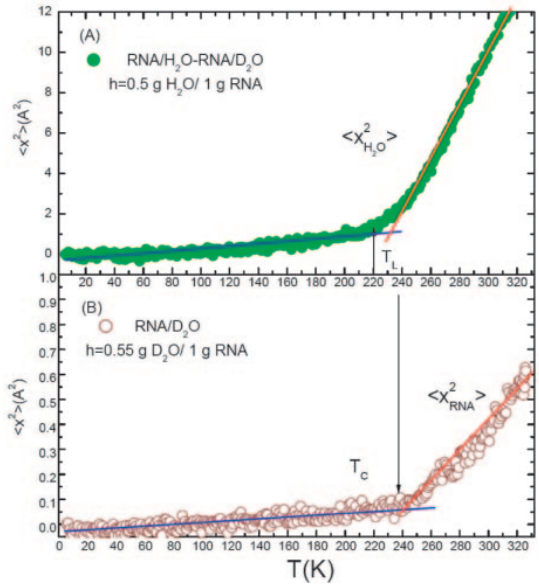

Fig. 52. – The MSD *vs.* T for RNA (B) and its hydration water (A). The slope is used as a measure of the biomaterial softness. As one can see, above the crossover temperature (T_C), the RNA becomes 15 times softer than its glassy state, while the hydration water becomes 20 times softer when crossing the temperature T_L [341].

pressure and low temperature in the deep ocean. The microorganisms living in the deepest ocean yet isolated and characterized were sampled at 11000 m depth or 1.1 kbar in the deep-sea sediments of the Marianas trench, where the Pacific oceanic lithosphere subducts into the Earth's mantle [342]. How can proteins in the microorganisms still function under these extreme conditions? Besides the fact that high pressure denatures most of the dissolved proteins above 3000 bar, the behaviors of proteins under pressures below the denaturation limit (< 2 kbar) both for structure and dynamics are relevant to the biological functions of proteins and are of great interest [343]. Furthermore, Monte Carlo (MC) simulation shows that the effect of pressure on the hydration water density is the key for understanding cold denaturation of proteins at high pressures [344].

Also in this case the incoherent neutron scattering experiments on a D_2O hydrated protein (lysozyme) sample can provide information on protein dynamics since neutrons scattered by atomic nuclei are more sensitive to hydrogen atoms than deuterium and other atoms in proteins and hydrogen atoms reflect the motions of the side chains and backbone to which they are bound. In addition, by measuring both H_2O and D_2O hydrated samples and taking their difference the signal contributed solely from hydration water can be obtained. During this subtraction process, the contribution from the instrumental background is also eliminated.

In the next the main results of these neutrons experiments are reported, *i.e.*, from the measured MSD it results that the temperature dependence of the protein dynamics closely follows that of the hydration water under different pressures. Figures 53 and 54 show these ENS results, in particular the calculated MSDs of the hydrogen atoms in

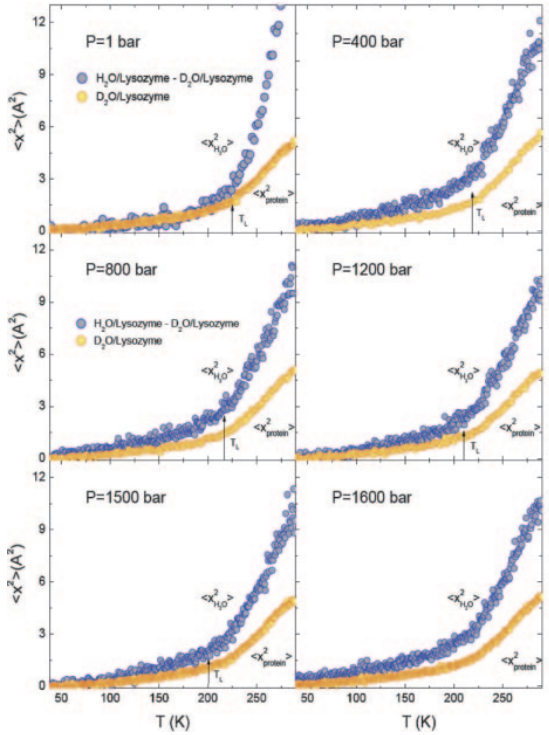

Fig. 53. – The MSD, $\langle X^2 \rangle$, of hydrogen atoms in lysozyme and in its hydration water, as a function of temperature, under different pressures. Dark circles indicate the data processed from the difference between the H_2O and D_2O hydrated samples, which gives a MSD of the H-atoms in the hydration water, following the scales on the left. Light circles represent the data processed from the D_2O hydrated sample, which gives a MSD of H-atoms in the protein.

the lysozyme molecule $\langle X^2_{\text{protein}} \rangle$ and that of the hydration water molecule, $\langle X^2_{\text{H}_2\text{O}} \rangle$, measured by ENS in the low-temperature range from 40 to 290 K under six different pressures up to 1600 bar. The observation time interval was about 2 ns, corresponding to the energy resolution of 0.8 μeV.

Figure 53 shows the MSD of lysozyme and its hydration water in the same scale. Figure 54 rescales the same data in fig. 53 by a factor of 4.2 to show the synchronization in the temperature dependence of the two MSDs at each pressure. One can see clearly that the temperature dependence of the MSDs of lysozyme and its hydration water follows the same trend, especially after rescaling them into the same amplitudes (by multiplying the MSD of the protein by a factor of 4.2). Each MSD shows a linear behavior close to zero at lower temperatures with a very small slope, which means that the force constant K is very large and that the protein is rigid, not soft.

Above a certain temperature T_D, the slope abruptly increases, and the K value is about 10 times smaller, which implies that the protein is about 10 times "softer" than its "glassy" state, and the protein flexibility and activities are restored above T_D. Note that the temperature-dependent behavior of MSD of the lysozyme molecules and their

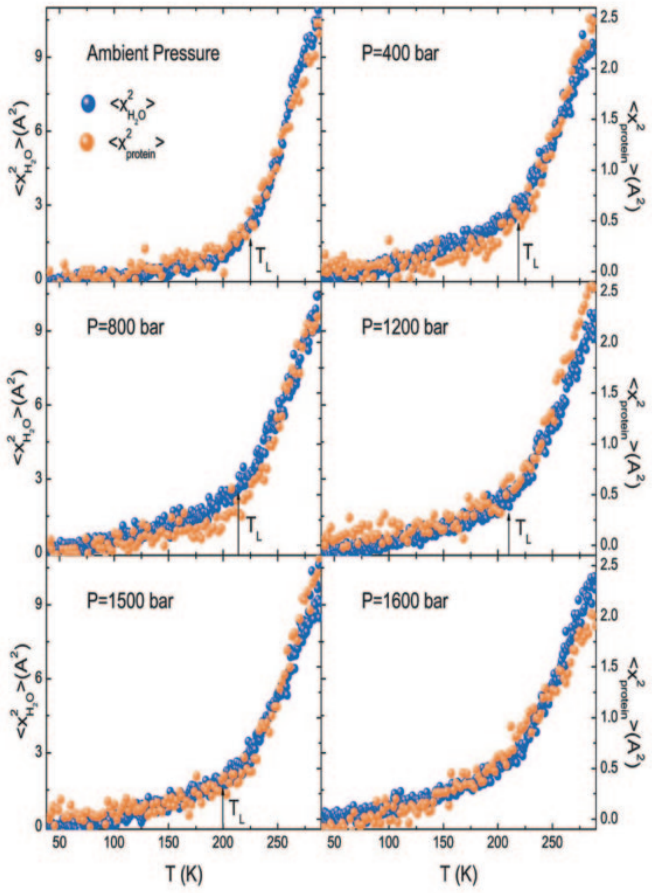

Fig. 54. – Reduced plot of pressure dependence of MSD of protein and its hydration water. It is to be noted in this figure that the crossover temperature of the protein and its hydration water is closely synchronized at a range of pressures below 2000 bar [345].

hydration water are visually the same, implying that the dynamic behavior in the protein is intimately related to the dynamic behavior in its hydration water. Since the dynamics of the hydration water is pressure-dependent like confined water (see fig. 19), this leads to a conclusion that the dynamics of proteins follows the same pressure dependence of its hydration water. Thus, in this temperature and pressure region, the role of hydration water is essential in the protein dynamics.

Therefore this ENS experiment indicates that the dynamic transition temperature of the protein, $T_D(P)$, coincides with its hydration water, $T_D(P) = T_L(P)$, by confirming the QENS indication coming from the average translational α-relaxation time $\langle \tau_T \rangle$ of the hydration water molecules; it is found that there is a dynamic crossover in hydration water occurring at a "universal" temperature $T_L = 225 \pm 5\,\mathrm{K}$ in the three biomolecules —lysozyme, B-DNA, and RNA— and that it can be described as a fragile-

to-strong dynamic crossover (FSC). Since this dynamic crossover of water is also observed in other substrates (1-D confinement in silica porous material and 3-D confinement in cement [346]), the phenomenon appears to be universal for confined water and one of the dynamic properties of water itself. Thus, the dynamic behavior in the protein is considered to be slaved by the dynamics of its hydration water.

This represents a remarkable result: the dynamical crossover temperature (*i.e.*, the Widom line) of the protein hydration water seems to coincide with the Widom line of the confined water in MCM-41-S. Another interesting finding is that these neutron data give strong evidence that hydrated proteins remain soft at lower temperatures under pressures. Furthermore, there is evidence, from these studies, that the relaxation time of water molecules is shorter under pressure. Thus, in this measured low-temperature region, increasing the pressure up to 1500 bar can have the same effect on the relaxation time as increasing the temperature. This faster motion in relaxation and fluctuation of the hydration water under pressure enables the protein to sample more conformational substates becoming active at lower temperatures. Moreover, the dynamic crossover in the structural relaxation time of protein hydration water from super-Arrhenius to Arrhenius behavior at a temperature $T_L(P)$ decreases with pressure.

This phenomenon may be rationalized either from the point of view of the existence of the second liquid-liquid critical point in the protein hydration water in the supercooled region or as the effect on the water structure of hydrophobic sites. On the other hand, it is shown in the literature that applying pressure can also induce an increase in protein-water interactions and improve water accessibility to the hydrophobic core of the protein. On this context the results of high-resolution quasi-elastic neutron scattering spectroscopy in H_2O hydrated double-wall carbon nanotubes DWNT [347] are of interest. The measurements have been made at a series of temperatures from 250 K down to 150 K and the relaxing-cage model was used to analyze the quasi-elastic spectra.

The obtained results are shown in fig. 55 that reports in the upper panel the extracted average translational relaxation time $\langle \tau_T \rangle$ from fitting of the quasi-elastic spectra of water confined in DWNT, inner diameter 16 Å, by RCM plotted in a log scale against $1/T$. It shows a well-defined cusplike dynamic crossover behavior occurring at $T_L = 190$ K. The solid line represents a fitted curve using the VFT law, while the dashed line is the fitting according to the Arrhenius law. The lower panel reports mean-squared atomic displacement, MSD, averaged over all the hydrogen atoms, $\langle X^2 \rangle$, extracted from the Debye-Waller factor measured by an elastic scan with resolution of 0.8 eV, as a function of temperature for the H_2O confined in DWNT. One can clearly see a sharp transition of slope at around 190 K, indicating the approximate location of the dynamic crossover temperature.

The comparison of these results with those of previous experiments on supercooled water confined in porous silica material MCM-41 with different pore sizes shows that the crossover temperature T_L is insensitive to confinement pore sizes. From the results shown in the upper and lower panels and the comparison with MCM-41 confined water, it results that the water confined in a hydrophobic substrate DWNT has a lower dynamic crossover temperature by $\Delta T_L \approx 35$ K, as compared to that in the hydrophilic silica substrate of the MCM.

By considering the previous results on lysozyme, DNA and RNA and MCM-41, one can detect only little differences in the crossover temperatures in these hydrated systems that on average are located at about 220 K; for example, in hydrated DNA the crossover is at 222 K whereas in the case of protein lysozyme T_L is 220 K, proposing that DNA has more hydrophilic interface presumably due to the presence of the phosphate groups. On these basis it can be conjectured that the magnitude of the crossover temperature T_L can

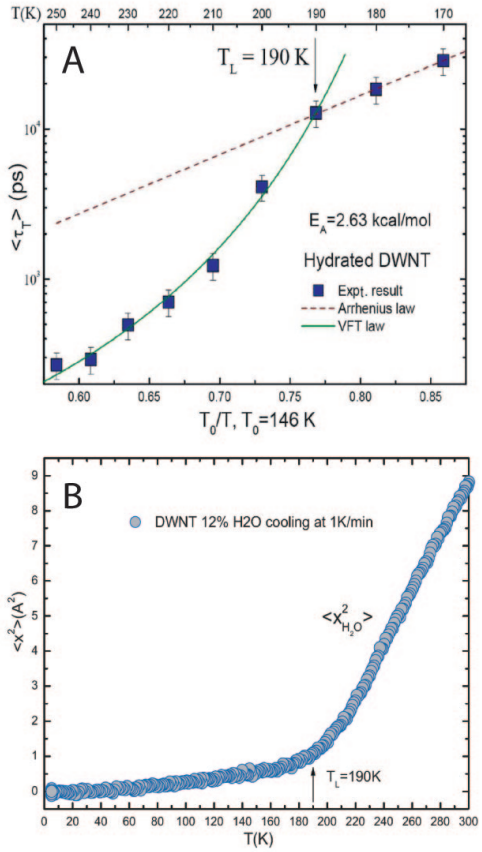

Fig. 55. – A) Extracted average translational relaxation time $\langle \tau_T \rangle$ from fitting of the neutron spectra of water confined in double-wall carbon nanotubes (DWNT) with an inner diameter of 16 Å, plotted in a log scale against T_0/T. As can be seen, in this case the cusp-like dynamic crossover occurs at about $T_L = 190\,\mathrm{K}$. The solid line represents a fitted curve using the VFT law, while the dashed line is the fitting according to the Arrhenius law. B) The mean-squared atomic displacement (MSD), as a function of T, averaged over all the hydrogen atoms, $\langle X^2 \rangle$, extracted from the Debye-Waller factor. In this case it can be observed a sharp transition of slope at around 190 K, indicating the approximate T_L location. Figure adapted from [347].

be used as an indicator of the hydrophilicity of the substrate. A good test of this idea may be to measure the crossover temperatures of protein hydration water with proteins of different hydrophilic and hydrophobic interfacial exposure.

Returning to the pressure effects on proteins, the behavior observed for water confined in hydrophobic structure can give the right explanation on the observed processes. The fact that water confined in a hydrophobic substrate has a lower crossover temperature T_L than that confined in a hydrophilic substrate, rationalizes the observation that the crossover temperature of protein hydration water decreases with pressure. This effect of

pressure is basically the increase in the protein-water interactions and the improvement of the water accessibility to the hydrophobic core of the protein [348]. Another case in which the effects of pressure on the dynamical properties of a biomolecule have been studied is represented by β-lactoglobulin, which is also a sensitive food protein. While in some studies lysozyme is considered to be the most pressure-resistant, others show that β-lactoglobulin presents similar pressure effects using other techniques such as UV spectroscopy [349]. These results suggest the universality of the observed pressure effects on proteins.

16. – The violation of the Stokes-Einstein relation

We have previously shown that for water confined in MCM-41-S meso-porous material of pore size 14 and 18 Å, there is a breakdown of the well-known Stokes-Einstein relation (SER) when the average translational relaxation time (or the α-relaxation time, just in terms the Mode coupling theory nomenclature) $\langle\tau_T\rangle$ crossovers from a super-Arrhenius behavior to an Arrhenius behavior at the crossover temperature, $T_L = 225\,\mathrm{K}$. The SER in water can be written as $D = (k_B T/4\pi\eta a)[(1+f)/1+3f/2]$, where k_B is the Boltzmann constant, T the temperature, η the shear viscosity, $a = 1.44\,\text{Å}$ the effective diameter of the water molecule, and $f = \beta a/3\eta$, where β is the slip coefficient at the sphere-liquid interface. Since η can be taken to be proportional to $\langle\tau_T\rangle$, the product $D\langle\tau_T\rangle/T$ should be independent of temperature if SER is valid. This is indeed the case for temperatures above 240 K; at the crossover temperature $T_L = 225\,\mathrm{K}$, this product is about 10 times larger than the constant value above 240 K. Furthermore, the breakdown of SER results in the emergence of a fractional SER in the form $D \sim \langle\tau_T\rangle^{-\xi}$ where the exponent $\xi = 1$ in the region SER is valid and becomes less than unity in the region where SER breaks down [238]. Furthermore it has been predicted for the Fredrickson-Andersen FA models [350], which correspond to strong glass formers, that $\xi = 2/3 = 0.67$ for $d = 1$ (one-dimensional confinement), $\xi = 2/2.3 = 0.87$ for $d = 2$ and $\xi = 2/2.1 = 0.95$ for $d = 3$ [238].

In this section, it will be briefly shown that the breakdown of SER in 2-d confined hydration water can also be observed experimentally by combining Neutron QENS data with NMR data. In fig. 56 panel A, $1/D$ *vs.* $1000/T$ measured by NMR [316, 351] and $\langle\tau_T\rangle$ *vs.* $1000/T$ measured by QENS [202] are reported. In panel B the verification of the theory of the fractional SER $D \sim \langle\tau_T\rangle^{-\xi}$ is shown. It can be seen from panel A that at the crossover temperature, T_L, $1/D \sim 3\cdot 10^{12}\,\mathrm{s/m^2}$ and $\langle\tau_T\rangle \sim 210^4\,\mathrm{ps}$. While above T_L (fragile region), $\xi \sim 1$ indicating that the SER is valid, below T_L (strong region), $\xi \sim 0.82 \pm 0.05$, in agreement with the theoretical prediction of $\xi \sim 0.87$ for two-dimensionally confined water. The decoupling of self-diffusion constant from the average relaxation time as manifested by the emergence of fractional SER can be attributed to the dynamic heterogeneity which grows to a significant size at and below the crossover temperature [352].

17. – The simulation results

The investigation of the population of the different HB and NHB water molecules by means of FTIR spectroscopy, the NMR self-diffusion coefficient and the proton longitudinal relaxation time of hydration water as a function of the temperature reveal that the protein is characterized by two dynamical transitions [202, 316]. The low-temperature FSC dynamic crossover transition at about 225 K is related to the protein "glass" transition which, according to the recent neutron scattering data on the

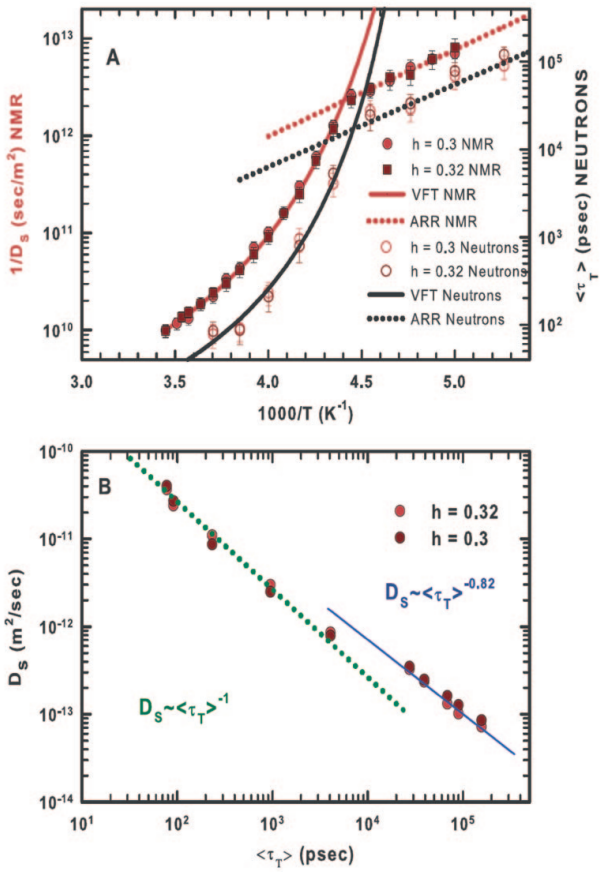

Fig. 56. – The existence of the FSC (panel A) and of the SER breakdown (panel B) in the case of the lysozyme hydration water with hydration levels of $h = 0.3$ and $h = 0.32$ are shown. Panel A shows the $1/D_S$ measured by NMR in a log-lin plot (left side) and the QENS average translational relaxation time $\langle \tau_T \rangle$ (right side) *versus* $1/T$. The obtained crossover temperatures are $T_{\mathrm{NMR}} = 226 \pm 2\,\mathrm{K}$ and $T_{\mathrm{QENS}} = 225 \pm 2\,\mathrm{K}$. Panel B shows the analysis of the scaled SER, *i.e.*, a log-log plot of D_S *vs.* $\langle \tau_T \rangle$, for both hydration levels. There are two scaling behaviors above and below T_L: in the super-Arrhenius region we have $\xi \approx 1$, whereas in the Arrhenius region $\xi \approx 0.82$, the value predicted by theory and numerical analysis for a $2d$ system [238]. Figure adapted from [351].

$\langle X^2 \rangle$ [202], is triggered by the strong coupling between protein and hydration water. At the high-temperature transition, associated with the lysozyme denaturation process, one can observe that the population of the non-hydrogen-bonded fraction of water molecules dominates. This latter result can be considered as a strong signal that changes in hydration water accompany those associated with the protein thermal unfolding. However, these experiments show unambiguously that both transitions are connected to the change of the local hydrogen bond pattern of the hydration water which in turn leads to mobility

changes of both the hydration water and the protein. In the following a special section is dedicated to the simulation studies on water in biomolecules. The main reason is that molecular dynamic simulations constitute actually a powerful tool to study physical properties of biosystems not only to confirm "true" experimental results or to check the validity of some theoretical models, but also to explore many complex situations not directly accessible to experiments, like for example the properties in the proteins involved in the Alzheimer disease see ref. [353]. On these bases it is of pedagogical importance treating with a certain emphasis the MD approaches to study the biomolecules hydration water.

The FTIR results combined with the NMR self-diffusion (D), the NMR spin-lattice relaxation time (T_1), and the Neutron scattering evidences [202] demonstrate the existence of two dynamical transitions due to the coupling between protein and the hydration water. However, these situations have been the subject of other studies by considering that being water an active subject in the protein activity its thermodynamics can be related with both the glass transition and the denaturation. First, it has been explored the hypothesis [201] that the observed glass transition in biomolecules [62,202,334,335,354-363] is related to the liquid-liquid phase transition of water using molecular dynamics (MD) simulations. Specifically, Kumar *et al.* [201] studied the dynamic and thermodynamic behavior of lysozyme and DNA hydration water. This MD experiment was made by using the five-point transferable intermolecular potential of water (TIP5P), by means of the software package GROMACS [364] for i) an orthorhombic form of hen egg-white lysozyme [365] and ii) a Dickerson dodecamer DNA [366] at constant pressure $p = 1\,\mathrm{atm}$, several constant temperatures T, and constant number of water molecules N (NPT ensemble) in a simulation box with periodic boundary conditions. Details of the work are the following: i) the system equilibration (at p and T constant) is obtained by means of the Berendsen method; ii) this initial equilibration is followed by a long run, during which the dynamic and static properties (equilibration times vary for different T from few ns for high-T to as much as 40 ns for low temperatures) are calculated. For lysozyme simulations, the system consists of a single protein in the native conformation solvated in $N = 1242$ TIP5P water molecules. These simulation conditions correspond to a ratio of water mass to protein mass of 1.56. The DNA system consists of a single DNA helix with 24 nucleotides solvated in $N = 1488$ TIP5P water molecules, which corresponds to an experimental hydration level of 3.68.

The simulation results for the mean square fluctuations $\langle X^2 \rangle$ of both protein and DNA are shown in fig. 57. Kumar *et al.* calculated the mean square fluctuations $\langle X^2 \rangle$ of the biomolecules from the equilibrated configurations, first for each atom over 1 ns, and then averaged over the total number of atoms in the biomolecule. They find that $\langle X^2 \rangle$ changes its functional form below $T_p \approx 245\,\mathrm{K}$, for both lysozyme, fig. 57(a), and DNA, fig. 57(b). Upon cooling, the diffusivity of hydration water exhibits a dynamic crossover from non-Arrhenius to Arrhenius behavior at the crossover temperature $T_{\mathrm{cr}} \approx 245 \pm 10\,\mathrm{K}$ (fig. 58(c)), a situation similar to that reported in the previous sections.

Subsequently, Kumar *et al.* calculated C_p by numerical differentiation of the total enthalpy of the system (protein and water) by fitting the simulation data for enthalpy with a fifth order polynomial, and then taking the derivative with respect to T. Figure 58(a) displays maxima of $C_p(T)$ at $T_{\mathrm{W}} \approx 250 \pm 10\,\mathrm{K}$ for both biomolecules.

Further, to describe the quantitative changes in structure of hydration water, Kumar *et al.* calculated the local tetrahedral order parameter Q [150, 168-170] for hydration water surrounding lysozyme and DNA. Figure 58(b) shows that the rate of increase of Q has a maximum at $245 \pm 10\,\mathrm{K}$ for lysozyme and DNA hydration water, the same temperature of the crossover in the behavior of mean square fluctuations.

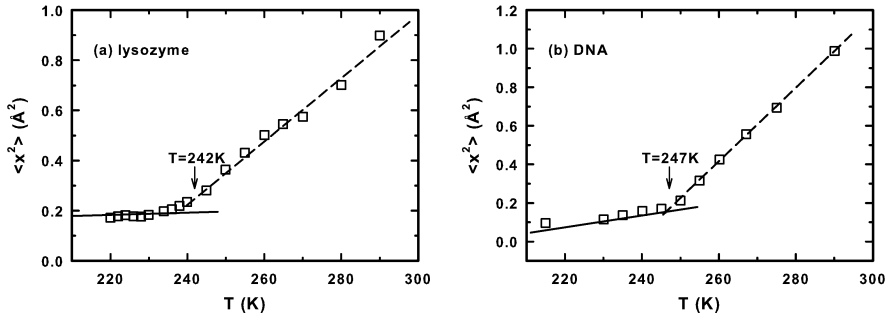

Fig. 57. – Mean square fluctuation of (a) lysozyme, and (b) DNA showing that there is a transition around $T_p \approx 242 \pm 10\,\mathrm{K}$ for lysozyme and around $T_p \approx 247 \pm 10\,\mathrm{K}$ for DNA. For very low T one would expect a linear increase of $\langle x^2 \rangle$ with T, as a consequence of harmonic approximation for the motion of residues. At high T, the motion becomes non-harmonic and the data are fitted by a polynomial. The dynamic crossover temperature T_p was determined from the crossing of the linear fit for low T and the polynomial fit for high T [201].

The coincidence of T_{cr} with T_p within the error bars indicates that the behavior of the protein is strongly coupled with the behavior of the surrounding solvent, in agreement with the recent experiments [202]. Note that T_{cr} is much higher than the glass transition temperature, estimated for TIP5P as $T_g = 215\,\mathrm{K}$. Thus this crossover is not likely to be related to the glass transition in water.

The fact that $T_p \approx T_{\mathrm{cr}} \approx T_{\mathrm{W}}$ is evidence of the correlation between the changes in protein fluctuations (fig. 57(a)) and the hydration water thermodynamics (fig. 58(a)). Thus, these results are consistent with the possibility that the protein glass transition is related to the Widom line (and hence to the hypothesized liquid-liquid critical point). Crossing the Widom line corresponds to a continuous but rapid transition of the properties of water from those resembling the properties of a local HDL structure for $T > T_{\mathrm{W}}(p)$ to those resembling the properties of a local LDL structure for $T < T_{\mathrm{W}}(p)$. A consequence is the expectation that the fluctuations of the protein residues in predominantly LDL-like water (more ordered and more rigid) just below the Widom line, should be smaller than the fluctuations in predominantly HDL-like water (less ordered and less rigid) just above the Widom line.

The quantitative agreement of the results for both DNA and lysozyme (figs. 57 and 58) suggests that indeed the changes in the properties of hydration water are responsible for the changes in dynamics of the protein and DNA biomolecules. These results are in qualitative agreement with recent experiments on hydrated protein and DNA [337] which found the crossover in side-chain fluctuations at $T_p \approx 225\,\mathrm{K}$.

Other simulation studies are of a certain interest since they have been made just to explore directly the previously cited experimental results obtained from the use of the NMR and Neutron techniques, *i.e.* the existence of the two crossovers, especially the one in the temperature region of the folding/unfolding process. Now the results obtained in the region of the fragile-to-strong dynamical crossover are reported.

This new study is in some way different from the previously reported MD simulation [201] made for a model of hydration water in protein lysozyme and Dickerson dodecamer DNA in which the mean effort was to give clear evidence of the connections

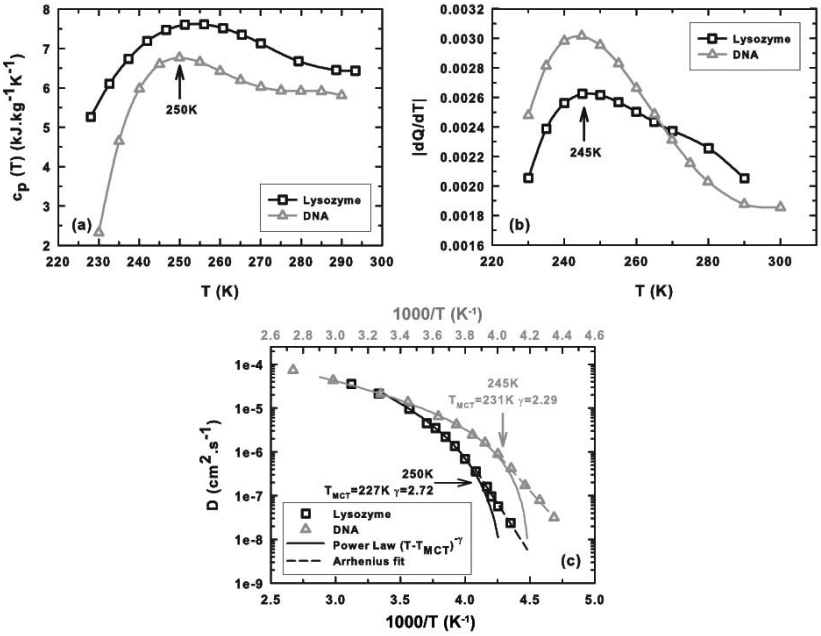

Fig. 58. – (a) The specific heat of the combined system lysozyme and water (black squares), and DNA and water (grey triangles), display maxima at $250 \pm 10\,\mathrm{K}$ and $250 \pm 12\,\mathrm{K}$, respectively, which are coincident within the error bars with the temperature T_p where the crossover in the behavior of $\langle x^2 \rangle$ is observed in figs. 57(a) and (b). (b) Derivative with respect to temperature of the local tetrahedral order parameter Q for lysozyme (black squares) and DNA hydration water (grey triangles). A maximum in $|\mathrm{d}Q/\mathrm{d}T|$ at the Widom line temperature suggests that the rate of change of local tetrahedrality of hydration water has a maximum at the Widom line. (c) Diffusion constant of hydration water surrounding lysozyme (black squares), and DNA (grey triangles) shows a dynamic transition from a power law behavior to an Arrhenius behavior at $T_{\mathrm{cr}} \approx 250 \pm 10\,\mathrm{K}$ for lysozyme and $T_{\mathrm{cr}} \approx 245 \pm 10\,\mathrm{K}$ for DNA, around the same temperatures where the behavior of $\langle x^2 \rangle$ has a crossover, and c_p and $|\mathrm{d}Q/\mathrm{d}T|$ have maxima. Figure from [201].

between the FSC observed in hydration water with crossing the Widom line. In this simulation, the model used was not a close enough representation of the hydrated powder samples used in the experiments to directly compare the temperature dependences of simulated quantities with the neutron scattering and the NMR experimental results. In fact, to better mimic the experimental system made on hydrated powder protein samples, the simulations have been performed on the random powder model [367, 368], a model that improves the agreement with experiments if compared to the protein/water cluster model previously described [201]. Such a realistic powder model has, in fact, reproduced experimental data (both neutron and NMR) within the statistical error bars. In particular, there has been shown the striking agreement of MD calculations with the temperature dependence of measured mean-square hydrogen atom displacements of the protein and its hydration water, $\langle X^2 \rangle$, such as the inverse of the self-diffusion constant,

$1/D$, and the translational α-relaxation time of the hydration water, $\langle \tau_T \rangle$. The significance of these comparisons is the following: one can demonstrate that the dynamic crossover observed in experiments can be attributed solely to the crossover phenomenon resulting from evaluation of the average translational α-relaxation time by analyses of the long-time decays of the self-intermediate scattering functions of the hydrogen atoms attached to a typical water molecule [369, 370]. It is the signature of crossing of the Widom line in a 2-d confined water. At high temperatures, the fragile behavior arises from water structure dominated by a high-density form (HDL), which is more fluid, and at low temperatures, upon crossing T_L, the water structure evolves into a predominantly low-density form (LDL), which is less fluid, and has a strong behavior. This sudden switch in mobility of hydration water at T_L serves to trigger the dynamic transition in protein [367, 368].

The choice of the force field before running a simulation is crucial for the achievement of a quantitative comparison with experiments. Since the interest was mainly on the dynamics of hydration water, the used water model was the well known TIP4P-Ew. This model has a computed self-diffusion constant in excellent agreement with the experimental values and a good correspondence of the temperature scale (its density maximum is at 274 K, only 3 K below the correct value) at least down to 230 K. Accordingly, an implemented OPLS-AA force field for the lysozyme molecules was used; this in conjunction with the TIP4P model has been proven to give satisfactory results in computing the free energies of binding of inhibitors on a protein, see refs. [371, 372].

In addition, the poor agreement with experiments of the so-called *cluster model* has to be taken into account, composed of a single protein covered by a shell (thin or thick) of water, which lacks the characteristic feature of the powder protein [373]; it in fact produces serious errors and artifacts for any calculated properties. Instead, a *crystal* (composed of two proteins) or a *powder* (eight proteins, oriented or random) model resulted in a realistic model to reproduce neutron scattering data, with little differences between them [367, 374].

On these bases the new simulation is made by putting in a box two OPLS-AA lysozyme molecules randomly oriented and 484 TIP4P-Ew water molecules ($h = 0.3$ for each protein): after an energy minimization of 5000 steps with the steepest-descent algorithm, the system was equilibrated in a NPT ensemble (isobaric-isothermal) for 10 ns at 300 K and for another 50 ns at 200 K. Then many simulations (11) at different temperatures (in the interval 180–280 K, with steps of 10 K) have been performed with a parallel-compiled version of GROMACS, [364] starting each simulation from the final configuration of the closest temperature. The Lennard-Jones interactions have been truncated beyond 1.4 nm, while electrostatic interactions, calculated with the particle mesh Ewald method [375] were truncated at 0.9 nm. In addition, all bonds were constrained at their equilibrium values using the linear constraint solver algorithm (LINCS [376]); simulations were performed using a triclinic cell with periodic boundary conditions, and each MD simulation length was 50 ns after the equilibration time.

A view of the simulation box is shown in fig. 59: the two proteins and the hydration water surrounding them are displayed together (the box dimensions are $4.3 \times 3.7 \times 3.2$ nm) [318]. As can be noted there are only a few water molecules (about 10 molecules) sandwiched between the two proteins while there are more water molecules around other parts of the protein surface. However, on average, $h = 0.3$ is supposed to be only one monolayer of water covering each protein. The resulting density of the modeled hydrated powder protein is in the range 1.2–1.3 g/cm^3, depending on the temperature, in agreement with experimental data for lysozyme crystals (1.23 g/cm^3 [377]).

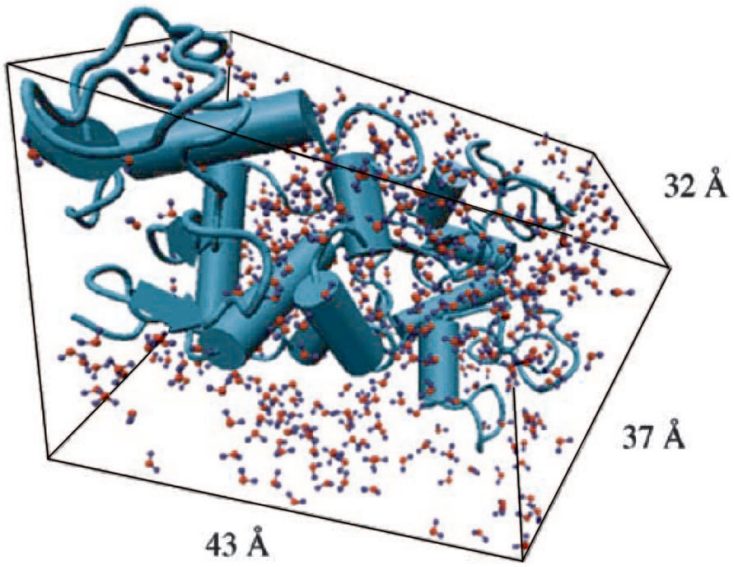

Fig. 59. – Snapshot from a MD simulation at $T = 250\,\mathrm{K}$ and $P = 1\,\mathrm{atm}$ of the hydrated lysozyme powder model, containing two protein molecules and 484 water molecules around them (hydration level $h = 0.3$). Figure adapted from [318].

Figure 60 reports the calculated average mean-squared hydrogen atom displacement (MSD) values for lysozyme, $\langle X^2_{PH}\rangle$, and its hydration water, $\langle X^2_{\mathrm{H_2O}}\rangle$ together with experimental values obtained from elastic neutron scattering [202,337]. For all the panels in the low-temperature regime is $\langle X^2\rangle \sim k_B T$ (straight lines), and this behavior extended up to the crossover temperature (T_L and T_C for water and protein, respectively). At the crossover temperature, the slope of $\langle X^2\rangle$ *vs.* T sharply increases, signaling a change in the dynamics of protein and its hydration water; this crossover takes place at the same temperature for the MSD of hydrogen atoms both in water and in protein, as shown by the arrow signs. Moreover, there is a quantitative agreement between MD simulations and experimental results about the crossover temperature. The occurrence of crossover at the same temperature for protein and its hydration water implies a strong correlation between the dynamics of hydration water and the protein [367,368].

Figure 61 shows the calculated self-intermediate scattering function (ISF) for the protons attached to a rigid molecule of hydration water for different temperatures as a function of time at fixed Q-value ($0.6\,\mathrm{Å}^{-1}$).

The ISFs are calculated at six different temperatures while the inset shows the ISF at $T = 220\,\mathrm{K}$ for different Q-values (namely from top to bottom 0.4, 0.5, 0.6, 0.7 and $0.8\,\mathrm{Å}^{-1}$). The solid lines are the best fits to the ISF according to the relaxing cage model (RCM) and cover the time range of seven orders of magnitude from 2 fs to 20 ns. As can be seen, the corresponding fits of the ISF are excellent allowing the opportunity to extract the long-time cage relaxation (α-relaxation) which leads to the long-time diffusional motion of the water molecule.

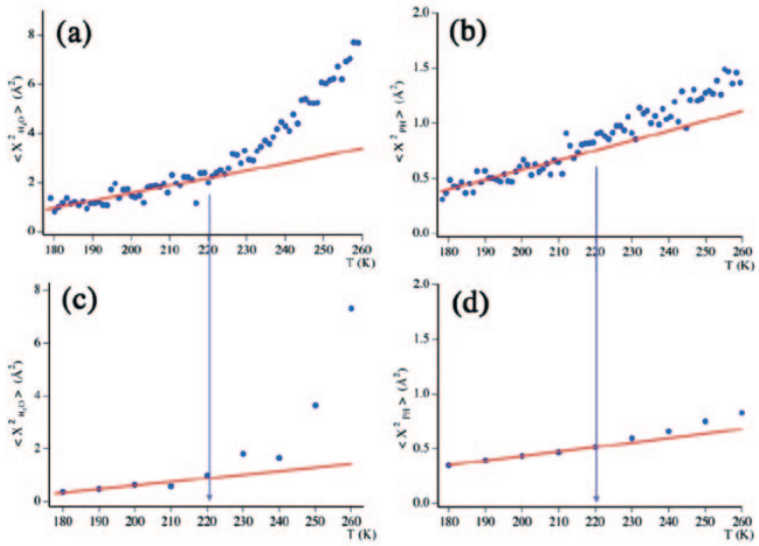

Fig. 60. – The hydrogen MSD, $\langle X^2 \rangle$, measured by elastic neutron scattering (protein hydration water (a) and protein hydrogen atoms (b)) and simulations (protein hydration water (c) and protein hydrogen atoms (d)). In MD, this quantity has been calculated considering the MSD after 500 ps and averaging over the time origins for the last 10 ns of each simulation. The experimental values were obtained by an elastic scan with an energy resolution of 0.8 μeV, corresponding to a sampling time of 5 ns duration [318].

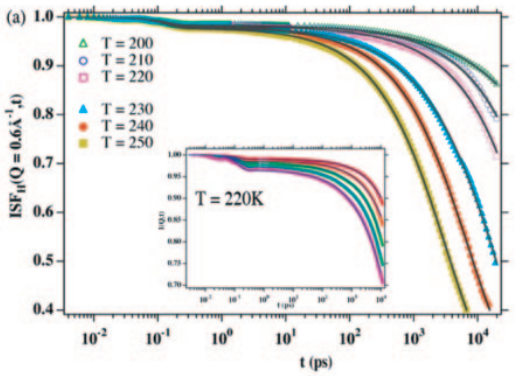

Fig. 61. – The water proton incoherent self-intermediate scattering functions calculated at six different temperatures. The ISF at five different Q-values (from top to bottom, 0.4, 0.5, 0.6, 0.7, and 0.8 Å^{-1}), inset. The solid curves are fits to the relaxing cage model in a wide time range of 7 orders of magnitude, between 2 fs and 20 ns. Figure adapted from [318].

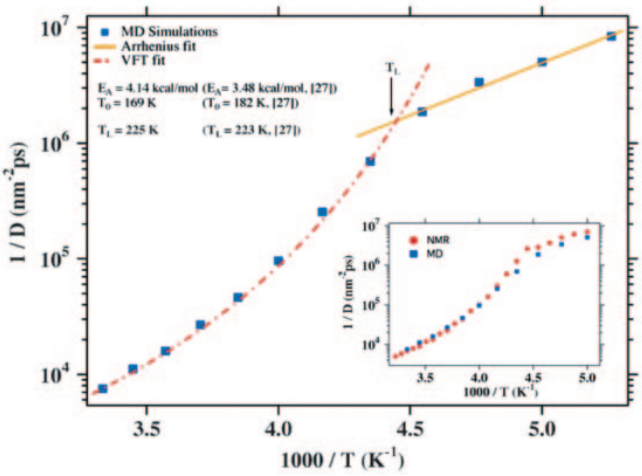

Fig. 62. – Temperature dependence of the inverse diffusion constant, $1/D$, from MD simulations. The diffusion constant has been calculated from the trajectories according to the Einstein relation, $\mathrm{Lim}_{t\to\infty}\langle X^2(t)\rangle = 2Dt$. The MSD fitting began after a time long enough for the water molecule to escape its cage and diffuse. Numerical data are fitted with a Vogel-Fulcher-Tammann law at high temperatures (dash-dotted lines) and with an Arrhenius law at low temperatures (solid line) but with the same prefactor (see text for details). Inset: comparison between MD simulations and NMR data [316]. Figure adapted from [318].

The choice of the Q-values was dictated by the low-limit value of $Q = 0.2\,\text{Å}^{-1}$ imposed by the box sizes and the high-limit value of $Q = 1\,\text{Å}$, below which rotational motion can be neglected. In these ISF's two contributions are evident: the first represents the short-time, in-cage vibrational motion and the second stretched exponential factor represents the long-time cage relaxation (α-relaxation) which leads to the long-time diffusional motion of the water molecule.

The inverse of the self-diffusion constant for hydration water, $1/D$, calculated by MD simulation as a function of $1/T$ is plotted in fig. 62, and its inset shows a comparison with experimental data obtained by NMR [316]. The diffusion constant has been calculated from the trajectories according to the Einstein relation $\mathrm{Lim}_{t\to\infty}\langle X(t)^2\rangle = 2Dt$. The fragile part has been fitted with a Vogel-Fulcher-Tammann (VFT) equation, $1/D = 142.8\exp -[520.5/(T-169)]$ ps, while the strong side, with an Arrhenius form, $1/D = 142.8\exp[2086.7/T]$ ps. The agreement with experimental results is again quantitative, as it can be seen also from the fitting parameters. In particular, it should be noted that the crossover temperature, T_L, is 225 K in the simulation case and 223 K in the experiment. They are essentially identical within the experimental uncertainty.

As one can see from fig. 61, the RCM fits of the ISF, both the time dependence and the Q-dependence, are excellent, allowing us to extract τ_0 as a function of temperature, as shown in fig. 63. The Q-dependent relaxation time, $\tau_T(Q)$, for $Q < 1\,\text{Å}^{-1}$ has been shown experimentally [115] and by a MD simulation [378] to be $\tau_T(Q) \cong \tau_0(aQ)^\gamma$, where a is a suitably chosen length scale that makes the parameter τ_0, having a dimension of time. A Q-independent average translational relaxation time can then be defined

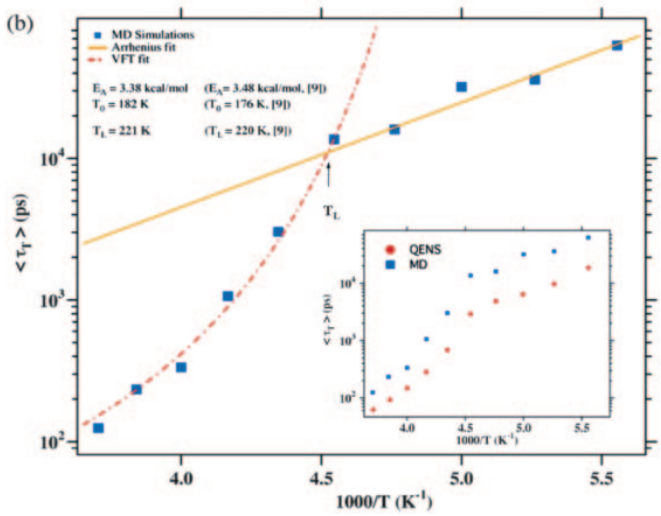

Fig. 63. – Temperature dependence of the average translational relaxation time, $\langle\tau_T\rangle$, from MD simulation; T_0 is the ideal glass transition temperature. Numerical data are fitted with a Vogel-Fulcher-Tammann (VFT) law at high temperatures and with an Arrhenius law at low temperatures (solid line) but with the same prefactor (see text for details). Inset: comparison between MD simulation and QENS data [202] the difference in the absolute scale is due to the different choices of the parameter a ($a_{\mathrm{MD}} = 1\,\text{Å}$, $a_{\mathrm{exp}} = 0.5\,\text{Å}$) in the equation relating $\tau_T(Q)$ and τ_0 in the fitting process [318].

as $\langle\tau_T\rangle = \tau_0\Gamma(1/\beta)/\beta$, where Γ is the gamma function and β is the stretch exponent. The absolute value of $\langle\tau_T\rangle$ is dependent on the value of the parameter a chosen to fit the quasi-elastic spectral line shape. Furthermore, even though $\langle\tau_T\rangle$ seems to exceed the length of the trajectories (50 ns) at low temperatures, it should be noted that the parameter extracted from the fitting procedure is τ_0, and this value is always within the limits of the simulations.

The crossover feature is clearly visible looking at the decay of the ISF below and above T_L. As for the inverse of the self-diffusion constant, the fragile part is fitted with a VFT expression, $\langle\tau_T\rangle = 5.0\exp[300/(T-182)]$, and the strong part with an Arrhenius equation, $\langle\tau_T\rangle = 5.0\exp[1704/T]$. The crossover temperature is determined to be $T_L = 221\,\text{K}$, very close to the experimental value of 220 K obtained in the neutron scattering experiments [202]. Considering the value obtained by the inverse of the self-diffusion fit, one can put the crossover at a temperature of $T_L(MD) = 223 \pm 2\,\text{K}$, while $T_L(\text{exp}) = 222 \pm 3\,\text{K}$, a remarkable agreement.

The inset reports the comparison between MD simulation and QENS data [202] the difference in the absolute scale is due to the different choices of the parameter a ($a_{\mathrm{MD}} = 1\,\text{Å}$, $a_{\mathrm{exp}} = 0.5\,\text{Å}$) in the equation relating $\tau_T(Q)$ and τ_0 in the fitting process. In summary, these results give demonstration by MD simulations that the low-temperature crossover phenomenon is due to the average translational motion of all the water molecules in the hydration layer; furthermore, by a simulation using a realistic powder model, one can quantitatively account for the temperature dependence of experimental data, both from NMR and from neutron scattering. The quality of the reported

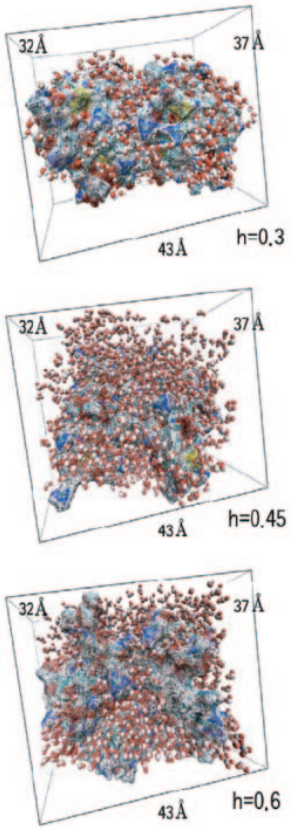

Fig. 64. – Snapshot from MD simulation at $T = 250\,\mathrm{K}$ of the hydrated lysozyme powder model at the three hydration levels: $h = 0.3$, 0.45, and 0.6. In the box are contained two lysozyme molecules and 484 water molecules around them [379].

results in the MD simulation of biological systems and their hydration water stimulated further studies and analysis in order to gain new information on bio-macromolecules, like the hydration level dependence of the dynamic crossover phenomenon and in particular how the relative amount of water that hydrates the protein powder affects its dynamics. For this the idea has been considered to focus the attention on different hydration levels by increasing it from the studied value of $h = 0.3$ to $h = 0.45$ (726 water molecules) and $h = 0.6$ (968 water molecules). In these cases, the simulation started from a random distribution of the water molecules in a box with the two proteins by equilibrating the systems in the NPT ($T = 280\,\mathrm{K}$, $P = 1\,\mathrm{bar}$) ensemble for several nanoseconds, until the edges of the box reached a constant length, then a 60 ns annealing simulation with a slow linear temperature ramp from 280 K to 190 K was ran (fig. 64).

Simulations at each temperature were then started from the equilibrated configuration of the annealing simulation. Each run lasted 50 more ns, and all the other details of the calculation are the same as in the $h = 0.3$ case. Figure 64 reports the snapshot of the

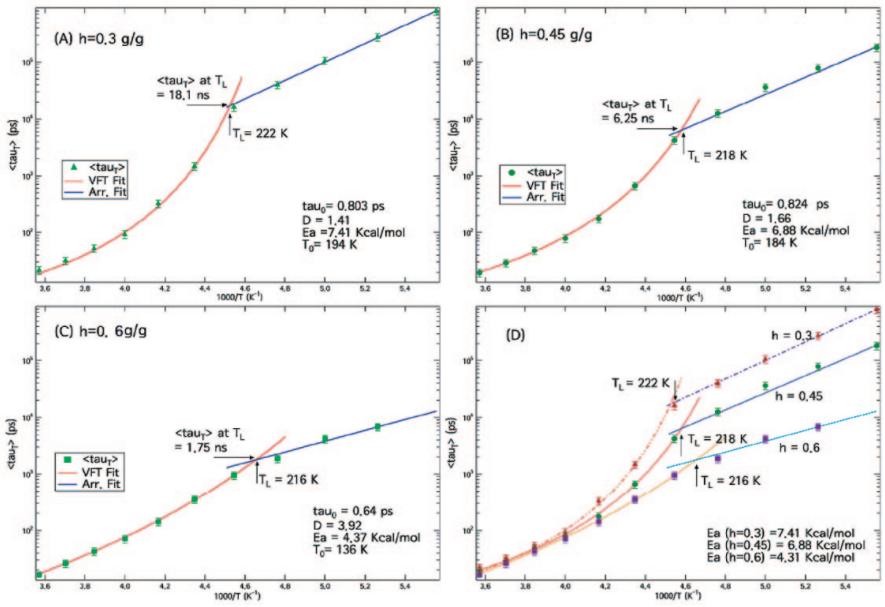

Fig. 65. – The hydration level dependence of the crossover temperature T_L for lysozyme hydration water. Note that, as the hydration level increases, the crossover temperature decreases and also the relaxation time $\langle \tau_T \rangle$ at $T_L(h)$ decreases [379].

simulation box of the 3 hydration levels considered; the picture gives evidence that when more and more solvent molecules are added, the water density becomes progressively more bulk-like. As previously said, the hydration level $h = 0.3$ corresponds to the average water coverage of the protein surface; thus when this parameter is increased, water is forced to keep its distance from the macromolecule. On this subject it has been shown [380] that the first hydration layer ($\sim 2\,\text{Å}$ from the protein surface) is about 15% more dense respect to bulk water, but that the normal density is recovered in the second hydration layer ($\sim 4.5\,\text{Å}$). Therefore, it is expected that going from the $h = 0.3$ to the $h = 0.6$ case, water properties would shift toward the bulk case. Such a situation has been confirmed by the behavior of the intermediate scattering functions (ISF); in fact from both the temperature and the Q-dependence at the hydration levels $h = 0.45$ and 0.6, one can see immediately that, as h increases, the dynamics is faster. This is in agreement with the view that water-water interactions are less strong than protein-water interactions, so that the bulk water limit corresponds to minimum relaxation times.

The panels of fig. 65, where the Arrhenius plot of the average τ is plotted as a function of the hydration level, confirm this statement.

Three situations, as h increases, are evident from this picture: i) average alpha-relaxation time decreases, ii) the crossover temperature T_L decreases, iii) the activation energy E_A of the Arrhenius part decreases. Both the first and the second point confirm the hypothesis that the bulk water case is a limit case. In fact, this study shows that a box of 512 TIP4P-Ew water molecules has $T_L = 215\,\text{K}$ ($T_L = 222$, 218, and 216 K for $h = 0.3$, 0.45, and 0.6, respectively). Such a result evidences that the protein-water

interactions shift the temperature dependence of water dynamics to higher T, and still the essential characteristics and phenomena present in hydration water are qualitatively preserved.

18. – The high-temperature (protein denaturation) dynamical crossover

As previously reported, lysozyme under thermal denaturation [276, 306, 336] exhibits intermediate structures (the same can be induced by pressure and chemical changes, see, *e.g.*, ref. [381]). Its unfolding process can therefore be considered as a three-state model $N \rightleftarrows I \longrightarrow U$. The first step is usually called reversible denaturation and can be seen as a kind of strong-to-fragile liquid transition associated with the configurational entropy change [382], while the second step is the irreversible denaturation and it is due to an association of unfolded lysozyme units [383].

In this section, we consider that this reversible denaturation may be related to the dynamic crossover that protein hydration water undergoes at $T_D \approx 345 \pm 5\,\mathrm{K}$. At this temperature, as showed by the previous reported NMR self-diffusion results [316], a sudden change in hydration water dynamics takes place, in fact the inverse diffusion constant switches from a super-Arrhenius behavior at low temperatures to an Arrhenius behavior at high temperatures. We have also reported as Neutrons (QENS) and NMR techniques can be properly used to study the protein hydration water as a function of the temperature, pressure and hydration level. The NMR measures the diffusion constant on a long time (ms) scale whereas the QENS measures cover a sub-nanosecond scale giving more accurate results from which other relevant data can be extracted like the atomic mean square displacement, MSD (fig. 66).

The existence of these crossovers can also be shown theoretically. In fact whenever the specific heat has a peak, the Arrhenius Plot of the inverse of the diffusion constant has a slope change. This can be seen with the well known Adam-Gibbs equation,

$$\frac{1}{D} = \frac{1}{D_0} = \exp(C/TS_{\mathrm{conf}}), \tag{55}$$

where $1/D_0$ is a prefactor, C a constant and S_{conf} represents the configurational entropy. If we assume that the Adam-Gibbs equation is valid also at high temperatures for hydration water, the specific heat peak observed by calorimetry during lysozyme thermal denaturation [276] agrees with the NMR data, *i.e.*, the existence of a high-temperature crossover phenomenon for the inverse of the diffusion constant [316]. This picture has been fully confirmed by the new interpretation of NMR data [306] for which a measure of the chemical shift δ gives the configurational specific heat. In particular, for the case of lysozyme (see fig. 43) it has been also found that the contribution of the configurational disorder to entropy is dominant, so $S_{\mathrm{conf}} \approx S$ and

$$S_{\mathrm{conf}}(T) \approx S_{\mathrm{conf}}(0) + \int_0^T \frac{C_p}{T}\mathrm{d}T, \tag{56}$$

a law that as has been found to be valid at low temperature in the supercooled region of water by MD computer simulations [384] and some experiments [385]. As a numerical example, the Arrhenius plot of the resulting $\ln D_0/D$ as obtained by substitution in the latter equation of C_p reported in [276] is shown in fig. 67. Both the plots of entropy and

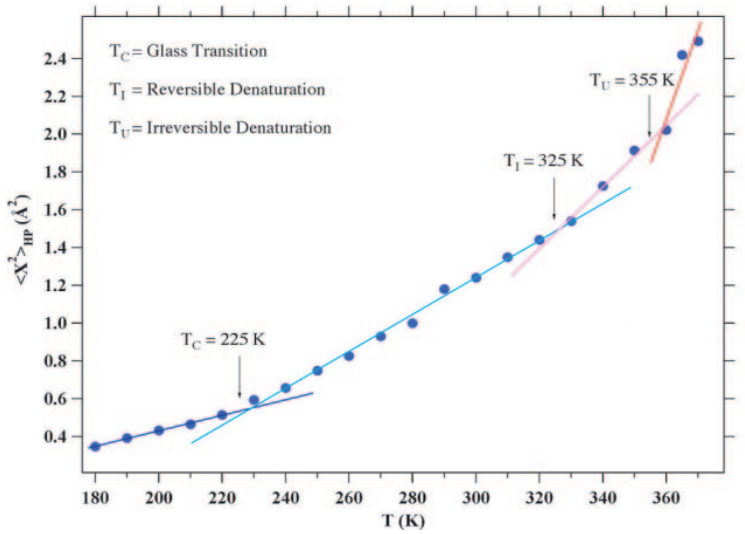

Fig. 66. – Mean square displacement $\langle X^2 \rangle_{HP}$ as a function of temperature for protein hydrogen atoms calculated from MD simulations after 500 ps [379].

$\ln D_0/D$ evidence a kink at 340 ± 5 K, corresponding approximately to the maximum in the configurational specific heat (see also fig. 43).

Here we discuss the inverse diffusion constant $1/D$ and the migration distance d of the hydration water molecules, extracted from QENS spectra. In addition we consider and compare with the corresponding QENS result, quantities calculated from MD simulations like: the $1/D$, the protein backbone root mean square displacement (RMSD), the hydrogen bond relaxation time τ_R and the protein hydrogen atom mean square displacement $\langle X^2 \rangle$. These quantities taken all together indicate that an abrupt change in the water-lysozyme hydrogen bonding occurs in the temperature interval between 330 K and 345 K, in the same T range found by calorimetric and Raman scattering measurements for the reversible conversion of $N \rightleftarrows I$ in lysozyme solutions.

To probe such a situation the experimental and MD methods used have been analogous to that regarding the low-temperature dynamic crossover taking place at the lowest temperatures regime ($T_L \approx 220$ K). There is however a special situation in the experimental approach (QENS experiments) that deserves some details reported in the following: in fact, for this experiment, in order to measure the diffusive motion of lysozyme hydration water from 290 K to 380 K for the first time the high-resolution (about 3.5 μeV, FWHM) backscattering spectrometer BASIS, at Spallation Neutron Source (SNS), the most intense pulsed neutron source in the world, was used. Specifically, BASIS is well suited for probing diffusive and relaxational motions but can also be effectively used for studying some types of collective excitations in condensed matter, such as boson peak. In the quasi-elastic regime of operation, BASIS can be used to probe dynamic processes on the picosecond to nanosecond time scale.

BASIS is an inverse geometry time-of-flight backscattering spectrometer that uses near-backscattering neutron reflections from Si(111) analyzer crystals to select the final

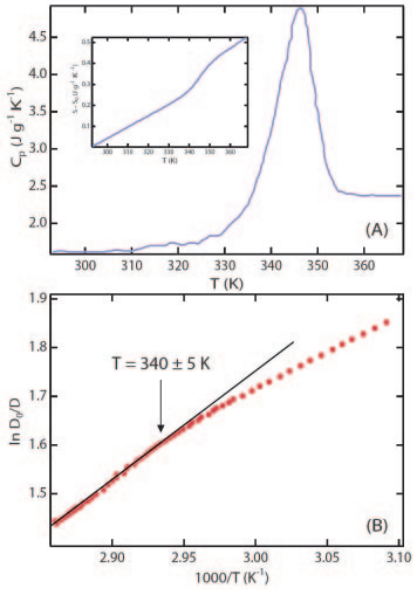

Fig. 67. – (A) Specific heat measurement of lysozyme solution from ref. [276]. Inset: entropy as a function of temperature calculated from integration of the experimental C_P from 290 K to 370 K. (B) Arrhenius plot of $\ln D_0/D$ *vs.* $1000/T$ calculated according to the Adam-Gibbs equation, see text for details. D_0 is the prefactor in the Adam-Gibbs equation, S_0 is S (290 K). As a numerical example, $S_0 = 1\,\mathrm{J/gK}$ and $C = 700\,\mathrm{J/g}$ are chosen. This equation predicts a change in the slope for the inverse of the diffusion constant at $\approx 340 \pm 5\,\mathrm{K}$. Figure adapted from [381].

energy of neutron of 2.08 meV (6.267 Å). The silicon analyzer crystals cover approximately 2.0 ster (16% of 4π). Neutrons are scattered by a sample illuminated by a polychromatic neutron beam, the bandwidth of which is defined by a set of neutron choppers. The dynamic range of the experiment can be adjusted by operating the choppers at either 60 Hz or a lower frequency. In this study, the choppers have operated at 30 Hz (matching the current accelerator frequency). A dynamic range $-200\,\mu\mathrm{eV} < E < +200\,\mu\mathrm{eV}$ has been selected; it was free of excessive signal contamination that resulted from the instrument background, which was not yet fully optimized at the time of the experiment. When the experiment was carried out, the proton accelerator beam power on the mercury target was stabilized around 160 kW, which is only 10% of the designed power of 1.4 MW.

In the experiment, both an H_2O hydrated and a D_2O hydrated lysozyme sample were considered. By subtracting the two spectra with correct mass and transmission ratios it was possible to obtain spectra with the contribution from hydration water only. (Note: BASIS can not measure the transmission of neutrons. However, its transmission was estimated by means of a separate experiment done with DCS (Disk Chopper Spectrometer) at NCNR (NIST Center for Neutron Research).) An example of the spectra before the subtraction is shown in fig. 68. Because of the very large incoherent cross-section of hydrogen atom, neutrons are predominantly scattered by an incoherent process from the

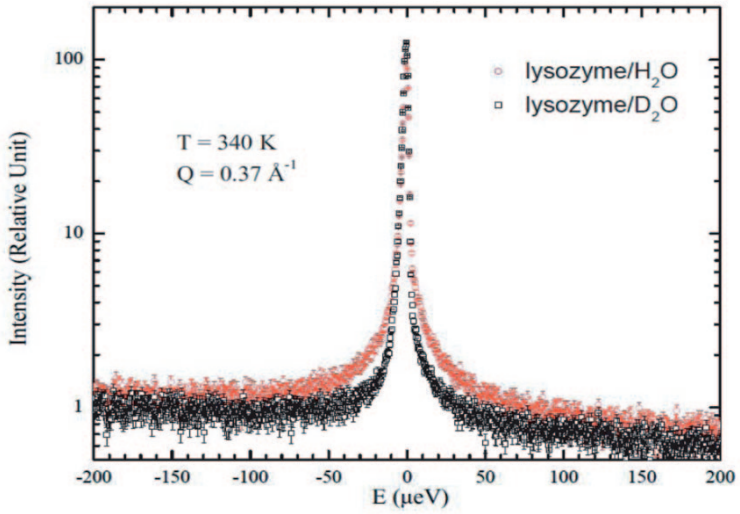

Fig. 68. – Typical spectra of hydrated lysozyme (H_2O and D_2O), obtained before the subtraction procedure from which one can obtain, by using the corresponding mass and transmission ratios, the contribution from hydration water only [381].

hydrogen atoms of water, rather than by the coherent scattering process from the oxygen atoms. In comparison, the scattering cross section from D_2O is much smaller than that from H_2O and contains both coherent and incoherent components. The dynamics of water in the temperature range from 290 K to 380 K, covering the protein denaturation process, spans from 5 μeV to 25 μeV in terms of half width at half maximum (HWHM). So BASIS is the only ideal tool to study the wide range of dynamics of the protein hydration water in the high temperature range with good resolution. The vanadium standard was measured for normalization of the detectors efficiency.

In this case QENS experiments essentially provide the incoherent dynamic structure factor $S_H(Q, E)$ of the hydrogen atoms of the water molecules in the protein hydration layer. The measured neutron intensity at each Q is analyzed with the following model:

$$I(Q, E) = A\,[p(Q)\delta(E) + (1 - p(Q))S_H(Q, E)] \otimes R(Q, E) - \mathrm{BG}, \tag{57}$$

where A is the normalization factor, $p(Q)$ is the elastic scattering component, taking into account the scattering from particles that do not move a length comparable to $2\pi/Q$ on the time scale corresponding to the spectrometer's elastic energy resolution function (1.351–1.78 μeV in terms of HWHM from the lowest $Q = 0.37\,\text{Å}^{-1}$ to the highest $Q = 1.94\,\text{Å}^{-1}$) and $R(Q, E)$ is the Q-dependent energy resolution function. BG is the nonlinear background processed by means of a power law term $\mathrm{BG} = \mathrm{const} \cdot (E + E_0)^{-1.5}$ where E_0 is the incident neutron energy 2.08 meV. In addition, being the resolution function $R(Q, E)$ of BASIS asymmetric, a sum of Gaussian function was used to represent it. A resolution function which is broader on the negative energy transfer side is fully expected at a spallation-source-based spectrometer such as BASIS, the fast rise and the slow decay reflect the pulse shape of the neutron moderator.

Generally, see *e.g.* sect. **8**˙3, the incoherent dynamic structure factor is a convolution of the translational dynamic structure factor, $S_T(Q,E)$, and the rotational one, $S_R(Q,E)$: $S_H(Q,E) = S_T(Q,E) \otimes S_R(Q,E)$. In addition, for small-Q spectra, $Q < 1\,\text{Å}^{-1}$ the rotational contribution can be made negligibly small [378], hence the incoherent dynamic structure factor of hydrogen atoms in hydration water is approximated by $S_T(Q,E)$. Hence, according to the previous discussions, the self-intermediate scattering function $F_H(Q,t)$ can be calculated as the Fourier transform of the incoherent dynamic structure factor $S_H(Q,E)$, where its long time decay is more like a stretched exponential $F_H(Q,t) = \exp[-\Gamma(Q)t]^{\beta}$. When the temperature is above the room temperature, the stretched exponent β is only slightly less than unity for low-Q spectra. A situation for which the exponential form $F_H(Q,t) \approx \exp(-\Gamma(Q)t)$ can be approximately used, or equivalently, in frequency domain the incoherent dynamics structure factor of water is approximated as a Lorentzian shape function [386],

$$S_H(Q,E) \approx S_T(Q,E) = \frac{1}{\pi}\frac{\Gamma(Q)}{E^2 + \Gamma(Q)}\,, \tag{58}$$

where $\Gamma(Q)$ is the half width at half maximum (HWHM). Its validity can also be confirmed by the good agreement between the experimental data and the fitted curve with the model for all temperatures and wave vector transfers. In the $Q \to 0$ limit, it is well known that $\Gamma(Q) = DQ^2$, where D is again the translational self-diffusion constant of water molecules. Thus for the finite, but small Q, we may take into account the next order correction to the Q^2 dependence as

$$\Gamma(Q) = DQ^2(1 - \xi^2 Q^2 + L) = \frac{DQ^2}{1 + \xi^2 Q^2}\,. \tag{59}$$

This latter equation is indeed independent of any model in the low-Q limit and represents very good approximation to extract D from low-Q spectra. In fact, the often used jump diffusion model is equivalent to putting $\xi^2 = D\tau_0$, where τ_0 is the average time duration that a water molecule spends oscillating in a cage forming by its nearest neighbors [386]. On the other hand, in the so-called Singwi-Sjölander model of water [387], the motion of a typical water molecule is described as: first trapping in a cage oscillating for a period τ_0, following by a diffusion of a duration τ_1, and this pattern of motion repeats itself. The HWHM in this model is given by (in the short diffusion time τ_1 limit)

$$\Gamma(Q) = \frac{1}{\tau_0}\left[1 - \frac{\exp(-2W)}{1 + DQ^2\tau_0}\right], \tag{60}$$

where the exponential form represents again the Debye-Waller factor (see eq. (47)) directly related with the MSD $\langle x^2 \rangle$ that in this case represents the mean square vibrational amplitude along the direction of Q. Being, as previously determined [378, 386], $\langle x^2 \rangle \approx (0.5)^2\,\text{Å}^2$ the Debye-Waller factor will approximately equal to unity for $Q < 1\,\text{Å}^{-1}$, a limit for which the two latter equations are identical with $\xi^2 = D\tau_0$.

In the case of protein hydration water, the realistic picture of the motions of the water molecules is describable neither by the jump diffusion model nor by the Singwi-Sjölander model. In the dense liquid state near the room temperature, a water molecule is first trapped in a site for a time interval τ_0, on the order of 0.1 ps, oscillating in a cage formed by adjacent water molecules connecting by hydrogen bonds. The hydrogen bonds are

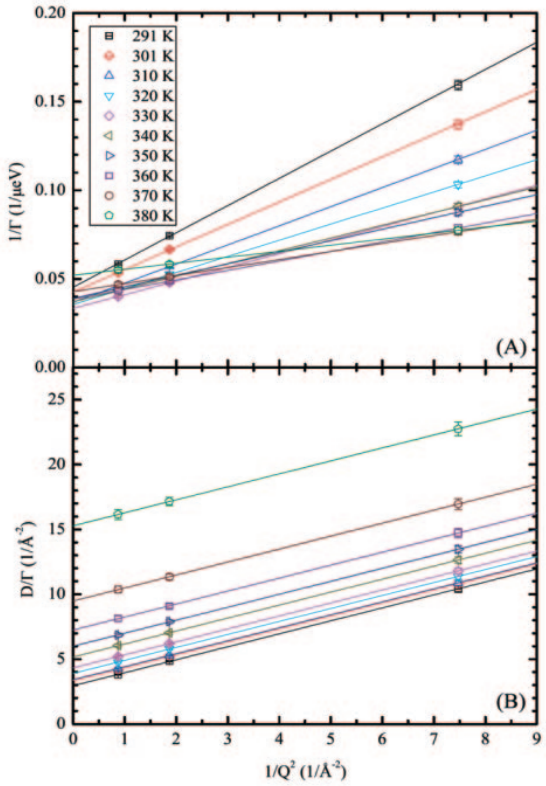

Fig. 69. – The plots of $1/\Gamma$ *vs.* $1/Q^2$ (panel A) and of D/Γ *vs.* $1/Q^2$ (panel B) for measured temperatures from 291 to 380 K at low $Q = 0.37$, 0.73, 1.07 Å^{-1}. The solid lines are the fitting results. The slopes of the straight lines in panel A give the inverse diffusion constant $1/D$, whereas the zero intercepts in panel B give ξ^2. Figure adapted from [381].

continuously breaking and reforming. After the time τ_0, the cage gradually relaxes, and then the water molecule starts to move away from the trapped site for a time interval τ_1, until it gets trapped again in a new site. However, the cage relaxation time τ_1 is not necessarily much less than τ_0. It depends on the temperature of water and can be, as observed in the many cases of confined water here presented, on the order of ps to ns at low temperatures.

Therefore D can be easily extracted if eq. (59) is written as $1/\Gamma(Q) = (1/D)((1/Q^2) + \xi^2)$, and plotting $1/\Gamma$ *vs.* $1/Q^2$; the result is a linear equation with a slope $1/D$ (see, *e.g.*, fig. 69).

On the other hand, after extracting D in this way, one can then plot D/Γ *vs.* $1/Q^2$. The result is a set of parallel straight lines with a zero intercept ξ^2 that can thus be extracted with tolerable accuracy. So, one can finally calculate the characteristic migration distance between successive traps of water molecules using ξ^2 as

$$d = \sqrt{\langle l^2 \rangle} = \sqrt{6\xi^2}. \tag{61}$$

It is a measure of the average distance that a water molecule travels between two successive traps. While the self-diffusion constant D represents how fast a molecule diffuses, the migration distance d represents how far the center of mass of a typical molecule translates in the cage relaxation process, before it gets trapped again.

Following the protein powder model discussed for the low temperature crossover, lysozyme molecules (Protein Data Bank file 1AKI.pdb) randomly oriented are put in a box two OPLSAA29 and 484 TIP4P-Ew water molecule, so that is $h = 0.3$ for each protein. Eight chloride ions for each protein were added to neutralize the system composed of 5872 atoms. The Lennard-Jones interactions were truncated beyond 1.4 nm, while electrostatic interactions, calculated with the Particle Mesh Ewald method were truncated at 0.9 nm. Three-dimensional periodic boundary conditions were applied and the equations of motions were integrated using the Verlet leap-frog algorithm with a 2 fs time step. All bonds were constrained at their equilibrium values using the LINear Constraint Solver algorithm (LINCS). After an energy minimization of 5000 steps with the Steepest Descent algorithm, the system was equilibrated in a NPT ensemble (isobaric-isothermal) for 10 ns at 300 K. Nine simulations were performed at different temperatures (from 290 K to 370 K, with 10 K intervals) with a parallel-compiled version of GROMACS33. Simulations were performed using a triclinic cell (box size $\sim 43 \times 37 \times 32$ Å) and each MD simulation length was 50 ns after the equilibration time. After that the hydrogen bond correlation function was calculated according to $c(t) = \langle h(0)h(t)\rangle / \langle h(t)\rangle$ where $h(t) = 1$ if the hydrogen bond exists and $h(t) = 0$ otherwise. From the decay of this correlation function one can calculate the hydrogen bond relaxation time τ_R, as the $1/e$ value of $c(t)$ [388].

The proposed model was thus used to analyze measured QENS spectra of the protein hydration water for temperatures ranging from 290 K to 380 K, covering the first stage of the denaturation process, occurring at the reversible protein denaturation temperature around 345 K. Jointly a MD simulation study was also developed for the same process, the main obtained results are exposed in the following.

Figure 69 shows the plot of $1/\Gamma$ *vs.* $1/Q^2$ extracted from spectra taken at all the temperatures (A). It displays clearly a series of straight lines. The slopes of these lines are, obviously, the inverse diffusion constants $1/D$. Using this way, the slopes of the straight lines are extracted accurately (see the error bars in fig. 70). However, the uncertainties of the intercepts are too large to show any useful information. In the same figure (B) the plots of $D/\Gamma(Q)$ *vs.* $1/Q^2$ are reported. In this case there is a series of parallel straight lines, the zero intercepts of which give ξ^2. In this way, the fitting of the original intercepts are bypassed and new intercepts ξ^2 within tolerable uncertainties are obtained.

Figure 70 shows the Arrhenius plot of the extracted $1/D$ *vs.* $1/T$ and d *vs.* T. Figure 70A shows an evidence of an Arrhenius to super-Arrhenius dynamic crossover as the temperature is raised across $T_D = 345 \pm 5$ K. Below T_D, the inverse diffusion constant can be fitted with the Vogel-Fucher-Tamman Law as $1/D = 1/D_0 \exp[CT_0/(T - T_0)]$ with $T_0 = 204 \pm 36$ K and $C = 0.94$. While above T_D, the inverse diffusion constant can be fitted with the Arrhenius Law $1/D = 1/D_0 \exp(E_A/RT)$ with $E_A = 5.97 \pm 0.55$ kcal/mol, which corresponds to about an energy needed to break 2.4 hydrogen bonds at T_D [389]. The exact value of T_D was then evaluated as the crossing point of the two laws. Figure 70B shows the extracted d, *i.e.* the migration distance of the water molecules between two successive trap sites. One can see that it is increasing slowly below T_D, from 4.2 to 5.6 Å, but rises sharply above T_D to 9.6 Å at 380 K. The result is consistent with the literature results 6–9 Å at room temperature. The sharp changes of both the self-diffusion

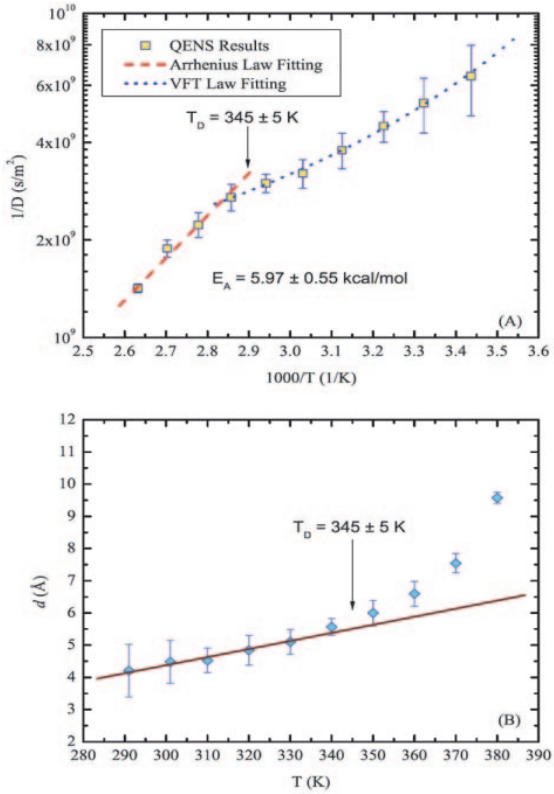

Fig. 70. – The Arrhenius plot of experimentally extracted $1/D$ *vs.* $1000/T$ of the protein hydration water shows an evidence of a super-Arrhenius nonlinear behavior to Arrhenius linear behavior dynamic crossover as the temperature is raised through $T_D = 345 \pm 5\,\mathrm{K}$ (panel A). Plot of experimentally extracted average migration distance d of the hydration water (panel B). This quantity is slowly increasing linearly within experimental error bars below T_D but rises sharply above T_D, indicating a longer migration of water molecules in between two successive trap sites. Figure adapted from [381].

constant D and the migration distance d indicate a large-scale enhanced movement of the water molecules above the crossover temperature T_D, when the lifetime of the HB network of the water molecules becomes shorter, and thus it is not able to maintain the shape of the protein.

The following MD simulation results together with the confirmation of this dynamic crossover give evidence that the dynamic crossover in protein hydration water is probably connected to the first stage of the unfolding process of the protein. The protein backbone root of mean square displacement (RMSD) calculated from the trajectories shows a sudden increase between 330 K and 340 K (fig. 71), signaling the beginning of the denaturation process.

Molecular Dynamics simulations are limited to a time-step on the order of fs, while protein unfolding occurs on timescales of the order of ms. In that cases, atomistic simu-

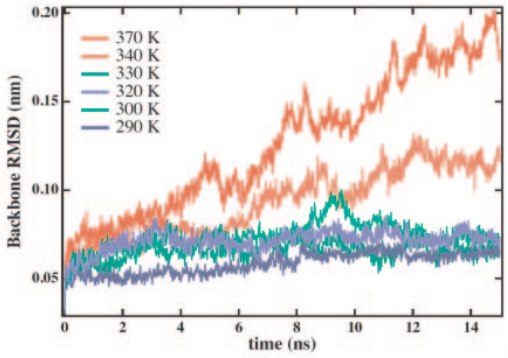

Fig. 71. – Comparison of the backbone RMSD as a function of time at different T. This quantity was calculated for the last 15 ns of the trajectories and averaged over the two lysozyme molecules. No remarkable change is detected until 340 K when the protein increases its flexibility [381].

lations of the whole denaturation process are still utopian for the conventional computers capabilities, nevertheless, a few ns are enough to capture at least its dynamic beginning. At the same temperature, the Arrhenius plot of $1/D$ (fig. 72) obtained from the MD simulation shows a change in its behavior at $T_D = 340 \pm 5$ K, reproducing well the neutron scattering data and qualitatively the Adam-Gibbs equation.

In particular, the extracted activation energy $E_A = 5.25 \pm 0.5$ kcal/mol is in agreement with the experimental value ($E_A = 5.97 \pm 0.55$ kcal/mol). The underlying physical mechanism for lysozyme reversible denaturation can be seen from the examination of the following three physical quantities calculated from the MD simulations. Figure 73A

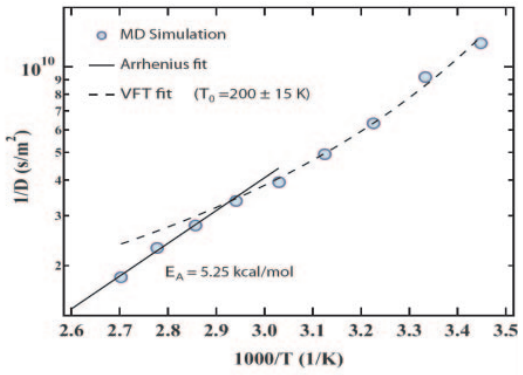

Fig. 72. – Arrhenius plot of the inverse diffusion constant for lysozyme hydration water, calculated from MD simulations. The curve shows an Arrhenius high T to super-Arrhenius low T dynamic crossover similar to the one observed by quasi-elastic neutron scattering (fig. 70). The D values were obtained from the trajectories according to the Einstein relation with a linear fit of water MSD from 300 to 600 ps. Numerical data are fitted with a VFT law at low temperatures (dashed line) and with an Arrhenius law at high temperatures (solid line) [381].

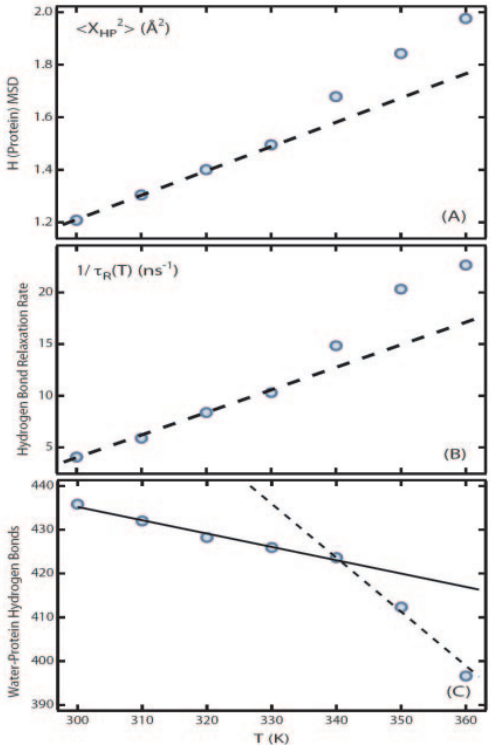

Fig. 73. – Protein hydrogen atom mean square displacement calculated from MD simulations after 500 ps and averaging over the time origins for the last 10 ns of each simulation (panel A). Inverse hydrogen bond relaxation time calculated from the $1/e$ value of the corresponding time correlation function (panel B). Only the hydrogen bonds (HB) between water molecules and protein were considered. Number of HBs between water molecules and protein as a function of temperature calculated averaging over the last 10 ns of the trajectories ($r_{\rm cut} = 0.35$ nm, $\theta_{\rm cut} = 30^\circ$) (Panel C). Figure adapted from [381].

displays the onset temperature of the reversible denaturation, T_D: the protein hydrogen atoms MSD has a sharp increase as a function of temperature between 330 K and 340 K, in agreement with the onset temperature for reversible denaturation determined by calorimetry [276].

Figure 73B shows that at the same temperature T_D, the inverse of the water-protein hydrogen bond relaxation time (relaxation rate) deviates from linearity, signaling the beginning of the breakdown of the hydrogen bond network around the protein. The increase in the hydrogen bond relaxation rate is therefore the cause of the enhanced protein flexibility, as already pointed out by Wood *et al.* [390] for the low-temperature protein dynamical transition. In that case, they found a correlation between the decrease of protein H-bond network relaxation time (due to the onset of water translational diffusion) and the sudden increase in the protein hydrogen atoms MSD at $T_L = 220$ K. The situation is qualitatively analogous for the high-temperature case, but with a quantitative difference: the solvent cage is not able to constrain the folded protein structure

anymore and the macromolecule increases its ability of sampling the configurational space. Due to the decrease of the hydrogen bond lifetime, its flexibility becomes large enough to start the unfolding process. Figure 73C shows that as T further increases, the number of hydrogen bonds between water and the protein has a sharp change in its rate of decrease at $T_D = 340\,\mathrm{K}$, from 0.3 to 1.2 HBs/K. That is to say, the dynamics of interfacial water and its interactions with the protein surface are critical for the stability of protein structure. As soon as the strength of HBs at the interface between water and protein reaches a certain value, the 2-d network around the protein that kept it folded collapses, allowing the macromolecule to increase its flexibility and to begin the denaturation process. We believe that the crossover phenomenon is a characteristic of the whole water-protein system: the decreased interaction at the water-protein interface is the cause of both the crossover and the denaturation. On one hand, water becomes more mobile (increased diffusion constant); on the other, protein is not constrained by the hydrogen bond network and can unfold.

In concluding this section, it is important to stress that the combination of both the low-Q QENS data and MD simulations allows us to understand on a molecular basis the onset of the reversible folding and the successive irreversible denaturation. In particular, by considering these results and the cited NMR and FTIR experimental data [306, 316] it is possible to conclude that the denaturation of the protein and the dynamic crossover in its hydration water are causally related. In fact, all of their coincidences suggest that this high-temperature dynamic crossover could be a significant factor in the reversible denaturation process. We also note that the organization of water/biomolecules constitutes an extremely important research field that, in the near future, may prove to be the key that allows statistical physics to play a central role in the rapidly expanding field of molecular biology.

19. – Concluding remarks

We have surveyed a wide range of research on confined water. We have examined both experimental and theoretical studies, and have highlighted recent discoveries that strongly indicate that confined water will soon enable us to effective examine the No Man's Land below the supercooled region. The most important results indicate i) the existence of a dynamical crossover FSC at a precise temperature, ii) the existence of the Widom line $T_{\mathrm{W}}(p)$, iii) the breakdown of the Stokes-Einstein relation (BSE) for $T < T_{\mathrm{W}}(p)$ [199, 327, 391-394], iv) the coincidence that the FSC singularity with the BSE at the same T_{W} gives support to the LLPT theory that liquid water consists of a mixture of two differing local liquid structures (the LDL and HDL phases), v) that there are systematic changes in the static structure factor $S(q)$ and the corresponding pair correlation function $g(r)$ which reveal that for $T < T_{\mathrm{W}}(p)$ the system resembles more the structure of LDL than HDL, vi) the appearance for $T < T_{\mathrm{W}}(p)$ of a shoulder in the dynamic structure factor $S(q, \omega)$ at a frequency $\omega \approx 60\,\mathrm{cm}^{-1} \approx 2\,\mathrm{THz}$ [202, 206], vii) the rapid increase in the degree of hydrogen bonding for $T < T_{\mathrm{W}}(p)$ [197,203], viii) a *minimum* in the density at low temperature [204,240], ix) a scaled equation of state near the critical point [205], and x) a clear maximum in the coefficient of thermal expansion at $T_{\mathrm{W}} \approx 225\,\mathrm{K}$ [240, 306, 223], which remarkably is the same temperature as the specific heat maxima, measured with conventional calorimetry [292], and by NMR [306]. It is possible that the phenomena that appear to occur on crossing the Widom line are in fact not coincidences, but are related to the changes in local structure that occur when the system changes from the "HDL-like" side to the "LDL-like" side. In this work we have

reviewed the evidence for changes in such dynamic transport properties as the diffusion constant and the relaxation time. Because these phenomena are evident only in confined water and cannot be explored in bulk water, it is possible that the physics of bulk water will differ significantly.

Of paramount importance are the two crossover phenomena observed in protein hydration water, which, on the basis of the many results we have described, can be considered responsible for the biological activity of macromolecules, including RNA and DNA (see, *e.g.*, [337]). neutron measurements of the MSD indicate, surprisingly, that the crossover temperature of biopolymer and its hydration water are closely synchronized. More precisely, FTIR experiments [316] indicate that when a biosystem restores its dynamics, the solvent crosses from a strong to a fragile liquid, *i.e.*, the HB networking changes from a thermal state in which LDL dominates to one in which HDL dominates (see, *e.g.*, fig. 46). At the same time, irreversible denaturation takes place when the HB numbers decrease to values for which only a few water molecules are bonded.

Some of these results have received criticism. For example, the analysis of the neutron data that indicates the existence of a density minimum [395-399] suggests that water, when confined in small enough cavities, cannot be considered a homogeneous fluid, and its local density can depend on the interaction and distance from the surface of the confining structure. More precisely, depending on the degree of hydrophilicity of the substrate, void regions may show up, either within the fluid (cohesive failure), or at the water-substrate interface (adhesive failure) [398]. The corresponding density fluctuations are reflected, and thus observable, in the shape of the density profiles across the pore radius. In such a situation, however, average quantities, such as density and any other function defined by an integral over the fluid volume, will be ill-defined, when void regions are present. These quantities describe indeed an "average fluid" which is only a very crude approximation of the real material.

In response to the idea that density profiles can provide a reliable description of water molecule arrangement within a pore, a different interpretation of the neutron spectra has been recently presented [399]. A more detailed analysis of the structure of the system may be obtained by performing a shell analysis of the structural quantities, choosing, *e.g.*, a cylindrical shell geometry, with the requirement that the density profile must be considered nearly constant within the shell thickness. This analysis is possible provided that, in order to collect molecular configurations compatible with experimental data, data at long- and intermediate-Q range are used in the atomistic simulation.

In one example of this, a neutron diffraction experiment that exploits the H/D isotopic substitution method on all exchangeable hydrogens of water confined in MCM-41-S-15 was conducted at four temperatures: 300 K, 240 K, 210 K, and 170 K. The experiment was performed at the SANDALS time of flight diffractometer at the ISIS spallation neutron source by covering a range of momentum transfer Q from 0.05 to 30 Å^{-1} [399].

From the obtained spectra it has been observed that when water is deeply supercooled, the intensity of the Bragg peak goes through a minimum at about $T = 210$ K, suggesting that the characteristic length scale of the density fluctuations is minimal at this temperature [204].

From this analysis, we see that Radial Distribution Functions (RDF) of the individual layers strongly differ from each other and have different thermal behaviors. At ambient temperature, the intensity of the first peak of the oxygen-oxygen RDF shows marked ongoing changes from the center of the pore towards the substrate, and for the layer closest to the pore surface a second peak can hardly be identified. These huge differences decrease on supercooling to 210 K, where they reach their minimum, while differences of

intensity and position of the peaks increase again at 170 K. At ambient conditions the first peak of the oxygen-hydrogen RDF, which is known as the hydrogen-bond peak, is extremely weak, while the second peak develops a double structure for the layers closer to the confining substrate. The T-evolution of these RDFs is characterized by changes in the intensity of the HB peak and in the relative intensity of the double structure of the second peak. The changes in the structure of the shells closer to the substrate (external water layers) can be ascribed to the temperature dependence of the interaction with the substrate, but we note that the coordination between first neighbors is strongly affected by temperature irrespective of distance from the walls. Significant changes in the orientational order have been observed by monitoring the distribution functions of the angle formed by the lines joining the oxygen atom of a given water molecule and those of its nearest neighbors, $P(\theta)$, and in the quantity defined as the orientational order parameter, q [150]. Thus, although the temperature behavior of the intensity of the measured density profiles seems consistent with the previous Neutron experiment, which proposes the existence of a water density minimum at 210 K, the main findings reported in this study contradict such a result. In particular:

i) In contrast to bulk water, confined water appears to be a non-homogeneous fluid characterized by a multitude of intricate structures dependent upon pore size and surface morphology. When cooled, these structures do not evolve towards a less dense, more ordered state at 210 K as suggested by [204].

ii) The radial distribution functions of the local geometry of confined water differ from those of bulk water. The tetrahedral order parameter q in confined water is generally lower at all temperatures than in bulk water, and even more so near the interface. At temperatures near 210 K, the structure undergoes a turning point —the density distribution appears most uniform at this temperature, and all water shells exhibit a similar structure. This change is associated with a movement of the main liquid diffraction peak to a position coincident with that found in both low-density amorphous ice (LDA) and crystalline ice I_h. In addition to the existence of this water density minimum, this latter result lends support to the dynamic crossover observed at T_L, although the temperature of 210 K is some degrees away from T_L. We hypothesize that such a structural turning point results from dynamical heterogeneities governing system behavior, especially in the supercooled regime. A structural analysis reveals this because the progressive freezing of the HB dynamics on decreasing temperature (the HB relaxation time τ increases by approximately six orders of magnitude, starting with picosecond measurements at ambient temperature, and extending down into the deep supercooled region).

It has recently been suggested that the dynamical crossover observed near T_L is a phenomenon caused by the constraint effects of the finite-sized confining materials [400]. This means there is no crossover process due to the thermal evolution of water from fragile-to-strong glass forming material, *i.e.*, the FSC. This hypothesis emerged from observations of the viscosity changes in glass forming materials (which agrees with the mode coupling theory approach in which the density-density ISF is characterized by a two-step α and β relaxation) [400]. The relaxation behavior of deeply supercooled liquids is typically described using the viscosity-related main α relaxation and one or several secondary β relaxation processes. The relaxation time τ_α of the α process shows some degree of super-Arrhenius temperature dependence (VFT-like), whereas β processes tend to follow the Arrhenius law. This anomalous crossover can be ascribed to the disappearance of strongly cooperative relaxation. This can be explained by noting that the viscosity-related main (α) relaxation of confined water vanishes at the temperature at which the volume required for cooperative relaxation becomes larger than the size of

the geometrically confined water cluster. This typically occurs around T_L, implying that above this temperature one may observe a merged α-β relaxation, whereas below it only a local (β) relaxation remains. Note that this does not mean that a real fragile-to-strong transition cannot occur in bulk water or bulk-like water where the α relaxation is actually observed in the deeply supercooled regime.

Studies of the T-dependences of structural relaxation times obtained from performing dielectric spectroscopy and quasi-elastic neutron scattering (QENS) on many different materials have assumed that the "normal" temperature dependence of the relaxation time of a liquid will closely resemble that of propylene glycol (PG) in the sense that both bulk and confined PG relax in the same way, and with an apparent continuity. This exhibits a thermal behavior of the main relaxation time that differs completely from that proposed for bulk and confined water. Confined water relaxation times appear substantially altered when compared to bulk water (which evidently is not the case in confined PG), but also shows an apparent fragile-to-strong transition. In addition, an even more dramatic change in the T-dependence of water confined in nanoporous MCM-41 is clearly evident. These results are not unique in that they simply exhibit the typical behavior of supercooled water in biological materials and other confinements. Hence, to take into account such a situation, bulk and confined ethylene glycol (EG) have been studied in detail. Figure 74 reports all the EG dielectric relaxation times studied. The bulk data come from two different experiments [400, 401] whereas all the confined EG results come from experiments by Huwe *et al.* [401] that report different confining geometries: sodalite (0.28 nm), silicalite (0.56×0.53 nm) and H-ZSM-5 (0.55×0.51 nm) pores, zeolite beta a $3d$ network (0.76×0.74 nm) and $AlPO_4$-5 a nanotube with a diameter of 0.73 nm.

Figure 74 clearly shows a crossover between two thermal behaviors in both bulk EG and for EG confined in the zeolite beta $3d$ network and $AlPO_4$-5 nanotubes, whereas a "strong" (*i.e.*, Arrhenius) behavior results from severe confinement, *i.e.*, when the alcohol is trapped in cages with a pore diameter less than 0.6 nm, at all temperatures studied. Note that the relaxation times for EG in sodalite are significantly slower than those in silicalite or H-ZSM-5. As previously mentioned, the thermodynamical behavior of supercooled liquids is typically characterized by two relaxations: i) a local relaxation (covering the short time regime of single molecule dynamics), and ii) a cooperative relaxation (covering many temporal orders of magnitude). In the cooperative relaxation, the corresponding density fluctuations are due to a certain number of molecules interacting on a characteristic length scale ξ that is larger than the characteristic molecular size a_0. When the liquid is severely confined, *i.e.*, when the confinement geometry l is $l \ll \xi$, a size so small it approaches the dimension of a molecule (is trapped in a "cage" of only a few molecules or even one molecule), only local relaxation survives. Keeping this in mind and considering only the τ data behavior of bulk EG and EG confined in silicalite and H-ZSM-5 (*i.e.*, the very severe confinement shown in fig. 74), it has been proposed that the crossover observed in supercooled confined water is only an apparent FSC, and that in reality it is due to a merged α-β relaxation at high temperature and is a pure β relaxation below the apparent transition.

Furthermore, after a series of proper considerations regarding the physics of water (in bulk and confined), such as the estimation of T_g, the authors of this study draw the following conclusions: i) in contrast to other liquids in similar confinements, confined supercooled water does not exhibit a true glass transition, and ii) this implies that deeply supercooled water in such biological systems as membranes and proteins usually exhibits only a local β relaxation. This is an important finding that alters our understanding of the low-temperature properties of biological materials.

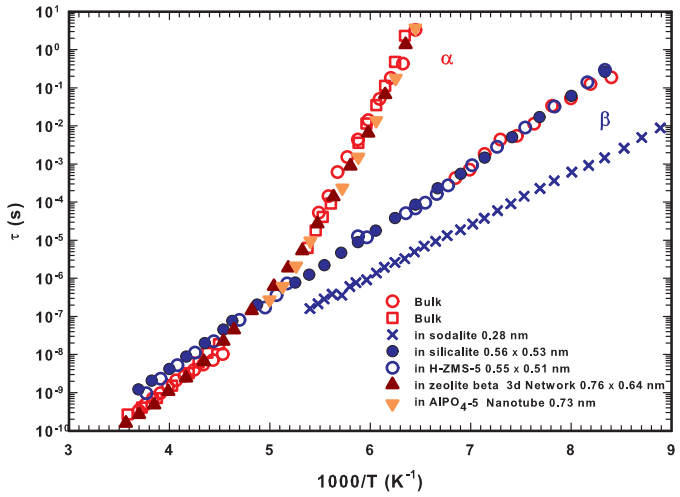

Fig. 74. – The ethylene glycol (EG), bulk and confined, dielectric relaxation times (τ) measured as a function of the temperature (and reported *vs.* $1000/T$ in a log-linear scale). Bulk EG data comes out from two different experiments [400, 401] whereas data for confined EG considers different confining geometries: sodalite (0.28 nm), silicalite (0.56×0.53 nm), H-ZSM-5 (0.55×0.51 nm), zeolite beta 3d network (0.76×0.74 nm) and $AlPO_4$-5 nanotube with a diameter of 0.73 nm [401]. The α relaxation is present both in bulk EG and in the EG confined in the network and in the nanotube. The β relaxation can be observed in the bulk for very low temperatures $T < 150$ K [400] and in EG in a very severe confinement at all the explored temperatures, *i.e.*, when the alcohol is trapped in cages with a pore diameter of about 0.55 nm.

Although we consider this approach interesting, we pursue some different considerations concerning crossover. First, fig. 74 clearly shows that the α relaxation is present in bulk EG as well as in EG confined in a zeolite beta 3d network and a $AlPO_4$-5 nanotube, at all temperatures studied. Second, these $\tau(T)$ data clearly indicate a well-defined crossover at ≈ 200 K. This invites a comparison among the EG molecules confined in the $AlPO_4$-5 nanotube and water confined in MCM-41. The EG ($OHCH_2CH_2OH$) molecules can interact with each other in the same way as water (*i.e.*, via the HB). The EG molecular size is $a_0 \sim 5.5$ Å, which is more than double that of water. Therefore, as reported in fig. 74, if the EG confined in a nanotube with a pore diameter 0.73 nm (the $AlPO_4$-5 case) can maintain its α relaxation, why does water $a_0 \sim 2.2$ Å confined in a 1.8 nm MCM-41 pore have to pass from α relaxation to pure β relaxation? If the intermolecular interactions are of the same type and if, in the EG case, only few interacting molecules are enough to giving rise to α relaxation, then analogous considerations should also hold for water. Also, although deeply supercooled water, unlike most other liquids, requires a greatly extended three-dimensional hydrogen bonded network in order to exhibit relaxation, more than 100 water molecules —a sufficient number to support the growing of a large cluster— can nevertheless fit inside a sphere of only diameter 1.8 nm. In addition, when the temperature is lowered the HB becomes increasingly stable, and a water network is able to develop. On the other hand, it is generally true that a hosting surface can locally affect water properties and significantly affect the forming of the cluster. As experimental confirmation that FSC occurs in bulk or bulk-like water we show in fig. 75

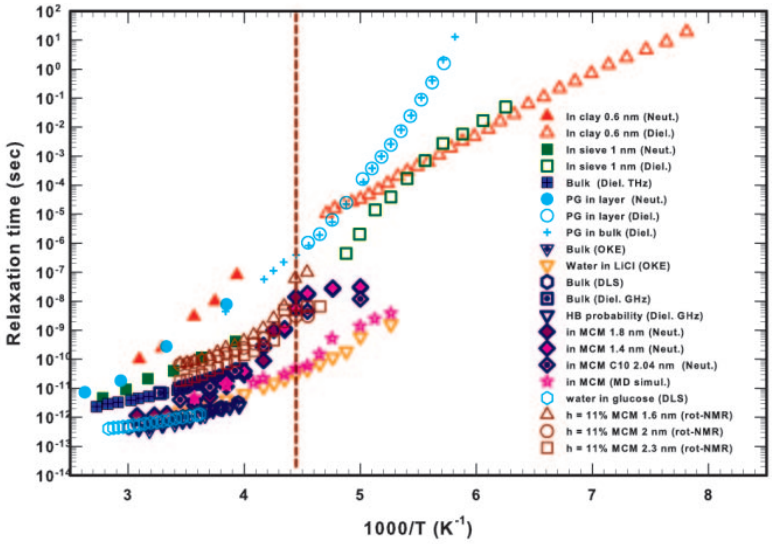

Fig. 75. – Relaxation times measured, as a function of the temperature, with different experimental techniques for water in bulk [402-406] and in very confining geometries. All data are reported *vs.* $1000/T$ in a log-linear scale. For comparison data of propylene glycol (PG) are also reported [407, 408]. Solid symbols regard neutron scattering, whereas the open ones deal with dielectric, Optical Kerr Effect (OKE), depolarized light scattering (DLS) and Nuclear Magnetic Resonance (rotational-NMR). The following data are also reported: water confined in clay [104, 409], in sieve [410, 411], in MCM-41 [98], in MCM-C10 [412], in MD simulation of MCM [413], DLS for water in solution with glucose [414], and finally confined on the surface of MCM ($h = 0.11$) in an experiment of quadrupole rotational NMR [415]. The dashed line represents the crossover temperature T_L.

the relaxation times measured —using a series of different experimental techniques— in bulk water and in confined water.

In fig. 75 experimental data reported in refs. [400, 407, 408] are also included, in particular those of PG. The relaxation times of bulk water [386, 402-406] and in a variety of confining geometries are reported. The solid symbols indicate neutron scattering and the open ones indicate the dielectric Optical Kerr Effect (OKE), depolarized light scattering (DLS), and nuclear magnetic resonance (rotational-NMR). Data also shown include: water confined in clay [104, 409], in a sieve [410, 411], in MCM-41 [98], in MCM-C10 [412], in the MD simulation of MCM [413], in solution with glucose [414], and on the surface of MCM $h = 0.11$ in an experiment of quadrupole rotational NMR or deuterons T_1 [415]. Figure 76 presents a log-linear plot that uses an amplified scale to display the same data (τ *vs.* $1000/T$) as shown in fig. 75. In addition, neutron scattering data obtained in bulk (incoherent [386] and coherent [416]) and in hydrated lysozyme with $h = 0.3$ [202] are reported.

It is clear that all the different experimental τ data concerning confined water show a crossover. Lysozyme hydration water ($h = 0.3$, *i.e.*, a single layer) has a behavior that coincides (within the experimental error) with that of the MCM sample with an hydration level $h = 0.11$. If in this latter sample $h = 0.5$ corresponds to full hydration,

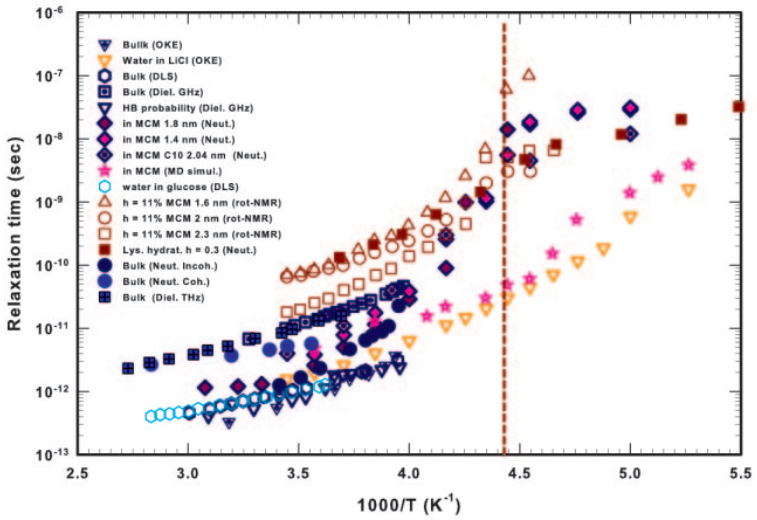

Fig. 76. – The figure, in a log-linear plot, shows in an enlarged scale the same data (τ *vs.* $1000/T$) as reported in fig. 75. In addition, neutron scattering data obtained in bulk (incoherent [386] ad coherent [416]) and in hydrated lysozyme with $h = 0.3$ [202] are reported.

then $h = 0.11$ corresponds to water molecules just being on the internal surface of the tube. Note that the temperature trend up to $\sim 250\,\mathrm{K}$ is nearly the same for confined and bulk water. The τ values differ, however. For example, although the bulk water relaxation time measured using dielectric relaxation differs by about one order of magnitude from that measured with light probes DLS and OKE, it appears that the NMR technique agrees with the neutron technique. These relaxation times differ according to the techniques used. Experiments that probe rotational or roto-translational motion are more sensitive than those that probe translational dynamics only. In addition, water confined on a surface (*e.g.*, lysozyme and MCM) has τ values two orders of magnitude slower with respect to light data. The τ data measured using the dielectric technique differ from τ data measured using light scattering because depolarized light scattering, unlike dielectric spectroscopy, probes the HB time (or probability) directly. Figure 76 reports such a quantity obtained from the τ measured using the dielectric relaxation technique (GHz range) by considering the formation of the HB network in terms of the percolation model [406]. This HB probability reported in fig. 76 coincides with bulk light scattering data and with data on the water glucose solution (measured with DLS) and with bulk water and water-LiCl solution data measured using the OKE technique. The OKE experiments are of particular interest because they are done in a bulk system: the H_2O-LiCl solution at the eutectic concentration of 6.82 M can be easily supercooled up to $\sim 200\,\mathrm{K}$ [404]. In the OKE experiments, the relaxation time is measured in terms of a stretched exponential decay (a similar non-exponential decay is observed in liquid and supercooled bulk water [403]). Since the techniques probe only translational motion, the dynamical crossover is not clear in the reported τ data, but we found that the corresponding stretched exponent decreases dramatically at $T = 220$–$230\,\mathrm{K}$, thus indicating an increase in the heterogeneity of water in nanoscale pools.

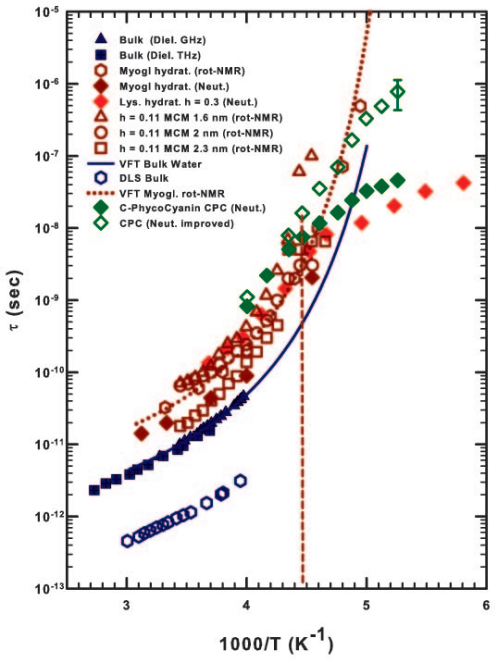

Fig. 77. – A log-linear plot of the relaxation times (τ *vs.* $1000/T$) of hydration water of proteins and on the surface of MCM-41 ($h = 0.11$); for comparison also the values measured in bulk water are reported. Bulk data are measured with DLS [405] and dielectric spectroscopy (in the GHz and in the THz range) [402, 406]. Proteins hydration water data regard: Myoglobin (rotational-NMR [417] and neutrons [418]), Lysozyme (neutrons [202]); and C-PhycoCyanin (neutrons [419]). Data of hydration water of MCM-41 nanotubes with different diameter at $h = 0.11$ are also reported (neutrons [415]). The dark blue curve represents the VTF law obtained by fitting the dielectric data of bulk water, whereas the dark red dotted curve is the VFT law corresponding to the fit of NMR data. Again, the dashed line represents the T_L value.

For a bulk system (*i.e.*, a system without constraints) the existence of a dynamic crossover in this temperature range can be seen when we compare the NMR self-diffusion data (D_s) with the corresponding measured macroscopic viscosity. This seems to confirm that the crossover is just a FSC and suggests that the increase in water heterogeneities when T is decreased may be directly related to dynamical heterogeneities characterizing materials approaching dynamical arrest.

In conclusion, we show that the crossover is also a property of protein hydration water by considering the relaxation times of hydration water around different biomolecules and comparing their temperature behavior with that of pure bulk water (fig. 77). More precisely, fig. 77 shows in a log-linear plot the relaxation times (τ *vs.* $1000/T$) of hydration water in lysozyme, Myoglobin and C-PhycoCyanin, and compares the data with those for water on the surface of MCM-41 ($h = 0.11$), and those for bulk water. Bulk water data are measured using DLS [405] and dielectric spectroscopy (in the GHz and in the THz range) [402, 406]. Protein hydration water data are reported for Myoglobin (rotational-NMR [417] and neutrons [418]), Lysozyme (neutrons [202]), and C-PhycoCyanin (neutrons [419]). Also data on hydration water of MCM-41 nanotubes with different diameters

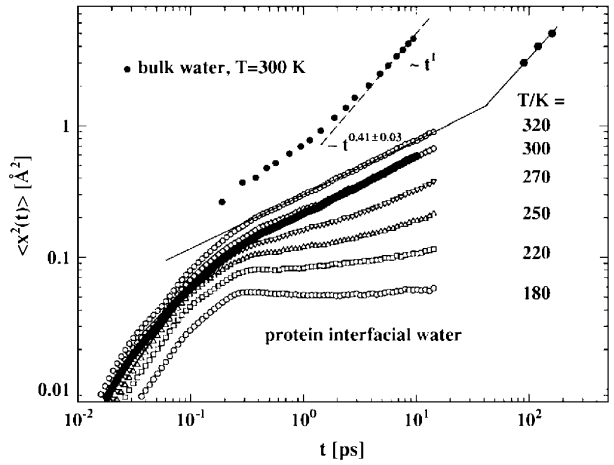

Fig. 78. – The figure reports the time-resolved mean square displacement ($\langle x^2(t)\rangle$ *vs.* t) of bulk water and of myoglobin hydration water ($h = 0.4$) measured by using neutron scattering [417]. Each curve corresponds to a different temperature in the range $180 < T < 320\,\mathrm{K}$.

at $h = 0.11$ are reported (neutrons [415]). Note that we have considered a VFT fit for the pure bulk water data (dark blue curve) and for the rotational NMR data of myoglobin hydration water (dark red curve). The dynamic crossover is evident in all the data but it is also clear that before the crossover ($T > T_L$) the $\tau(T)$ behavior as a function of the temperature coincides, within the experimental error, to that of bulk water (see *e.g.*, the nearly identical two VFT curves).

Figure 78 reports the time-resolved mean square displacement ($\langle x^2(t)\rangle$ *vs.* t) of bulk water and of myoglobin hydration water ($h = 0.4$) measured using neutron scattering [417].

Each curve corresponds to a temperature in the range $180 < T < 320\,\mathrm{K}$. The behavior of $\langle x^2(t)\rangle$ *vs.* t depends on the diffusional motion, $\langle x^2(t)\rangle = 2Dt^\gamma$, and for $\gamma = 1$ the dynamics are Brownian, otherwise ($\gamma \neq 1$) the dynamics become fractal-like, *i.e.*, with different probabilities that they will take "flight," moving from one cluster to another, or will be aggregated into a network. Different $\langle x^2(t)\rangle$ curves for the different T can be observed: for $T = 180\,\mathrm{K}$ the $\langle x^2(t)\rangle$ curve is nearly flat ($\gamma \sim 0$, in the picosecond region), showing that water molecules are trapped on the protein surface in a glass state. By increasing T, a dynamical change is observable at $T > 220\,\mathrm{K}$, and a further temperature increase corresponds to a dynamical evolution *toward* the behavior of bulk water.

* * *

Research in Messina is supported by the PRA-Unime-2005 and PRIN2008. Research at Massachusetts Institute of Technology is supported by Department of Energy Grants DE-FG02-90ER45429 and 2113-MIT-DOE-591. Research at Boston University is supported by National Science Foundation Chemistry Division Grants CHE0616489, CHE0908218, and CHE0911389. This work utilized facilities supported in part by the National Science Foundation under Agreement DMR-0086210.

REFERENCES

[1] Mallamace F. and Stanley H. E., *The Physics of Complex Systems*, *Proceedings of the International School of Physics "Enrico Fermi", Course CXXXIV*, edited by Mallamace F. and Stanley H. E. (IOS Press, Amsterdam) 1997; *The Physics of Complex Systems (New Advances and Perspectives)*, *Proceedings of the International School of Physics "Enrico Fermi", Course CLV*, edited by Mallamace F. and Stanley H. E. (IOS Press, Amsterdam and SIF, Bologna) 2004.

[2] Waller R. (Translator), *Essays of Natural Experiments* (original in Italian by the Secretary of the Accademia del Cimento), Facsimile of 1684 English translation (Johnson Reprint Corporation, New York) 1964.

[3] Stanley H. E., *Mater. Res. Bull.*, **24** (1999) 22.

[4] Angell C. A., Oguni M. and Sichina W. J., *J. Phys. Chem.*, **86** (1982) 998; Angell C. A., *Water: a Comprehensive Treatise*, Vol. **7**, edited by Franks F. (Plenum, New York) 1982, pp. 1-81.

[5] Debenedetti P. G. and Stanley H. E., *Phys. Today*, **56** (2003) 40.

[6] Mishima O. and Stanley H. E., *Nature*, **396** (1998) 329.

[7] Kell G. S., *J. Chem. Eng. Data*, **12** (1967) 66; **20** (1975) 97.

[8] Johari G. P., Hallbrucker A. and Mayer E., *Science*, **273** (1996) 90.

[9] Speedy R. J. and Angell C. A., *J. Chem. Phys.*, **65** (1976) 851.

[10] Mishima O., Calvert L. D. and Whalley E., *Nature*, **310** (1984) 393.

[11] Mishima O., Calvert L. D. and Whalley E., *Nature*, **314** (1985) 76.

[12] Mishima O., *Nature*, **384** (1996) 546.

[13] Burton E. F. and Oliver W. F., *Proc. R. Soc. London, Ser. A*, **153** (1936) 166.

[14] Heide H.-G., *Ultramicroscopy*, **14** (1984) 271.

[15] Bellissent-Funel M.-C., Bosio L., Hallbrucker A., Mayer E. and Sridi-Dorbez R., *J. Chem. Phys.*, **97** (1992) 1282.

[16] Bellissent-Funel M.-C. and Bosio L., *J. Chem. Phys.*, **102** (1995) 3727.

[17] Loerting T., Salzmann C., Kohl I., Mayer E. and Hallbrucker A., *Phys. Chem. Chem. Phys.*, **3** (2001) 5355.

[18] Finney J. L., Bowron D. T., Soper A. K., Loerting T., Mayer E. and Hallbrucker A., *Phys. Rev. Lett.*, **89** (2002) 503.

[19] Smith K. H., Shero E., Chizmeshya A. and Wolf G. H., *J. Chem. Phys.*, **102** (1995) 6851.

[20] Poole P. H., Grande T., Sciortino F., Stanley H. E. and Angell C. A., *J. Comput. Mat. Sci.*, **4** (1995) 373.

[21] Finney J. L., *Philos. Trans. R. Soc. London, Ser. B: Biol. Sci.*, **359** (2004) 1145.

[22] Mayer E., *Hyperquenched Glassy Bulk Water: A Comparison with Other Amorphous Forms of Water, and with Vitreous but Freezable Water in a Hydrogel and on Hydrated Methemoglobin*, in *Hydrogen Bond Networks*, edited by Bellissent-Funel M.-C. and Dore J. C. (Kluwer Academic Publishers, Dordrecht) 1994, pp. 355-372.

[23] Essmann U. and Geiger A., *J. Chem. Phys.*, **103** (1995) 4678.

[24] Tse J. S., Klug D. D., Guthrie M., Tulk C. A., Benmore C. J. and Urquidi J., *Phys. Rev. B*, **71** (2005) 214107.

[25] Brovchenko I., Geiger A. and Oleinikova A., *J. Chem. Phys.*, **118** (2003) 9473.

[26] Brovchenko I., Geiger A. and Oleinikova A., *J. Chem. Phys.*, **123** (2005) 044515.

[27] Jedlovszky P. and Vallauri R., *J. Chem. Phys.*, **122** (2005) 081101.

[28] White J. A., *Physica A*, **346** (2004) 347.

[29] Christie J. K., Guthrie M., Tulk C. A., Benmore C. J., Klug D. D., Taraskin S. N. and Eliot S. R., *Phys. Rev. B*, **72** (2005) 012201.

[30] Finney J. L., Hallbrucker A., Kohl I., Soper A. K. and Bowron D. T., *Phys. Rev. Lett.*, **88** (2002) 225503.

[31] Velikov V., Borick S. and Angell C. A., *Science*, **294** (2001) 2335.

[32] Angell C. A., *Science*, **319** (2008) 582.

[33] Eisenberg D. and Kauzmann W., *The Structure and Properties of Water* (Oxford University Press, New York) 1969.
[34] Bernal J. D. and Fowler R. H., *J. Chem. Phys.*, **1** (1933) 515.
[35] Pople J. A., *Proc. R. Soc. London, Ser. A*, **205** (1951) 163.
[36] Frank H. S. and Wen W.-Y., *Disc. Faraday Soc.*, **24** (1957) 133.
[37] Némethy G. and Scheraga H. A., *J. Chem. Phys.*, **36** (1962) 3382.
[38] Kamb B., *Ice Polymorphism and the Structure of Water*, in *Structural Chemistry and Molecular Biology*, edited by Rich A. and Davidson N. (Freeman, San Francisco) 1968, pp. 507-542.
[39] Röntgen W. C., *Annu. Phys. Chem.*, **45** (1892) 91.
[40] Pauling L., *The Structure of Water*, in *Hydrogen Bonding*, edited by Hadzi D. (Pergamon Press, New York) 1959, pp. 1-5.
[41] Speedy R. J., *J. Phys. Chem.*, **86** (1982) 982.
[42] Sastry S., Debenedetti P., Sciortino F. and Stanley H. E., *Phys. Rev. E*, **53** (1996) 6144.
[43] Stanley H. E., Teixeira J., Geiger A. and Blumberg R. L., *Physica A*, **106** (1981) 260.
[44] Stanley H. E., *J. Phys. A*, **12** (1979) 329.
[45] Stanley H. E. and Teixeira J., *J. Chem. Phys.*, **73** (1980) 3404.
[46] Geiger A. and Stanley H. E., *Phys. Rev. Lett.*, **49** (1982) 1749.
[47] Errington J. R., Debenedetti P. G. and Torquato S., *Phys. Rev. Lett.*, **89** (2002) 215503.
[48] Poole P. H., Sciortino F., Essmann U. and Stanley H. E., *Nature*, **360** (1992) 2002.
[49] Debenedetti P. G., *J. Phys.: Condens. Matter*, **15** (2003) 669.
[50] Ponyatovskii E. G., Sinitsyn V. V. and Pozdnyakova T. A., *JETP Lett.*, **60** (1994) 360.
[51] Moynihan C. T., *Mater. Res. Soc. Symp. Proc.*, **455** (1997) 411.
[52] Poole P. H., Sciortino F., Grande T., Stanley H. E. and Angell C. A., *Phys. Rev. Lett.*, **73** (1994) 1632.
[53] Borick S. S., Debenedetti P. G. and Sastry S., *J. Phys. Chem.*, **99** (1995) 3781.
[54] Tejero C. F. and Baus M., *Phys. Rev. E*, **57** (1998) 4821.
[55] Franzese G. and Stanley H. E., *Physica A*, **314** (2002) 508.
[56] Franzese G. and Stanley H. E., *J. Phys.: Condens. Matter*, **14** (2002) 2193.
[57] Franzese G., Marqués M. I. and Stanley H. E., *Phys. Rev. E.*, **67** (2003) 011103.
[58] Franzese G. and Stanley H. E., *J. Phys.: Condens. Matter*, **19** (2007) 205126.
[59] Trinh E. and Apfel R. E., *J. Chem. Phys.*, **72** (1980) 6731.
[60] Levelt J. M. H., *Measurements of the Compressibility of Argon in the Gaseous and Liquid Phase*, Ph.D. Thesis (University of Amsterdam, Van Gorkum and Co.) 1958.
[61] Anisimov M. A., Sengers J. V. and Levelt-Sengers J. M. H., *Near-Critical Behavior of Aqueous Systems in Aqueous System at Elevated Temperatures and Pressures: Physical Chemistry* in *Water, Stream and Hydrothermal Solutions*, edited by Palmer D. A., Fernandez-Prini R. and Harvey A. H. (Elsevier, Amsterdam) 2004.
[62] Yamada M., Mossa S., Stanley H. E. and Sciortino F., *Phys. Rev. Lett.*, **88** (2002) 195701.
[63] Kanno H., Speedy R. and Angell C. A., *Science*, **189** (1975) 880.
[64] Mishima O., *J. Chem. Phys.*, **100** (1994) 5910.
[65] Mishima O. and Stanley H. E., *Nature*, **392** (1998) 164.
[66] Whalley E., Klug D. D. and Handa Y. P., *Nature*, **342** (1989) 782.
[67] Johari G. P., Fleissner G., Hallbrucker A. and Mayer E., *J. Phys. Chem.*, **98** (1994) 4719.
[68] Speedy R. J., Debenedetti P. G., Smith R. S., Huang C. and Kay B. D., *J. Chem. Phys.*, **105** (1996) 240.
[69] Bartell L. S. and Huang J., *J. Phys. Chem.*, **98** (1994) 7455.
[70] Brüggeller P. and Mayer E., *Nature*, **288** (1980) 569.
[71] Bridgman P. W., *J. Chem. Phys.*, **3** (1935) 597.

[72] Poole P. H., Essmann U., Sciortino F. and Stanley H. E., *Phys. Rev. E*, **48** (1993) 4605.
[73] Tanaka H., *J. Chem. Phys.*, **105** (1996) 5099.
[74] Harrington S., Zhang R., Poole P. H., Sciortino F. and Stanley H. E., *Phys. Rev. Lett.*, **78** (1997) 2409.
[75] Sciortino F., Poole P. H., Essmann U. and Stanley H. E., *Phys. Rev. E*, **55** (1997) 727.
[76] Harrington S., Poole P. H., Sciortino F. and Stanley H. E., *J. Chem. Phys.*, **107** (1997) 7443.
[77] Jorgensen W. L., Chandrasekhar J., Madura J., Impey R. W. and Klein M., *J. Chem. Phys.*, **79** (1983) 926.
[78] Paschek D., *Phys. Rev. Lett.*, **94** (2005) 217802.
[79] Shiratani E. and Sasai M., *J. Chem. Phys.*, **108** (1998) 3264.
[80] Bellissent-Funel M.-C., *Europhys. Lett.*, **42** (1998) 161.
[81] Stanley H. E., Buldyrev S. V., Canpolat M., Mishima O., Sadr-Lahijany M. R., Scala A. and Starr F. W., *Phys. Chem. Chem. Phys.*, **2** (2000) 1551.
[82] Soper A. K. and Ricci M. A., *Phys. Rev. Lett.*, **84** (2000) 2881 and references therein.
[83] Mitus A. C., Patashinskii A. Z. and Shumilo B. I., *Phys. Lett. A*, **113** (1985) 41.
[84] Mitus A. C. and Patashinskii A. Z., *Acta Phys. Pol. A*, **74** (1988) 779.
[85] Zangi R. and Mark A. E., *J. Chem. Phys.*, **119** (2003) 1694.
[86] Zangi R., *J. Phys.: Condens. Matter*, **16** (2004) S5371.
[87] Wiggins P. M., *Microbiol. Rev.*, **54** (1990) 432.
[88] Wiggins P. M., *Prog. Polym. Sci.*, **20** (1995) 1121.
[89] Bellissent-Funel M.-C., Zanotti J.-M. and Chen S.-H., *Faraday Discuss.*, **103** (1996) 281.
[90] Crupi V., Magazu S., Majolino D., Migliardo P., Venuti V. and Bellissent-Funel M.-C., *J. Phys.: Condens. Matter*, **12** (2000) 3625.
[91] Bellissent-Funel M.-C., *J. Mol. Liq.*, **84** (2000) 39.
[92] Bellissent-Funel M.-C., Chen S.-H. and Zanotti J. M., *Phys. Rev. E*, **51** (1995) 4558.
[93] Bellissent-Funel M.-C., Teixeira J., Bradley K. F. and Chen S.-H., *J. Phys. I*, **2** (1992) 995.
[94] Chen S.-H., Gallo P. and Bellissent-Funel M.-C., *Can. J. Phys.*, **73** (1995) 703.
[95] Dohnálek Z., Kimmel G. A., Ciolli R. L., Stevenson K. P., Smith R. S. and Kay B. D., *J. Chem. Phys.*, **112** (2000) 5932.
[96] Truskett T. M., Debenedetti P. G. and Torquato S., *J. Chem. Phys.*, **114** (2001) 2401.
[97] Zanotti J. M., Bellissent-Funel M.-C. and Chen S.-H., *Europhys. Lett.*, **71** (2005) 91.
[98] Liu L., Chen S.-H., Faraone A., Yen C.-W. and Mou C.-Y., *Phys. Rev. Lett.*, **95** (2005) 117802.
[99] Green M. E. and Lu J., *J. Colloid Interface Sci.*, **171** (1995) 117.
[100] Koga K., Zeng X. C. and Tanaka H., *Phys. Rev. Lett.*, **79** (1997) 5262.
[101] Slovak J., Koga K., Tanaka H. and Zeng X. C., *Phys. Rev. E*, **60** (1999) 5833.
[102] Koga K., Zeng X. C. and Tanaka H., *Chem. Phys. Lett.*, **285** (1998) 278.
[103] Koga K., Zeng X. C. and Tanaka H., *Nature*, **408** (2000) 564.
[104] Bergman R. and Swenson J., *Nature*, **403** (2000) 283.
[105] Webber B. and Dore J., *J. Phys.: Condens. Matter*, **16** (2004) S5449.
[106] Teixeira J., Zanotti J. M., Bellissent-Funel M.-C. and Chen S.-H., *Physica B*, **234** (1997) 370.
[107] Gallo P., *Phys. Chem. Chem. Phys.*, **2** (2000) 1607.
[108] Gallo P., Rovere M., Ricci M. A., Hartnig C. and Spohr E., *Europhys. Lett.*, **49** (2000) 183.
[109] Gallo P., Rovere M., Ricci M. A., Hartnig C. and Spohr E., *Philos. Mag. B*, **79** (1999) 1923.

[110] Rovere M., Ricci M. A., Vellati D. and Bruni F., *J. Chem. Phys.*, **108** (1998) 9859.
[111] Bellissent-Funel M.-C., Sridi-Dorbez R. and Bosio L., *J. Chem. Phys.*, **104** (1996) 10023.
[112] Forsman J., Jonsson B. and Woodward C. E., *J. Phys. Chem.*, **100** (1996) 15005.
[113] Meyer M. and Stanley H. E., *J. Phys. Chem. B*, **103** (1999) 9728.
[114] Netz P. A. and Dorfmuller T., *J. Phys. Chem. B*, **102** (1998) 4875.
[115] Zanotti J. M., Bellissent-Funel M.-C. and Chen S.-H., *Phys. Rev. E*, **59** (1999) 3084.
[116] Bellissent-Funel M.-C. and Teixeira J., *Structural and Dynamic Properties of Bulk and Confined Water*, in *Freeze-Drying/Lyophilization of Pharmaceutical and Biological Products*, edited by Rey L. and May J. C. (Marcel Dekker, New York) 1999, Chapter 3, pp. 53-77.
[117] Tanaka H. and Ohmine I., *J. Chem. Phys.*, **87** (1987) 6128.
[118] Ohmine I., Tanaka H. and Wolynes P. G., *J. Chem. Phys.*, **89** (1988) 5852.
[119] Tanaka H. and Ohmine I., *J. Chem. Phys.*, **91** (1989) 6318.
[120] Ohmine I. and Tanaka H., *J. Chem. Phys.*, **93** (1990) 8138.
[121] Ohmine I. and Tanaka H., *Dynamics of Liquid Water: Fluctuations and Collective Motions* in *Molecular Dynamics Simulations*, edited by Yonezawa F. (Springer Verlag, Berlin) 1991, pp. 130-138.
[122] Okabe I., Tanaka H. and Nakanishi K., *Phys. Rev. E*, **53** (1996) 2638.
[123] Tanaka H., *Phase Diagram for Supercooled Water and Liquid-Liquid Transition*, in *ACS Symposium Series on Experimental and Theoretical Approaches to Supercooled Liquids*, edited by Fourkas J. (American Chemical Society) 1997, Chap. 18, pp. 233-245.
[124] Kabeya T., Tamai Y. and Tanaka H., *J. Phys. Chem. B*, **102** (1998) 899.
[125] Tamai Y. and Tanaka H., *Phys. Rev. E*, **59** (1999) 5647.
[126] Tanaka H., Yamamoto R., Koga K. and Zeng X. C., *Chem. Phys. Lett.*, **304** (1999) 378.
[127] Gao G. T., Zeng X. C. and Tanaka H., *J. Chem. Phys.*, **112** (2000) 8534.
[128] Bellissent-Funel M.-C., *Eur. Phys. J. E*, **12** (2003) 83.
[129] Bellissent-Funel M.-C., *C. R. Geosci.*, **337** (2005) 173.
[130] Hemmer P. C. and Stell G., *Phys. Rev. Lett.*, **24** (1970) 1284.
[131] Canpolat M., Starr F. W., Sadr-Lahijany M. R., Scala A., Mishima O., Havlin S. and Stanley H. E., *Chem. Phys. Lett.*, **294** (1998) 9.
[132] Sastry S., Sciortino F. and Stanley H. E., *J. Chem. Phys.*, **98** (1993) 9863.
[133] Roberts C. J., Panagiotopulos A. Z. and Debenedetti P. G., *Phys. Rev. Lett.*, **77** (1996) 4386.
[134] Franzese G., Malescio G., Skibinsky A., Buldyrev S. V. and Stanley H. E., *Nature*, **409** (2001) 692.
[135] Franzese G., Malescio G., Skibinsky A., Buldyrev S. V. and Stanley H. E., *Phys. Rev. E*, **66** (2002) 051206.
[136] Skibinsky A., Buldyrev S. V., Franzese G., Malescio G. and Stanley H. E., *Phys. Rev. E*, **69** (2004) 061206.
[137] Malescio G., Franzese G., Skibinsky A., Buldyrev S. V. and Stanley H. E., *Phys. Rev. E*, **71** (2005) 061504.
[138] Franzese G., *J. Mol. Liq.*, **136** (2007) 267.
[139] Barros de Oliveira A., Franzese G., Netz P. A. and Barbosa M. C., *J. Chem. Phys.*, **128** (2008) 064901.
[140] Shiratani E. and Sasai M. J., *Chem. Phys.*, **104** (1996) 7671.
[141] Tanaka H., *Phys. Rev. Lett.*, **80** (1998) 113.
[142] Angell C. A., Shuppert J. and Tucker J. C., *J. Phys. Chem.*, **77** (1973) 3092.
[143] Sciortino F., Fabbian L., Chen S.-H. and Tartaglia P., *Phys. Rev. E*, **56** (1997) 5397.
[144] Sciortino F., Gallo P., Tartaglia P. and Chen S.-H., *Phys. Rev. E*, **54** (1996) 6331.
[145] Kumar P., Franzese G., Buldyrev S. V. and Stanley H. E., *Phys. Rev. E*, **73** (2006) 041505.

[146] Xie Y., Ludwig K. F., Morales G., Hare D. E. and Sorensen C. M., *Phys. Rev. Lett.*, **71** (1993) 2051.
[147] Sciortino F., Poole P. H., Stanley H. E. and Havlin S., *Phys. Rev. Lett.*, **64** (1990) 1686.
[148] Luzar A. and Chandler D., *Nature*, **379** (1996) 55; Luzar A. and Chandler D., *Phys. Rev. Lett.*, **76** (1996) 928.
[149] Starr F. W., Nielsen J. K. and Stanley H. E., *Phys. Rev. Lett.*, **82** (1999) 2294; Starr F. W., Nielsen J. K. and Stanley H. E., *Phys. Rev. E*, **62** (2000) 579.
[150] Errington J. R. and Debenedetti P. G., *Nature*, **409** (2001) 318.
[151] Kincaid J. M., Stell G. and Hall C. K., *J. Chem. Phys.*, **65** (1976) 2161.
[152] Jagla E. A., *J. Phys.: Condens. Matter*, **11** (1999) 10251.
[153] Jagla E. A., *Phys. Rev. E*, **63** (2001) 061509.
[154] Sadr-Lahijany M. R., Scala A., Buldyrev S. V. and Stanley H. E., *Phys. Rev. Lett.*, **81** (1998) 4895.
[155] Scala A., Sadr-Lahijany M. R., Giovambattista N., Buldyrev S. V. and Stanley H. E., *Phys. Rev. E*, **63** (2001) 041202.
[156] Scala A., Reza Sadr-Lahijany M., Giovambattista N., Buldyrev S. V. and Stanley H. E., *J. Stat. Phys.*, **100** (2000) 97.
[157] Kumar P., Buldyrev S. V., Sciortino F., Zaccarelli E. and Stanley H. E., *Phys. Rev. E*, **72** (2005) 021501.
[158] Debenedetti P. G., Raghavan V. S. and Borick S. S., *J. Phys. Chem.*, **95** (1991) 4540.
[159] Henriques V. B. and Barbosa M. C., *Phys. Rev. E*, **71** (2005) 031504.
[160] Guillot B. and Guissani Y., *J. Chem. Phys.*, **119** (2003) 11740.
[161] Henriques V. B., Guisoni N., Barbosa M. A., Thielo M. and Barbosa M. C., *Mol. Phys.*, **103** (2005) 3001.
[162] Jagla E. A., *J. Chem. Phys.*, **111** (1999) 8980.
[163] Hall T. H., Merril L. and Barnett J. D., *Science*, **146** (1964) 1297.
[164] Kumar P., Franzese G. and Stanley H. E., *Phys. Rev. Lett.*, **100** (2008) 105701.
[165] D'Arrigo G., Maisano G., Mallamace F., Migliardo P. and Wanderlingh F., *J. Chem. Phys.*, **75** (1981) 4264; Angell C. A. and Rodgers V., *J. Chem. Phys.*, **80** (1984) 6245.
[166] Schwegler E., Galli G. and Gygi F., *Phys. Rev. Lett.*, **84** (2000) 2429; Raiteri P., Laio A. and Parrinello M., *Phys. Rev. Lett.*, **93** (2004) 087801 and references therein.
[167] Scala A., Starr F. W., La Nave E., Sciortino F. and Stanley H. E., *Nature*, **406** (2000) 166.
[168] Yan Z., Buldyrev S. V., Giovambattista N. and Stanley H. E., *Phys. Rev. Lett.*, **95** (2005) 130604.
[169] Yan Z., Buldyrev S. V., Giovambattista N., Debenedetti P. G. and Stanley H. E., *Phys. Rev. E*, **73** (2006) 051204.
[170] Yan Z., Buldyrev S. V., Kumar P., Giovambattista N., Debenedetti P. G. and Stanley H. E., *Phys. Rev. E*, **76** (2007) 051201.
[171] Giovambattista N., Rossky P. J. and Debenedetti P. G., *Phys. Rev. E*, **73** (2006) 041604.
[172] Xu L., Kumar P., Buldyrev S. V., Chen S.-H., Poole P. H., Sciortino F. and Stanley H. E., *Proc. Natl. Acad. Sci. U.S.A.*, **102** (2005) 16558.
[173] Angell C. A., *Annu. Rev. Phys. Chem.*, **55** (2004) 559.
[174] Poole P. H., Grande T., Angell C. A. and McMillan P. F., *Science*, **275** (1997) 322.
[175] Yarger J. L. and Wolf G. H., *Science*, **306** (2004) 820.
[176] Mallamace F., Broccio M., Corsaro C., Faraone A., Wanderlingh U., Liu L., Mou C.-Y. and Chen S.-H., *J. Chem. Phys.*, **124** (2006) 161102.
[177] Faraone A., Liu L., Mou C.-Y., Yen C.-W. and Chen S.-H., *J. Chem. Phys.*, **121** (2004) 10843.

[178] Liu L., *Study of Slow Dynamics in Supercooled Water by Molecular Dynamics and Quasi-Elastic Neutron Scattering* (Ph.D. thesis, M.I.T.) September 2005.
[179] Bellissent-Funel M.-C., *Hydration Processes in Biology: Theoretical and Experimental Approaches*, in *Proc. NATO Advanced Study Institutes*, Vol. **305** (IOS Press, Amsterdam) 1999.
[180] Robinson G. W., Zhu S.-B., Singh S. and Evans M. W., *Water in Biology, Chemistry, and Physics: Experimental Overviews and Computational Methodologies* (World Scientific, Singapore) 1996.
[181] Angell C. A., Bressel R. D., Hemmatti M., Sare E. J. and Tucker J. C., *Phys. Chem. Chem. Phys.*, **2** (2000) 1559.
[182] Angell C. A., *J. Phys. Chem.*, **97** (1993) 6339.
[183] Starr F. W., Angell C. A. and Stanley H. E., *Physica A*, **323** (2003) 51.
[184] Horbach J. and Kob W., *Phys. Rev. B*, **60** (1999) 3169.
[185] Lang E. W. and Lüdemann H. D., *Angew. Chem. Intl. Ed. Engl.*, **21** (1982) 315.
[186] Prielmeier F. X., Lang E. W., Speedy R. J. and Lüdemann H. D., *Phys. Rev. Lett.*, **59** (1987) 1128.
[187] Ito K., Moynihan C. T. and Angell C. A., *Nature*, **398** (1999) 492.
[188] Tanaka H., *J. Phys.: Condens. Matter*, **15** (2003) L703.
[189] Swenson J., Jansson H., Howells W. S. and Longeville S., *J. Chem. Phys.*, **122** (2005) 084505.
[190] Sastry S. and Angell C. A., *Nat. Mater.*, **2** (2003) 739.
[191] Saika-Voivod I., Poole P. H. and Sciortino F., *Nature*, **412** (2001) 514.
[192] Rapaport D. C., *The Art of Molecular Dynamics Simulation* (Cambridge University Press, Cambridge) 1995.
[193] Stillinger F. H. and Rahman A., *J. Chem. Phys.*, **57** (1972) 1281.
[194] Götze W. and Sjögren L., *Rep. Prog. Phys.*, **55** (1992) 241.
[195] Poole P. H., Saika-Voivod I. and Sciortino F., *J. Phys.: Condens. Matter*, **17** (2005) L431.
[196] Jakse N., Hennet L., Price D. L., Krishnan S., Key T., Artacho E., Glorieux B., Pasturel A. and Sabougni M.-L., *Appl. Phys. Lett.*, **83** (2003) 4734.
[197] Kumar P., Starr F. W., Buldyrev S. V. and Stanley H. E., *Phys. Rev. E*, **75** (2007) 011202.
[198] Kumar P., Buldyrev S. V., Starr F., Giovanbattista N. and Stanley H. E., *Phys. Rev. E*, **72** (2005) 051503.
[199] Chen S.-H., Mallamace F., Mou C.-Y., Broccio M., Corsaro C., Faraone A. and Liu L., *Proc. Natl. Acad. Sci. U.S.A.*, **103** (2006) 12974.
[200] Mallamace F., Broccio M., Corsaro C., Faraone A., Majolino D., Venuti V., Liu L., Mou C.-Y. and Chen S.-H., *Proc. Natl. Acad. Sci. U.S.A.*, **104** (2007) 424.
[201] Kumar P., Yan Z., Xu L., Mazza M. G., Buldyrev S. V., Chen S.-H., Sastry S. and Stanley H. E., *Phys. Rev. Lett.*, **97** (2006) 177802.
[202] Chen S.-H., Liu L., Fratini E., Baglioni P., Faraone A. and Mamontov E., *Proc. Natl. Acad. Sci. U.S.A.*, **103** (2006) 9012.
[203] Kumar P., Yan Z., Xu L., Mazza M. G., Buldirev S. V., Chen S.-H., Sastry S. and Stanley H. E., *Soft Matter under Extreme Pressures: Fundamentals and Emerging Technologies.*, in *Proc. NATO ARW, Odessa, Oct. 2005*, edited by Rzoska S. J. and Mazur V. (Springer, Berlin) 2006.
[204] Liu D., Zhang Y., Chen C.-C., Mou C.-Y., Poole P. H. and Chen S.-H., *Proc. Natl. Acad. Sci. U.S.A.*, **104** (2007) 9570.
[205] Fuentevilla D. A. and Anisimov M. A., *Phys. Rev. Lett.*, **97** (2006) 195702.
[206] Mallamace F., Branca C., Broccio M., Corsaro C., Gonzalez-Segredo N., Spooren J., Stanley H. E. and Chen S.-H., *Eur. Phys. J. ST*, **161** (2008) 19.
[207] Shih P. C., Lin H. P. and Mou C.-Y., *Stud. Surf. Sci. Catal.*, **146** (2003) 557.
[208] Lin Y., Zhang W. and Pinnavaia T. J., *J. Am. Chem. B*, **122** (2000) 8791.
[209] Ryoo R., Joo S. H. and Kim J. M., *J. Phys. Chem. B*, **103** (1999) 7435.

[210] Liu L., Chen S.-H., Faraone A., Yen C.-W., Mou C.-Y., Kolesnikov A. I., Mamontov E. and Leao J., *J. Phys.: Condens. Matter*, **18** (2006) S2261.
[211] Morishige K. and Nobuoca K., *J. Chem. Phys.*, **107** (1997) 6965.
[212] Schreiber A., Ketelsen I. and Findenegg G. H., *Phys. Chem. Chem. Phys.*, **3** (2001) 1185.
[213] Grünberg B., Emmler T., Gedat E., Shenderovich J., Findenegg G. H., Limbach H. H. and Buntkowsky G., *Chem. Eur. J.*, **10** (2004) 5689.
[214] Overloop K. and Van Gerven L., *J. Magn. Res., Ser. A*, **101** (1993) 147.
[215] Hansen E. W., Schmidt R., Stöcker M. and Akporiaye D., *J. Phys. Chem.*, **99** (1995) 4148.
[216] Berendsen H. J. C., Grigera J. R. and Straatsma T. P., *J. Phys. Chem.*, **91** (1987) 6269.
[217] Soper A. K., *Mol. Phys.*, **99** (2001) 1503.
[218] Kusalik P. G. and Svishchev I. M., *Science*, **256** (1994) 1219.
[219] The main reason is that the scattering cross-section of hydrogen is about 80 barns, and is much larger (at least 20 times) than that of other atoms in the protein-hydration-water system, composed of oxygen, carbon, nitrogen and sulfur atoms. Furthermore, neutron scattering cross-section of a hydrogen atom is mostly incoherent so that QENS and INS spectra reflect, essentially, the self-dynamics of the hydrogen atoms in the protein or water. Combining this dominant cross-section of hydrogen atoms with the use of spectrometers having different energy resolutions, we can study the molecular dynamics of water in a wide range of time scale, encompassing picoseconds to tens of nanoseconds. In addition, investigating different Q values (Q being the magnitude of the wave vector transfer in the scattering) in the range from $0.2\,\text{Å}^{-1} \leq Q \leq 2\,\text{Å}^{-1}$, the spatial characteristics of water dynamics can be investigated at the sub-nanometer level.
[220] van Hove L., *Phys. Rev.*, **95** (1954) 249.
[221] Chen S. H. and Kotlarchyk M., *Interaction of Photons and Neutrons with Matter*, second edition (World Scientific Publishing) 2007.
[222] Liu L., Faraone A. and Chen S.-H., *Phys. Rev. E*, **65** (2002) 041506.
[223] Chen S.-H., Mallamace F., Liu L., Liu D. Z., Chu X. Q., Zhang Y., Kim C., Faraone A., Mou C.-Y., Fratini E., Baglioni P., Kolesnikov A. I. and Garcia-Sakai V., *AIP Conf. Proc.*, **982** (2008) 39.
[224] Bosio L., Chen S.-H. and Teixeira J., *Phys. Rev. A*, **27** (1983) 1468.
[225] Walrafen G. E., *J. Chem. Phys.*, **47** (1967) 114; Walrafen G. E., Fisher M. R., Hokmabadi M. S. and Yang W.-H., *J. Chem. Phys.*, **85** (1986) 6970.
[226] Brubach J. B., Mermet A., Filabozzi A., Gerschel A. and Roy P., *J. Chem. Phys.*, **122** (2005) 184509.
[227] Walrafen G. E., in *Structure of Water and Aqueous Solutions*, edited by Luck W. A. P. (Verlag Chemie, Weinheim) 1974.
[228] D'Arrigo G., Maisano G., Mallamace F., Migliardo P. and Wanderlingh F., *J. Chem. Phys.*, **75** (1985) 4264.
[229] Venkatesh C. G., Rice S. A. and Bates J. B., *J. Chem. Phys.*, **63** (1975) 1065; Sivakumar T. C., Rice S. A. and Sceats M. G., *J. Chem. Phys.*, **69** (1978) 3468.
[230] Ediger M. D., *Annu. Rev. Phys. Chem.*, **51** (2000) 99.
[231] Fujara F., Geil B., Sillescu H. and Fleishcer G., *Z. Phys. B*, **88** (1992) 195.
[232] Swallen S. F., Bonvallet P. A., McMahon R. J. and Ediger M. D., *Phys. Rev. Lett.*, **90** (2003) 01590.
[233] Chang J. and Sillescu H., *J. Phys. Chem. B*, **101** (1997) 8794.
[234] Cicerone M. T. and Ediger M. D., *J. Chem. Phys.*, **104** (1996) 7210.
[235] Xia X. Y. and Wolynes P. G., *J. Phys. Chem. B*, **105** (2001) 6570.
[236] Ngai K. L., Magill J. H. and Plazek D. J., *J. Chem. Phys.*, **112** (2000) 1887.
[237] Pan A. C., Garrahan J. P. and Chandler D., *Chem. Phys. Chem.*, **6** (2005) 1783.
[238] Jung Y.-J., Garrahan J. P. and Chandler D., *Phys. Rev. E*, **69** (2004) 061205.
[239] Yamamoto R. and Onuki A., *Phys. Rev. Lett.*, **81** (1998) 4915.

[240] Mallamace F., Branca C., Broccio M., Corsaro C., Mou C.-Y. and Chen S.-H., *Proc. Natl. Acad. Sci. U.S.A.*, **104** (2007) 18387.
[241] Smith R. S., Huang C. and Kay B. D., *J. Phys. Chem. B*, **101** (1997) 6123.
[242] Floriano M. A., Handa Y. P., Klug D. D. and Whalley E., *J. Chem. Phys.*, **91** (1989) 7187.
[243] Sorensen C. M., *J. Chem. Phys.*, **79** (1983) 1455.
[244] Vedamuthu M., Singh S. and Robinson G. W., *J. Phys. Chem.*, **100** (1996) 3825.
[245] Modig K., Pfrommer B. and Halle B., *Phys. Rev. Lett.*, **90** (2003) 075502.
[246] Soper A. K., Bruni F. and Ricci M. A., *J. Chem. Phys.*, **106** (1997) 247.
[247] Donth E., *The Glass Transition* (Springer, Berlin) 2001.
[248] Debenedetti P. G. and Stillinger F. H., *Nature*, **410** (2001) 259.
[249] Corwin E. I., Jaeger H. M. and Nagel S. R., *Nature*, **435** (2005) 1075.
[250] Bennemann C., Donati C., Baschnagel J. and Glotzer S. C., *Nature*, **399** (1999) 246.
[251] Donati C., Franz S., Glotzer S. C. and Parisi G., *J. Non-Cryst. Solids*, **307-310** (2002) 215.
[252] Whitelam S., Berthier L. and Garrahan J. P., *Phys. Rev. Lett.*, **92** (2004) 185705.
[253] Struick L. C., *Physical Aging in Amorphous Polymers and Other Materials* (Elsevier, Amsterdam) 1978.
[254] Zürcher A. and Keyes T., *Phys. Rev. E*, **55** (1997) 6917.
[255] Diezemann G., Mohanty U. and Oppenheim I., *Phys. Rev. E*, **59** (1999) 2067.
[256] Buchenau U., *Phys. Rev. B*, **63** (2001) 104203; Buchenau U., *J. Phys.: Condens. Matter*, **15** (2003) S995.
[257] Büchner S. and Heuer A., *Phys. Rev. E*, **60** (1999) 6507.
[258] Goldstein M., *J. Chem. Phys.*, **51** (1969) 3728.
[259] Wales D. J., *Energy Landscapes* (Cambridge University Press, Cambridge) 2003.
[260] Sciortino F., *J. Stat. Mech.: Theory Exp.*, (2005) P05015.
[261] Tombari E., Ferrari C., Salvetti G. and Johari P. G., *Phys. Rev. B*, **77** (2008) 0242304.
[262] Stillinger F. H. and Weber T. A., *Phys. Rev. A*, **25** (1982) 978.
[263] Stillinger F. H., *Science*, **225** (1984) 983; **267** (1995) 1935.
[264] Sastry S., Debenedetti P. G. and Stillinger F. H., *Nature*, **393** (1998) 554.
[265] Sciortino F., Kob W. and Tartaglia P., *Phys. Rev. Lett.*, **83** (1999) 3214.
[266] Schröder T. B., Sastry S., Dyre J. and Glotzer S. C., *J. Chem. Phys.*, **112** (2000) 9834.
[267] Kob W., Sciortino F. and Tartaglia P., *Europhys. Lett.*, **49** (2000) 590.
[268] Sciortino F. and Tartaglia P., *Phys. Rev. Lett.*, **86** (2001) 107.
[269] Utz M., Debenedetti P. G. and Stillinger F. H., *Phys. Rev. Lett.*, **84** (2000) 1471.
[270] Cloitre M., Borrega R. and Leibler L., *Phys. Rev. Lett.*, **85** (2000) 4819.
[271] Cipelletti L., Manley S., Ball R. C. and Weitz D. A., *Phys. Rev. Lett.*, **84** (2000) 2275.
[272] Nicodemi M. and Coniglio A., *Phys. Rev. Lett.*, **82** (1999) 916.
[273] Birge N. O. and Nagel R. S., *Phys. Rev. Lett.*, **54** (1985) 2674; Birge N. O., *Phys. Rev. B*, **34** (1986) 1631.
[274] Salvetti G., Cardelli C., Ferrari C. and Tombari E., *Thermochim. Acta*, **364** (2000) 11.
[275] Tombari E, Ferrari C., Salvetti G. and Johari J. P., *J. Chem. Phys.*, **130** (2009) 124505.
[276] Salvetti G., Tombari E., Mikheeva L. and Johari G. P., *J. Phys. Chem. B.*, **106** (2002) 6081.
[277] Angell C. A., *Annu. Rev. Phys. Chem.*, **34** (1983) 593.
[278] Angell C. A., *Science*, **267** (1995) 1924.
[279] Kivelson D. and Tarjus G., *J. Phys. Chem. B*, **105** (2001) 6220.
[280] Cho C. H., Urquidi J., Singh S. and Wilse Robinson G., *J. Phys. Chem. B*, **103** (1999) 1991.

[281] Tombari E., Ferrari C. and Salvetti G., *Chem. Phys. Lett.*, **300** (1999) 749.
[282] Kohl I., Bachmann L., Mayer E., Hallbrucker A. and Loerting T., *Nature*, **435** (2005) E1.
[283] Handa Y. P. and Klug D. D., *J. Phys. Chem.*, **92** (1988) 3323.
[284] Oguni M. and Angell C. A., *J. Chem. Phys.*, **73** (1980) 1948.
[285] Rasmussen D. H., Mackenzie A. P., Tucker J. C. and Angell C. A., *Science*, **181** (1973) 4079.
[286] Johari G. P., *J. Chem. Phys.*, **107** (1997) 10154.
[287] Rennie G. K. and Clifford J., *J. Chem. Soc. Faraday Trans. 1*, **73** (1977) 680.
[288] van Miltenburg J. C. and van der Eerder J. P., *J. Crystal Growth*, **128** (1993) 1143.
[289] Takamuku T., Yamagami M., Wakita H., Masuda Y. and Yamaguchi T., *J. Phys. Chem. B*, **101** (1997) 5370.
[290] Hansen E. W., Gran H. C. and Sellevold E. J., *J. Phys. Chem. B*, **101** (1997) 7027.
[291] Tombari E., Ferrari C. and Salvetti G., *J. Chem. Phys.*, **122** (2005) 104712.
[292] Maruyama S., Wakabayashi K. and Oguni M., *AIP Conf. Proc.*, **708** (2004) 675.
[293] Oguni M., Maruyama S., Wakabayashi K. and Nagoe A., *Chem. Asian J.*, **2** (2007) 514.
[294] Ferrari G., Salvetti G., Tomari E. and Johari G. P., *Phys. Rev. E*, **54** (1996) R1058.
[295] Westrum E. F. jr., Furukawa G. T. and McCullough J. P., *Experimental Thermodynamics*, Vol. **1**, edited by McCullough J. P. and Scott D. W. (Butterworths, London) 1968, p. 133.
[296] Fujimori H. and Oguni M., *J. Phys. Chem. Solids*, **54** (1993) 271.
[297] Haida O., Matsuo T., Suga H. and Seki S., *J. Chem. Thermodyn.*, **6** (1974) 815.
[298] Oguni M., Matsuo T., Suga H. and Seki S., *Bull. Chem. Soc. Jpn.*, **48** (1975) 379.
[299] Suga H. and Seki S., *Faraday Discuss. Chem. Soc.*, **69** (1980) 221.
[300] Oguni M., Kanke Y. and Namba S., *AIP Conf. Proc.*, **982** (2004) 34.
[301] Schmidt R., Hansen E. W., Stoecker M., Akporiaye D. and Ellestad O. H., *J. Am. Chem. Soc.*, **117** (1995) 4049.
[302] Morishige K. and Iwasaki H., *Langmuir*, **19** (2003) 2808.
[303] Mondal P., Lunkenheimer P. and Loidl A., *Z. Phys. B*, **99** (1996) 527.
[304] Matsuo T., Suga H., David W. I. F., Ibberson R. M., Bernier P., Zahab A., Fabre C., Rassat A. and Dworkin A., *Solid State Commun.*, **83** (1992) 711.
[305] Hagen M. H. J., Meijer E. J. and Moolj G. C. A. M., *Nature*, **365** (1993) 5147.
[306] Mallamace F., Corsaro C., Broccio M., Branca C., González-Segredo N., Spooren J., Chen S.-H. and Stanley H. E., *Proc. Natl. Acad. Sci. U.S.A.*, **105** (2008) 12725.
[307] Matubayasi M., Wakai C. and Nakahara M., *Phys. Rev. Lett.*, **78** (1997) 2573.
[308] Modig K. and Halle B., *J. Am. Chem. Soc.*, **124** (2002) 12031.
[309] Modig K., Pfrommer B. G. and Halle B., *Phys. Rev. Lett.*, **90** (2003) 075502.
[310] Sebastiani D. and Parrinello M., *Chem. Phys. Chem.*, **3** (2002) 675.
[311] Svishchev I. M. and Kusalik P. G., *J. Am. Chem. Soc.*, **115** (1993) 8270.
[312] Gun'ko V. M. and Turov V. V., *Langmuir*, **15** (1999) 6405.
[313] Muller N., *J. Chem. Phys.*, **43** (1965) 2555.
[314] Hindman J. C., *J. Chem. Phys.*, **44** (1966) 4582.
[315] Hoffmann M. M. and Conradi M. S., *J. Am. Chem. Soc.*, **119** (1997) 3811.
[316] Mallamace F., Chen S.-H., Broccio M., Corsaro C., Crupi V., Majolino D., Venuti V., Baglioni P., Fratini E., Vannucci C. and Stanley H. E., *J. Chem. Phys.*, **127** (2007) 045104.
[317] Oleinikova A., Smolin N. and Brovchenko I., *Biophys. J.*, **93** (2007) 2986.
[318] Lagi M., Chu X. Q., Kim C. S., Mallamace F., Baglioni P., Chen S. H., *J. Phys. Chem. B*, **112** (2008) 1571.
[319] Purcell E. M., Torrey H. C. and Pound R. V., *Phys. Rev.*, **69** (1946) 37.
[320] Bloch F., *Phys. Rev.*, **70** (1946) 460.

[321] Becker E. D., in *Encyclopedia of Nuclear Magnetic Resonance*, edited by Grant D. M. and Harris R. K. (Wiley, Chichester) 1996, p. 2409.
[322] Grant D. M., in *Encyclopedia of Nuclear Magnetic Resonance*, edited by Grant D. M. and Harris R. K. (Wiley, Chichester) 1996, p. 1298.
[323] Abragam A., *The Principles of Nuclear Magnetism* (Clarendon, Oxford) 1961.
[324] Angell C. A., Shuppert J. and Tucker J. C., *J. Phys. Chem.*, **77** (1973) 3092.
[325] Pfrommer B. G., Mauri F. and Louie S. G., *J. Am. Chem. Soc.*, **122** (2000) 123.
[326] Stanley H. E., Kumar P., Xu L., Yan Z., Mazza M. G., Buldyrev S. V., Chen S. H. and Mallamace F., *Physica A*, **386** (2007) 729.
[327] Kumar P., Buldyrev S. V., Becker S. L., Poole P. H., Starr F. W. and Stanley H. E., *Proc. Natl. Acad. Sci. U.S.A.*, **104** (2007) 9575.
[328] Ball P., *Chem. Rev.*, **108** (2008) 74.
[329] Rupley J. A. and Careri G., *Adv. Protein Chem.*, **41** (1991) 37.
[330] Rupley J. A., Yang P. H. and Tollin G., *Water in Polymers*, edited by Rowland S. P. *ACS Symp. Ser.*, Vol. **127** (1980) p. 111.
[331] Gregory R. B., *Protein Solvent Interaction* (Marcel Dekker, New York) 1995.
[332] Iben I. R. T. *et al.*, *Phys. Rev. Lett.*, **62** (1989) 1916.
[333] Parak F. and Knapp E. W., *Proc. Natl. Acad. Sci. U.S.A.*, **81** (1984) 7088.
[334] Doster W., Cusak S. and Petry W., *Nature*, **337** (1989) 754.
[335] Rasmussen B. F., Stock M., Ringe D. and Petsko G. A., *Nature*, **357** (1992) 423.
[336] Caliskan G., Kisliuk A. and Sokolov A. P., *J. Non-Crystal Solids*, **307-310** (2002) 868.
[337] Chen S.-H., Liu L., Chu X., Zhang Y., Fratini E., Baglioni P., Faraone A. and Mamontov E., *J. Chem. Phys.*, **125** (2006) 171103.
[338] Bloemberger N., Purcell E. M. and Pound R. V., *Phys. Rev.*, **73** (1948) 679.
[339] Zaccai G., *Science*, **288** (2000) 1604.
[340] Bee M., *Quasielastic Neutron Scattering* (Adam Hilger, Philadelphia) 1988.
[341] Chu X. Q., Fratini E., Baglioni P., Faraone A. and Chen S. H., *Phys. Rev. E*, **77** (2008) 011908.
[342] Daniel I., Oger P. and Winter R., *Chem. Soc. Rev.*, **35** (2006) 858.
[343] Heremans K. and Smeller L., *Biochim. Biophys. Acta*, **1386** (1998) 353; Boonyaratanakornkit B. B., Park C. B. and Clark D. S., *Biochim. Biophys. Acta*, **1595** (2002) 235.
[344] Marques M. I., Borreguero J. M., Stanley H. E. and Dokholyan N. V., *Phys. Rev. Lett.*, **91** (2003) 138103.
[345] Chu X. Q., Faraone A., Kim C., Fratini E., Baglioni P., Leao J. B. and Chen S. H., *J. Phys. Chem. B*, **113** (2009) 5001.
[346] Zhang Y., Lagi M., Ridi F., Fratini E., Baglioni P., Mamontov E. and Chen S. H., *J. Phys.: Condens. Matter*, **20** (2008) 502101.
[347] Chu X. Q., Kolesnikov A. I., Moravsky A. P., Garcia-Sakai V. and Chen S. H., *Phys. Rev. E*, **76** (2007) 021505.
[348] Boonyaratanakornkit B. B., Park C. B. and Clark D. S., *Biochim. Biophys. Acta*, **1595** (2002) 235.
[349] Kolakowski P., Dumay E. and Cheftel J. C., *Food Hydrocolloids*, **15** (2001) 215.
[350] Fredrickson G. H. and Andersen H. C., *Phys. Rev. Lett.*, **53** (1984) 1244.
[351] Mallamace F., Branca C., Corsaro C., Leone N., Spooren J., Stanley H. E. and Chen S.-H., *J. Phys. Chem. B*, **114** (2010) 1870.
[352] Kumar P., *Proc. Natl. Acad. Sci. U.S.A.*, **103** (2006) 12955.
[353] Urbanc B., Borreguero J. M., Cruz L. and Stanley H. E., *Methods Enzymol.*, **412** (2006) 314.
[354] Zanotti J. M., Bellissent-Funel M.-C. and Parrello J., *Biophys. J.*, **76** (1999) 2390.
[355] Ringe D. and Petsko G. A., *Biophys. Chem.*, **105** (2003) 667.
[356] Wang J., Cieplak P. and Kollman P. A., *J. Comput. Chem.*, **21** (2000) 1049; Sorin E. J. and Pande V. S., *Biophys. J.*, **88** (2005) 2472.

[357] Vitkup D., Ringe D., Petsko G. A. and Karplus M., *Nat. Struct. Biol.*, **7** (2000) 34.
[358] Sokolov A. P., Grimm H., Kisliuk A. and Dianoux A. J., *J. Chem. Phys.*, **110** (1999) 7053.
[359] Norberg J. and Nilsson L., *Proc. Natl. Acad. Sci. U.S.A.*, **93** (1996) 10173.
[360] Tarek M. and Tobias D. J., *Phys. Rev. Lett.*, **88** (2002) 138101.
[361] Hartmann H., Parak F., Steigemann W., Petsko G. A., Ponzi D. R. and Frauenfelder H., *Proc. Natl. Acad. Sci. U.S.A.*, **79** (1982) 4067.
[362] Tournier A. L., Xu J. and Smith J. C., *Biophys. J.*, **85** (2003) 1871.
[363] Lee A. L. and Wand A. J., *Nature*, **411** (2001) 501.
[364] Lindahl E., Hess B. and van der Spoel D., *J. Mol. Modeling*, **7** (2001) 306.
[365] Artymiuk P. J., Blake C. C. F., Rice D. W. and Wilson K. S., *Acta Crystallogr. B*, **38** (1982) 778.
[366] Drew H. R., Wing R. M., Takano T., Broka C., Tanaka S., Itakura K. and Dickerson R. E., *Proc. Natl. Acad. Sci. U.S.A.*, **78** (1981) 2179.
[367] Tarek M. and Tobias D. J., *Phys. Rev. Lett.*, **88** (2002) 138101.
[368] Tournier A. L., Xu J. and Smith J. C., *Biophys. J.*, **85** (2003) 1871.
[369] Swenson J., *Phys. Rev. Lett.*, **97** (2006) 189801; Swenson J., Jansson H., Hedstrom J. and Bergman R., *J. Phys.: Condens. Matter*, **19** (2007) 205109.
[370] Chen S.-H., Liu L. and Faraone A., *Phys Rev. Lett.*, **97** (2006) 189803.
[371] Jorgensen W. L. and Tirado-Rives J. J., *Am. Chem. Soc.*, **110** (1988) 1657.
[372] Udier-Blagovic M., Tirado-Rives J. and Jorgensen W. L., *J. Am. Chem. Soc.*, **125** (2003) 6016.
[373] Tarek M. and Tobias D. J., *Biophys. J.*, **79** (2000) 3244.
[374] Tarek M. and Tobias D. J., *Phys. Rev. Lett.*, **89** (2002) 275501.
[375] Essmann U., Perera L., Berkowitz M. L., Darden T., Lee H. and Pedersen L. G., *J. Chem. Phys.*, **103** (1995) 8577.
[376] Hess B., Bekker H., Berendsen H. J. C. and Fraaije J. G. E. M., *J. Comput. Chem.*, **18** (1997) 1463.
[377] Garcia-Ruiz J. and Moreno A., *Acta Crystallogr. D*, **51** (1995) 278.
[378] Chen S. H., Liao C., Sciortino F., Gallo P. and Tartaglia P., *Phys. Rev. E*, **59** (1999) 6708.
[379] Kim C., *Simulation Studies of Slow Dynamics of Hydration Water in Lysozyme: Hydration Level Dependence and Comparison with Experiment using New Time Domain Analysis*, MS Thesis, Department of Nuclear Science and Engineering, MIT, August 2008.
[380] Merzel F. and Smith J. C., *Proc. Natl. Acad. Sci. U.S.A.*, **99** (2002) 5378.
[381] Zhang Y., Lagi M., Liu D., Mallamace F., Fratini E., Baglioni P., Mamontov E., Hagen M. and Chen S. H., *J. Chem. Phys.*, **130** (2009) 135101.
[382] Hedoux A. *et al.*, *J. Chem. Phys.*, **124** (2006) 014703.
[383] Smeller L., Meersman F. and Heremans K., *Biochim. Biophys. Acta*, **1764** (2006) 497.
[384] Scala A., Starr F., La Nave E., Sciortino F. and Stanley H. E., *Nature*, **406** (2000) 166.
[385] Angell C. A., Finch E. D., Woolf L. A. and Bach P., *J. Chem. Phys.*, **65** (1976) 3063.
[386] Chen S. H., Teixeira J. and Nicklow R., *Phys. Rev.*, **26** (1982) 3477.
[387] Singwi K. S. and Sjölander A., *Phys. Rev.*, **119** (1960) 863.
[388] Luzar A. and Chandler D., *Nature*, **379** (1996) 55.
[389] Suresh S. J. and Naik V. M., *J. Chem. Phys.*, **113** (2000) 9727.
[390] Wood K. *et al.*, *J. Am. Chem. Soc.*, **130** (2008) 4586.
[391] Xu L., Mallamace F., Starr F. A., Yan Z., Buldyrev S. V. and Stanley H. E., *Nat. Phys.*, **5** (2009) 565.
[392] Kumar P., Buldyrev S. V. and Stanley H. E., arXiv:0807.4699v1[cond-mat.soft].
[393] Mazza M. G., Giovambattista N., Starr F. W. and Stanley H. E., *Phys. Rev. Lett.*, **96** (2006) 057803.

[394] Mazza M. G., Giovambattista N., Stanley H. E. and Starr F. W., *Phys. Rev. E*, **76** (2007) 031202.
[395] Lee S. H. and Rossky P. J., *J. Chem. Phys.*, **100** (1994) 3334.
[396] Gallo P., Ricci M. A. and Rovere M., *J. Chem. Phys.*, **116** (2002) 342.
[397] Giovambattista N., Rossky P. J. and Debenedetti P. G., *J. Phys. Chem. B*, **113** (2009) 13723.
[398] Lombardo T. G., Giovambattista N. and Debenedetti P. G., *Faraday Discuss.*, **141** (2009) 359.
[399] Mancinelli R., Bruni F. and Ricci M. A., *J. Phys. Chem. Lett.*, **1** (2010) 1277.
[400] Swenson J., Jansson H. and Bergman R., *Phys. Rev. Lett.*, **96** (2006) 247802.
[401] Huwe A. *et al.*, *J. Phys. IV*, **10** (2000) 59.
[402] Rønne C., Åstarnd P.-O. and Keiding S. R., *Phys. Rev. Lett.*, **82** (1999) 2888.
[403] Torre R., Bartolini P. and Righini R., *Nature*, **428** (2004) 296.
[404] Private communication.
[405] Mallamace F., Earnshaw J. C., Micali N., Trusso S. and Vasi C., *Physica A*, **231** (1996) 207.
[406] Bertolini D., Cassettari M. and Savetti P., *J. Chem. Phys.*, **76** (1982) 3285.
[407] Bergman R., Mattson J., Svanberg C., Schwartz G. A. and Swenson J., *Europhys. Lett.*, **64** (2003) 675.
[408] Swenson J., Schwartz G. A., Bergman R. and Howells W. S., *Eur. Phys. J. E*, **12** (2003) 179.
[409] Swenson J., Bergman R. and Longeville S., *J. Chem. Phys.*, **115** (2001) 11299.
[410] Jansson H. and Swenson J., *Eur. Phys. J. E*, **12** (2003) S51.
[411] Swenson J., Jansson H., Howells W. S. and Longeville S., *J. Chem. Phys.*, **122** (2005) 084505.
[412] Yoshida K., Yamaguchi T., Kittara S., Bellissent-Funel M. C. and Fourquet P., *J. Chem. Phys.*, **129** (2008) 054702.
[413] Gallo P., Rovere M. and Chen S.-H., *J. Phys. Chem. Lett.*, **1** (2010) 729.
[414] Paolantoni M., Sassi P., Morresi A. and Santini S., *J. Chem. Phys.*, **127** (2007) 024504.
[415] Hwang D. W., Chu C.-C., Sinha A. K. and Hwang L.-P., *J. Chem. Phys.*, **127** (2007) 044702.
[416] Teixeira J., Luzar A. and Longeville S., *J. Phys.: Condens. Matter*, **18** (2006) S2353.
[417] Doster W. and Settles M., *Biochim. Biophys. Acta*, **1749** (2005) 173.
[418] Jansson H. and Swenson J., *Biochim. Biophys. Acta*, **1804** (2010) 20.
[419] Doster W., Busch S., Gaspar A. M., Appavou M.-S., Wuttke J. and Scheer H., *Phys. Rev. Lett.*, **104** (2010) 098101.